University of Trento
Department of Civil, Environmental and Mechanical Engineering

Aldo Madaschi

A nonlinear viscoplastic double yield surface constitutive model for geologic materials

April 2015

Doctoral school in
Engineering of Civil and Mechanical Structural Systems
XXVII Cycle

University of Trento
Department of Civil, Environmental and Mechanical Engineering
Doctoral school in
Engineering of Civil and Mechanical Structural Systems
XXVII Cycle – Scientific Disciplinary Sector ICAR/07

Aldo Madaschi

A NONLINEAR VISCOPLASTIC DOUBLE YIELD SURFACE CONSTITUTIVE MODEL FOR GEOLOGIC MATERIALS

Advisor: Prof. Alessandro Gajo

Trento, April 2015

University of Trento
Doctoral school in Engineering of Civil and Mechanical Structural Systems

PhD program head: Prof. Paolo Scardi

Final examination: 24/04/2015

Board of Examiners

Prof. Claudio Di Prisco	Politecnico di Milano (IT)
Prof. Enrico Canuto	Politecnico di Torino (IT)
Prof. Ernesto D'Avanzo	University of Salerno (IT)

Substitutes members

Prof. Oreste Salvatore Bursi	University of Trento (IT)
Prof. Radu Madare	Aalborg University (DK)

Abstract

A new constitutive model is proposed to describe the stress-strain-time behaviour of clays and organic soils. This approach is based on the framework of overstress viscoplastic theory and can be applied to any elastoplastic (inviscid) model.

The most innovative idea of the proposed model is the identification of two components of strain for each deformation mechanism. In particular, in both the elastic and the plastic regimes a fast and a slow strain mechanism are assumed to be present. To this aim the constitutive model is based on two yield surfaces based on overstress viscoplasticity theory: one is quasi-instantaneous (for the fast part of plastic deformations) and the other is viscous (for the slow part of plastic deformations).

This assumption permits the reliable simulation of the mechanical behaviour of a wide range of clayey soils: from inorganic clay (a.e. kaolinite and bentonite), to organic clays and peats.

A further interesting aspect of the proposed model is the capability of simulate both the normally consolidated and the overconsolidated regime within a unique constitutive approach.

An extensive experimental program on three different peaty soils has been performed to validate the constitutive model. The experimental tests include a wide range of oedometric tests (with very different loading conditions), and a series of triaxial tests conducted on NC and OC peats. The model has been validated also by simulating the settlements of a real embankment founded on a thick layer of organic clay.

Acknowledgements

First and foremost, I bring my deepest gratitude to my advisor, Prof. Alessandro Gajo, for his help, support and encouragements throughout this research work.

I am highly thankful to Dr. Francesco Cecinato for his constant support, to Mr F. Fedrizzi for his invaluable help in performing some of the laboratory tests, and Mr G. Nardin and Mr F. De Polo for supplying the peat samples.

Moreover, I would like to thank Dr. Davide Trapani, Dr. Emiliano Debiasi, Dr. Luca Argani, and Dr. Daniele Veber for their friendship, and all my colleagues: Dr. Federico Bosi, Dr. Mattia Bacca, Ing. Summer Shazad, and Ing. Eliana Bortot, the people that worked side by side with me in these years.

I would also like to thank Dr. Severine Romero Baivier and all members of Enabling Technology group of Vesuvius s.a. for their hospitality and cooperation.

Finally, I am particularly indebted to all my family for their continuing encouragement and, I express my thank to my beloved Marija for her patience and never-ending support.

List of publications

1. A. Gajo, A. Madaschi, F. Girardi, R. Di Maggio. Improving the mechanical response of kaolinite and bentonite through exposure to organic and metallorganic compounds. *Géotechnique*, Volume 63, Issue 11, March 2013, 977-982.

2. S. Muraro, A. Madaschi, A. Gajo. On the reliability of 3D numerical analyses on passive piles used for slope stabilization in frictional soils. *Géotechnique*, Volume 64, Issue 6, May 2014, 486-492.

3. A. Madaschi, A. Gajo. One-dimensional response of peaty soils subjected to a wide range of oedometric conditions. *Geotechnique* DOI: 10.1680/geot.14.P.144, 2015.

4. A. Madaschi, A. Gajo, M. Molinari and D. Zonta. Characterization of the dynamic behavior of shallow foundations with full-scale dynamic tests. *Journal of Geotechnical and Geoenvironmental Engineering* (In press).

5. S. Muraro, A. Madaschi, A. Gajo. Passive soil pressure on sloping ground and design of retaining structures for slope stabilization. *Géotechnique* (In press).

6. A. Madaschi, A. Gajo. A one-dimensional viscoplastic constitutive approach for modelling the delayed behavior of clayey and organic soils. (In preparation).

7. A. Madaschi, A. Gajo. A viscoplastic double yield surface constitutive model for geologic materials. (In preparation).

8. A. Madaschi, C. Di Maio, A. Gajo. Modelling of very long time behaviour of peats: a viscoelastic-viscoplastic approach. (In preparation).

9. A. Madaschi, A. Gajo, M. Molinari and D. Zonta. Dynamic characterization of a steel wind turbine tower. (In preparation).

Contents

List of Figures

List of Tables

CHAPTER 1

Introduction

The need for reliable constitutive models capable of providing a realistic description of the time-dependent behaviour of soils has increased in recent years, as the use of very soft and highly compressible clay layers (as it typically occurs in coastal areas) or even of organic clays and peats (as it typically occurs in mountain areas) as foundation soil has increased. In most of these cases, time dependency is generally too significant to be ignored (Bjerrum 1967). The challenges for geotechnical engineers involve the capacity of predicting the long-term response of these soils when subjected to complex loading histories, such as large loading/unloading cycles and small load increments/decrements, applied after a creep or relaxation phase, or sudden changes in the strain rate.

A great number of constitutive models describing the time-dependency of clays has been proposed in the literature. Most of these models have been reviewed in a fairly recent paper by Liingaard et al. (2004), where the authors proposed the following general classification:

- *empirical models* which are obtained by fitting experimental results and generally have a validity which is limited to specific boundary and loading conditions;

- *rheological models* which are relevant to uniaxial conditions and can be based either on a differential representation (that can be visualized by elastic springs, plastic sliders, viscous dashpots), on engineering theories of creep, or on the so-called hereditary approach;

- *general stress-strain-time models* which provide a multiaxial formulation, usually expressed in incremental form (which is suitable for implementation in finite element codes), and can be based on different approaches, such as the overstress theory by Perzyna (1963a), the non-stationary flow surface theory by Naghdi and Murch (1963), or others.

The constitutive model proposed in this work belongs to both the second and the third of the above categories. In fact, it has been firstly developed in a uniaxial framework by employing a series of non-linear rheologic elements, and then extended to the general multiaxial formulation resorting to the overstress theory.

The uniaxial model is based on a differential representation in which non-linear springs, sliders and viscous dashpots are used. The non-linearity of these elementary mechanical elements has been deduced from empirical models, with particular reference to the strain rate approach (i.e. the so-called isotach model) firstly proposed by Suklje (1957), and later investigated in detail by Leroueil, Kabbaj, et al. (1985). Then, the proposed uniaxial model has been extended to multiaxial stress conditions, allowing us to formulate the model within the framework of Perzyna's overstress theory and extending the concepts developed for uniaxial conditions to multiaxial tests.

The resulting model is a strain hardening model, formulated in such a way that the time variable does not feature in the hardening relationships, in order to avoid the difficulties that usually arise in the definition of an equivalent time, whenever complicated loading histories are considered.

The innovative aspects of the proposed constitutive approach are essentially three. The first one concerns the distinction between a short-term (immediate) and a long-term elastic and plastic response. This approach has never been proposed in the literature so far, and is particularly useful to distinguish between the behaviour of inorganic clays and the behaviour of organic clays and peats. In particular, in inorganic clays, short-term deformations are large compared to those occurring at later stages, in contrast with organic soils where the short-term deformation behaviour is negligible. This concept has been developed in the uni-axial framework and then extended, with slight modifications, to the multiaxial formulation. The existence of a short- and a long-term plastic mechanism has important consequences in the general model formulation, as it requires to incorporate two Perzyna's overstress yield surfaces: the first one represents the quasi-instantaneous deformation mechanism, whereas the second one represents the viscous part of plastic deformation.

The second innovative aspect of the proposed model concerns the use of a logarithmic law for the viscous effects that, although often employed in general models based on overstress theory, it is has been rarely used for a general model valid both in normally consolidated and in overconsolidated regimes. The logarithmic relationship is shown to simulate consistently all the well-accepted empirical laws concerning the delayed behaviour of soils, such as the Sukjle's isotach concepts (1957), the Bjerrum's theory (1973) of time dependent com-

pression, the concept of overconsolidation due to ageing, and the concept of constant C_α/C_c ratio by Mesri and Godlewski (1977).

A further element of originality of the proposed approach is that it takes into account viscous deformation both in elastic and plastic phases. The definition of viscoelastic behaviour allows the simulation of unloading phases and cyclic unloading-reloading processes accounting for the viscous deformation of the solid skeleton.

In oedometric conditions the proposed model reliably simulates most of the possible experimental set-ups, thus the following aspects of soil's delayed behaviour are correctly captured: the isotach concept (Suklje 1957) postulating the existence of a unique stress-strain curve for each strain rate; the concept of preconsolidation induced by ageing at constant stress (Bjerrum 1967); the effects of strain rate on the preconsolidation pressure (Leroueil, Kabbaj, et al. 1985); the concept of constant C_α/C_c ratio Mesri and Castro 1987; Terzaghi et al. 1996; Mesri and Ajlouni 2007); and the secondary deformations induced by a small stress increment ratio (Fox, Edil, and Lan 1992; Mesri, Stark, and Chen 1994; Mesri, Stark, Ajlouni, et al. 1997).

Also in axisymmetric conditions the model is shown to simulate with good accuracy the main features of clays' delayed response. In particular, the following aspects can be reliably simulated: the strain rate effect both in normally consolidated (Tatsuoka et al. 1998) and strongly overconsolidated regimes (Augustesen et al. 2004), the tertiary creep phenomenon in undrained triaxial tests, and the triaxial relaxation (and the related strain rate effects) (Lacerda and Houston 1973; Silvestri et al. 1988).

To validate the proposed constitutive framework, an extensive experimental program has been carried out on three different peats with very different organic contents. The testing program involved a number of conventional and unconventional oedometer tests and some triaxial test. The oedometer laboratory tests involved multi-stage loading (MSL) with small and large load increments/decrements and loading/unloading cycles, as well as tests at constant rate of stress (CRSS) and at constant rate of strain (CRSN), and measurements of pore pressure dissipation in a Rowe consolidation cell (RC-MSL). The triaxial testing program involved both drained and undrained tests in both normally consolidated and highly overconsolidated regimes. Simulations of all the performed tests have been performed with the proposed model, corroborating the capabilities of the model to predict the delayed behaviour of peat, also for very complicate boundary conditions.

The thesis is organized as follows. Chapter 2 shows a brief literature review of the most important evidences of stress-strain-time behaviour of clays both in

one-dimensional and triaxial conditions. Chapter 3 describes a comprehensive set of experimental data concerning the time-dependent behaviour of organic clays and peats. The experimental analyses concerned three different peaty soils (either undisturbed or remoulded) with fairly different index properties (the organic content ranged between 20% and 70%) that were submitted to various kinds of 1D consolidation and triaxial tests. Chapter 4 deals with a review of the constitutive approaches to the modelling of time dependent behaviour of clays.

The one-dimensional viscoelastic-viscoplastic constitutive model is described in Chapter 5. The basic hypotheses and the theoretical formulation are shown, together with the implementation of the constitutive relationship in the FEM code Abaqus (Hibbitt et al. 2009), and the simulation of several tests with a wide range of boundary conditions.

The general multiaxial constitutive model is presented in Chapter 6. In this Chapter, the extension of the one-dimensional constitutive model to the multiaxial case is treated. In the first part, the additional constitutive hypotheses for the extension to 3D case, and the numerical implementation in FE environment, are described. In the second part, the model is used for the simulation of a series of experiments on clay and peat.

Chapter 7 treats the application of the proposed model to the simulation of the settlements of a real embankment founded on a thick layer of organic clay. The measured settlement after one year from construction was of about 1 m, and the model (calibrated through a classical oedometric test) is shown to be able to capture with good accuracy the real behaviour of the infrastructure.

Conclusions are finally drawn in Chapter 8.

CHAPTER 2

Literature evidences of time-dependent behaviour of clays

This chapter presents a review of the main experimental results on time dependent phenomena of clayey soils both in oedometric and in triaxial conditions. The possible experimental set-up to investigate the stress-strain-time behaviour of materials are creep, relaxation and rate dependency tests. The most interesting studies are shown and commented in order to highlight the major feature of soils viscous behaviour. One of the main outcome of this literature review is that most of the possible time dependent effects of clay follows the isotach principle.

2.1 Introduction

In the evaluation of the performance of civil structures the deformations of the foundation soil, play a crucial role in the global response of the structure. For clayey soils, it is well known that the response in terms of serviceability limit states is often more constrictive than that of ultimate limit states. Analysing the response of real structures founded on clay, one of the problematic aspects is that of the time-dependent deformations (Mesri and Choi 1985; Tanabashi et al. 1988; Crawford and Morrison 1996). In the case of organic clays or peats, the most important phenomenon in determining the mechanical response of the soil is the rheological behaviour(Hartlén and Wolski 1996; Kazemian et al. 2011).

In order to optimize the design of civil structures, it is necessary to have reliable constitutive models based on laboratory and field investigations. Laboratory tests in particular, represent the main source of information for the

formulation and validation of constitutive models.

This chapter reviews the main experimental evidences concerning time dependent behaviour of cohesive soils, such as clay and peat. This will allow the general characteristics of the rheological behaviour of clay to be identified, in order to formulate the hypothesis of the proposed constitutive framework.

A considerable number of studies have been published regarding the experimental evaluation of the time-dependent response of clayey and peaty soils. A noteworthy contribution is that of Augustesen et al. (2004) where the most important studies on the characterization of the viscous behaviour of clays are explained.

This chapter continues on the basis of the structure proposed by Augustesen et al. (2004) and following a brief note regarding the terminology and the peculiarity of saturated soil creep, it analyses the most important contributions concerning oedometer and triaxial testing.

In this analysis the temperature effects have not been considered, and the description has been restricted only to the stress-strain-time response, without any consideration regarding the involved phenomena at the micro-scale.

2.2 Time-dependent behaviour: definition of creep

In continuum mechanics, all deformation processes involving a direct dependence to the time variable are identified as creep phenomena. Considering a simple mono-dimensional example, with stress and strain involved as macroscopic quantities, there are two simple experiments that can highlight material creep behaviour: the *creep test* (Fig. 2.1a), performed by maintaining a constant applied stress, and the *relaxation test* (Fig. 2.1b) performed by measuring the evolution of stress at constant strain.

These two types of experimental configurations highlight two different aspects of the same physical phenomenon: viscous deformation related to micro scale material structure modifications. In many cases, depending on the problem being analysed, one of the two aforementioned testing approaches is preferred, neglecting the correlation with the other. As a consequence, the resulting analysis and modelling approach are only applicable to problems in which the deformation process involves the specific creep evidence used in the formulation.

The formulation of a reliable constitutive framework, applicable to a generic boundary value problem, must be based on a wide range of experimental obser-

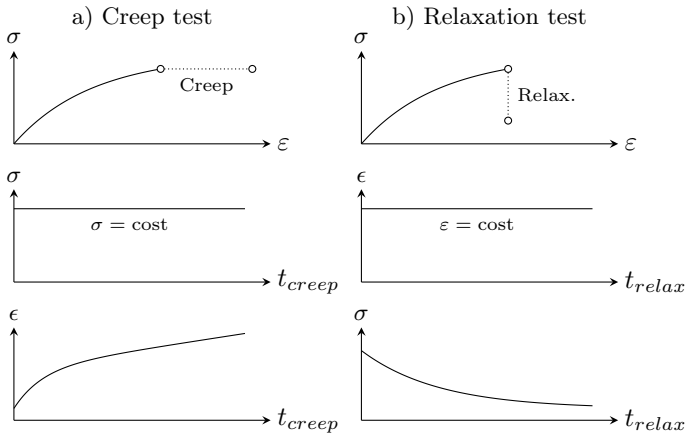

Figure 2.1: Typical tests to investigate the viscous behaviour of materials: a) Creep test, and b) Relaxation test.

vations, involving different boundary conditions and test set-ups. This would allow, the validation of the constitutive approach to be extended to a generic multi-dimensional problem that entails general and variable boundary conditions.

2.2.1 Identification of creep regimes

The essential feature in the delayed behaviour of an engineering material can be identified by observing a typical uniaxial creep curve (Fig. 2.2a). In the classical theory of creep, three regimes of the creep process may be distinguished: the *primary creep*, the *secondary* or *steady state creep*, and the *tertiary creep* (Skrzypek 1993). In the primary creep regime, as time increases, the strain rate decreases, in the secondary creep it remains approximately constant, and during the tertiary creep phase an increase in the strain rate is observed and the material deterioration causes a *creep rupture* (Fig. 2.2a).

Similarly in soil mechanics, though a different terminology has been defined starting from the results of a classical incremental loading oedometer test; there are three compression phases: *primary compression*, coincident with the primary consolidation; *secondary compression*, in which the strains are purely viscous and increase with slope approximately constant in a strain-log time plot; and,

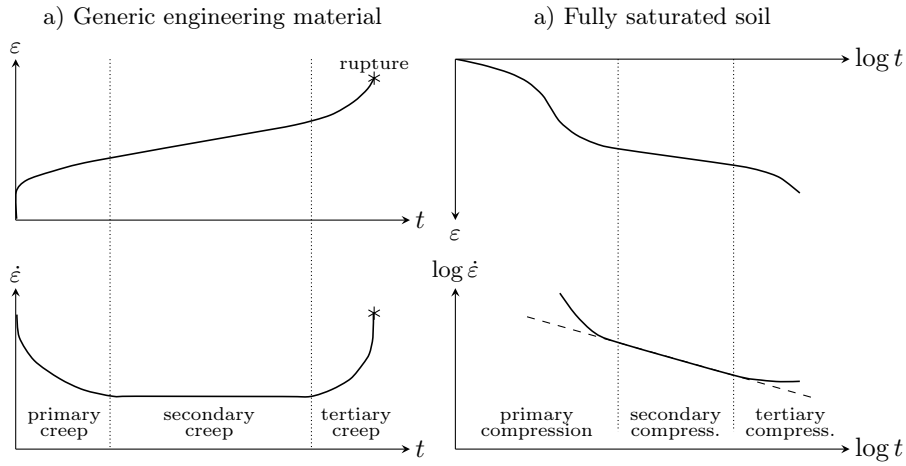

Figure 2.2: a) Definition of creep phases for engineering materials from a constant stress test; b) definition of compression phases for fully saturated soil from an oedometer creep test

in some cases, the *tertiary compression*, in which the curve strain-log time shows a nonlinear trend (Fig. 2.2b).

These two descriptions are widely used in soil mechanics; however it is worth highlighting the difference between *creep* and *compression*. In particular, observing the evolution of the strain rate during an oedometer test it is possible to deduce that both secondary and tertiary compression can be identified as primary creep, since the strain rate is decreasing in the two cases (Augustesen et al. 2004, Fig. 2.2b).

2.2.2 Delayed behaviour of saturated soils

The stress-strain behaviour of saturated soils is strongly affected by the coupling between the solid skeleton and the liquid phase. The consolidation theory (Terzaghi 1925) explains the development of the primary deformation and its dependency on the dissipation of the excess pore pressure induced by loading. The consolidation phenomenon, although introducing a delay in the strain development, cannot be considered as creep because it does not involve the viscosity of the solid phase.

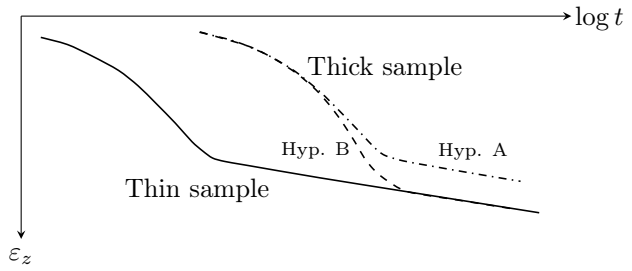

Figure 2.3: Hypotheses A and B in a oedometer test with different sample thickness (after Ladd et al. (1977)).

The combination of the consolidation process with the creep deformation of the solid phase leads to the problem of defining the exact end time of primary consolidation (EOP) (Fig. 2.3). This problem, also known as the *problem of reference time* (Augustesen et al. 2004), deeply affects the evaluation of secondary compression in clayey soils. The issue lies in identifying when the creep deformation starts.

The problem of reference time has been analysed in depth in the relevant literature, and two well-accepted approaches have been proposed for the estimation of the secondary deformations, namely hypotheses A and B (Ladd et al. 1977):

- *Hypothesis A*: the sample thickness has no effect on the location of EOP. As a consequence, it is possible to define a unique value of strain at EOP. In other words, the soil does not show creep deformation during the primary consolidation (Ladd et al. 1977; Mesri and Choi 1985);

- *Hypothesis B*: creep deformations also occur during pore pressure dissipation, and the strain at EOP is not unique (Suklje 1957; Bjerrum 1967; Leroueil, Kabbaj, et al. 1985; among other authors).

The experimental evidences presented in the literature cannot clarify whether one of the two hypotheses represents real soil behaviour. The author's opinion is that the real behaviour of clay is somewhere between the two limit cases represented by *Hypothesis A* and *Hypothesis B*. The dissipation of pore pressure, and the consequent increase in effective stress, induces a gradual and growing viscous effect. As a result, at the beginning of the consolidation process the viscous effects can be neglected. The viscous deformations become increasingly

important during the development of primary consolidation, since the effective stress, and thus the stress applied to the solid skeleton, increases.

Another peculiar aspect of saturated soils, related to the coupling between solid and liquid phases, is the distinction between drained and undrained conditions. The differences in the effective stress-strain response induced by the two different drainage conditions are well known, and can be highlighted performing classical triaxial tests. Triaxial tests can be used also to investigate the delayed behaviour of the soil performing creep or relaxation tests.

In the case of creep test, the selected drainage condition deeply affects the test results and the interpretation method.

In drained triaxial creep test the effective stress is maintained constant during the creep phase and as a consequence, it represents a true creep test. On the other hand, considering the effective stress path for an undrained triaxial creep test, this kind of test does not reproduce a pure creep condition but rather a mixed test. In particular, during the creep phase performed at constant deviatoric stress, the effective isotropic pressure decreases, due to the development of pore pressure related to the accumulated viscous strains. Therefore, undrained triaxial creep tests represent a creep test for the deviatoric component of the stress tensor, and a relaxation test for the isotropic part.

These observations must be considered during the interpretation of the experimental results, and can be a useful validation for the formulation of a general multi-axial constitutive model.

2.3 One-dimensional behaviour

The most common laboratory test performed to examine the delayed behaviour of soils is the oedometer test. This is performed by loading the sample in unidimensional strain conditions. Two test setups are usually employed in the definition of time-dependent behaviour of clays:

- Incremental Loading (IL) test performed applying a series of different steps with constant total stress and measuring the evolution of vertical strain; and

- Constant Rate of Strain (CRS) test which consists in the application of a constant rate of strain, measuring the vertical stress by means of a load cell.

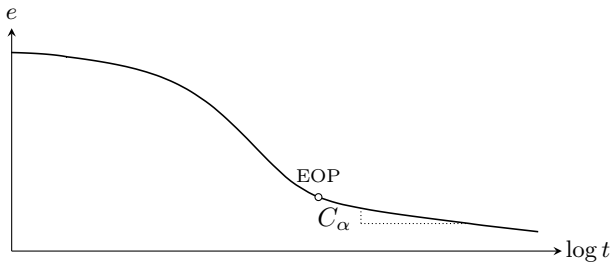

Figure 2.4: Example of oedometer curve from standard IL test.

2.3.1 Incremental Loading Oedometer tests

The standard test routine for Incremental Loading oedometer test (as described in ASTM-D2435-11 (2011)) consists in a series of steps involving 'a load increment ratio of one' with a 'standard load increment duration... of 24 h'. The typical result of a load increment is shown in Figure 2.4. For most soils, it is easy to identify the end of primary consolidation and the subsequent secondary compression phase (as defined in Section 2.2.1).

The parameter that describe the viscous behaviour of soil is the coefficient of secondary compression, C_α (Mesri 1973), which represents the slope of the oedometer curve, in a void ratio-logarithm of time plot ($e - \log t$), after primary consolidation has come to an end. The coefficient of secondary consolidation can also be expressed as a function of vertical strain (eq. (2.1)).

$$C_\alpha = -\frac{\Delta e}{\Delta \log t} \qquad C_{\alpha\varepsilon} = \frac{\Delta \varepsilon}{\Delta \log t} = \frac{C_\alpha}{1 + e_0}. \tag{2.1}$$

Starting from eq. (2.1b) it is possible to derive a simple relationship for a first rough estimation of the secondary compression strains:

$$\varepsilon_{\mathrm{z}}^{\mathrm{v}}(t) = C_{\alpha\varepsilon} \log\left(1 + \frac{t}{t_{\mathrm{i}}}\right), \tag{2.2}$$

in which $\varepsilon_{\mathrm{z}}^{\mathrm{v}}(t)$ represents the viscous strain at time t, and t_{i} represents the reference time of start of viscous deformations. As mentioned in *problem of reference time* the determination of the reference time is a key issue that deeply affects the results of this calculation.

In most of the cases, C_α cannot be directly used for the evaluation of the

viscous deformation but represents a good index to define the soils' viscous behaviour.

In particular, Mesri and co-workers highlight the strong correlation between C_α and the 'local' compression index $C_c = -\Delta e/\Delta\sigma'_z$ (Mesri and Godlewski 1977; Mesri and Castro 1987; Terzaghi et al. 1996; Mesri and Ajlouni 2007). Starting from a large number of oedometer tests conducted on a wide range of different soils, Mesri and co-workers identified a narrow range of variation of the C_α/C_c ratio that is almost constant for a specific soil. Table 2.1 below shows the values of C_α/C_c evaluated for various geotechnical materials (Terzaghi et al. 1996).

Material	C_α/C_c
Granular soils including rockfill	0.02 ± 0.01
Shale and mudstone	0.03 ± 0.01
Inorganic clays and silts	0.04 ± 0.01
Organic clays and silts	0.05 ± 0.01
Peat and muskeg	0.06 ± 0.01

Table 2.1: Values of C_α/C_c for geotechnical materials (Terzaghi et al. 1996)

This coupling allows to define an approximate value of C_α from the deformability of the soil. Starting from this observation it is possible to conclude that the coefficient of secondary consolidation depends on the effective stress, σ'_z, and on the preconsolidation pressure σ'_{pc}. In particular, it reaches a maximum around σ'_{pc}, then decreases and reaches a steady state values for high applied stresses. This trend has been confirmed experimentally by several authors (Tavenas et al. 1978; Graham et al. 1983; Lancellotta 2008).

Another aspect related to the concept of constant C_α/C_c ratio is the effect of the stress increment ratio on the strain development with respect to time. The classical strain-log t curve for an oedometer step shown in Figure 2.4, is valid for stress increment comparable with the previous effective stress ($\Delta\sigma_z/\sigma'_z \simeq 1$). The application of smaller load increments leads to a change in the shape of strain-log t. In particular, the classical 'S' shape tends to vanish when the stress increment ratio is reduced. Additionally, for very low values of $\Delta\sigma_z/\sigma'_z$ the curves show a first phase with negligible primary settlements, followed by significant secondary settlements with a markedly increasing slope in the log time plot.

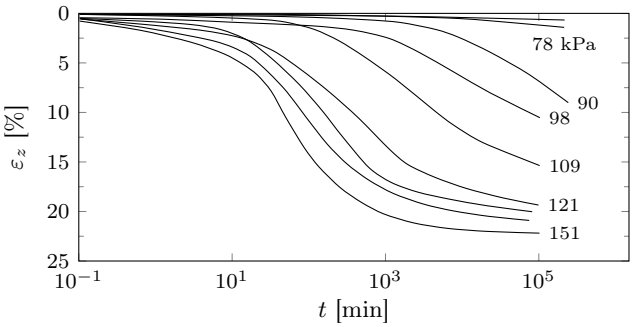

Figure 2.5: Results of IL oedometer tests on undisturbed Batiscan clay with different load increment ratio (Leroueil, Kabbaj, et al. 1985).

Many authors highlighted this aspect (Leroueil, Kabbaj, et al. 1985; Fox, Edil, and Lan 1992; Mesri, Stark, and Chen 1994; Mesri, Stark, Ajlouni, et al. 1997). Figure 2.5 shows the IL oedometer tests performed by Leroueil, Kabbaj, et al. (1985) on undisturbed specimens of Batiscan clay. It is worth noting that the preconsolidation pressure of Batiscan clay, was of about 88 kPa. As a result, the effect of stress increment ratio on the shape of the consolidation curves can therefore be noted.

The shape of the IL compression curves differs from the classical shape (Fig. 2.4) for soils with high organic content such as peat soils. In many cases, peats present large secondary deformations that make the primary consolidation difficult to identify. The 'S' shape hence becomes difficult to identify as the strain-log time curve is, according to laboratory time scale, almost linear (Dhowian and Edil 1980; Mesri and Ajlouni 2007). When the test time is increased, the compression curves ($\varepsilon - \log t$) for peats show a pronounced non-linearity with a constant increase of the slope of secondary phase. As a consequence, the estimation of secondary settlement of peaty soils using a constant C_α (determined with classical laboratory time-scale) can be affected by large error.

Another fundamental work in the comprehension of time dependent behaviour of clays in oedometric conditions is that of Bjerrum (1967). In this study the author highlighted the development of a reserve resistance against compression during the delayed compression at constant effective load. This concept was formulated observing the results of an experimental study on Drammen plastic clay (Figure 2.6) performed loading the sample up to the load of $p_0 = 13\,\mathrm{ton}/m^2$, and maintaining the load constant for about 30 days. Subse-

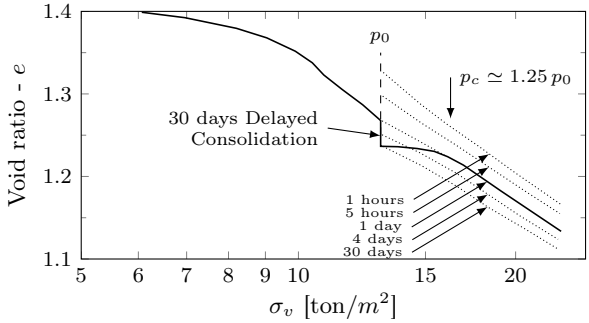

Figure 2.6: Oedometer test on plastic Drammen clay demonstrating the development of reserve resistance against further compression during 28 days of delayed consolidation (Bjerrum 1967).

quently the sample was loaded in steps lasting one day. The curve thus obtained shows that the specimen developed a critical pressure, $p_c \simeq 1.25 \times p_0$. This effect was called *quasi-preconsolidation* effect, and denotes the preconsolidation induced by ageing.

2.3.2 Constant Rate of Strain oedometer tests

The strain rate dependency of clays delayed behaviour has been deeply investigated by Constant Rate of Strain (CRS) oedometer tests. This kind of test was first proposed by Hamilton and Crawford (1959) and then developed by several other authors (a. e. Smith and Wahls 1969; Lowe et al. 1969). Among the advantages of CRS set-up there is the reduced test time as well as the possibility of determination of a continuous stress-strain curve (with a direct evaluation of preconsolidation pressure). In this test, the strain rate is chosen so that 'significant' pore pressure does not develop in the specimen and therefore effective stress is assumed to be equal to applied stress (Gorman et al. 1978).

The CRS oedometer test can be employed in order to focus the soil rheological behaviour changing the strain rate applied to the specimen. The main outcome of this test is that the higher the strain rate the higher the effective stress is at the same strain level (Crawford 1965; Leroueil, Kabbaj, et al. 1985, shown in Fig. 2.7a). From Figure 2.7a it is possible to deduce the strong correlation between the applied strain rate and the observed preconsolidation pressure, σ'_{pc} (in particular, σ'_{pc} is almost linear with respect to $\log \dot{\varepsilon}_{\mathrm{z}}$).

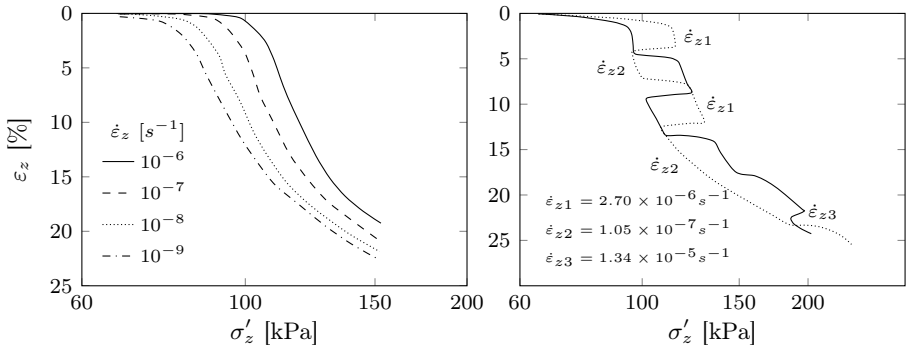

Figure 2.7: Results of strain-rate controlled oedometer tests on undisturbed Batiscan clay: a) Constant Rate of Strain tests, b) Step-Changed Strain Rate tests (Leroueil, Kabbaj, et al. 1985).

This observation is consistent with the 'isotach behaviour' proposed by Suklje (1957) and confirmed by Bjerrum (1967). The 'isotach' concept postulates a unique relationship between stress, strain and strain rate.

The existence of a correlation between the stress-strain curve and the strain rate is confirmed by observing the results of step-changed rate of strain tests (Leroueil, Kabbaj, et al. 1985; Lansivaara and Nordal 2000). The step in the applied strain rate leads to a reversible step in the compression curve (Fig. 2.7b).

2.4 Triaxial behaviour

The delayed behaviour of clays in triaxial conditions has been explored with four types of test:

- drained triaxial creep test: performed applying the deviatoric stress in drained conditions, and maintaining the effective stress state constant in the following creep phase (measuring the deviatoric and volumetric deformations);

- undrained triaxial creep test: performed applying the deviatoric stress in undrained conditions, and maintaining the total stress state constant

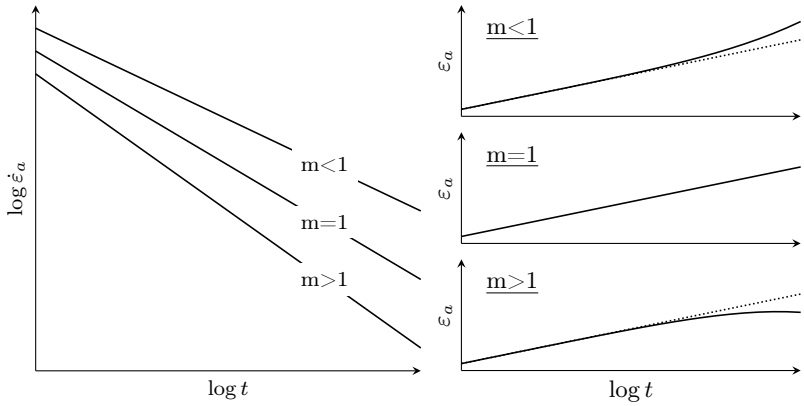

Figure 2.8: Creep characteristics for three different m values, and the related $\varepsilon_a - \log t$ curves (after Augustesen et al. 2004).

in the following creep phase (measuring the deviatoric strains, and, if possible, the pore pressure);

- undrained triaxial relaxation test: performed alternating load phases at constant axial strain rate with relaxation phases at constant axial strain (measuring the decay of the deviatoric stress and the development of the pore pressure);

- undrained triaxial test with different strain rates and with step changed strain rates.

Several studies have been performed regarding undrained triaxial creep of clays. However, there are relatively few reports of drained creep and relaxation test available in the literature. The following section reports the main outcomes of the existing studies.

2.4.1 Drained triaxial creep

The most representative graphs to analyse the results of triaxial drained creep tests are the $\log \dot{\varepsilon}_a - \log t$ and the $\log \dot{\varepsilon}_v - \log t$ plots. The standard $\log - \log$ diagram shows a series of lines with almost constant slope as well as strain rate growing with respect to the deviatoric stress level. The creep behaviour can

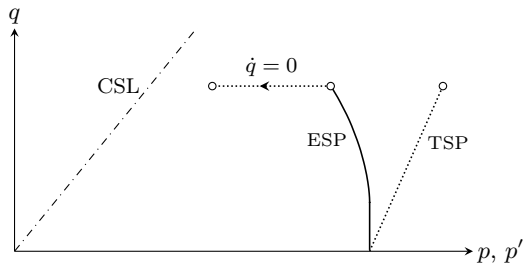

Figure 2.9: Total Stress Path (TSP) and Effective Stress Path (ESP) for a undrained triaxial creep test.

therefore be analysed through the parameter $m = -\Delta \log \dot{\varepsilon} / \Delta \log t$, which is the average slope of the creep lines in the $\log \dot{\varepsilon}$ plot (Augustesen et al. 2004).

In order to understand the effect of different m values on delayed response of the soil, it is useful to draw the $\varepsilon_a - \log t$ plots corresponding to three different values of m (Fig. 2.8). The strain-time curve is a straight line for $m = 1$ and presents an upward concavity for $m < 1$, and a downward concavity for $m > 1$.

Many authors have tried to analyse the evolution of the logarithmic creep slope, m, with respect to deviatoric load. The results are contrasting, and it is therefore not possible to draw a clear relationship to define a unique trend of m parameter. Particularly, Singh and Mitchell (1968) and Den Haan (1994) found that values of m are somewhat independent from the deviatoric stress level, while Bishop and Lovenbury (1969), Tian et al. (1994), Feda (1992) and Zhu et al. (1999) reported a stress dependence in the logarithmic creep slope.

Regarding the values of m, the experimental works show a general agreement. In particular, most of the authors found that m varies between 0.7 and 1 with the lower values for peats and organic clays.

Most of the studies regarding drained triaxial creep do not observe tertiary creep, and the strain rate continuously decreases by increasing the elapsed time. Tavenas et al. (1978) shows a series of drained triaxial creep tests on lightly overconsolidated clay. In some cases, for high levels of deviatoric stress the typical tertiary creep behaviour was observed. To the best of the author?s knowledge, this is the only available example of tertiary creep founded in drained triaxial tests.

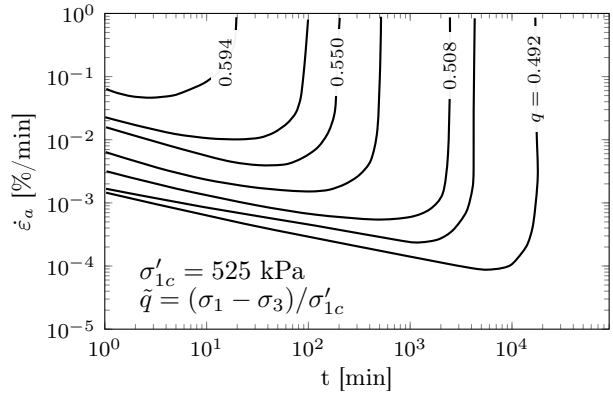

Figure 2.10: Results of undrained triaxial creep test on normally consolidated clay (Campanella and Vaid 1972).

2.4.2 Undrained triaxial creep

The undrained triaxial creep does not represent a pure creep test (Section 2.2). During the creep phase the developed pore pressure induces a change in the effective isotropic stress with constantly applied total stress (Fig. 2.9).

Several studies have been published regarding undrained triaxial creep tests on clay. The most important results of test performed on undisturbed normally consolidated clays are those of Murayama and Shibata (1958), Campanella and Vaid (1972), and Campanella and Vaid (1974).

The common results of these tests is that, for deviatoric stress levels far from the rupture, the response is linear in a $\log \dot{\varepsilon}_a - \log t$ plot. On the other hand, increasing the stress level, the specimens show tertiary creep where the logarithm of the time of rupture is related almost linearly to the applied deviatoric stress (Fig. 2.10).

The development of pore pressure during the creep phase of a specimen subjected to creep rupture has been previously analysed by Campanella and Vaid (1974). They reported the comparison between the pore pressure measured during the tertiary creep phase and that measured from a classical undrained triaxial test. The development of the excess of pore pressure with respect to axial strain and its final amplitude resulted to be nearly the same for the two tests. As a consequence, Campanella and Vaid (1974) demonstrated that the failure envelope of creep rupture, in $q - p'$ space, is the same of the standard

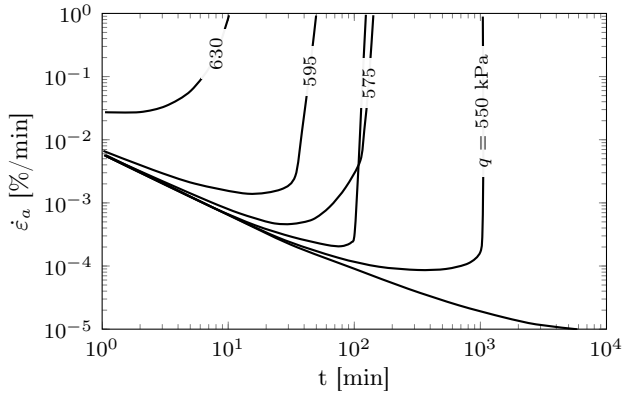

Figure 2.11: Results of undrained triaxial creep test on strongly overconsolidated St. Jean-Vianney clay (Vaid and Campanella 1977).

constant rate of strain undrained triaxial tests.

This kind of behaviour has also been observed for strongly overconsolidated clays by Vaid and Campanella (1977). Figure 2.11 shows the undrained creep curves for strongly overconsolidated St. Jean-Vianney clay. In this case, the excess of pore pressure developed during the creep phase is negative as the effective isotropic stress increases.

Although the isotropic effective stress is not constant during the creep phase, the undrained creep rupture can be useful from the modelling point of view allowing the verification of the more general multi-axial constitutive framework.

2.4.3 Triaxial relaxation

Historically, the standard approach to time-dependent phenomena in geomechanics has been the study of the evolution of strain at constant applied stress. Relaxation phenomena of soils have been ignored for their minor influence from the engineering point of view. Many of the proposed modelling approaches have been formulated starting from creep test results and are inapplicable to real cases where the stress is relaxing due to the viscous deformation. Since the creep and relaxation phenomena are two sides of the same phisical process, the formulation of a consistent constitutive framework for time-dependent behaviour of soil must be applicable to general boundary value problems. The

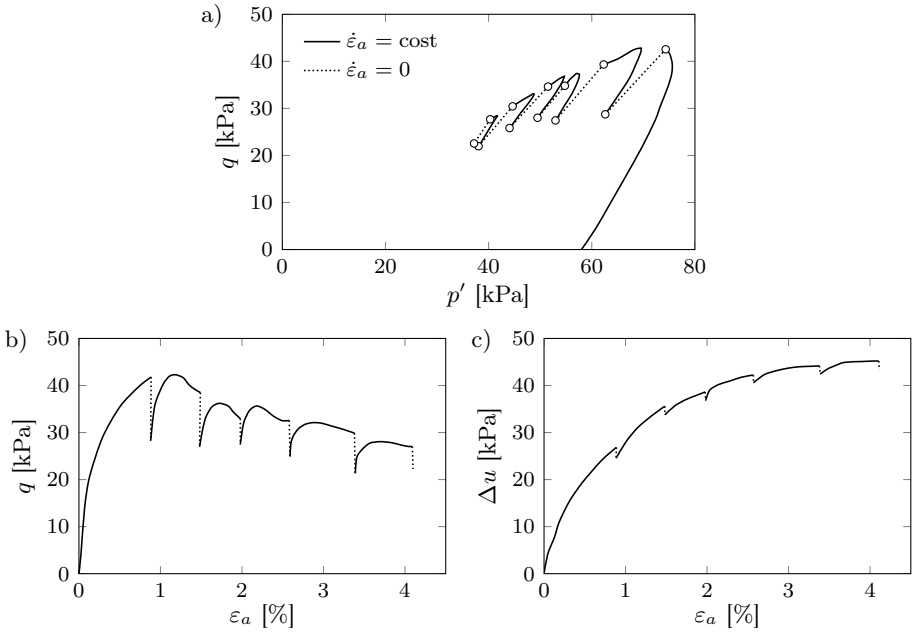

Figure 2.12: Results of CIU triaxial relaxation test on normally consolidated (Silvestri et al. 1988): a) effective stress path; b) deviatoric stress vs axial strain curve; c) excess of pore pressure vs axial strain curve.

validation of the model with different kind of experimental tests is an indicator of the quality of the constitutive hypotheses.

The typical relaxation test is performed applying the deviatoric stress loading the specimen with constant rate of strain and successively maintaining constant the strain for a certain period of time (generally for some hours). After the relaxation phase the load can be recovered with the initial axial strain rate. The results are displayed in terms of relaxation curves ($\varepsilon_{a,relax} - \log t$) with the standard undrained triaxial plots ($q - p'$, $q - \varepsilon_a$, and $\Delta u - \varepsilon_a$).

Triaxial stress relaxation of clays tests have been subjected to relatively fewer studies. Most of the works (Murayama and Shibata 1961; Christensen and Wu 1964; Lacerda and Houston 1973) show a linear development of the relaxation

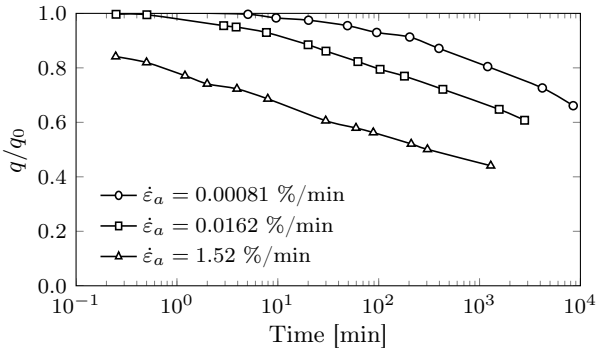

Figure 2.13: Relationship of q/q_0 vs. $\log t$ for different loading strain rates of San Francisco Bay Mud (Lacerda and Houston 1973).

stress with respect to $\log t$.

Figure 2.12 below shows the results of the test performed by Silvestri et al. (1988). From the effective stress path the elastic anisotropy of the tested materials is clearly visible. In terms of relaxation, the deviatoric stress drop is more than 1/4 of the initial stress.

Silvestri et al. (1988) performed several relaxation tests with different initial deviatoric stresses. They observed that the stress states after one day of relaxation are located on a unique curve, called 'static effective stress path'. This 'static' curve may also be obtained performing undrained triaxial tests with very slow strain rate. It is also worth noting the analogy of this experimental observation with the concept of 'static yield surface' proposed by Perzyna (1966) in the formulation of overstress theory.

Further observations regarding the relaxation process concern the development of pore pressures during the constant strain phase. Many authors observed that the pore pressure drops slightly during the relaxation phase (Lacerda and Houston 1973; Silvestri et al. 1988; Sheahan et al. 1994). The relative variation, with respect to the total excess of pore pressure, is smaller compared to the relative drop in the deviatoric stress (Figs. 2.12b and 2.12c).

Another aspect of the relaxation process is the correlation between the time of the beginning of the stress relaxation and the strain rate applied during the application of the deviatoric load. Lacerda and Houston (1973) highlighted that the slower the loading phase, the greater is the delay at the beginning of the relaxation (Fig. 2.13). This observation therefore confirms the correlation

between stress relaxation and the rate dependent creep phenomena.

2.4.4 Strain rate effect in undrained triaxial test

Section 2.3.2 shows the strain rate effects in oedometer Constant Rate of Strain Tests. From the experimental point of view, it is possible to reproduce a similar test in triaxial conditions changing the strain rate during the application of deviatoric load.

Starting from normally consolidated clays Tatsuoka et al. (1998) highlighted the classical response to changes in the axial strain rate during undrained triaxial test. The results obtained for Fujinomori clay are shown in Fig. 2.14a. The steps in the applied strain rates correspond to steps in the deviatoric stress. The increase of the strain rate induces an increase of the deviatoric load and the comparison with a constant rate of strain test shows very good consistency for the same strain rate. This behaviour is similar to that observed in oedometric condition by Leroueil, Kabbaj, et al. (1985) (Fig. 2.7b).

Another interesting observation on strain rate effect of clay can be deduced from the stress path of undrained triaxial tests performed at different strain rates. (Hinchberger and Rowe 2005) shows that the deviatoric stress at failure is affected by the applied strain rate whereas the failure envelope is independent of the rate of application of the deviatoric load (Fig. 2.14c).

The strain rate behaviour of strongly overconsolidated (OC) clays has some analogies with that of normally consolidated clays. The typical stress-strain curve of OC clays shows a peak of strength followed by a softening phase. The results of undrained triaxial tests on Saint Jean-Vianney clay are reported in Figure 2.14b, (Vaid, Robertson, et al. 1979). Analysing the position of the peak stress for different strain rates shows that increasing the loading strain leads to an increase of the rate the peak stress as well as an increase in the axial strain at stress peak. This behavioural patterns have been observed by many other authors (Tavenas et al. 1978; Lefebvre and LeBoeuf 1986; Zhu et al. 1999).

2.5 Conclusions

In this Chapter the most important contribution regarding time-dependent behaviour of clay has been described. The most important outcome of this review is that the main characteristics of delayed behaviour of non structurated clay can be efficaciously described by isotach concept.

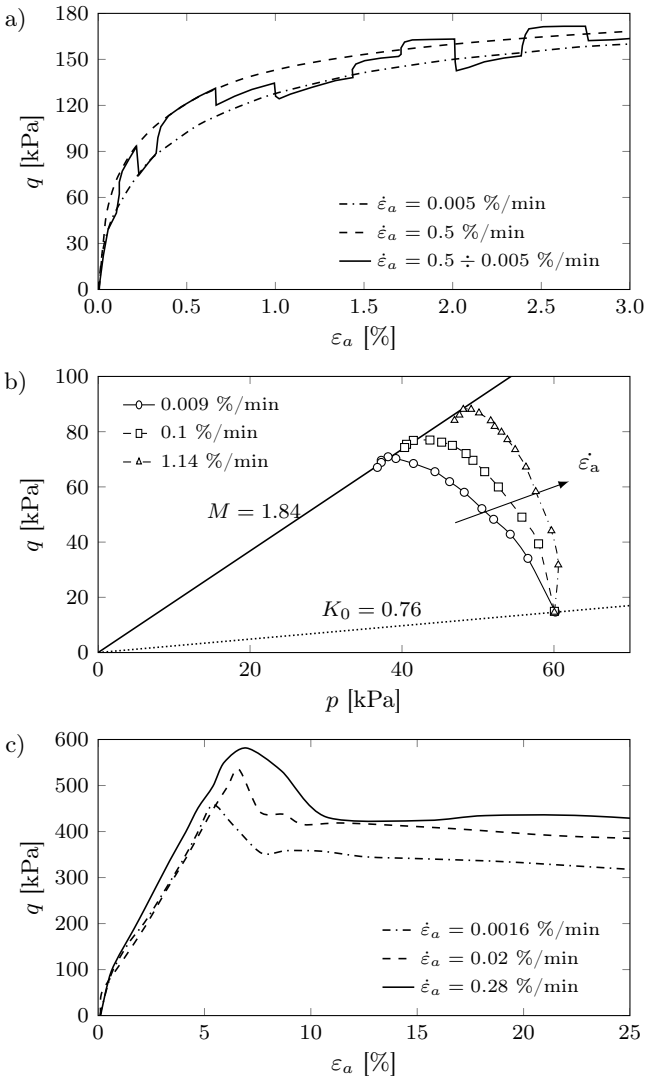

Figure 2.14: Strain rate effect in triaxial tests:
a) step changed strain rate on TxCU test on NC Fujinomori clay (Tatsuoka et al. 1998); b) Stress paths of TxCAU tests performed at different strain rates on NC Sackville clay (Hinchberger and Rowe 2005); c) TxCU tests on OC Saint Jean-Viannej clay (Vaid, Robertson, et al. 1979).

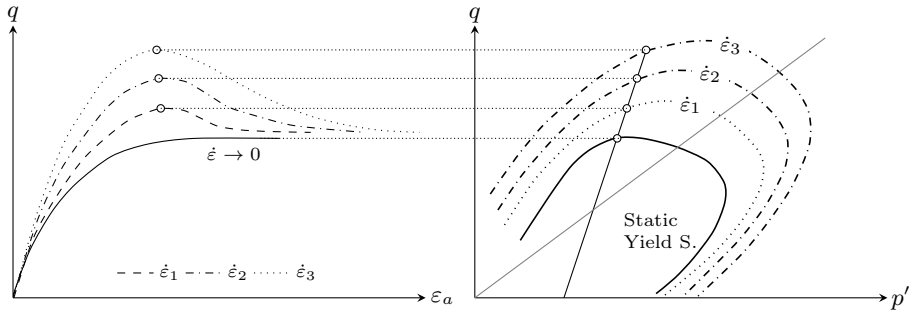

Figure 2.15: Schematics of strain rate effect on limit state surface (Augustesen et al. 2004).

In addition, from a comprehensive view on all the rate dependent effects on clays in a general multiaxial conditions (CRS oedometric conditions, triaxial relaxation and CRS) it is reasonable to suppose the existence of a limit state surface influenced by the strain rate which determine the viscous behaviour of clayey soils. This observation has been effectively represented by Augustesen et al. (2004) in their scheme of limit state surface (reported in Fig. 2.15).

CHAPTER 3

Experimental results of laboratory tests on peat

This chapter describes a comprehensive set of experimental data concerning the mono-dimensional and triaxial, time-dependent behaviour of organic clays and peats. The experimental analyses concerned three different peaty soils (either undisturbed or remoulded) with fairly different index properties (the organic content ranged between 20% and 70%) that were submitted to various kinds of 1D consolidation tests. The experimental data confirm that peats and organic clays have many aspects of their delayed behaviour in common. The main outcome of this experimental work is a good-quality, comprehensive and meaningful set of data for use in developing and calibrating constitutive models for simulating the delayed response of soils, with an emphasis on organic clays and peats.

3.1 Introduction

In geotechnical engineering practice, organic clays and peaty soils are often considered difficult subsoils due to their considerable compressibility and long-term, time-dependent response to loading. Remediation techniques usually involve completely removing the peat layer (if it is shallow) or using deep foundations, or applying a surcharge load, or accepting late settlements (adopting geotextiles in order to reduce the embankment's lateral movements, Rowe et al. 1984) and adopting re-levelling techniques in the engineering construction. In many cases, the first two methods may be economically unfeasible, while the surcharge load can be applied effectively to contain secondary settlement (Mesri and Feng 1991). In design practice, however, using the latter two methods generally makes it difficult to predict long-term performance. In engineering practice, reliable tools are often needed to predict the long-term, mechanical response of peaty

soils with complicated loading histories, whether they involve large load/unload cycles or small load increments/decrements. The development of reliable constitutive models for predicting the mechanical behaviour of peaty soils during the course of complex loading histories is therefore of great practical importance for the reliable analysis of engineering structures interacting with peaty soils.

The time-dependent response of peaty soils depends on a number of factors (Mesri 1973; Fox and Edil 1996; Kazemian et al. 2011), including loading rate, amplitude of the load/unload increments, strain rate, temperature, and previous loading history. So far, the major part of research effort has been paid to the delayed behaviour of inorganic, fine-grained soils which have been subjected to intensive experimental investigations. The fundamental works (Suklje 1957; Bjerrum 1967; Berre and Nersen 1972; Mesri 1973; Mesri and Godlewski 1977) investigated the time-dependent behaviour of inorganic soils and traced the general framework of the soils delayed response, starting with laboratory investigations. More recently, Navarro and Alonso (2001), Y. Wang and Xu (2007), and Hu and Hueckel (2007) took new perspectives on the possible causes of inorganic soil creep that might be attributable to local soil dehydration, double porosity changes, and chemo-mechanical effects.

If we restrict our attention to 1D compression, the most important aspects of the delayed behaviour of inorganic soils - which are applicable to peaty soils, with relevant practical and theoretical implications - can be summarized as follows:

- the dependence of the coefficient of secondary compression C_α on the compression index C_c (Mesri and Godlewski 1977; Mesri and Castro 1987);
- the quasi-preconsolidation effect induced by ageing under constant stress (Bjerrum 1967; Schmertmann 1983; Mesri and Castro 1987);
- the influence of small stress increments/decrements on the soil's delayed behaviour (K. Lo 1961; Mesri and Feng 1991; Fox, Edil, and Lan 1992)
- the effects of the strain rate and loading rate on compression behaviour and apparent preconsolidation pressure (Leroueil, Kabbaj, et al. 1985);
- the influence of delayed response on pore pressure dissipation (Berry and Vickers 1975).

The long-term response of peaty soils has been the object of less research than is the case for inorganic soils. Published laboratory findings on the mechanical behaviour of peaty soils have mainly shown that: secondary deformations

of peaty soils are significantly larger than primary ones in many cases (Mesri, Stark, Ajlouni, et al. 1997; Gunaratne et al. 1998); the time-compression relationship is rather different from that of most inorganic soils and, under particular conditions, the coefficient of secondary compression C_α is not constant over time (Dhowian and Edil 1980; Fox, Edil, and Lan 1992); the C_α/C_c ratio (where C_c denotes the local slope of $e-\log\sigma'_v$) is slightly larger ($0.04-0.07$, Terzaghi et al. 1996) than for inorganic clays ($0.03-0.05$, Terzaghi et al. 1996); and peaty soils exhibit a variety of mechanical properties, with a broad array of indexes and compressibility characteristics (Santagata et al. 2008). Although Mesri, Stark, Ajlouni, et al. (1997) and Mesri and Ajlouni (2007) have shown that many of the features of the delayed response of inorganic soils are applicable to peaty soils too (e.g. the quasi-preconsolidation effect, and the effects of surcharge ratio and of strain rate), some aspects (such as the influence of delayed response on pore pressure dissipation) remain unexplored for peaty soils.

The aim of this work was to produce a comprehensive set of experimental data concerning the 1D, delayed behaviour of peaty soils. All the above-mentioned aspects were considered with a view to confirming and verifying to what extent the well-accepted concepts concerning the delayed behaviour of inorganic clays are also applicable to peaty soils. Three different peaty soils (one undisturbed, one partially disturbed, and one remoulded) with fairly different index properties (the organic content ranged between 20% and 70%) were submitted to several different 1D consolidation tests. A series of incremental loading (IL) tests was run using standard oedometric equipment, with standard and non-standard load increments/decrements and loading/unloading cycles. In this paper, the term 'standard' denotes the oedometer tests commonly used for practical design purposes, as described in ASTM-D2435-11 (2011) for instance (involving 'a load increment ratio of one', point 11.4.1, and a 'standard load increment duration ... of 24 h', point 11.5.1). Tests on the constant rate of stress (CRSS) and constant rate of strain (CRSN) were performed as well to thoroughly examine the rate effects in both the virgin loading and in the unloading/reloading phases. The effects of delayed response on pore pressure dissipation after 1D compression were analysed using a Rowe consolidation cell and an incremental loading program (RC-IL).

It is worth adding that the experimental research presented below was originally motivated by the need to have a complete and comprehensive set of experimental data for the development and calibration of a constitutive model that will be presented in a companion paper. That is why we have deliberately provided the experimental data without any reasoning associated with a given conceptual model or constitutive framework. This obviously does not imply that our ex-

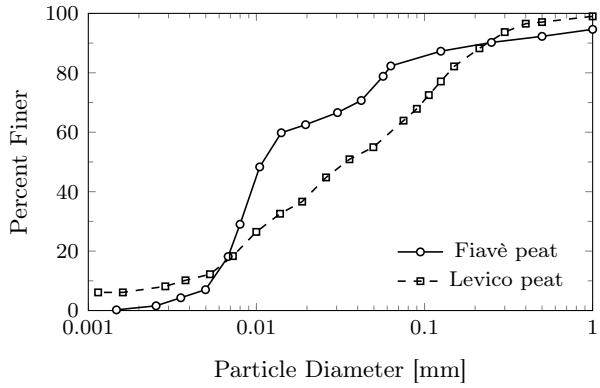

Figure 3.1: Particle size distribution of Fiavè and Levico peat.

perimental findings are in contrast with the models proposed in the literature. However, the comprehensive nature of these experimental results will certainly make them useful for calibrating and validating other constitutive models designed to simulate the delayed response of soils, and peaty soils in particular. These experimental results will also be of practical interest in any engineering application involving complex histories of load increments/decrements.

3.2 Materials

Three different types of fibrous peat were tested in this study. All the peat samples were collected from sites in the Trentino and Southern-Tyrol area of northern Italy (the first sample came from a lacustrine swamp in Fiavè, the second from a bog near Levico, and the third from a deep layer in Egna). The Fiavè peat specimens were obtained with a Shelby sampler with a diameter of 101.6 mm at a depth of 7.5 m. The Levico specimens were partially disturbed because they were collected from a surficial excavation at a depth of about 3 m, without strictly applying the procedure for collecting cubic samples (ASTM-D7015-13 2013). The samples from Fiavè and Levico were thus defined as 'natural'. In contrast, the disturbed samples from Egna were collected from a bore hole at a depth of 10 m without using any kind of undisturbed sampling method. The three peat samples are denoted below as *Fiavè*, *Levico* and *Egna* peats, respectively.

Specimen		Levico Peat	Fiavè Peat	Egna Peat
Mean Specific Gravity G_s		2.25	1.83	1.59
Inorganic Specific Gravity G_{sm}		2.72	2.70	2.63
Organic Specific Gravity G_{so}		1.33	1.37	1.37
Organic matter (%)		19.9	49.3	71.0
Liquid limit w_L (%)		$114^{(1)}$	$305^{(1)}$	$346^{(2)}$
Natural water content w (%)		$150 \div 180$	209	280
Plastic limit w_p (%)		$76^{(3)}$	$183^{(3)}$	$226^{(4)}$ ($272^{(3)}$)
Plastic index I_p (%)		38	126	$121^{(4)}$ ($74^{(3)}$)
Compression index C_c	Nat.	$1.05 \div 1.39$	1.67	-
	Rem.	0.82	1.72	1.87
Swelling index C_s	Nat.	$0.11 \div 0.13$	0.21	-
	Rem.	0.11	0.29	0.28

(1) measured with the Casagrande cup, (ASTM-D4318-10 2010)
(2) measured with liquid limit penetrometer
(3) measured according to ASTM-D4318-10 (2010)
(4) measured with the fall-cone penetration method (Feng 2000).

Table 3.1: Index properties for peat specimen.

The particle size distribution of the samples was ascertained in accordance with ASTM-D6913-04 (2009) and ASTM-D422-63 (2007), and the organic content was assessed by igniting samples oven-dried in a furnace at $440 \pm 40\,^{\circ}\mathrm{C}$ (ASTM-D2974-14 2014). All the oven-drying procedures needed to classify the soil were completed at a temperature of $60\,^{\circ}\mathrm{C}$ (Head 2014) to prevent oxidation of the organic content.

The specific gravity of the soils was measured with a pycnometer in accordance with ASTM-D854-14 (2014). The procedure was conducted on the original material to obtain the mean specific gravity of the solid phase G_s, and on the ash remaining after burning the samples in the furnace to ascertain the specific gravity of the inorganic solid phase G_{sm}. Starting from the organic content, the specific gravity of the organic matter G_{so} can be estimated from

the well-known phase relationships of saturated soils. The resulting G_{so} values were consistent with the values in the literature for peat with a high organic content (Kazemian et al. 2011).

Due to the high organic fibre content the liquid limit of Egna peat could not be evaluated with the Casagrande cup thus the liquid limit penetrometer was employed, in contrast with the evaluations performed on Levico and Fiavè peats. The liquid limits reported in Table 3.1 clearly increase with the increase of organic content. Equivalently, due to fibre content, the plastic limit of Egna peat could be assessed with difficulty using the standard procedure, thus, in addition, the fall-cone method (Feng 2000) was adopted for the sake of comparison. Figure 3.2 shows the position of the three peats in the plasticity chart.

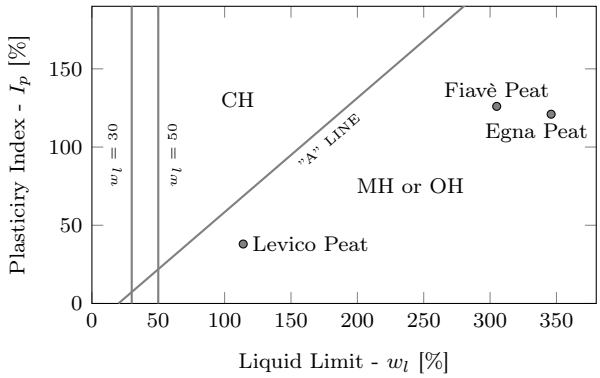

Figure 3.2: Plasticity chart (Casagrande 1948).

Grain size analysis was only done on the Fiavè and Levico peats, which can both be classified as sandy silts with an organic content of about 49% and 20%, respectively. The organic content of the Egna peat was 71%. The main characteristics of the peats are given in Table 3.1, and the particle size distributions are shown in Figure 3.1.

Since the Levico peat was found to contain much coarser portions than the others, some homogeneous remoulded samples were obtained from the peat collected in Levico by mixing a large amount of material - after removing the coarsest and most fibrous portions (including organic fibres more than about 10 mm long, which corresponded to less than 10% of the volume). It is worth noting that the natural water content of Levico peat is higher than the liquid limit (in Table 3.1). This has been seen in other peats too (Huat et al. 2009)

and may relate to numerous factors (e.g. cementation, thixotropic hardening), one of which may be the chemical composition of the fluid added to the sample to establish its liquid limit (Yang and Dykes 2006). For the sake of completeness one remoulded sample was obtained from the Fiavè peat too. The remoulded samples were obtained by adding distilled water up to a water content approximately $1.5 \times w_L$. All remoulded samples were prepared by pouring the liquid soil into the oedometric cells, except for the remoulded sample submitted to oedometric consolidation in the Rowe cell, which was first consolidated up to 30 kPa, in a large consolidation cell.

3.3 Experimental program

The experimental program described below consisted of three types of oedometer test:

- Incremental Loading (IL) tests in standard oedometer cells, with standard and non-standard load increments and durations, one of which lasted for more than a year;
- Constant Rate of Strain (CRSN) tests in standard oedometer cells, performed in the virgin loading phase;
- cyclic Constant Rate of Stress (CRSS) tests in standard oedometer cells, performed at different stress rates in the reloading phase;
- Rowe Cell, Incremental Loading (RC-IL) tests, under single drainage conditions, measuring the pore pressure at the bottom of the specimen.

Most of the tests was performed without any strict temperature control, so the estimated range of temperature variation was 16 ± 4°C in winter and 22 ± 3°C in summer. The only exceptions were the IL tests performed on all the remoulded samples and the RC-IL test, which were performed under strict temperature control (20 ± 1°C).

The different tests enabled an in-depth examination of some particular aspects of the rheological behaviour of peaty soils, as described below.

In addition to the extensive program of oedometer tests, some triaxial tests have been performed on remoulded samples of Levico peat. The triaxial tests program consists of five undrained tests with different constant strain rates, and one drained test with stepped axial strain rate.

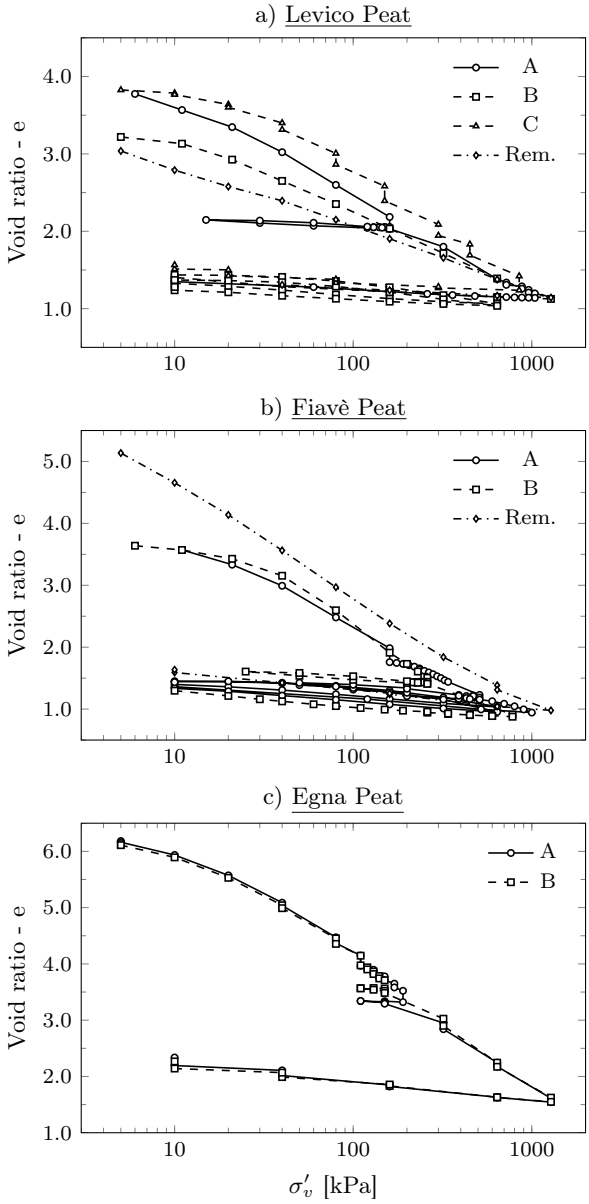

Figure 3.3: Oedometric Compression Curves:
a) Levico Peat; b) Fiavè Peat; c) Egna Peat.

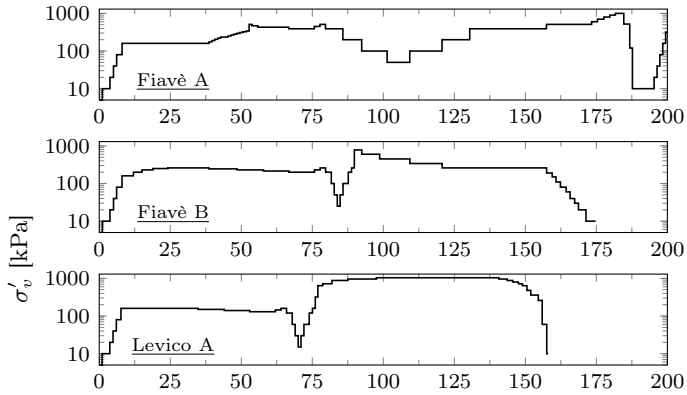

Figure 3.4: Schematics of the loading history applied for the non-standard MLS oedometer tests on: a) Fiavè (spec. A); b) Fiavè (spec. B); c) Levico (spec. A); d) Egna (spec. A); e) Egna (spec. B).

3.4 Results of IL Oedometer Tests

Oedometer tests were performed on each of the peats investigated, i.e. undisturbed samples of Fiavè and Levico peats, and remoulded samples of all peats. The initial sample size was 80 mm in diameter and 20 mm in height. The loading history of each test is briefly summarised below. The salient aspects of the delayed soil response measured are described in detail in the following sections (all the experimental results are provided in the electronic supplementary material).

The loading histories applied to the two samples of undisturbed Fiavè peat (denoted as Fiavè A and Fiavè B), and to the 'natural' Levico A specimen are schematically shown in Fig. 3.4, where we can see that long creep tests (30 days) alternated with steps lasting 24 hours and involving small or large load variations. The Levico B specimen, and the remoulded samples from Levico and Fiavè were tested with standard loading increments and decrements (not shown in Fig. 3.4), each lasting 24 hours in both the loading and the unloading phases (Fig. 3.3b).

The 'natural' Levico C specimen underwent standard sequential loading up to 900 kPa, with standard load increments and decrements that were kept constant for about 1 month each, so that the total duration of the test was more

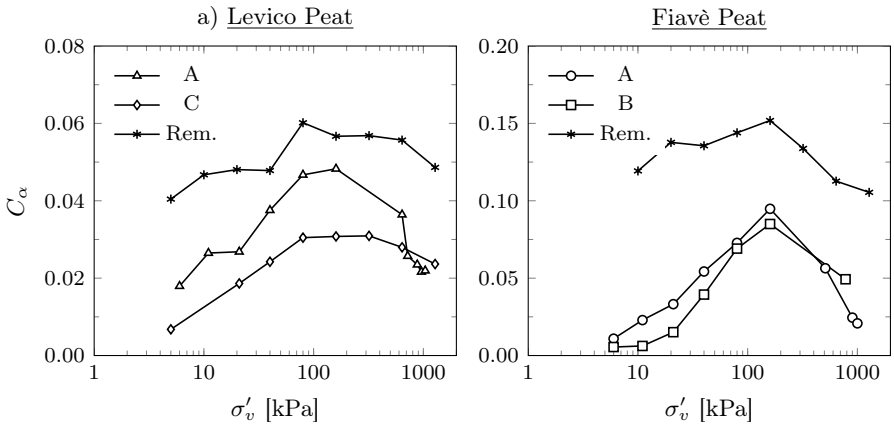

Figure 3.5: Secondary compression index C_α for Fiavè and Levico specimens.

than a year. Note, in Fig. 3.3a, that the delayed compression and swelling phases are highlighted with a vertical segment to distinguish them from the deformation after 24 hours.

It is worth emphasising that the Fiavè and Egna specimens were more homogeneous, in terms of initial water content and compressibility, than the Levico specimen. From Fig. 3.3a it can be argued that the initial non-homogeneity of the Levico samples could not be eliminated by means of a simple pre-loading step up to the effective in-situ stress (about 20 kPa).

It is worth noting that, in all the tests discussed below, the peat's 1D behaviour was dominated by secondary compression and the large viscous deformation makes it difficult to ascertain when primary consolidation ended (EOP). The oedometric compression curves shown in Fig. 3.3 (and in the figures below) consequently correspond to 24 h of consolidation (except for the very long loading steps, for which two symbols denote the consolidation after 24 h and at the end of the loading step, respectively, Figs. 3.3a and 3.3c).

Analysing the oedometric consolidation curves for the Fiavè peat (Fig. 3.3a) with Casagrande's well-known graphical method provides preconsolidation pressure values σ'_{vp} ranging between 30 kPa and 40 kPa. The vertical effective in-situ stress is about 40 kPa, so the sample can reasonably be considered normally consolidated. It is worth noting that, from the estimated soil age ($5000 \div 10000$ years, since the soil was deposited after the last ice age) and measured soil prop-

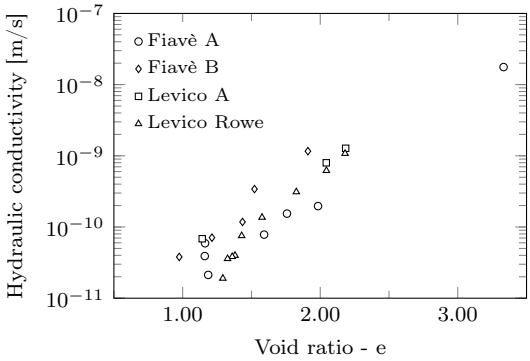

Figure 3.6: Hydraulic conductivity versus void ratio for tested materials.

erties (from C_α/C_c, see Fig. 3.7), a quasi preconsolidation ratio due to aging of about $1.2 \div 1.5$ would be expected Mesri and Castro 1987. This is in contrast with the experimental observations (showing a preconsolidation ratio of about 1.0) and might be due to sample disturbance. In contrast, the Levico specimens (Fig. 3.3a) were much less homogeneous in terms of initial water content due to the shallow depth of collection (which was close to the water table), prior history and possible disturbance during sampling. This non-homogeneity had little influence on the compression indexes or preconsolidation pressure, however, and the latter ranged between 15 kPa and 20 kPa. A comparison of the preconsolidation pressure with the expected vertical effective in-situ stress (about 20 kPa) leads us to conclude that the Levico peat was normally consolidated too.

The compression and swelling indexes calculated from the oedometric compression curves are shown in Table 1. The indexes are clearly related to the organic content, which also affects the Atterberg limits. It is worth adding that, for the Levico peat, the compression index of the 'natural' soil was considerably larger than that of the remoulded sample, unlike the case of the Fiavè peat. The greater compressibility and the large natural water content (which is larger than liquid limit, Table 3.1) of the natural soil brings to mind the effects induced by cementation bonds in structured soils, although the compressibility might also be affected by the fact that the longest organic fibres had been removed from the remoulded sample for the sake of homogeneity.

Figure 3.6 shows the hydraulic conductivity assessed by means of falling head measurements obtained during the oedometer compression tests on undisturbed

samples of Fiavè A and B, and Levico A, together with the indirect assessments obtained from the rate of pore dissipation measured when the remoulded Levico sample was submitted to the Rowe consolidation test (Section 3.4.6). Falling head measurements are useful for assessing the order of magnitude of hydraulic conductivity values because very small variations in hydraulic head (of a few millimeters) can be assessed in 2-3 hours. It is also worth mentioning that the falling head measurements on the Levico peat, specimen A, were consistent with indirect assessments obtained in the Rowe cell (see Fig. 3.6). The hydraulic conductivities shown in Fig. 3.6 lie within a fairly narrow range, which is the same for the 'natural' and remoulded samples, and for the Levico and Fiavè peats.

The delayed behaviour of soils under 1D compression is traditionally described using the coefficient of secondary compression $C_\alpha = -\Delta e/\Delta \log t$ (Mesri 1973), which represents the slope of the oedometric curve, in a $e-\log t$ plot, after primary consolidation has come to an end. This parameter is easy to obtain with the IL oedometer test and can be used directly for an initial, rough estimation of the viscous response, as is often done in practical design situations. Using a constant C_α for peats may lead to large errors, however, as shown below.

C_α is typically defined for large load increments ($\Delta\sigma'/\sigma' = 1$). The effects of small load increments are discussed in Section 3.4.2. Figure 3.5 shows the C_α values obtained with standard IL using 24-hour steps, based on a conventional interpretation of the void ratio versus time compression curves for the Fiavè and Levico peats, under large load increments. The results for the Egna peat were very similar to those obtained for the remoulded Fiavè peat so they are not shown in Fig. 3.5, for the sake of brevity. For the Fiavè samples (Fig. 3.5a), the secondary compression index peaks at a vertical stress of about 120 kPa, which is about four times the preconsolidation pressure, σ'_{vp}. The peak is followed by a sharp decrease in C_α. This sort of behaviour is consistent with the results found in many natural Italian clays (Lancellotta 2008), showing a peak C_α at about 1.5-2.0 times σ'_{vp}.

The evolution of C_α measured on the Levico A and B samples (Fig.3.5b) is smoother and shows a gradual increase, reaching a maximum at around 100 kPa, i.e. about five times σ'_{vp}. The C_α behaviour of the remoulded Levico and Fiavè peats differs considerably from that of the 'undisturbed' samples: C_α is much larger (about 1.5 times) than for the 'undisturbed' samples and, unexpectedly, it shows a non-negligible peak, as if remoulding had been unable to cancel the previous load history completely.

Mesri and Godlewski (1977) highlighted the correlation between the secondary compression coefficient C_α and the compression index C_c. According

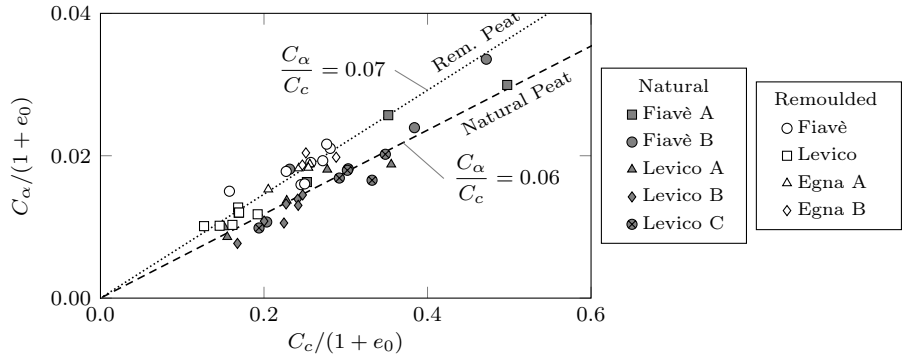

Figure 3.7: C_α versus C_c for load increment $\Delta\sigma'/\sigma' \simeq 100\%$.

to Mesri and Godlewski (1977), the ratio C_α/C_c is almost constant for the different types of soil; for peats and organic clays in particular, the ratio ranges between 0.05 and 0.1. The values of C_α/C_c measured on the three peats in the virgin compression phase are shown in Figure 3.7. The C_α/C_c ratio acquires two different values for the 'natural' and remoulded peats: the mean value of C_α/C_c is about 0.06 for 'natural' peat, and about 0.07 for remoulded peat (as we can see from the linear interpolations shown in Fig. 3.7. These values are consistent with other evaluations reported in the literature (0.04-0.06 for organic soils, Terzaghi et al. 1996, and 0.05-0.07 for fibrous peats, Mesri and Ajlouni 2007).

3.4.1 Quasi-preconsolidation effect

The quasi-preconsolidation effect induced by ageing is a well-known aspect of the rheological behaviour of fine-grained soils. This effect was first mentioned by Bjerrum 1967 and later confirmed by many other authors (e.g. Mesri and Castro 1987). Figure 3.8 shows the quasi-preconsolidation induced on Fiavè A peat by ageing the sample at a constant vertical stress of 160 kPa for 30 days, then resuming the loading process and applying small load increments (about 10% of the applied load) once every 24 h. Figure 3.8 shows that the compression curve gradually reached the virgin compression slope (the dotted line in Fig. 3.8, obtained with 24 h loading stages), with an apparent quasi-preconsolidation pressure of about 250 kPa. This result is consistent with the findings of Mesri and Ajlouni (2007) and with the empirical relationship proposed by Mesri and

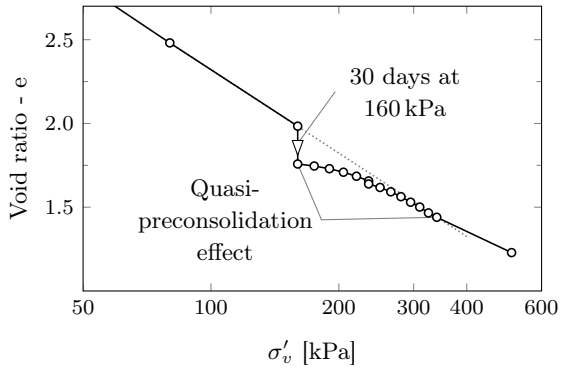

Figure 3.8: Quasi-preconsolidation effect after ageing (30 days) for Fiavè A Peat.

Castro (1987) for assessing the quasi-preconsolidation induced by ageing in inorganic clays.

3.4.2 Effects induced by small load increments during virgin compression

The viscous response of peaty soils under small load increments is of interest in many engineering applications, such as the re-levelling of a road embankment after primary and secondary settlement. The delayed behaviour induced by small load increments was first analysed by Mesri et al. (1994) and by Mesri, Stark, Ajlouni, et al. (1997).

In defining the load history applied to the samples, it is useful to introduce the effective surcharge ratio R'_s (Mesri and Feng 1991)

$$R'_s = \frac{\sigma'_{vs}}{\sigma'_{vf}} - 1, \tag{3.1}$$

where σ'_{vf} and σ'_{vi} represent the effective vertical pressure at the end and at the beginning of the loading increment.

It is worth noting that the points representing the EOP in the figures discussed below were only assessed approximately, and were obtained from theoretical considerations based on vertical compressibility and hydraulic conductivity measurements (Fig. 3.6). The EOP was found to be slightly overestimated

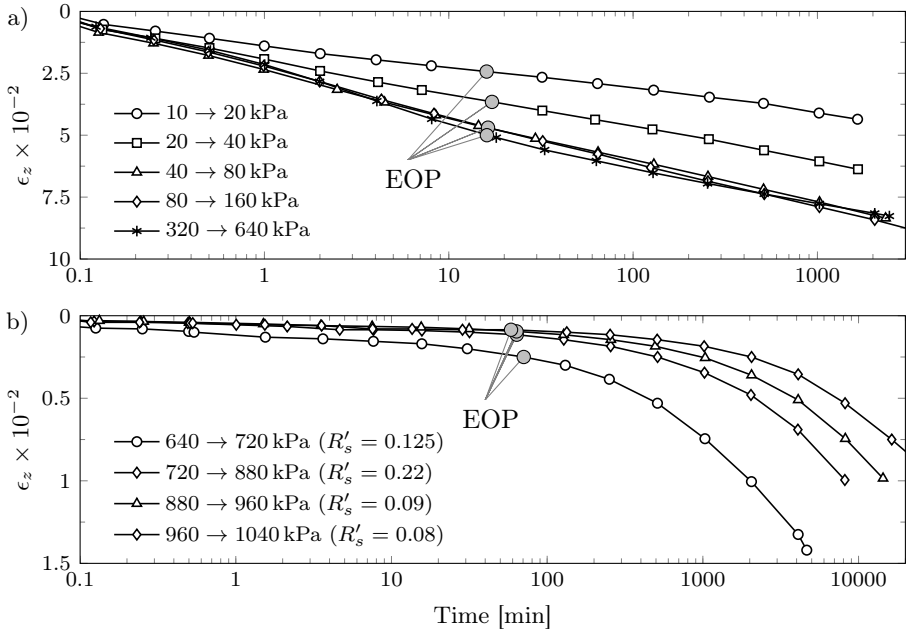

Figure 3.9: Time-settlement curve for Levico peat (spec. A): a) $\Delta\sigma'/\sigma' = 100\%$ ($R'_s = 0$) b) $\Delta\sigma'/\sigma' \simeq 10\%$ ($R'_s = 0.08 \div 0.22$).

when the pore pressure dissipation measurements performed in the Rowe consolidation cell were used (see Section 3.4).

Figure 3.9 compares the strain histories induced by large (Fig. 3.9a) and small (Fig. 3.9b) load increments applied to Levico peat (specimen A). Large load increments ($R'_s = 1$, Fig. 3.9a) induced a slope that remained fairly constant of the strain versus log time curves once primary compression was over (EOP). In contrast, small load increments (Fig. 3.9b) induced negligible primary settlements followed by significant secondary settlements with a markedly increasing slope in the log time plot. The change of slope apparently occurs later, the smaller the R'_s ratio.

Figure 3.10 shows the strain versus log time curves calculated for the two remoulded samples of Egna peat, which were submitted to small, equal stress increments ($\Delta\sigma'/\sigma' \approx 15$ and 20% and $R'_s \approx 0.07 \div 0.18$, that were kept constant for about 4 days) applied after ageing the samples for 7 days. The curves almost

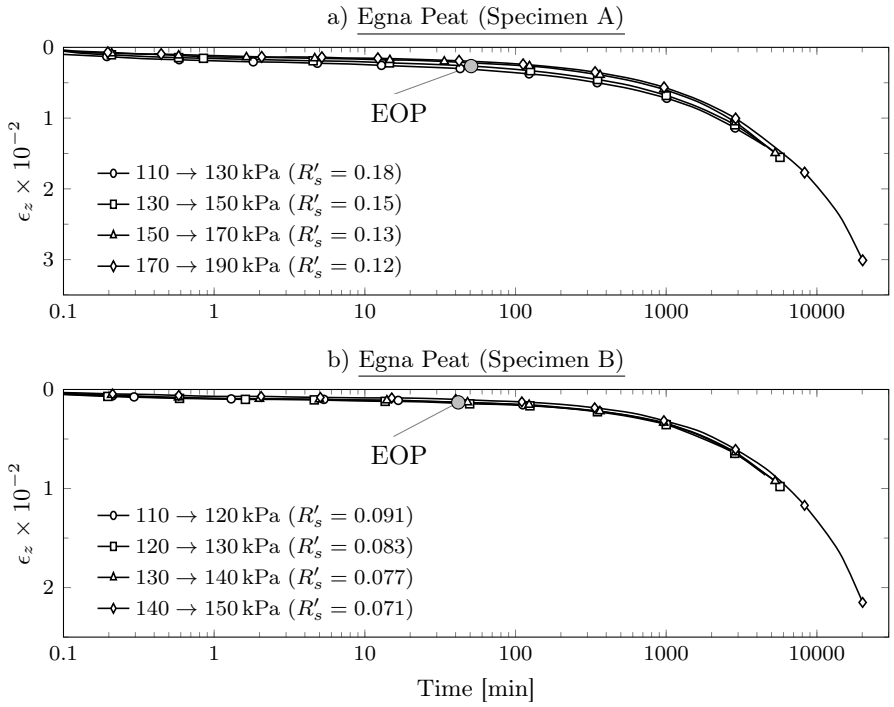

Figure 3.10: a) Egna A - small virgin loading ($R'_s = 0.18 \div 0.12$) after 7 days of ageing b) Egna B - small unloading ($R'_s = 0.09 \div 0.07$) after 7 days of ageing.

coincided with one other.

Figure 3.11 shows the delayed effects induced by small load increments on the Fiavè peat. In particular, the results shown in Fig. 3.11a (Fiavè A) were obtained after ageing for 30 days at $\sigma'_v = 160\,\text{kPa}$, whereas the results shown in Fig. 3.11b (Fiavè B), concern a sample that underwent no initial ageing. The Fiavè A specimen was also submitted to a constant $\Delta\sigma' = 15\,\text{kPa}$ (involving R'_s ranging between 0.068 and 0.094), whereas the Fiavè B specimen was loaded in a wider range of R'_s values (between 0.04 and 0.25). If we compare Figs. 3.10 and 3.11a, the initial ageing time (30 days) appears to mainly affect the final slope of the strain versus log time curves (i.e. the slope in the final phase, after the change of slope).

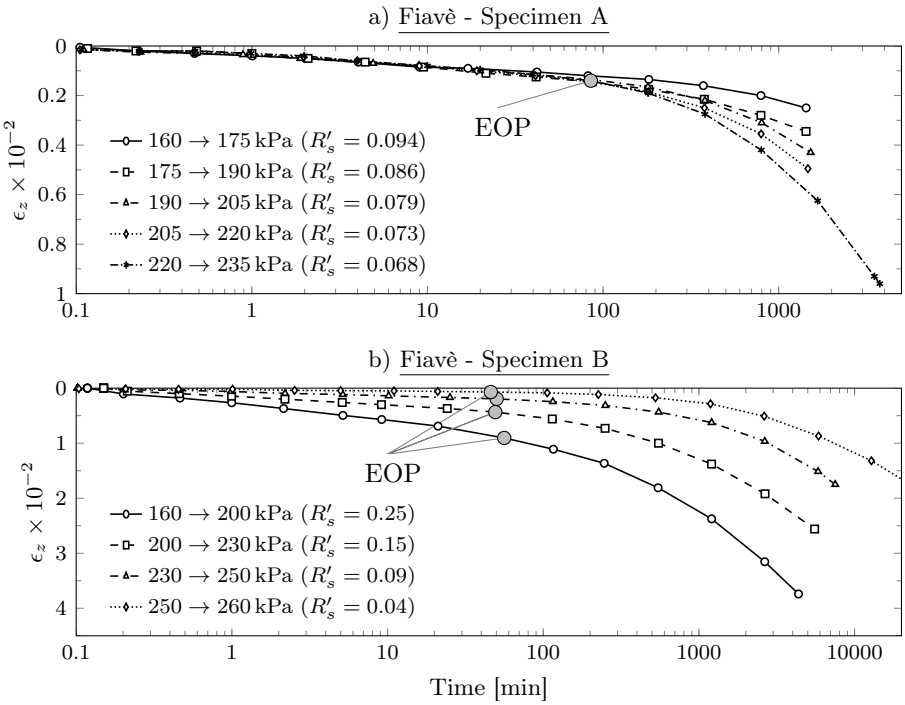

Figure 3.11: a) Fiavè A - small virgin loading ($R'_s \simeq 0.09 \div 0.07$) after 30 days of ageing b) Fiavè B - small virgin loading ($R'_s = 0.25 \div 0.04$) after 4 days of ageing.

Figure 3.11b shows that the R'_s ratio plays the most important part in defining the initial slope and the instant when it changes: the higher the ratio, the larger the initial slope and the sooner it changes.

The experimental results shown in Figs. 3.9 and 3.11 are consistent with previous works by K. Lo (1961), Leonards and Girault (1961), Mesri and Castro (1987), Fox, Edil, and Lan (1992), Mesri, D. Lo, et al. (1994) and Mesri, Stark, Ajlouni, et al. (1997), who found that the slope of the consolidation curve in a strain versus log time plot is not constant for peaty soils in the case of small load increments.

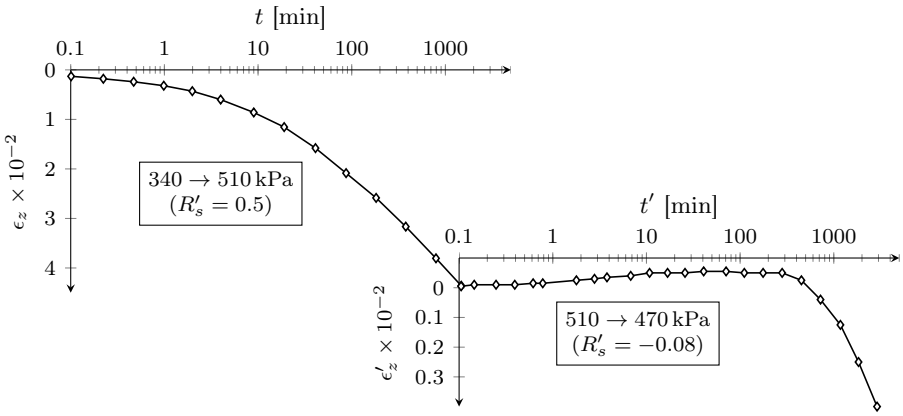

Figure 3.12: Settlement after small unloading for Fiavè A Peat in subsequent steps.

3.4.3 Effects induced by small load reversals

Mesri and Feng (1991) demonstrated that a load reversal (from loading to unloading) may induce first a delayed swelling and then a delayed compression in soft clays. This kind of delayed behaviour under load reversal is of practical interest for pre-loaded embankments and was investigated for the case of Fiavè peat. Figure 3.12 shows the typical delayed response for a small unloading, starting from the virgin compression phase. Figure 3.12 can be compared directly with Mesri's results (1991), and confirms that Mesri's observation holds for peats as well (Mesri and Ajlouni 2007). Figure 3.13a shows the delayed behaviour for three subsequent, equal-sized, small unloading steps ($\Delta\sigma' = -40\,\text{kPa}$, $R'_s = -0.08$). The change from delayed swelling to delayed compression clearly does not occur only in the first unloading step, but also in subsequent steps, although the change from delayed swelling to delayed compression occurs later and later, the more the unloading steps involved: the change occurs after about 500 min for the first unloading step (A in Fig. 3.13a), and takes nearly 6000 min for the third one (C in Fig. 3.13a). These experimental evidences are consistent with the results recently presented by Kawabe and Tatsuoka (2013).

In contrast with the results shown in Fig. 3.13a, which were obtained with

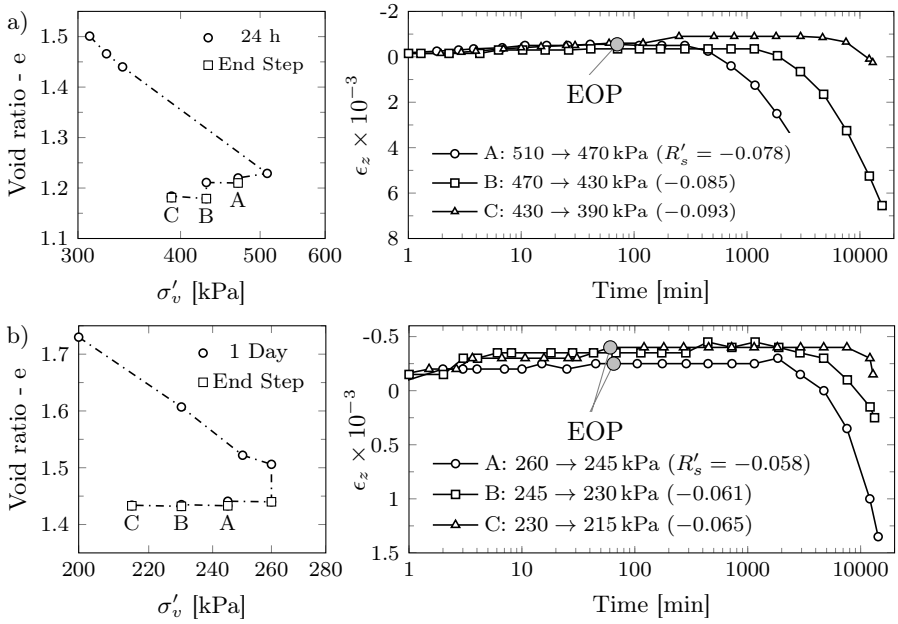

Figure 3.13: Settlement after small unloads on Fiavè Peat:
a) Specimen A; b) Specimen B.

unloading steps applied soon after the consolidation in the virgin loading phase was complete, the results shown in Fig. 3.13b were obtained by applying small unloading steps after ageing the specimen for a month during the virgin compression phase. The same load decrements of Fig. 3.13a were applied in the case of Fig. 3.13b. As a result, Fig. 3.13b enables us to appreciate the effects induced by ageing before unloading. The change from delayed swelling to delayed compression occurs generally later in Fig. 3.13b than in Fig. 3.13a, ranging between 2000 and nearly 10 000 min in the former, as opposed to $500 - 6000$ min in the latter. The delayed compression after ageing was also much smaller (about five times smaller) than in the case without ageing (in Fig. 3.13a). Similar results were obtained for the two specimens of remoulded Egna peat, so they are not shown here for the sake of brevity.

Although the delayed effects of load reversal from unloading to reloading are probably of less interest from an engineering point of view, they are still impor-

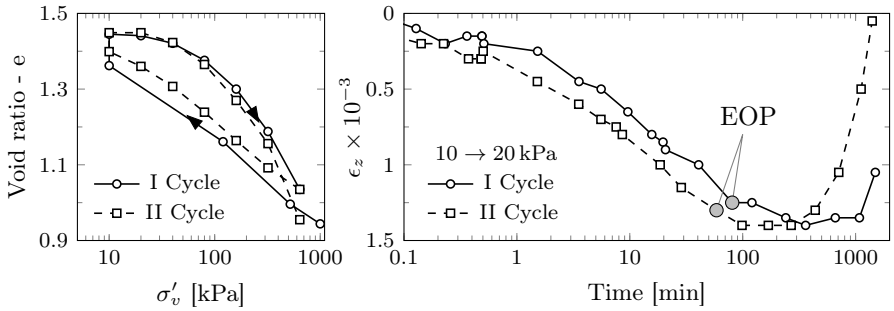

Figure 3.14: Fiavè Peat (Spec. A) - Swelling after small reloads.

tant for shedding light on the mechanisms of delayed soil behaviour. Figure 3.14 shows that, after an initial compression, delayed swelling occurs in the reversal from unloading to reloading too. This effect has been recently investigated also by Kawabe and Tatsuoka (2013). Figure 3.14 shows the results obtained in two unloading-reloading cycles with the Fiavè A sample. The first reloading was applied after large load decrements and after ageing for 6 days at $\sigma'_v = 10$ kPa, while the second reloading was applied after small load decrements and no ageing. Then the same, large load reversal was applied in both cases ($R'_s = 1$ from unloading to reloading). Figure 3.14 shows that the change from delayed compression to delayed swelling occurred quite quickly (after about $200 - 500$ min) in both cases and, at a given time, the second reloading cycle (with no ageing) generated the greatest swelling.

3.4.4 Results of CRSN Oedometer Tests

Two samples of 'natural' Levico peat were submitted to a CRSN test using a standard oedometer cell loaded in a conventional loading frame. The two samples were collected very close to each other from within a region in which the Levico peat was sufficiently homogeneous.

The first sample was loaded at a constant strain rate of 1.5×10^{-1} %/min, while the second was initially loaded at the strain rate of 7.5×10^{-3} %/min; then, at a vertical effective stress of 260 kPa, the strain rate was reduced to 7.5×10^{-4} %/min and kept constant up to a vertical stress of 580 kPa. The initial strain rate of 7.5×10^{-3} %/min was subsequently resumed until the end of the test. Note that the ratio between the highest and lowest strain rates

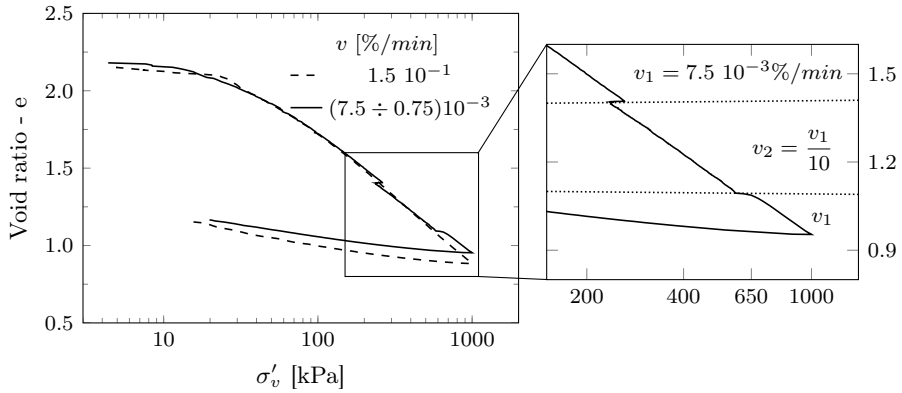

Figure 3.15: Results of CRSN oedometer tests on Levico 'natural' peat.

was 200. Notwithstanding the selected velocity of the first sample (1.5×10^{-1} %/min) was fairly larger than the recommendations of Gorman (1981) on the basis of the consolidation coefficient (see also ASTM D4186, which refers to this work for the selection of strain rates for CRSN tests) to ensure a small excess pore pressure within the sample (5×10^{-3} %/min), the results from the first sample are consistent with those from the second, which was tested at a velocity approximately consistent with recommendations.

The results of the CRSN tests are shown in Fig. 3.15. The responses of the two samples were very similar and the strain rate induced small, but not negligible effects. The small effects induced by the strain rate and the initial samples' small non-homogeneities prevent any definite conclusions from being drawn from the comparison between the two tests. In fact, the range of strain rates applied (1.5×10^{-1} - 7.5×10^{-3} %/min) was too narrow to reveal any significant strain rate effect on the preconsolidation pressure (see Leroueil, Kabbaj, et al. 1985 for the effects of strain rate on the preconsolidation pressure of structured, inorganic natural clay). The importance of the results shown in Fig. 3.15 lies instead in the effects induced by a change in the strain rate during the virgin loading phase (Levico B specimen). These results are very useful for the purposes of validating constitutive models.

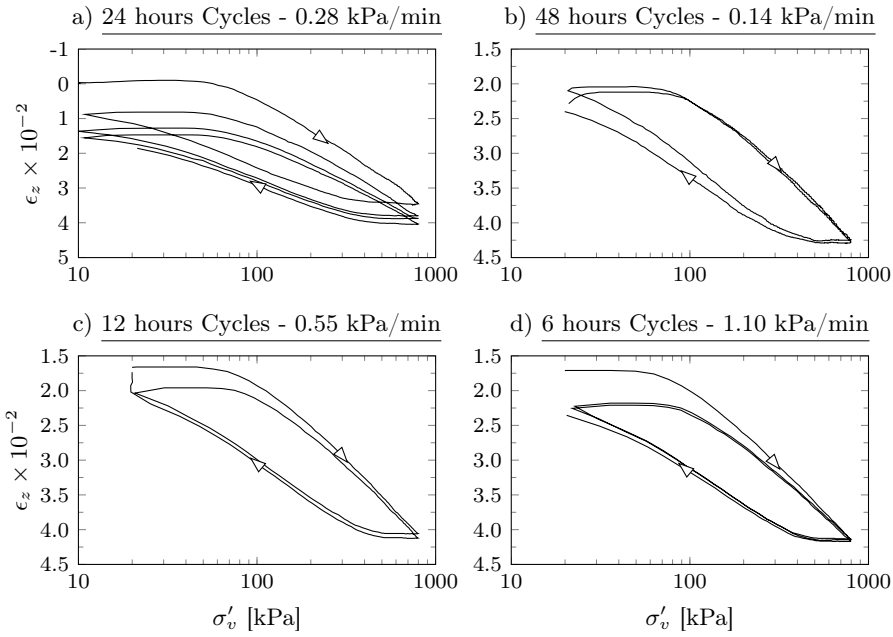

Figure 3.16: Results of CRSS oedometer tests on Levico 'natural' peat (Spec. A).

3.4.5 Results of CRSS Oedometer Tests

After being loaded and unloaded in the standard IL tests (see Section 3.4), the Levico Peat sample A was subsequently loaded in a loading frame operated by a computer-controlled pneumatic piston. Then the sample was submitted to several constant load rate (CRSS) cyclic tests in which the stress applied varied between 10-20 kPa and 800 kPa. The cyclic tests were performed at loading rates ranging between 0.14 kPa/min (48-hour loading cycle) and 1.10 kPa/min (6-hour loading cycle). The results are plotted in Fig. 3.16. The tests at constant loading rates were chosen to enhance the hysteresis in the compression curves (as shown in Fig. 3.16), by comparison with the constant strain rate. The hysteresis is slightly larger for the fastest loading rates than for the slowest ones, though the differences are rather small given the narrow range of loading rates investigated. It is worth mentioning that the first loading cycle (Fig. 3.16a)

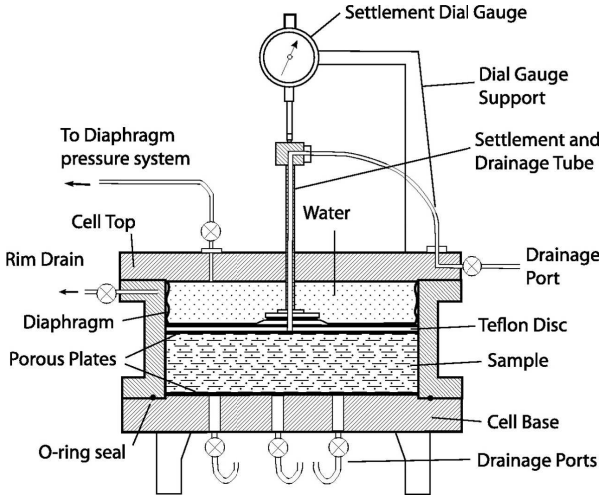

Figure 3.17: Scheme of the Rowe consolidation cell apparatus.

shows some greater ratcheting due to the influence of the previous unloading phase, unlike the subsequent cycles, in which a situation closer to a steady state (in terms of delayed behaviour) was reached.

3.4.6 Results of Rowe Cell Oedometer Tests on remoulded Levico peat

One saturated sample of remoulded Levico peat was submitted to an oedometer test in a computer-controlled Rowe cell 75.7 mm in diameter (Fig. 3.17), obtaining pore pressure measurements. First the sample was saturated by increasing the back pressure, then it was submitted to an increasing vertical pressure (that was kept constant in each loading step), draining from the upper end of the sample and measuring the pore pressure at the lower end. This made it possible to compare the strain versus time curves with the dissipation of the excess pore pressures.

The evolution of the vertical strains and excess pore pressures measured at the various loading steps are shown in Fig. 3.18. In the loading steps $50 \rightarrow 100$ kPa, $100 \rightarrow 200$ kPa and $200 \rightarrow 400$ kPa, the change of slope in the strain versus time curve coincides with the end of excess pore pressure dissipation. Under the small load increments applied subsequently, however, the pore pressure dis-

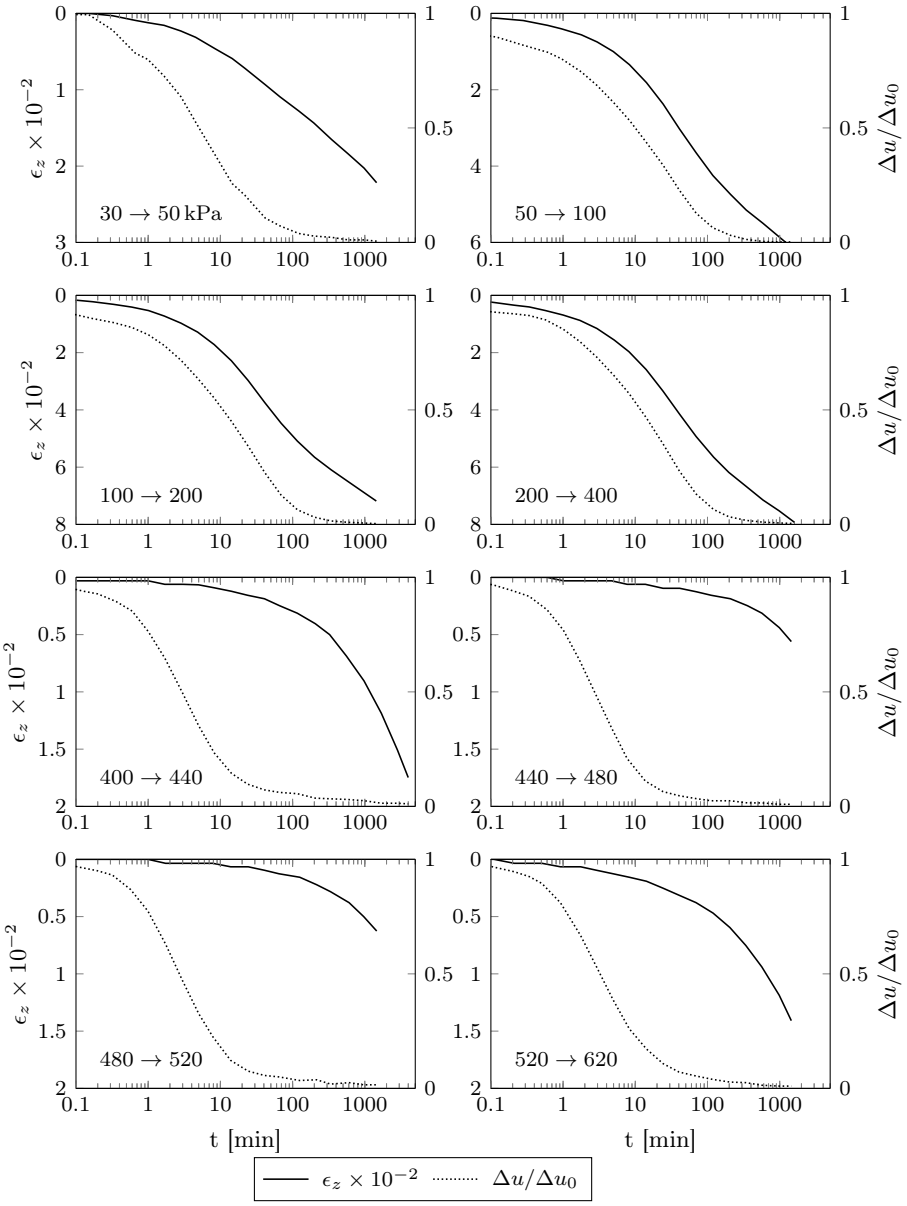

Figure 3.18: Results of Rowe Cell Consolidation test for Levico remoulded peat.

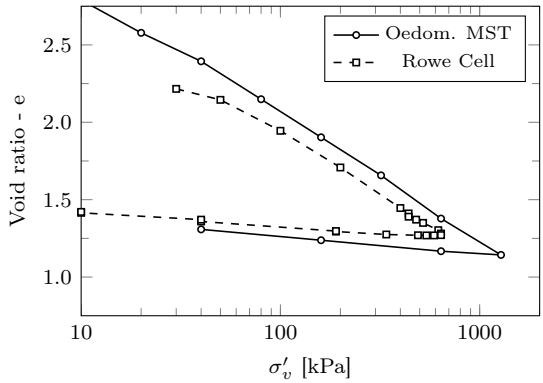

Figure 3.19: Oedometric Compression Curve for Levico Remoulded Peat.

sipation ended much earlier than the change of slope of the strain versus time curve, definitively proving that the increase in slope in the delayed compression observable under small load increments (see also Fig. 3.11) is related not to pore pressure dissipation, but to a phenomenon that is wholly due to the rheological response of the solid skeleton. Finally, it is worth noting that, due to the very rigid soil response under small load increments, pore pressure dissipation was much faster (about $10 - 20$ min) than with the previous, large load increments (about 100 min).

Fig. 3.18 shows that the EOP deduced from pore pressure dissipation (for the small sample thickness) is consistent with the estimate obtained from the evolution of the settlements, according to Casagrande's construction. The results shown in Fig. 3.18 are useful for validating numerical models devised to analyse boundary value problems involving pore pressure dissipation and the delayed behaviour of the solid skeleton during primary consolidation.

The resulting 1D compression curve measured in the IL oedometer test performed in the Rowe cell is compared in Fig. 3.19 with the results of a similar IL oedometer test performed in a standard apparatus on remoulded Levico peat. Apart from the slight difference in the initial void ratio (due to sample preparation), the results obtained with the two types of apparatus are consistent.

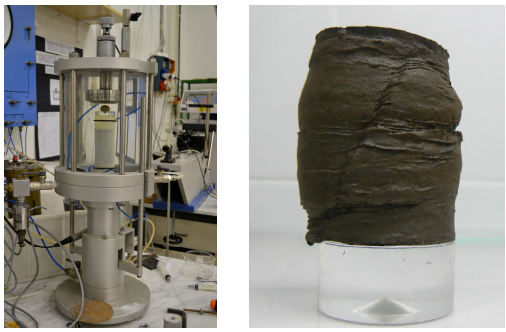

Figure 3.20: a) Bishop-Wesley triaxial apparatus of UniTn Laboratory; b) specimen TxCU-B of Levico peat at the end of the test.

3.5 Results of triaxial tests

Triaxial tests were performed on saturated remoulded specimens of Levico peat. The samples were obtained by pouring the liquid soil (with water content of about $1.5 \times w_l$) in a 38 mm consolidation cell, and by consolidating up to 30 kPa. The consolidation was conducted in three phases adding the liquid soil gradually in order to reduce the non homogeneity induced by the side friction. The saturation of the specimens was checked in the triaxial apparatus before starting the consolidation phase.

The tests were conducted partly by the Geotechnical Laboratory of University of Trento (UTN), and partly by the Geotechnical Laboratory of the Autonomous Province of Trento (PAT). The former is equipped with a Bishop-Wesley (Bishop and Wesley 1975) for controlled stress-path triaxial apparatus (Fig. 3.20a), and the latter uses a classical triaxial cell with a load frame.

3.5.1 Consolidated Undrained tests on NC Levico peat

The original aim of the undrained triaxial tests performed on Levico remoulded peat was to obtain information about strain rate effect in triaxial conditions. The tests were conducted with the classical test routine (with saturation, consolidation, and shear at constant strain rate phases) changing the axial strain rate for the application of the deviatoric load.

The saturation was conducted by applying a back pressure to the specimen in different steps. At the end of the saturation process the specimens were

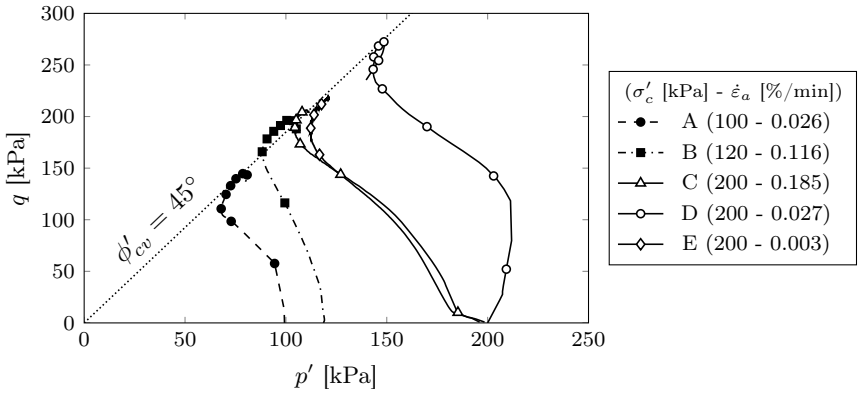

Figure 3.21: Stress paths of triaxial CU test results for NC Levico Remoulded Peat.

consolidated at different cell pressure and then submitted to the shear phase at constant axial strain rate. The procedure of sample preparation from slurry soil and the isotropic consolidation up to the cell pressure allows as to consider all the specimens normally consolidated.

In Table 3.2 the main characteristics of the undrained specimens are shown. In particular, three test were conducted with a cell pressure of 200 kPa, one with $\sigma'_c = 120$ kPa, and one with $\sigma'_c = 100$ kPa. The applied axial strain rate ranged between $0.0032 \div 0.185$ %/min.

Figure 3.21 shows the effective stress path for the five tests. The specimens

Specimen	A	B	C	D	E
Laboratory	PAT	UTN	UTN	PAT	UTN
Eff. Cell pressure, σ'_c [kPa]	100	120	200	200	200
Back pressure [kPa]	150	100	150	150	150
$\Delta V/V_0$ at shear start [%]	11.21	15.0	18.77	11.38	20.0
EOP, t_{100} [min]	488	357	480	586	505
$\dot{\varepsilon}_a$ [%/min]	0.0261	0.116	0.185	0.0268	0.0032

Table 3.2: Triaxial specimens and test conditions.

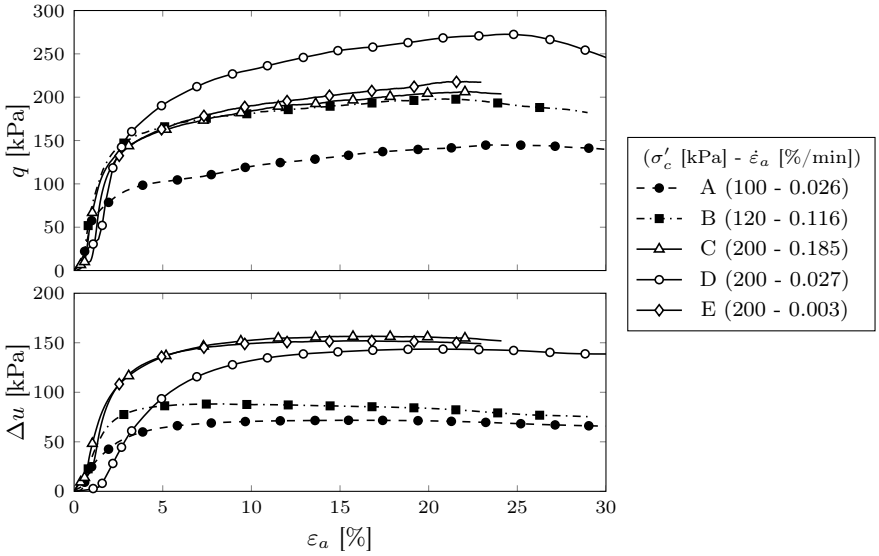

Figure 3.22: Triaxial CU test results for NC Levico Remoulded Peat.

exhibit the same shear strength (corresponding to a critical state friction angle of 45°), whereas the maximum deviatoric stresses and the values of the final pore pressure shows a significant scattering. The very high friction angle measured on Levico peat is typical of fibrous peats that can be greater than 50° (Mesri and Ajlouni 2007). In this kind of soils the tensile strength of fibres contributes to particle interlocking (Landva and La Rochelle 1983).

Figure 3.22 shows the $\varepsilon_a - q$ and $\varepsilon_a - \Delta u$ plots for the phase of application of the deviatoric strain. The mentioned scattering of the results is quite evident, and any clear correlation between the applied strain rate and the response of the material cannot be highlighted. This can be related to the scattering of the initial specimens (in terms of water content and homogeneity), or to the loss of alignment between the top cap and the cell piston during the consolidation phase. When the cell piston approaches the top cap, it realigns the specimen to the cell axis and introduces a disturbance that can lead to an abrupt increment of the pore pressure at the beginning of shear phase. This kind of response can be clearly observed in specimen C and D ($\sigma'_c = 200$ kPa).

Another font of error can be the different duration of the consolidation stages.

Step	σ'_c [kPa]	t_{step} [min]	t_{100} [min]	$\Delta\varepsilon_{v,step}$ [%]
L1	25	120	31.4	4.91
L2	50	210	67.2	4.35
L3	100	480	94.1	5.66
L4	200	1414	161.3	5.82
L5	400	1487	201.6	6.03
L6	700	16060	324.0	6.64
U1	550	1440	240.2	-0.13
U2	400	6797	210.2	-0.56
U3	200	1440	144.0	-0.84
U4	70	10436	289.0	-2.55

Table 3.3: Summary of consolidation steps of TxCD on Levico Peat.

The loose peat shows huge secondary effects, and any difference in the consolidation period affects the conditions of the specimen at the beginning of the shear phase.

3.5.2 Consolidated Drained test on OC Levico peat

The results of the undrained triaxial tests do not permit the formulation of any considerations about the strain rate effect on the tested peat. In order to remove the uncertainly related to the scattering between the initial condition of the specimens, a different approach was followed in testing overconsolidated peats: changing the strain rate during the deviatoric load phase allowing the direct measure of the strain rate effect, without any problems related to the non homogeneity of the tested material.

A remoulded specimen of Levico peat was submitted to a consolidated drained triaxial test with step changed strain rate during the shear phase; the intent of the test was to focus the viscous behaviour of strongly overconsolidated peaty soil.

The maximum cell pressure applicable by the PAT laboratory apparatus was 800 kPa. Starting from the apparatus limits, the chosen test routine was carried out in three phases: the consolidation of the specimen up to the effective cell pressure of 700 kPa, the unload of the cell effective pressure to 70 kPa, and the

Step	$\dot{\varepsilon}_a$ [$\times 10^{-3}$ %/min]	Δt_{step} [min]	$\Delta \varepsilon_{a,\text{step}}$ [%]
S1 - v_1	4.21	1385	5.84
S2 - $v_1/10$	0.50	2655	1.34
S3 - $v_1/20$	0.20	8515	1.73
S4 - v_1	4.40	360	1.58
S5 - $v_1/20$	0.19	9630	1.87
S6 - $v_1/10$	0.52	7259	3.78
S7 - v_1	4.22	457	1.93
S8 - $v_1/10$	0.51	9762	5.00
S9 - v_1	4.43	1707	7.56

Table 3.4: Summary of deviatoric load phase of TxCD on remoulded Levico Peat.

shear phase with different steps of strain rate. Side drains were used to increase the rate of consolidation and to obtain a drained test with feasible axial strain rate. During the consolidation and unloading phases the back pressure was 50 kPa. The maximum axial strain rate was selected starting from the EOP time, in order to ensure the development of negligible pore pressure changes (Head and Epps 2014).

Table 3.3 shows a summary of the preliminary consolidation and unloading phases. It is worth noting that the effective isotropic stress of 700 kPa was maintained for about 11 days, in order to develop a certain amount of viscous deformation before the unload. The same procedure was chosen before the beginning of the shear phase; the cell pressure was maintained at 70 kPa for about 7 days.

After the isotropic loading and unloading, the drained shear phase with three different axial strain rates was performed. Considering a strain at failure of 20 % and a precautionary value of $t_{100} = 300$ min. The maximum applicable strain rate is 4.8 %/min (corresponding to the time of failure of $14 \times t_{100}$, (Head and Epps 2014)). The selected maximum strain rate is $v_1 = 4.2$ %/min, and the lower strain rates are of about $v_1/10$ and $v_1/20$. The sequence of strain rates during the TxCD test is shown in Table 3.4.

The results of the test are shown in Figure 3.23. The $q - \varepsilon_a$ curve exhibits clearly the jumps of deviatoric stress when the strain rate is changed. The

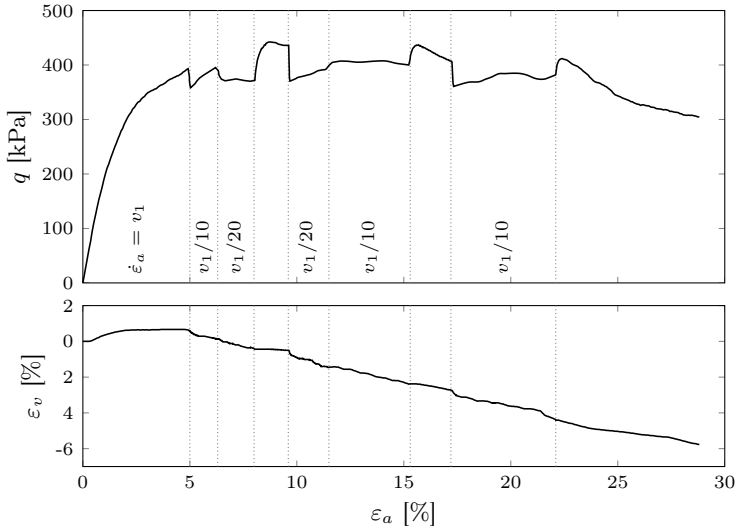

Figure 3.23: Triaxial CD test results for OC Levico Remoulded Peat.

increments and decrements of strain rate appear to be reversible as observed for NC clays by Tatsuoka et al. (1998) (see Section 2.4.4). On the other hand, the volumetric strains measured during the shear phase are not affected by the strain rate effect, and only minimal change in the slope of $\varepsilon_v - \varepsilon_a$ can be appreciated.

The triaxial drained test on OC sample of remoulded Levico peat confirms the existence of the strain rate effect also in the strongly overconsolidated field. This result suggests that the viscous effects observed for normally consolidated clays can be extended, with the proper revision, to strongly overconsolidated clays.

3.6 Conclusions

This Chapter presents a comprehensive set of experimental data concerning the delayed behaviour of organic clays and peats. The experimental analyses were conducted on three different (undisturbed or remoulded) peaty soils with fairly different index properties (the organic content ranged between 20% and 70%), which were submitted to various 1D consolidation tests, including incremen-

tal loading (IL) tests in a standard oedometer apparatus (using standard and non-standard load increments/decrements, and loading/unloading cycles, in the sense described by ASTM-D2435-11 (2011)), constant rate of stress (CRSS) and constant rate of strain (CRSN) tests, and IL tests in a Rowe consolidation cell with pore pressure dissipation measurements. In addition to oedometer tests were presented a series of triaxial tests (undrained ad drained) performed on remoulded peat in both normally consolidated and highly overconsolidated field.

The experimental analyses confirm that peats have delayed behaviour features very similar to those of inorganic clays. The experimental data presented here also enable a complete and organic analysis of the delayed effects, that had hitherto been examined separately by various Authors on different inorganic and organic soils.

The main value of this experimental study relates to the calibration and validation of constitutive models for simulating the delayed response of soils, and peaty soils in particular. In fact, the experimental program was originally designed to obtain a good-quality, comprehensive and meaningful set of data for the purpose of developing and calibrating a constitutive model, which will be presented in a companion paper. For this reason any considerations on the reliability of a given conceptual model have been deliberately minimized.

CHAPTER 4

Existent models for rate dependent behaviour of clay

In this chapter are described the main constitutive approaches to the modelling of viscous effects in clayey soils. The models proposed in the literature can be classified in three categories: empirical, rheological, and general stress-strain-time models. Empirical relations are formulated to fit the experimental results of a specific test and are applicable only to specific boundary conditions. Rheological models can be used for soils taking into account the typical non-linear response in terms of stress-strain and time response. The most interesting approach to modelling is that of general multiaxial models that extend the concept of the classical rate-independent elastoplasticity to the viscous case.

4.1 Introduction

The accurate estimation of soil deformations induced by the construction of civil structures and infrastructure is one of the most challenging problems for present day geotechnical engineers. For example, building high-rise structure and urban excavations are deeply influenced by the need for preserving existing structures; or, in the high velocity railway field, the accurate prediction of ground deformation is of paramount importance in the design of the infrastructure. In order to perform reliable analyses of these complex problems, the accurate modelling of the constitutive behaviour of the foundation soil is essential.

The response of real structures founded on clayey soils is often affected by the time-dependent phenomena (Mesri and Choi 1985; Tanabashi et al. 1988; Crawford and Morrison 1996). To obtain realistic solutions from the simulation of real structures founded soils subjected to delayed deformation, it is crucial

to use a constitutive framework that accounts for time dependency in the formulation of the stress-strain law.

In literature many studies have been proposed regarding the evaluation of viscous behaviour of soil. Most of these studies are based on the empirical fitting of the experimental results for a particular laboratory test (namely creep, relaxation, constant rate of strain). The advantage of this kind of models is mainly the wide experimental base of data used for the formulation, that is representative of real observed phenomena. On the other hand, the main drawback of empirical formulations is that they are applicable only to specific boundary and loading conditions, and can not be extended to a general multi-axial constitutive framework.

A different approach to the modelling of viscous behaviour of soil is to formulate a constitutive framework by extending the classical concepts of the elastoplasticity theory to the viscous case. These kinds of approaches are, in most cases, three-dimensional models, and are suitable to numerical implementation in a Finite Element environment. The formulation of a general model, valid for all the possible boundary value problems, is in most cases theoretically challenging and is further complicated by the strong non-linearity of soil behaviour.

The most important constitutive models proposed in the literature will be briefly exposed in this chapter. The exposition follows the classification suggested by Liingaard et al. (2004); they divided the constitutive models into three categories:

- empirical models obtained by fitting the experimental results. They are applicable only to the specific boundary and loading condition for which have been formulated;

- rheological models based on the composition of simple stress-strain-strain rate elements, and formulated in terms of differential equations;

- general stress-strain-time models obtained by extending a particular multi-axial elastoplastic formulation to viscous problems. This kind of model is generally implemented in FEM environment and can simulate a general boundary value problem.

The following consider the models which concern the macro-mechanical properties stress, strain and time, neglecting the micro-mechanical approaches.

4.2 Empirical models

Empirical models have been developed starting mainly from experimental evidences and can be applied to real problems involving boundary and load conditions complying that of the test used for the formulation.

4.2.1 Semilogarithmic creep law

Starting from oedometric conditions, many experimental studies emphasized the linear relationship between viscous strain and logarithm of time (see Section 2). Starting from the definition of coefficient of secondary consolidation (eq. (2.1)) it is possible to estimate the viscous deformation, once the reference time of the beginning of viscous phenomena is defined (eq. (2.2)).

The approach of constant C_α is the simplest way to obtain a rough estimation of delayed behaviour. However, this method is only able to define the order of magnitude of secondary deformations and cannot be applicable to long term phenomena (for $t \to \infty$ the viscous deformation $\varepsilon_z^v \to \infty$).

In order to improve this simple method, many studies proposed a modification of the logarithmic law introducing different elements affecting the coefficient of secondary consolidation. In particular, Walker and Raymond (1968) and then Mesri and Godlewski (1977) highlighted the dependence of C_α on the effective stress level, and postulated that the ratio C_α/C_c can be assumed approximately constant. As a consequence, eq. (2.2) can be modified and leads to

$$\varepsilon_z^v(t) = \frac{1}{m'}\, C_{c\varepsilon}\, \log\left(1 + \frac{t}{t_i}\right), \quad m' = \frac{C_{c\varepsilon}}{C_{\alpha\varepsilon}}, \tag{4.1}$$

in which $C_{c\varepsilon}$ is the compression index, with respect to ε_z, calculated in the point where viscous deformation must be determined.

The relationship reported in eq. (4.1) takes into account the effective stress dependency of viscous phenomena, but ignores the time dependence of C_α and fall back into the paradox of infinite viscous deformation when $t \to \infty$.

In order to avoid this drawback, Yin (1999) (starting from the approach of Yin and Graham (1989)) proposed a different non-linear creep function in which

the coefficient of secondary deformation decreases with time.

$$\varepsilon_{\mathrm{z}}^{\mathrm{v}}(t) = \frac{\psi}{v}\ \ln\left(1 + \frac{t + t_0}{t_0}\right) \tag{4.2a}$$

$$\frac{\psi}{v} = \frac{1}{v}\frac{C_{\alpha\varepsilon}}{\ln(10)} = \frac{\psi_0'}{1 + \dfrac{\psi_0'}{\varepsilon_{\mathrm{z},\infty}^{\mathrm{v}}}\ \ln\left(1 + \dfrac{t + t_0}{t_0}\right)} \tag{4.2b}$$

where $v = 1 + e$ is the specific volume, $\varepsilon_{\mathrm{z},\infty}^{\mathrm{v}}$ is the viscous strain for $t \to \infty$, and the parameters t_0 and ψ_0' are reference values related to the initial state of the viscous phenomena.

The main problem of this approach is the definition of the initial reference parameters (the *problem of reference time* mentioned in Section 2.2.2). For complex loading histories the method becomes inapplicable due to the impossibility in the definition of the origin of the time scale. The *problem of reference time* is common to many constitutive approaches.

One of the more advanced one-dimensional models for time-dependent behaviour of soil was proposed by Yin and Graham (1989) and then improved in the following paper (Yin and Graham 1994). This model is capable of describing the behaviour of both creep and relaxation tests and has been developed starting from isotach behaviour showed by Bjerrum (1967) and from strain rate dependence evidences.

The basic concept is the definition of the 'equivalent time', t_{eq}, that identifies the state of the soil referring to the two lines in the $\varepsilon_{\mathrm{z}} - \sigma_{\mathrm{z}}'$ plot: the *reference time line*, corresponding to $t_{\mathrm{eq}} = 0$; and the *limit time line* corresponding to $t_{\mathrm{eq}} = \infty$. The viscous strain rate is a function of t_{eq}. For a normally consolidated specimen loaded in a classical IL oedometer test, t_{eq} is equal to the load increment time, whereas, if the specimen is in overconsolidated range, the value of t_{eq} is dependent on the OCR.

In order to understand the general behaviour of the model, in eq. (4.3) the general equation for the determination of the strain in elastoplastic load is reported. (Yin and Graham 1994).

$$\varepsilon_{\mathrm{z}} = \varepsilon_{\mathrm{z}}^{\mathrm{ep}} + \varepsilon_{\mathrm{z}}^{\mathrm{tp}} = \varepsilon_{\mathrm{z0}}^{\mathrm{ep}} + \frac{\lambda}{v}\ \ln\left(\frac{\sigma_{\mathrm{z}}'}{\sigma_{\mathrm{z0}}'}\right) + \frac{\psi}{v}\ \ln\left(\frac{t_0 + t_{\mathrm{eq}}}{t_0}\right), \tag{4.3}$$

where $\varepsilon_{z0}^{\mathrm{ep}}$ is the reference strain corresponding to the reference effective stress σ_{z0}', v is the specific volume, λ is the slope of elastoplastic load in $\varepsilon_{\mathrm{z}} - \log \sigma_{\mathrm{z}}'$ plot, t_0 is the intrinsic time parameter, and ψ is a creep parameter constant for a given soil.

Once the t_{eq} has been properly defined, starting from the definition of the *reference time line* and the *limit time line* the strain increment can be incrementally calculated starting from (4.3).

4.2.2 Experimental fitting of triaxial tests

Starting from the observation of the results of triaxial creep and relaxation tests (see Section 2.4) many authors proposed models capable of fitting one particular triaxial set-up.

Singh and Mitchell (1968) proposed an empirical relation for the estimation of creep deformation in undrained triaxial tests. This model was based on the experimental observation of creep tests performed with deviatoric stress $q = 30 \div 90\%$ of the strength measured in the same conditions. The authors find the following best fitting power law

$$\dot{\varepsilon}_{\mathrm{a}}^{\mathrm{v}}(t) = A \ \exp(\bar{\alpha} \ \bar{q}) \left(\frac{t_{\mathrm{i}}}{t}\right)^{m}, \tag{4.4}$$

where $\bar{\alpha} = \alpha \ q_{\max}$, and $\bar{q} = q/q_{\max}$ (in which $q_{\max}$ denotes the maximum compressive strength, and q the applied deviatoric stress). The three parameters A, α, and m define the soil properties, the stress influence on creep process, and the axial strain rate, respectively.

Equation (4.4) allow the modelling of triaxial creep processes with a general response in terms of $\varepsilon_{\mathrm{a}}^{\mathrm{v}} - \log t$. The main drawback of this power law approach, in addition to the mentioned problem of reference time, is that it is applicable only to constant stress, and for the first time loading.

The interpretation of relaxation tests has been proposed by many authors. Among these, the two most cited studies are those by Lacerda and Houston (1973) and Prevost (1976).

Starting from the Singh and Mitchell (1968) model, Lacerda and Houston (1973) proposed the following relation, for a relaxation test after straining the soil under constant rate of strain:

$$\frac{q(t)}{q_0} = \frac{\bar{q}(t)}{\bar{q}_0} = 1 - s \ \log\left(\frac{t}{t_0}\right), \tag{4.5}$$

in which the overbar denotes the normalized stress level with respect to strength, q_0 represents the deviatoric stress, t_0 is the reference time of stress relaxation, and s is the slope of stress relaxation curve in a $q/q_0 - \log t$ curve. Starting from

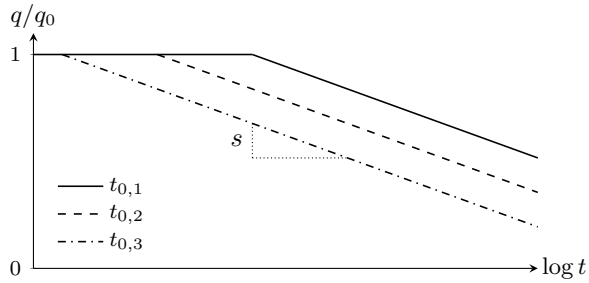

Figure 4.1: Stress relaxation curves obtained with Lacerda and Houston (1973) model.

the Singh and Mitchell (1968) model, the relation between s and m of equation (4.4) can be written as follows:

$$s = \frac{\Phi}{\bar{q}_0} = \frac{1}{\bar{q}_0} \frac{2.3(1-m)}{\bar{\alpha}}. \tag{4.6}$$

It is worth noting that eq. (4.5) corresponds to a linear relationship in $q/q_0 - \log t$ plot (Figure 4.1). The parameter t_0 does not correspond to the time of beginning of relaxation test but is affected by a sort of delay related to the stress level (see Section 2.4.3, Fig. 2.13). This relaxation model is affected by the same disadvantages of Singh and Mitchell (1968) one-dimensional relation. The relaxation model by Lacerda and Houston (1973) predicts a continuous decrement of the deviatoric stress. Other authors considered the introduction of a steady state value of the relaxation stress. For example, Prevost (1976)) suggested a hyperbolic function of $\log t$ to characterize the transition between the start of relaxation and the steady state condition.

$$q(\varepsilon_{1,0}, t) = q(\varepsilon_{1,0}, t_0) - [q(\varepsilon_{1,0}, t_0) - q(\varepsilon_{1,0}, 0)] \tanh \left[b \, \frac{t}{t_0} \right], \tag{4.7}$$

where $q(\varepsilon_{1,0}, t)$ is the relaxed deviatoric stress at constant axial strain $\varepsilon_{1,0}$, $q(\varepsilon_{1,0}, t_0)$ is the deviatoric stress at the time of start of the relaxation process, t_0, and $q(\varepsilon_{1,0}, 0)$ is the deviatoric stress at a strain equal to $\varepsilon_{1,0}$ in a extremely slow undrained triaxial test ($\dot{\varepsilon}_a \simeq 0$).

The Prevost (1976) model interprets the undrained triaxial relaxation tests performed after straining the specimen at constant stress, and was successfully

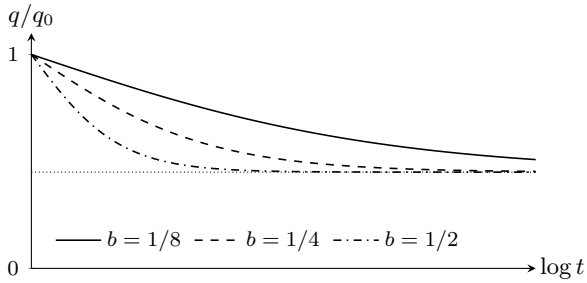

Figure 4.2: Stress relaxation curves obtained with Prevost (1976) model (eq. (4.7)).

employed by Silvestri et al. (1988) for the interpretation of many relaxation tests on different clays.

The models presented so far were formulated referring to the mono dimensional problems of undrained creep and relaxation. To the best of the author's knowledge, the first multi-axial constitutive approach was proposed by Kavazanjian and Mitchell (1977). They formulated a general model by splitting the axial and volumetric part of the total deformation. The volumetric component of the strain rate is based on the concept of constant C_α in a normally consolidated field, whereas the axial strain rate is developed starting from the Singh and Mitchell (1968) model. The deviatoric component of strain rate can be deduced starting from axial and volumetric parts.

4.3 Rheological models

The modelling of uniaxial behaviour of viscous materials can be efficiently represented in terms of elementary rheological elements. A proper composition of elastic springs, plastic sliders, and viscous dampers allows the idealization of a wide range of viscous behaviour both in viscoelastic and in viscoplastic fields.

The basic ingredients of rheological models are the three basic elements:

- the elastic spring represents the reversible deformations, and its stress-strain behaviour is defined by a general elastic law. The deformation associated to this element is purely elastic and recoverable;

- the viscous damper allows the modelling of time dependent phenomena.

The applied stress is related, with a general relationship, to the strain rate. If the loading process is extremely slow (and thus $\dot{\varepsilon} \simeq 0$) the stress sustained by the damper tends to zero; vice versa, for extremely fast loading the stiffness of the damper tends to infinity;

- the plastic slider represents the irreversible deformations. For a perfectly plastic slider the stiffness is infinite for stress below the yield stress and null for stress exceeding the yield stress. If the slider is associated to hardening the yield stress evolves with plastic deformation (through a proper hardening rule) and the stiffness in the plastic regime has a finite value.

The combination of this three simple elements allows the modelling of many different time dependent behaviours. In particular, in literature three units made of linear elements have been proposed: the *Maxwell* unit (composed of a spring and a damper elements connected in series), the *Kelvin-Voigt* unit (that consists of a spring and a damper element connected in parallel), and the *Bingham* unit (that consist of a plastic slider and a damper elements connected in parallel).

In order to give a brief introduction to the rheological models approach two basic models are briefly described: the standard viscoelastic model, and the Bingham elastic-viscoplastic model. For the sake of effectiveness, simple linear elements will be analysed.

Standard viscoelastic model

The three-parameter Standard model is composed of two elements, the spring, and the Kelvin-Voigt unit connected in series (Fig. 4.3a).

Starting from the definition of the stress-strain behaviour of the single elements it is possible to write the following algebraic-differential system of equation governing the response of the model

$$\begin{cases} \varepsilon = \varepsilon_{\mathrm{e}}^{\mathrm{i}} + \varepsilon_{\mathrm{e}}^{\mathrm{v}} \\ \sigma = E^{\mathrm{i}}\, \varepsilon_{\mathrm{e}}^{\mathrm{i}} = E^{\mathrm{v}}\, \varepsilon_{\mathrm{e}}^{\mathrm{v}} + \eta\, \dot{\varepsilon}_{\mathrm{e}}^{\mathrm{v}}, \end{cases} \tag{4.8}$$

where $\varepsilon_{\mathrm{e}}^{\mathrm{i}}$ and $\varepsilon_{\mathrm{e}}^{\mathrm{v}}$ are the two parts of the deformation (instantaneous and viscous respectively), E^i and E^v are the stiffness of the springs (instantaneous and viscous respectively), and η represents the coefficient of the viscous damper.

Starting from eq. (4.8) it is possible to solve a generic problem with different boundary conditions. In Figure 4.3b-c the results in terms of stress-time and

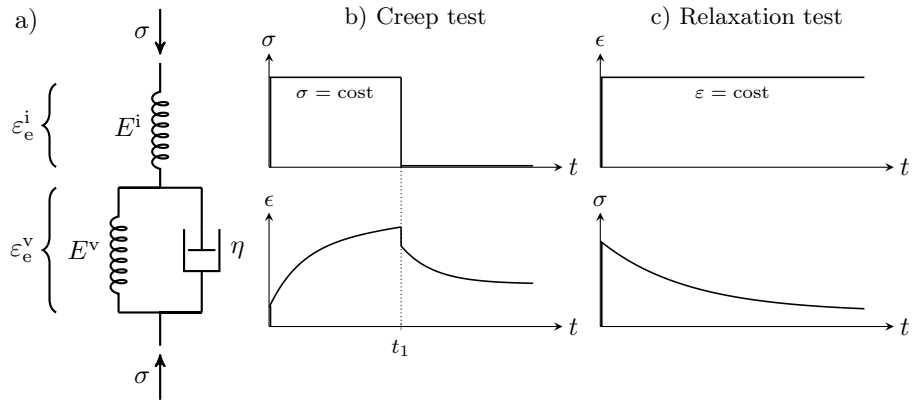

Figure 4.3: Standard viscoelastic material response: a) rheological model, b) creep strain and recovery at constant stress input, c) stress relaxation at constant strain (Skrzypek 1993).

strain-time curves for two generic creep and relaxation tests are reported. The jump in the applied stress leads to a jump in the strain curves due to the instantaneous part of the total deformation. The relative amount of instantaneous and viscous deformation can be calibrated choosing a proper E^v/E^i ratio.

Bingham elastic-viscoplastic model

The three-parameter Bingham elastic-viscoplastic model is composed of two elements, the spring, and the Bingham unit connected in series (Fig. 4.4a).

The classical approach of rheological modelling perfectly adopts plastic sliders for the plastic part of deformation. In geomechanics the use of hardening sliders has many advantages and can properly describe different features of stress-strain behaviour of clays in uniaxial conditions. In this exposition a linear hardening slider will be used in order to introduce the main aspects of the model in a relatively simple mathematical framework.

The strain decomposition in the case of Bingham elastic-viscoplastic is shown in eq. (4.9). It holds true for all the possible states of stress.

$$\varepsilon = \varepsilon_e^i + \varepsilon_p^v. \tag{4.9}$$

The hardening rule, assuming a linear strain hardening law,gives the result

$$\sigma_{\mathrm{pc}}(\varepsilon_{\mathrm{p}}^{\mathrm{v}}) = \tilde{\lambda}\ \varepsilon_{\mathrm{p}}^{\mathrm{v}}. \tag{4.10}$$

in which $\tilde{\lambda}$ is the hardening material parameter.

The equations governing the response of the model are different for the two possible regimes: purely elastic ($\sigma < \sigma_{\mathrm{pc}}(\varepsilon_{\mathrm{p}}^{\mathrm{v}})$), and elasto-viscoplastic ($\sigma \geq \sigma_{\mathrm{pc}}(\varepsilon_{\mathrm{p}}^{\mathrm{v}})$).

The constitutive equations for the elastic regime become

$$\sigma = E^{\mathrm{i}}\ \varepsilon_{\mathrm{e}}^{\mathrm{i}}, \qquad \dot{\varepsilon}_{\mathrm{p}}^{\mathrm{v}} = 0 \tag{4.11}$$

and for the elastic-viscoplastic regime they are

$$\sigma = E^{\mathrm{i}}\ \varepsilon_{\mathrm{e}}^{\mathrm{i}} = \sigma_{\mathrm{pc}}(\varepsilon_{\mathrm{p}}^{\mathrm{v}}) + \eta\ \dot{\varepsilon}_{\mathrm{p}}^{\mathrm{v}}. \tag{4.12}$$

Equation (4.11) and (4.12) can be summarized in a unique system of differential equation as follows (Liingaard et al. 2004)

$$\dot{\varepsilon} = \begin{cases} \dot{\varepsilon}_{\mathrm{e}}^{\mathrm{i}} = \dfrac{\dot{\sigma}}{E^{\mathrm{i}}} & \text{for} \quad \sigma < \sigma_{\mathrm{pc}} \\ \dot{\varepsilon}_{\mathrm{e}}^{\mathrm{i}} + \dot{\varepsilon}_{\mathrm{p}}^{\mathrm{v}} = \dfrac{\dot{\sigma}}{E^{\mathrm{i}}} + \dfrac{\sigma - \sigma_{\mathrm{pc}}(\varepsilon_p^v)}{\eta} & \text{for} \quad \sigma > \sigma_{\mathrm{pc}}. \end{cases} \tag{4.13}$$

The integration of the constitutive model can be done for a general boundary condition.

In Figure 4.4b the results of a classical creep test with two different stress levels are shown. If the load is lower than the initial yield stress ($\sigma_{\mathrm{pc}}^{\mathrm{ini}}$ in Fig. 4.4) the response is purely elastic and the strain is immediately recovered when the stress is removed. When the applied stress exceeds the initial yield stress the material shows a viscoplastic response and the deformation evolves with time. Once the stress decreases and becomes lower than the hardened yield stress, the viscoplastic mechanism stops and the behaviour is again purely elastic.

Figure 4.4c reports a sketch of the strain rate effect of a viscoplastic material modelled with Bingham elastic-viscoplastic model. In this example the stress has been applied with different strain rates ($\dot{\varepsilon}$ in Figure). The stress-strain response is a function of the rate of loading, and is included between two limit curves: the quasi-static curve ($\dot{\varepsilon} \simeq 0$) that corresponds to the classical rate independent elastoplastic solution, and the curve for extremely fast loading ($\dot{\varepsilon} \simeq \infty$) for which the material behaves like a purely elastic material.

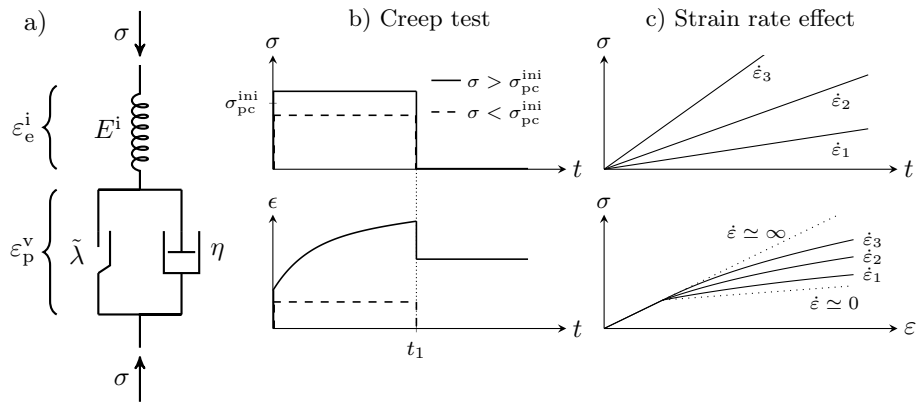

Figure 4.4: Bingham elastic viscoplastic with hardening material response: a) rheological model, b) creep strain and recovery at constant stress input, c) strain rate effect of the model (modified from Skrzypek (1993)).

The classical rheological models approach have some shortcomings for the simulation of geotechnical problems.

The use of linear basic elements cannot represent the strongly non-linear behaviour of soil. It is well accepted that the elastic, plastic and viscous behaviours of soil are highly non-linear. A reliable rheological model for soil must involve non-linear spring, slider and dashpot.

Another drawback of this kind of approach is the fact that the Maxwell model gives good results for relaxation, whereas the Kelvin-Voigt model shows good results for creep simulation. In order to obtain a general model it is necessary to complicate the rheological approach by assembly more basic units.

In the past, many authors used the differential rheological approach to formulate constitutive models for geologic materials. Among these, that of Murayama and Shibata (1961), Barden (1965) and Murayama (1983) are the most relevant.

4.4 General multiaxial models

The models presented in the previous sections were formulated for a specific boundary and load condition. In most cases they cannot be applicable to a general boundary value problem, and their implementation into multiaxial finite element codes remains difficult or impossible.

A different strategy for the modelling is the formulation of general models by extending the classical rate-independent theory to the viscous case. This extension must be based on the experimental evidence, and the empirical or semi-empirical relationship proposed in literature can be used as a base for the generalization in a more consistent constitutive framework.

The general approaches to time dependent modelling can be classified in two classes (Liingaard et al. 2004): elasto-viscoplastic models based on the concept of non-stationary flow surface, and elasto-viscoplastic models based on the overstress theory.

4.4.1 Nonstationary flow surface theory

The framework of the nonstationary flow surface theory (NSFS) was introduced by Naghdi and Murch (1963) and Olszak and Perzyna (1966). The following description is based on Naghdi and Murch (1963) and Liingaard et al. (2004). In the exposition of the theory boldface characters denote the second order tensors.

The nonstationary flow surface theory was formulated starting from rate independent elastoplasticity through a different definition of the yield condition. In the inviscid elastoplasticity with work hardening the yield surface depends on the state of stress $\boldsymbol{\sigma}$, on the plastic strains $\boldsymbol{\varepsilon}^{\mathrm{p}}$, and on the hardening parameter $\boldsymbol{\kappa}$. The modified yield condition of NSFS is

$$f = f(\boldsymbol{\sigma}, \boldsymbol{\varepsilon}^{\mathrm{p}}, \boldsymbol{\kappa}, \boldsymbol{\chi}) \tag{4.14}$$

where $\boldsymbol{\chi}$ is the time dependent variable. The yield condition of eq. (4.14) is *nonstationary*, due to the time dependency introduced by $\boldsymbol{\chi}$. As a consequence the yield surface can vary with time also at constant values of the plastic strains.

The possible states of stress are within or on the nonstationary yield surface and therefore $f \leq 0$. If $f < 0$ the material is in the elastic regime, whereas for $f = 0$ the material is in the viscoplastic state. The time rate form of the NSFS yield surface is

$$\dot{f} = \frac{\partial f}{\partial \boldsymbol{\sigma}} \dot{\boldsymbol{\sigma}} + \frac{\partial f}{\partial \boldsymbol{\varepsilon}^{\mathrm{p}}} \dot{\boldsymbol{\varepsilon}}^{\mathrm{p}} + \frac{\partial f}{\partial \boldsymbol{\kappa}} \dot{\boldsymbol{\kappa}} + \frac{\partial f}{\partial \boldsymbol{\chi}} \dot{\boldsymbol{\chi}}. \tag{4.15}$$

From equation 4.15 it is possible to define the loading criterion of the model. To this aim it is useful to introduce the following operator

$$\mathcal{L}(\dot{\boldsymbol{\sigma}}, \dot{\boldsymbol{\chi}}) = \frac{\partial f}{\partial \boldsymbol{\sigma}} \dot{\boldsymbol{\sigma}} + \frac{\partial f}{\partial \boldsymbol{\chi}} \dot{\boldsymbol{\chi}}, \tag{4.16}$$

that, together with f, allows the definition of the loading state of the material:

$$\begin{array}{lll} \mathcal{L}(\dot{\boldsymbol{\sigma}}, \dot{\boldsymbol{\chi}}) < 0, & f < 0 & \text{(unloading)} \\ \mathcal{L}(\dot{\boldsymbol{\sigma}}, \dot{\boldsymbol{\chi}}) = 0, & f = 0 & \text{(neutral loading)} \\ \mathcal{L}(\dot{\boldsymbol{\sigma}}, \dot{\boldsymbol{\chi}}) > 0, & f = 0 & \text{(loading)} \end{array} . \tag{4.17}$$

The first and the third conditions of eq. 4.17 can be interpreted in the classical way. The condition of *neutral loading* is associated to $\dot{\boldsymbol{\varepsilon}}^{\mathrm{p}} = \dot{\boldsymbol{\kappa}} = 0$ but some changes in the state variables ($\dot{\boldsymbol{\sigma}}$, dt, and so on) lead to another viscoelastic-plastic state ($f = \dot{f} = 0$).

The strain decomposition of NSFS theory is

$$\dot{\boldsymbol{\varepsilon}} = \dot{\boldsymbol{\varepsilon}}^{\mathrm{e}} + \dot{\boldsymbol{\varepsilon}}^{\mathrm{vp}}, \tag{4.18}$$

where $\dot{\boldsymbol{\varepsilon}}^{\mathrm{e}}$ is the elastic part of the total strain rate.

The plastic strain rate is defined according to the flow rule:

$$\dot{\boldsymbol{\varepsilon}}^{\mathrm{vp}} = \langle \Lambda \rangle \frac{\partial g}{\partial \boldsymbol{\sigma}}, \tag{4.19}$$

in which $\langle \Lambda \rangle$ is a non negative multiplier and g is the viscoplastic potential. $\langle\ \rangle$ is the Macaulay brackets operator that ensures that the plastic strains occur only when loading from a plastic strain. The plastic multiplier Λ is determined through the consistency rule and has the same meaning as the plastic multiplier of the inviscid plasticity theory. The difference with respect to rate independent plasticity is that Λ includes the time dependence through the term $\boldsymbol{\chi}$. This dependency allows the simulation of creep processes in which the plastic strains evolve at constant applied stress.

The nonstationary flow surface theory is capable of simulating creep and stress relaxation with initial stress outside the initial yield surface. The introduction of time dependence is related to the definition of the variable function $\boldsymbol{\chi}$. The proper definition of the time dependent variable is the key issue in the formulation of the model.

In the field of soil mechanics many constitutive models based on nonstationary flow surface theory have been proposed. Among these, the most important are those by Sekiguchi (1977), Nova (1982), and Matsui and Abe (1985).

4.4.2 Overstress theory

The general foundations of the overstress theory can be recognised in the study of viscoplastic problems by Hohenemser and Prager (1932), Prager (1937), and Malvern (1951). Perzyna (1963a,b, 1966, 1974), formulated the multi-axial overstress theory as a three dimensional version of Malvern uniaxial constitutive law.

The first constitutive assumption of Perzyna approach is that the viscous properties of the material become manifest only in the plastic state, and in the elastic region the material behaves as a rate independent material. The proposed strain decomposition results in

$$\dot{\boldsymbol{\varepsilon}} = \dot{\boldsymbol{\varepsilon}}^{\mathrm{e}} + \dot{\boldsymbol{\varepsilon}}^{\mathrm{p}}, \tag{4.20}$$

where $\dot{\boldsymbol{\varepsilon}}^{\mathrm{e}}$ represents the elastic strain rate, and $\dot{\boldsymbol{\varepsilon}}^{\mathrm{p}}$ represents the combined viscous and plastic effects (note that the boldface characters denote second order tensor quantities).

The definition of the yield criterion, when the material is in the elastic field, does not differ from the yield condition of the inviscid theory of plasticity, and is called *static yield criterion*. Perzyna introduces the *static yield function*, $F(\boldsymbol{\sigma}, \boldsymbol{\varepsilon}^{\mathrm{p}})$ in the following general form

$$F(\boldsymbol{\sigma}, \boldsymbol{\varepsilon}^{\mathrm{p}}) = \frac{f(\boldsymbol{\sigma}, \boldsymbol{\varepsilon}^{\mathrm{p}})}{\kappa} - 1, \tag{4.21}$$

where the function $f(\boldsymbol{\sigma}, \boldsymbol{\varepsilon}^{\mathrm{p}})$ depends on the stress state $\boldsymbol{\sigma}$ and on the plastic strain, and $\kappa = \tilde{\kappa}(W^{\mathrm{p}})$ is the strain hardening parameter that depends on the plastic work W^{p}.

It is worth noting, that the distinction between *static* and *dynamic* yield condition has been intuitively proposed by many authors observing the results of strain rate effect on clayey soils (see Section 2.4.3).

The flow surface is assumed regular and convex. The key assumption of overstress theory is the definition of the inelastic part $\dot{\boldsymbol{\varepsilon}}^{\mathrm{p}}$ of eq. (4.20)

$$\dot{\boldsymbol{\varepsilon}}^{\mathrm{p}} = \gamma \left\langle \Phi(F) \right\rangle \frac{\partial f}{\partial \boldsymbol{\sigma}} \ , \tag{4.22}$$

in which γ is a viscous parameter and $\langle \Phi(F) \rangle$ represents the viscous nucleus.

Starting from eq. (4.22) and (4.21) it is possible to write the general relationship

$$f(\boldsymbol{\sigma}, \boldsymbol{\varepsilon}^{\mathrm{p}}) = \kappa \left[1 + \langle \Phi^{-1}(\dot{\boldsymbol{\varepsilon}}^{\mathrm{p}}) \rangle \right]. \tag{4.23}$$

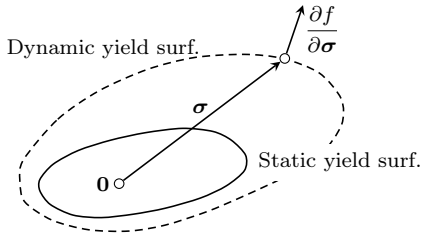

Figure 4.5: Static and dynamic yield surfaces and flow rule in the general stress space (Perzyna 1966).

Equation (4.23) represents implicitly the *dynamic yield condition* for elastic viscoplastic, work hardening materials. The function $\langle \Phi^{-1}(\dot{\varepsilon}^{\mathrm{p}}) \rangle$ is called viscosity function and can be derived from the viscous nucleus $\langle \Phi(F) \rangle$. Starting from eq. (4.23) it is possible to define the dependence of the yield surface on the plastic strain rate. Figure 4.5 shows a sketch of the static and dynamic yield surfaces as reported by Perzyna (1966).

The evolution of the static yield surface is related to the classical work hardening effects, whereas the dynamic yield surface depends also on the viscoplastic strain rate.

The function $\Phi(F)$ that defines the viscous response of the material must satisfy the following condition

$$\langle \Phi(F) \rangle = \begin{cases} 0 & \text{for} \quad F \leq 0 \\ \Phi(F) & \text{for} \quad F > 0. \end{cases} \tag{4.24}$$

that represents the loading criterion for the inelastic deformations.

The main feature of the overstress theory is that the state of stress can be on, within or outside the static yield surface. In particular $\boldsymbol{\sigma}$ lies outside the static surface when $\dot{\varepsilon}^{\mathrm{p}} > 0$. This implies that the consistency condition of the static yield surface is invalid, and the real consistency conditions must be imposed for the dynamic yield surface (that involves the plastic strain rate). The distance between the state of stress and the static yield surface is called *overstress* and is related to the plastic strain rate through the viscosity function $\langle \Phi^{-1}(\dot{\varepsilon}^{\mathrm{p}}) \rangle$.

The determination of the viscous nucleus (and therefore of the viscosity function) is based on experimental evidence. In the field of soil mechanics many experts proposed the derivation of the viscous nucleus from tests (Adachi and

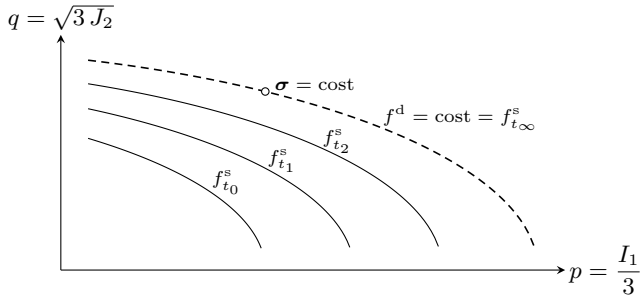

Figure 4.6: Example of a generic overstress model response for a creep test (Liingaard et al. 2004).

Oka 1982; Adachi and Okano 1974; Oka et al. 1986; Di Prisco and Imposimato 1996). The most used forms are power law and exponential functions.

From the analytical formulation of the overstress theory, it can be easily deduced that for $\dot{\boldsymbol{\varepsilon}}^{\mathrm{p}} \to 0$ the dynamic yield surface coincides with the static yield surface. Referring to undisturbed soil specimens, the determination of the initial position of the static yield surface can be performed through extremely slow tests (Wood 1991).

Analysing the classical response of a material modelled using the overstress theory, it is possible to highlight the advantages of this constitutive approach:

- the model is capable of representing the creep process, and (with a proper definition of the viscous nucleus) the decrement of the plastic strain rate during the creep process. Since the stress state is constant during the creep phase, the dynamic yield surface maintains constant while the static yield surface evolves towards the DYS (Fig. 4.6). The two coincide when the viscous nucleus vanishes (in general for $t = \infty$);

- the model can simulate the strain rate effect in the plastic regime. This aspect can be emphasized referring to a stepwise variation of the applied strain rate: the change in the strain rate causes a sudden variation of the dynamic yield surface that reproduces the observed steps in the stress state during oedometer and triaxial tests (Section 2.3.2 and 2.4.4);

- the overstress theory defines the viscous behaviour of the material without defining any reference time. Once the initial state of the static yield surface is defined, the stress-strain-time problem can be modelled for any kind of

boundary and loading condition. The definition of the initial state yield surface is therefore the crucial issue of the model calibration.

The drawbacks of the overstress theory is that the framework neglects the viscous behaviour in the elastic regime, and that the plastic deformation is entirely associated to the viscous nucleus without the possibility of modelling any instantaneous plastic strain.

CHAPTER 5

The proposed one-dimensional viscoelastic-viscoplastic constitutive model

A new one-dimensional viscoelastic-viscoplastic constitutive model will be presented in this chapter. The theoretical approach is the one-dimensional formulation of the multiaxial overstress theory. The basic assumption of the constitutive approach are: the total strain is decomposed in four components, two elastic (instantaneous and viscous), and two plastic (instantaneous and viscous); the model is based on a logarithmic viscosity function. The model has been validated on a series of literature evidences and on the experimental evidences shown in Chapter 3.

5.1 Introduction

The accurate estimation of soil deformations induced by the construction of civil structures and infrastructure is one of the most challenging problems in for the present geotechnical engineers. For example, building high-rise structure and urban excavations are deeply influenced by the need of preserving existing structures; or, in high velocity railway field, the accurate prediction of ground deformation is of paramount importance in the design of the infrastructure. In order to perform reliable analyses of this complex problems, the accurate modelling of the constitutive behaviour of the foundation soil is an essential task.

The response of real structures founded on clayey soils is often affected by the time-dependent phenomena (Mesri and Choi 1985; Tanabashi et al. 1988; Crawford and Morrison 1996). To obtain realistic solutions from the simulation of real structures founded soils subjected to delayed deformation, it is essential to use a constitutive framework that accounts for time dependency in the formulation of the stress-strain law.

In literature many studies have been proposed regarding the evaluation of viscous behaviour of soil. Limiting the analysis to the mono-dimensional case, most of the studies proposed in the literature are based on the empirical fitting of the experimental results for a particular laboratory test (a.e. creep, relaxation, constant rate of strain). The advantage of this kind models is mainly the wide experimental base of data used for the formulation, that is representative of real observed phenomena. On the other hand, the main drawback of empirical formulations is that are applicable only to specific boundary and loading conditions, and can not be extended to a general multi-axial constitutive framework.

The most important evidences, that allow the definition of the characters of viscous response of soils, are: the isotach concept (Suklje 1957), that postulates the existence of a unique stress-strain curve for each strain rate; the observation of preconsolidation related to ageing at constant stress (Bjerrum 1967); the effect of the strain rate on the preconsolidation pressure in constant rate of strain tests (Leroueil, Kabbaj, et al. 1985); the constancy of the ratio between the coefficient of secondary consolidation C_α and the 'local' compression index C_c (Mesri and Godlewski 1977; Mesri and Castro 1987; Terzaghi et al. 1996; Mesri and Ajlouni 2007); and the effect of the stress increment ratio on the shape of secondary phase (Fox, Edil, and Lan 1992; Mesri, Stark, and Chen 1994; Mesri, Stark, Ajlouni, et al. 1997).

Some examples of empirical uniaxial models are that of Suklje (1957), Walker and Raymond (1968), Mesri (1973), Mesri and Choi (1985), and Yin (1999). Starting from this basic models, many works proposed the extension of rate-independent models of viscous aliquots of deformation (Tavenas et al. 1978; Yin and Graham 1989).

The main drawback of this models is that they have been formulated depending on a sort of reference time referred to the initial time of viscous deformation. The definition of the reference time can be problematic, even impossible, for complicate load histories.

More complete and consistent constitutive models have been proposed in the literature for a triaxial state of stress. This approaches are formulated by linking the viscous effect to the plastic strain rate. Example of such approaches are that

of Kutter and Sathialingam (1992), Yin, Zhu, et al. (2002) and Hinchberger and Qu (2009).

In this Chapter a new constitutive approach will be proposed. The theoretical framework is that of rheological model, based on a differential representation in which non-linear springs, sliders and viscous dashpots are used. The most important aspects of the proposed model are essentially three:

- the material response is divided in two phenomenon: a short-term (immediate) and a long-term (delayed) response;
- viscous effects are modelled by using a logarithmic law of the viscous strain rate;
- viscous deformation have been considered both in elastic and plastic phases

Starting from this basic assumption the resulting model is based on the splitting of the deformation in four components: two elastic (instantaneous and viscous), and two plastic (instantaneous and viscous).

The Chapter is organized as follows: firstly the most important constitutive hypotheses and the numerical implementation strategy are described; then the parametric analyses with some hints for the calibration of the model is shown; finally an extensive validation of the model based on a wide experimental survey is presented.

5.2 Formulation of the constitutive model

The proposed constitutive model has been deduced from the measured time-dependent, 1D response of different types of both organic and inorganic soils, as observed in our laboratory tests (Chapter 3) and as presented in the literature. Although the delayed response of fine grained soils subjected to oedometer conditions is strongly related to the mineralogical composition, some aspects of soil response are common to all soils. These aspects can be summarized as follows:

- the time evolution of the deformation in a creep test (i.e. at constant stress) is generally linear in a logarithm of time plot, with a slope that is related to the coefficient of secondary compression C_α, (Suklje 1957; Bjerrum 1967);
- time-dependent deformations affects both the elastic and the plastic regime, thus soil's general behaviour can be classified as both visco-elastic and visco-plastic;

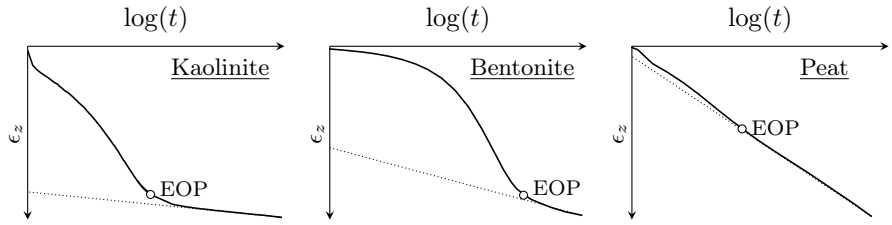

Figure 5.1: Time-dependent behaviour of different type of soils in oedometer condition at constant stress.

- assuming in a first approximation that viscous deformations are linear in the logarithmic of time plot during the whole primary consolidation (according to the dotted line in Fig. 5.1), the relative amount of viscous deformation at the end of the primary consolidation with respect to the total deformation, strongly depends on the nature of the considered soil: it can be very small in kaolinite, fairly larger in bentonite, and predominant in peats (Fig. 5.1).

The constitutive model is developed referring to the effective stress, and the modelled time dependent phenomena are related only to the viscosity of the solid skeleton. The coupling between solid and liquid phase has been accounted separately with the classical mono-dimensional consolidation theory (Terzaghi 1925).

Starting from these basic observations, we propose to model the soil's oedometer response with the rheological model shown in fig. 5.2. The most important assumption of the model is that the deformation is assumed to consist partly of a short-term, instantaneous fraction and partly of a long-term, viscous part. As a result, since soil deformation at the end of the primary consolidation is mostly given by the short-term, instantaneous mechanism (and just in minor part by the long-term, viscous one), considering the example of fig. (5.1) the short-term, instantaneous deformation is expected to be large in kaolinite and bentonite, and negligible in peats. It is worth adding that the simplest assumption for short-term mechanism of deformation is that it is instantaneous. However the assumption of instantaneous behaviour could be equivalently substituted by that one of a short-term, viscous response. The reliability of the assumption concerning the short term response (i.e. instantaneous or short-term, viscous) could be evaluated through a better insight in the mechanisms ruling the primary consolidation, for instance through the analysis of pore pres-

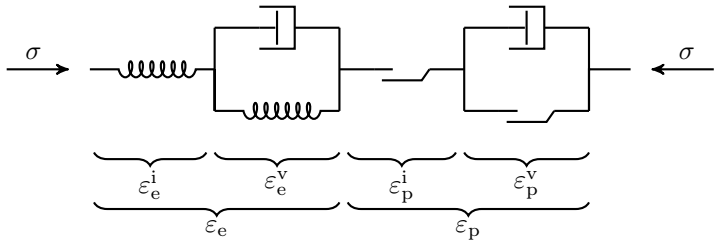

Figure 5.2: Proposed rheological model.

sure dissipation within the primary consolidation.

The resulting rheologic model consists of four elements (fig. 5.2): the first two represent the elastic part, whereas the last two concern the plastic (irreversible) part of the deformation. Both the elastic and plastic parts consist of both a short-term, instantaneous and a long-term, viscous mechanism. Thus the short-term, instantaneous mechanism consists of a spring (for the elastic strain) combined with a slider element (for the irreversible strain), whereas the long-term delayed component consists of a spring-dashpot (for the elastic strain) and a slider-dashpot element (for the irreversible strains), thus both Kelvin and Bingham rheologic elements are included in the model (fig. 5.2).

The decomposition of the total deformation is expressed by the following equation 5.1.

$$\varepsilon = \underbrace{\varepsilon_{\mathrm{e}}^{\mathrm{i}} + \varepsilon_{\mathrm{e}}^{\mathrm{v}}}_{\varepsilon_{\mathrm{e}}} + \underbrace{\varepsilon_{\mathrm{p}}^{\mathrm{i}} + \varepsilon_{\mathrm{p}}^{\mathrm{v}}}_{\varepsilon_{\mathrm{p}}}, \tag{5.1}$$

in which the index 'e' and 'p' denotes the type of deformation component (elastic and plastic, respectively), and the apex identifies the time-dependent character of the deformation component ('i' for instantaneous, and 'v' for viscous). The proposed rheological approach has the advantage of preserving the intuitive decomposition of the total deformation into an elastic and a plastic part (permitting a simple approach for model calibration), although the proposed strain decomposition complicates the numerical implementation of the model with respect to the rheological models based on stress decomposition (e.g. the generalized Maxwell model Haupt 2002), because the single fractions of total strain can be evaluated through the solution of a highly non-linear system of equations.

The asymptotic behaviour at very large (infinite) time of soil is assumed to follow the usual, well-accepted stress-strain response of clays under one di-

mensional conditions, namely the compression response in terms of the vertical strain versus the logarithm of stress is assumed bilinear, with initial slope κ for purely elastic response (with $OCR > 1$, if $OCR = \sigma_{\mathrm{pc}}/\sigma$, where σ is the current vertical stress, and σ_{pc} is the preconsolidation stress) and λ for elasto-plastic strains (with $OCR = 1$). As a result, the asymptotic (at an infinitely large time) elastic and plastic strains, under a given constant stress σ, are expressed by

$$\varepsilon_{\mathrm{e}} = \varepsilon_0 + \kappa \ln\left(\frac{\sigma}{\sigma_0}\right) \tag{5.2a}$$

$$\varepsilon_{\mathrm{p}} = \varepsilon_0 + (\lambda - \kappa) \ln\left(\frac{\sigma}{\sigma_0}\right) \tag{5.2b}$$

where σ_0 is the reference pressure (usually 1 kPa), corresponding to the initial strain ε_0 (usually assumed null).

Equation (5.2a) represents a non-linear spring, taking account of the elastic deformation, and eqn. (5.2b) represents a non-linear hardening slider, taking account of plastic deformation. If the applied stress is below the preconsolidation stress, only the elastic spring mechanism is active, but if the stress exceeds the preconsolidation stress, then both the elastic and plastic mechanisms are active. As a result, the asymptotic (at an infinitely large time) behaviour coincides with classical Cam Clay model.

The proposed model extends these well-accepted concepts to viscous materials, by splitting the two mechanisms of (5.2) into an instantaneous and a viscous part, thus starting from eqn. (5.2a) the following instantaneous and viscous elastic relationships are obtained

$$\sigma_{\mathrm{e}}^{\mathrm{i}} = \sigma_0 \ \exp\left(\frac{\varepsilon_{\mathrm{e}}^{\mathrm{v}} - \varepsilon_0}{\alpha_{\mathrm{e}}\ \kappa}\right) \tag{5.3a}$$

$$\sigma_{\mathrm{e}}^{\mathrm{v}} = \sigma_0 \ \exp\left(\frac{\varepsilon_{\mathrm{e}}^{\mathrm{v}} - \varepsilon_0}{(1-\alpha_{\mathrm{e}})\ \kappa}\right) \left[1 + \psi_{\mathrm{e}}(\dot{\varepsilon}_{\mathrm{e}}^{\mathrm{v}})\right], \tag{5.3b}$$

where $\psi_{\mathrm{e}}(\dot{\varepsilon}_{\mathrm{e}}^{\mathrm{v}})$ is a viscosity function that will be defined in Subsection 5.2.1 and α_{e} is a partition coefficient, ranging between 0 and 1. The effect of the partition coefficient is splitting the elastic deformation into an instantaneous and a delayed part, in such a way that when $\alpha_{\mathrm{e}} \to 0$ a purely viscous response is obtained, and when $\alpha_{\mathrm{e}} \to 1$ a purely instantaneous response is simulated. Note that in order to guarentee the equilibrium, $\sigma_{\mathrm{e}}^{\mathrm{i}} = \sigma_{\mathrm{e}}^{\mathrm{v}}$.

The same approach is used for the instantaneous and viscous parts of the plastic strain, thus from eqn. (5.2b) we obtain

$$\sigma_{\mathrm{p}}^{\mathrm{i}} = \sigma_0 \ \exp\left(\frac{\varepsilon_{\mathrm{p}}^{\mathrm{v}} - \varepsilon_0}{\alpha_{\mathrm{p}}\ (\lambda - \kappa)}\right) \tag{5.4a}$$

$$\sigma_{\mathrm{p}}^{\mathrm{v}} = \sigma_0 \ \exp\left(\frac{\varepsilon_{\mathrm{p}}^{\mathrm{v}} - \varepsilon_0}{(1-\alpha_{\mathrm{p}})(\lambda - \kappa)}\right)\left[1 + \psi_{\mathrm{p}}(\dot{\varepsilon}_{\mathrm{p}}^{\mathrm{v}})\right]. \tag{5.4b}$$

where $\psi_{\mathrm{p}}(\dot{\varepsilon}_{\mathrm{e}}^{\mathrm{v}})$ and α_{p} have the same meaning of $\psi_{\mathrm{e}}(\dot{\varepsilon}_{\mathrm{e}}^{\mathrm{v}})$ and α_{e}. It is worth adding that in eqns. (5.4) we can distinguish two yield stresses, $\sigma_{\mathrm{pc}}^{\mathrm{i}}$ and $\sigma_{\mathrm{pc}}^{\mathrm{v}}$

$$\sigma_{\mathrm{pc}}^{\mathrm{i}} = \sigma_0 \ \exp\left(\frac{\varepsilon_{\mathrm{p}}^{\mathrm{v}} - \varepsilon_0}{\alpha_{\mathrm{p}}\ (\lambda - \kappa)}\right) \tag{5.5a}$$

$$\sigma_{\mathrm{pc}}^{\mathrm{v}} = \sigma_0 \ \exp\left(\frac{\varepsilon_{\mathrm{p}}^{\mathrm{v}} - \varepsilon_0}{(1-\alpha_{\mathrm{p}})(\lambda - \kappa)}\right). \tag{5.5b}$$

Thus short term (istantaneous) plastic strains occur when $\sigma_{\mathrm{e}}^{\mathrm{i}} = \sigma_{\mathrm{e}}^{\mathrm{v}} = \sigma_{\mathrm{p}}^{\mathrm{v}}$, whereas long term (viscous) deformations occurs when $\sigma_{\mathrm{e}}^{\mathrm{i}} = \sigma_{\mathrm{e}}^{\mathrm{v}} = \sigma_{\mathrm{pc}}^{\mathrm{v}}\left[1 + \psi_{\mathrm{p}}(\dot{\varepsilon}_{\mathrm{p}}^{\mathrm{v}})\right]$. As a result, the term $\left[1 + \psi_{\mathrm{p}}(\dot{\varepsilon}_{\mathrm{p}}^{\mathrm{v}})\right]$ has the role of increasing the yield stress, within the framework of visco-plasticity proposed by Perzyna (1966). According to overstress model by Perzyna (1966), viscous plastic strains will occur when $\sigma_{\mathrm{e}}^{\mathrm{i}} = \sigma_{\mathrm{e}}^{\mathrm{v}} = \sigma_{\mathrm{pc}}^{\mathrm{v}}\left[1 + \psi_{\mathrm{p}}(\dot{\varepsilon}_{\mathrm{p}}^{\mathrm{v}})\right]$ (and $\dot{\sigma}_{\mathrm{e}}^{\mathrm{i}} = \dot{\sigma}_{\mathrm{e}}^{\mathrm{v}} > 0$), whereas according to non-viscous elasto-plasticity, instantaneous plastic strains will occur when $\sigma_{\mathrm{e}}^{\mathrm{i}} = \sigma_{\mathrm{e}}^{\mathrm{v}} = \sigma_{\mathrm{pc}}^{\mathrm{i}}$ (and $\dot{\sigma}_{\mathrm{e}}^{\mathrm{i}} = \dot{\sigma}_{\mathrm{e}}^{\mathrm{v}} > 0$). Thus the yield stresses $\sigma_{\mathrm{pc}}^{\mathrm{i}}$ and $\sigma_{\mathrm{pc}}^{\mathrm{v}}\left[1 + \psi_{\mathrm{p}}(\dot{\varepsilon}_{\mathrm{p}}^{\mathrm{v}})\right]$ play the role of two consolidation pressures. The latter, in particular, will be denoted below as *dynamic yield stress*.

The viscosity functions $\psi_{\mathrm{e}}(\dot{\varepsilon}_{\mathrm{e}}^{\mathrm{v}})$ and $\psi_{\mathrm{p}}(\dot{\varepsilon}_{\mathrm{p}}^{\mathrm{v}})$ rule the evolution of the viscous strains with respect to time and are expressed in term of strain rates ($\dot{\varepsilon}_{\mathrm{e}}^{\mathrm{v}}$ for the viscoelastic mechanism, and $\dot{\varepsilon}_{\mathrm{p}}^{\mathrm{v}}$ for the viscoplastic one). The viscosity functions must vanish when the strain rate is null ($\dot{\varepsilon}_{\mathrm{e}}^{\mathrm{v}} = 0$ and $\dot{\varepsilon}_{\mathrm{p}}^{\mathrm{v}} = 0$) in order to ensure the equivalence of viscous and instantaneous models for extremely slow processes. In this case the constitutive equations of eq. (5.3) and (5.4) become equivalent of the non-viscous problem, shown in eq. (5.2).

The choice of the viscosity functions is critical for a good prediction of the delayed response and must be based on the experimental observation of the material behaviour.

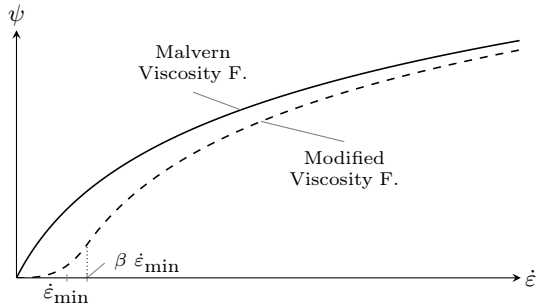

Figure 5.3: Viscosity function.

5.2.1 Choice of the Viscosity Function

The simulated delayed model response deeply depends on the selected viscosity function. As a result the choice of the viscosity function is particularly important and must be performed starting from the experimental evidences. In fine grained soils, the typical strain-time response, obtained from a large load-increment, constant-stress oedometer test, is almost linear with respect to the logarithm of elapsed time, after the end of the primary consolidation (Fig. 5.1). This evidence is well-accepted and was observed in different soils (Suklje 1957; Bjerrum 1967; Berre and Nersen 1972; Mesri 1973; Mesri and Godlewski 1977).

Starting from this experimental evidence, the general form of the viscosity functions is given by the following equation:

$$\psi(\dot{\varepsilon}^{\mathrm{v}}) = \Gamma \ln\left(\frac{\dot{\varepsilon}^{\mathrm{v}}}{\dot{\varepsilon}_{\min}} + 1\right), \tag{5.6}$$

where Γ and $\dot{\varepsilon}_{\min}$ are two constitutive parameters. Equation (5.6) is a slight modification of a proposal made firstly by Malvern (1951) and later by Perzyna (1963b). The main difference consists in the introduction of the additional constitutive parameter Γ, which increases the flexibility of model calibration.

The viscosity function proposed in eqn. (5.6) is null for $\dot{\varepsilon}^{\mathrm{v}} = 0$ and provides a linear response in a $\varepsilon^{\mathrm{v}} - \log t$ plot, only for strain rates much larger than $\dot{\varepsilon}_{\min}$. In other terms $\dot{\varepsilon}_{\min}$ must be negligible with respect to the analysed strain-rates.

In order to overcome this defect, a slightly different viscosity function has been considered in order to obtain a strictly linear response in terms of the logarithmic strain rate, independently of $\dot{\varepsilon}^{\mathrm{v}} = 0$ and $\dot{\varepsilon}_{\min}$ values. The alternative

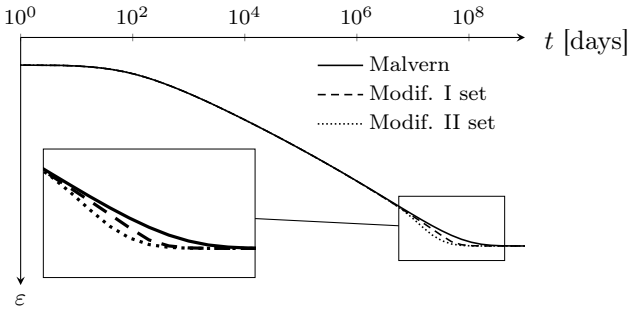

Figure 5.4: Example of results of oedometer test with the two different viscosity functions.

viscosity function is assumed to be composed by a logarithmic branch which is smoothly linked with a polynomial expression, close to the axis origin, namely

$$\psi(\dot{\varepsilon}^{\mathrm{v}}) = \begin{cases} \Gamma \ln\left(\dfrac{\dot{\varepsilon}^{\mathrm{v}}}{\dot{\varepsilon}_{\min}}\right) & \text{for} \quad \dot{\varepsilon}^{\mathrm{v}} > \beta\ \dot{\varepsilon}_{\min} \\ \Gamma\left[\dfrac{\dot{\varepsilon}^{\mathrm{v}}}{\beta\ \dot{\varepsilon}_{\min}}\ a - \left(\dfrac{\dot{\varepsilon}^{\mathrm{v}}}{\beta\ \dot{\varepsilon}_{\min}}\right)^2 b + \left(\dfrac{\dot{\varepsilon}^{\mathrm{v}}}{\beta\ \dot{\varepsilon}_{\min}}\right)^3 c\right] & \text{for} \quad \dot{\varepsilon}^{\mathrm{v}} \leq \beta\ \dot{\varepsilon}_{\min}. \end{cases} \tag{5.7}$$

where the polynomial coefficients a, b and c are detailed in the Appendix, and in turn depend on two further constitutive parameters, β and Ψ, defining the position of the transition point (between the logarithmic and polynomial branches) and the tangent of the viscosity function in the axis origin, respectively.

Figure 5.3, shows the comparison between the two viscosity functions. It can be observed that at large strain rates the two functions practically coincide with each other, whereas minor differences exists for strain rates close to $\dot{\varepsilon}_{\min}$.

Although the modified viscosity function (eqn. (5.7)) is more flexible than the original one (eqn. (5.6), as proposed by Malvern (1951)), the modified viscosity function requires two additional constitutive parameters (i.e. β and Ψ) and involves a more complex implementation, due to the two branches.

The typical simulated strain-time responses for a constant-stress, creep test, obtained with the two viscosity functions (eqn. (5.6) and (5.7)) are compared in Fig. 5.4. The plots show the results of the simulation of the strains induced by a sudden increase of the stress, that is later maintained constant. The evolution of the viscous strain is plotted in terms of the logarithm of the elapsed time. It

is possible to appreciate that the two formulations gives very similar strain-time responses, except for vanishingly small strain rates. Different calibrations of the two parameters β and Ψ permits to modify the shape of the final part of the stress-strain curve.

In the following, the Modified Malvern viscosity function (eq. (5.6)) will be used below for the sake of simplicity.

5.3 Numerical integration of constitutive functions

The numerical implementation of the constitutive model of the 1D formulation described in the previous sections has been performed through a fully implicit back-Euler algorithm. Thus, once a strain increment $\Delta\varepsilon$ is assigned (from the FEM code) in a given time step increment Δt, the strain increment is initially assumed elastic. As a result a non linear system of 2 equations must be initially solved to evaluate the two elastic increments $\Delta\varepsilon_{\mathrm{e}}^{\mathrm{i}}$ and $\Delta\varepsilon_{\mathrm{e}}^{\mathrm{v}}$, namely from eqn. (5.3)

$$\exp\left(\frac{(\varepsilon_{\mathrm{e}}^{\mathrm{i}})_{\mathrm{n}} + \Delta\varepsilon_{\mathrm{e}}^{\mathrm{i}} - \varepsilon_0}{\alpha_{\mathrm{e}}\,\kappa}\right) = \exp\left(\frac{(\varepsilon_{\mathrm{e}}^{\mathrm{v}})_{\mathrm{n}} + \Delta\varepsilon_{\mathrm{e}}^{\mathrm{v}} - \varepsilon_0}{(1-\alpha_{\mathrm{e}})\,\kappa}\right)[1 + \psi_{\mathrm{e}}(\Delta\varepsilon_{\mathrm{e}}^{\mathrm{v}}/\Delta t)] \quad (5.8a)$$

$$\Delta\varepsilon = \Delta\varepsilon_{\mathrm{e}}^{\mathrm{i}} + \Delta\varepsilon_{\mathrm{e}}^{\mathrm{v}}, \quad (5.8b)$$

where $(\varepsilon_{\mathrm{e}}^{\mathrm{i}})_{\mathrm{n}}$ and $(\varepsilon_{\mathrm{e}}^{\mathrm{v}})_{\mathrm{n}}$ are the instantaneous elastic and viscous strains evaluated at the previous time step. The non-linear problem was solved with a conventional Newton-Rapson scheme. The *elastic* stress that is computed using eqn. (5.3), constitutes the so-called *elastic predictor*. If both yield conditions are not violated, then the computed *elastic* stress is valid, and the next time step is considered.

Alternatively, the *elastic* stress may violate one or both the yield stress conditions, namely the stress exceeds only the viscous preconsolidation pressure ($\sigma_{\mathrm{pc}}^{\mathrm{v}}$ of eqn. (5.5b)) or both the instantaneous and viscous preconsolidation pressures ($\sigma_{\mathrm{pc}}^{\mathrm{v}}$ and $\sigma_{\mathrm{pc}}^{\mathrm{v}}$ of eqn. (5.5)). In the former case we must solve a non-linear system of three equations, namely eqns. (5.8a) plus the following equations (deduced

from eqns. (5.3b) and (5.4a), and from the strain decomposition rule)

$$\exp\left(\frac{(\varepsilon_{\mathrm{e}}^{\mathrm{i}})_{\mathrm{n}}+\Delta\varepsilon_{\mathrm{e}}^{\mathrm{i}}-\varepsilon_0}{\alpha_{\mathrm{e}}\,\kappa}\right)=\exp\left(\frac{(\varepsilon_{\mathrm{p}}^{\mathrm{v}})_{\mathrm{n}}+\Delta\varepsilon_{\mathrm{p}}^{\mathrm{v}}-\varepsilon_0}{(1-\alpha_{\mathrm{p}})(\lambda-\kappa)}\right)\left[1+\psi_{\mathrm{p}}(\Delta\varepsilon_{\mathrm{p}}^{\mathrm{v}}/\Delta t)\right], \tag{5.9a}$$

$$\Delta\varepsilon=\Delta\varepsilon_{\mathrm{e}}^{\mathrm{i}}+\Delta\varepsilon_{\mathrm{e}}^{\mathrm{v}}+\Delta\varepsilon_{\mathrm{p}}^{\mathrm{v}}, \tag{5.9b}$$

where $(\varepsilon_{\mathrm{p}}^{\mathrm{v}})_{\mathrm{n}}$ is the viscous plastic strain evaluated at the previous time step and three unknowns are involved, namely $\Delta\varepsilon_{\mathrm{e}}^{\mathrm{i}}$, $\Delta\varepsilon_{\mathrm{e}}^{\mathrm{v}}$ and $\Delta\varepsilon_{\mathrm{p}}^{\mathrm{v}}$.

In contrast, if both yield conditions are violated, we must solve a non-linear system of four equations, namely eqns. (5.8a and 5.9a) plus the following two equation (deduced from eqns. (5.4a) and (5.4b), and from the strain decomposition)

$$\exp\left(\frac{(\varepsilon_{\mathrm{e}}^{\mathrm{i}})_{\mathrm{n}}+\Delta\varepsilon_{\mathrm{e}}^{\mathrm{i}}-\varepsilon_0}{\alpha_{\mathrm{e}}\,\kappa}\right)=\exp\left(\frac{(\varepsilon_{\mathrm{p}}^{\mathrm{i}})_{\mathrm{n}}+\Delta\varepsilon_{\mathrm{p}}^{\mathrm{i}}-\varepsilon_0}{\alpha_{\mathrm{p}}(\lambda-\kappa)}\right), \tag{5.10a}$$

$$\Delta\varepsilon=\Delta\varepsilon_{\mathrm{e}}^{\mathrm{i}}+\Delta\varepsilon_{\mathrm{e}}^{\mathrm{v}}+\Delta\varepsilon_{\mathrm{p}}^{\mathrm{i}}+\Delta\varepsilon_{\mathrm{p}}^{\mathrm{v}}, \tag{5.10b}$$

where $(\varepsilon_{\mathrm{p}}^{\mathrm{i}})_n$ is the instantaneous plastic strain evaluated at the previous time step and four unknowns are involved, namely $\Delta\varepsilon_{\mathrm{e}}^{\mathrm{i}}$, $\Delta\varepsilon_{\mathrm{e}}^{\mathrm{v}}$, $\Delta\varepsilon_{\mathrm{p}}^{\mathrm{i}}$ and $\Delta\varepsilon_{\mathrm{p}}^{\mathrm{v}}$. In all cases the non-linear problems were solved with a conventional Newton-Rapson scheme.

The integration algorithm is summarized in Box 1, in which it is possible to recognize the elastic predictor (step 1) and the three cases of: viscoelastic increment (step 3.i), plastic increment that violates only the viscous yield condition (step 3.ii), and plastic increment that violates both the yield conditions (step 3.iii).

The numerical algorithms were implemented in the Fortran User Subroutine UMAT of the finite element, commercial code ABAQUS Standard (Hibbitt et al. 2009).

5.4 Typical model's responses

In this section, some well-known and widely-accepted experimental responses taken from the literature will be simulated, in order to highlight the typical capabilities of the proposed constitutive approach. The constitutive parameters characteristics of an inorganic clay have been selected. The simulations concern a 20 mm thick, oedometer sample.

Box 1: Fully implicit algorithm for numerical integration of the uniaxial model

0. Strain decomposition of the discretized problem:

$$\Delta\varepsilon^{\mathrm{i}}_{\mathrm{e,n+1}} + \Delta\varepsilon^{\mathrm{v}}_{\mathrm{e,n+1}} + \Delta\varepsilon^{\mathrm{i}}_{\mathrm{p,n+1}} + \Delta\varepsilon^{\mathrm{v}}_{\mathrm{p,n+1}} = \Delta\varepsilon_{\mathrm{n+1}}$$

$$\dot{\varepsilon}^{\mathrm{v}}_{\mathrm{e,n+1}} = \frac{\Delta\varepsilon^{\mathrm{v}}_{\mathrm{e,n+1}}}{\Delta t_{\mathrm{n+1}}},\ \dot{\varepsilon}^{\mathrm{v}}_{\mathrm{p,n+1}} = \frac{\Delta\varepsilon^{\mathrm{v}}_{\mathrm{p,n+1}}}{\Delta t_{\mathrm{n+1}}}$$

1. Initialize:

$$\Delta\varepsilon^{\mathrm{i,trial}}_{\mathrm{e,n+1}} = \Delta\varepsilon_{\mathrm{n+1}},\ \Delta\varepsilon^{\mathrm{v,trial}}_{\mathrm{e,n+1}} = 0,\ \Delta\varepsilon^{\mathrm{i}}_{\mathrm{p,n+1}} = 0,\ \Delta\varepsilon^{\mathrm{v}}_{\mathrm{p,n+1}} = 0$$

2. Elastic predictor: solve the viscoelastic problem and evaluate the *trial viscoelastic state*

from $\quad \left\{\sigma^{\mathrm{i}}_{e}(\Delta\varepsilon^{\mathrm{i,trial}}_{\mathrm{e,n+1}}) - \sigma^{\mathrm{v}}_{e}(\Delta\varepsilon^{\mathrm{v,trial}}_{\mathrm{e,n+1}})\right\} = \{0\}$ (Box 1.1)

obtain $\quad \varepsilon^{\mathrm{i,trial}}_{\mathrm{e,n+1}}\ ,\ \ \varepsilon^{\mathrm{v,trial}}_{\mathrm{e,n+1}}$

3. Check the plastic admissibility (with $\sigma^{\mathrm{trial}}_{\mathrm{n+1}} = \sigma^{\mathrm{i}}_{e}(\varepsilon^{i,\mathrm{trial}}_{\mathrm{e,n+1}})$)

i IF $\quad \sigma^{\mathrm{trial}}_{\mathrm{n+1}} \leq \sigma^{\mathrm{i}}_{\mathrm{pc}} \quad$ AND $\quad \sigma^{\mathrm{trial}}_{\mathrm{n+1}} \leq \sigma^{\mathrm{v}}_{\mathrm{pc}}$

THEN $\quad \Delta\varepsilon^{\mathrm{i}}_{\mathrm{e,n+1}} = \Delta\varepsilon^{\mathrm{i,trial}}_{\mathrm{e,n+1}}\ ,\ \Delta\varepsilon^{\mathrm{v}}_{\mathrm{e,n+1}} = \Delta\varepsilon^{\mathrm{v,trial}}_{\mathrm{e,n+1}}\ ,\ \sigma_{\mathrm{n+1}} = \sigma^{\mathrm{trial}}_{\mathrm{n+1}}$

ii IF $\quad \sigma^{\mathrm{trial}}_{\mathrm{n+1}} \leq \sigma^{\mathrm{i}}_{\mathrm{pc}} \quad$ AND $\quad \sigma^{\mathrm{trial}}_{\mathrm{n+1}} > \sigma^{\mathrm{v}}_{\mathrm{pc}}$

THEN $\quad$ Return mapping:

from $\quad \begin{Bmatrix} \sigma^{\mathrm{i}}_{e}(\Delta\varepsilon^{\mathrm{i}}_{\mathrm{e,n+1}}) - \sigma^{\mathrm{v}}_{e}(\Delta\varepsilon^{\mathrm{v}}_{\mathrm{e,n+1}}) \\ \sigma^{\mathrm{i}}_{e}(\Delta\varepsilon^{\mathrm{i}}_{\mathrm{e,n+1}}) - \sigma^{\mathrm{v}}_{\mathrm{p}}(\Delta\varepsilon^{\mathrm{v}}_{\mathrm{p,n+1}}) \end{Bmatrix} = \begin{Bmatrix} 0 \\ 0 \end{Bmatrix}$ (Box 1.2)

obtain $\quad \Delta\varepsilon^{\mathrm{i}}_{\mathrm{e,n+1}}\ ,\ \ \Delta\varepsilon^{\mathrm{v}}_{\mathrm{e,n+1}}\ ,\ \ \Delta\varepsilon^{\mathrm{v}}_{\mathrm{p,n+1}}\ ,\ \ \sigma_{\mathrm{n+1}}$

iii IF $\quad \sigma^{\mathrm{trial}}_{\mathrm{n+1}} > \sigma^{\mathrm{i}}_{\mathrm{pc}} \quad$ AND $\quad \sigma^{\mathrm{trial}}_{\mathrm{n+1}} > \sigma^{\mathrm{v}}_{\mathrm{pc}}$

THEN $\quad$ Return mapping:

from $\quad \begin{Bmatrix} \sigma^{\mathrm{i}}_{e}(\Delta\varepsilon^{\mathrm{i}}_{\mathrm{e,n+1}}) - \sigma^{\mathrm{v}}_{e}(\Delta\varepsilon^{\mathrm{v}}_{\mathrm{e,n+1}}) \\ \sigma^{\mathrm{i}}_{e}(\Delta\varepsilon^{\mathrm{i}}_{\mathrm{e,n+1}}) - \sigma^{\mathrm{i}}_{\mathrm{p}}(\Delta\varepsilon^{\mathrm{i}}_{\mathrm{p,n+1}}) \\ \sigma^{\mathrm{i}}_{e}(\Delta\varepsilon^{\mathrm{i}}_{\mathrm{e,n+1}}) - \sigma^{\mathrm{v}}_{\mathrm{p}}(\Delta\varepsilon^{\mathrm{v}}_{\mathrm{p,n+1}}) \end{Bmatrix} = \begin{Bmatrix} 0 \\ 0 \\ 0 \end{Bmatrix}$ (Box 1.3)

obtain $\quad \Delta\varepsilon^{\mathrm{i}}_{\mathrm{e,n+1}}\ ,\ \ \Delta\varepsilon^{\mathrm{v}}_{\mathrm{e,n+1}}\ ,\ \ \Delta\varepsilon^{\mathrm{i}}_{\mathrm{p,n+1}}\ ,\ \ \Delta\varepsilon^{\mathrm{v}}_{\mathrm{p,n+1}}\ ,\ \ \sigma_{\mathrm{n+1}}$

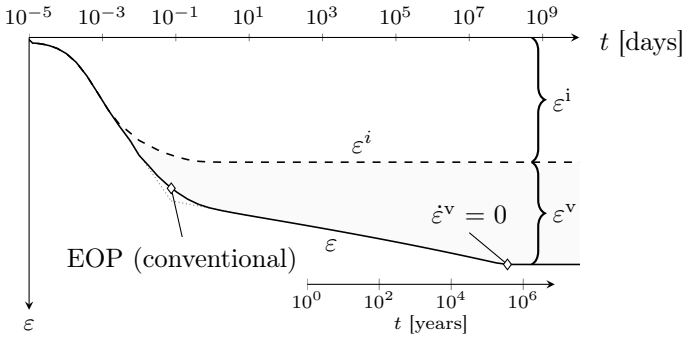

Figure 5.5: Simulation of the strain-time response for a constant stress test on a thick specimen of inorganic clay

The most widely-used experimental set up for investigating the compression behaviour of fine-grained soils, is the Incremental Loading (IL) oedometer test. In this test, large load increments are typically applied and the vertical stress is kept constant for at least 24 h. In each load increment, delayed clay response is typically linear in terms of vertical strain versus the logarithm of time. Thus the first validation of the proposed model consists in the simulation of the well known IL response induced by a sudden doubling of the applied load (Fig. 5.1).

Figure 5.5 shows the strain vs $\log(t)$ simulations of a thick specimen. The model response is characterized by the primary and the secondary consolidation; the first follows the well-known strain development, and the latter is represented by a nearly linear plot in the $\log(t)$. The dashed lines highlight the two different contributions of the strain increment (i.e. the short-term, instantaneous, and the long term, viscous strain increment) defined in eq. 5.1. The time evolution of the instantaneous strain is affected by pore pressure dissipation, whereas the long-term, viscous deformation is ruled by the viscosity function. The duration of the secondary consolidation depends on the proper calibration of the constitutive parameter $\dot{\varepsilon}_{\min}$: in Fig. 5.5 the $\varepsilon^{\mathrm{v}} - \log(t)$ plot is linear up to nearly one million of years (with $\dot{\varepsilon}_{\min} = 10^{-10}$ min^{-1}).

The results shown in Fig. 5.5 concern the elasto-plastic response. However this behaviour is typical also of the elastic phase, because the rheological structure of the model and the viscosity functions used in the elastic and elasto-plastic phases mostly coincide with each other.

In order to validate the proposed model in terms of the isotach concept

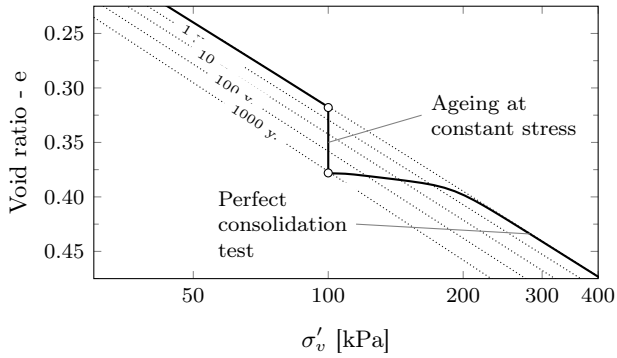

Figure 5.6: Model simulation of quasi-preconsolidation effect due to ageing on NC clay (Bjerrum 1967).

(Suklje 1957) and quasi-preconsolidation effect (Bjerrum 1967) in normally consolidated clays, the following simulation has been performed: an oedometer sample of NC clay was loaded up to 100 kPa under a constant strain rate equal to $\dot{\varepsilon}^{\mathrm{v}} = 10^{-6}$ min^{-1}. Then the loading process was interrupted and the vertical load was kept constant for a very long time, in order to simulate a creep phase (aging). Finally the loading phase was resumed under the same constant strain rate of the initial phase (i.e. $\dot{\varepsilon}^{\mathrm{v}} = 10^{-6}$ min^{-1}). In Fig. 5.6 the results of the simulation are shown with a continuous line, whereas different isotaches (corresponding to the NC compression lines obtained at different strain rates) are represented with dashed lines. It can be observed that model simulations are consistent with the concepts of isotach and the development of a quasi-preconsolidation pressure due to ageing at constant stress, proposed by Bjerrum (1967).

It is worth noting that, at the instant of resuming the loading process, the sudden jump of strain rate induces an abrupt increase of the *dynamic yield stress* $\sigma_{\mathrm{p}}^{\mathrm{v}}\left[1+\psi_{\mathrm{p}}(\dot{\varepsilon}_{\mathrm{p}}^{\mathrm{v}})\right]$, whereas $\sigma_{\mathrm{p}}^{\mathrm{v}}$ remains unchanged (because there was no accumulation of plastic strains yet), this implies that two kinds of strain increments are mostly involved in the initial phase, namely: $\varepsilon_{\mathrm{e}}^{\mathrm{v}}$ and $\varepsilon_{\mathrm{p}}^{\mathrm{v}}$. As a result, the initial slope after loading resume is given by the instantaneous elastic and plastic compressibilities.

Constant Rate of Strain oedometer tests (CRS) are generally considered as useful, different means for evaluating the delayed response of soils. The typical response of the proposed constitutive model was thus validated on the CRS tests

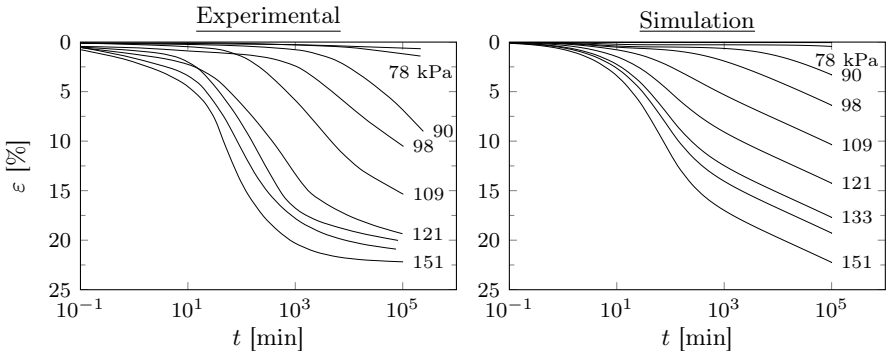

Figure 5.7: Simulation of creep oedometer tests on Batiscan clay (Leroueil, Kabbaj, et al. 1985).

performed with different strain rates on Batiscan clay by Leroueil, Kabbaj, et al. (1985).

The constitutive parameters of the model were calibrated on the Incremental loading creep tests performed on Batiscan clay by Leroueil, Kabbaj, et al. (1985). The excellent comparison between simulations and measurements obtained on the creep tests is shown in Fig. 5.7. The constitutive parameters obtained from creep tests are shown in Table (5.1) and were used also for the simulation of the CRS tests by Leroueil, Kabbaj, et al. (1985). These tests involved a very wide range of strain rates. The consistency between model simulations and experimental results is shown in Fig. 5.8. Finally Fig. 5.9 shows the comparison between simulations and measurements performed on a special CRS performed by Leroueil, Kabbaj, et al. (1985) obtained by changing the strain rate during the loading test.

The results shown in Figs. 5.7 - 5.9 prove the general agreement of model simulations with the experimental results. In particular, the constitutive model accurately simulates the differences of delayed response induced by large stress increments (for which the strain-log t curves have the typical 'S' shape) with respect to those induced by small stress increments (presenting stress-strain curves with a continuous increment of slope) as shown in Fig. 5.7.

Observing model simulations of Figs. 5.6 - 5.9 it can be concluded that the constitutive model simulates accurately both the creep tests (with a constant applied stress) and the constant strain rate tests. The main inconsistency concerns simulated stress-strain curves that have a constant slope (in a strain

Param.	Batiscan Clay
κ	0.004
α_{e}	0.05
Γ_{e}	0.04
λ	0.38
α_{p}	0.05
Γ_{p}	0.04
$\dot{\varepsilon}_{\mathrm{min}}$ [1/min]	10^{-10}
$\sigma^{\mathrm{i}}_{\mathrm{pc}}$ [kPa]	65
$\sigma^{\mathrm{v}}_{\mathrm{pc}}$ [kPa]	65

Table 5.1: Calibrated constitutive parameters for Batiscan clay (Leroueil, Kabbaj, et al. 1985).

versus logarithmic of stress plot, Figs. 5.8 and 5.9) in contrast with the measured curved lines which are most probably related to destructuration phenomena in this structured, natural clay.

5.5 Parametric analysis

The proposed model for 1D compression is based on 6 constitutive parameters, namely: 2 parameters κ and λ for describing the slopes of elastic and elasto-plastic compression curves in a $\varepsilon_v - \log \sigma_v$ plot, 2 partition coefficients α_{e} and α_{p} and 2 parameters for describing the viscous strain rates.

In this section, the effects induced by each constitutive parameter will be discussed, through a parametric analysis in which each single parameter is varied while keeping the values of the others constant. Reference is made to a 20 mm thick, axial symmetric, sample, which has been discretized with a column of 10 finite elements having linear pore pressure (4 nodes) and quadratic solid displacements (8 nodes). The hydro-mechanical coupled analysis was performed with the commercial code ABAQUS (Hibbitt et al. 2009), in which the proposed model was implemented. In this way the effects induced by each constitutive parameter are analysed with regards to the simulation of an edometric test. In particular the soil response induced by an instantaneous doubling of the imposed vertical stress, with null transversal displacements, is considered.

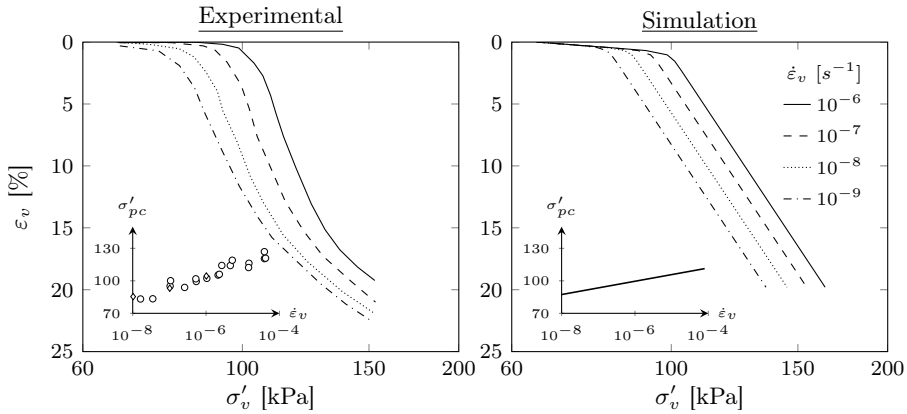

Figure 5.8: Simulation of Constant Rate of Strain tests on Batiscan clay (Leroueil, Kabbaj, et al. 1985).

The parametric analyses have been conducted assuming that the applied stresses are below the preconsolidation pressure, thus soil remains in the elastic regime. As a result the analyses below will concern the elastic parameters Γ_e, α_e and κ. The observations are however valid also for the viscoplastic regime (namely for the parameters Γ_p, α_p and λ), because the model structure and the viscosity functions are practically the same for the viscoelastic and viscoplastic regimes. The assumed permeability is equal $K = 8.3 \times 10^{-7}$ m/s. Null initial strain rate is assumed as initial condition, $\dot{\varepsilon} = 0$.

The parameter Γ_e represents the viscosity of the dashpot in the rheological model shown in Fig. 5.2. The effects induced by Γ_e on the material response are shown in the strain versus logarithm of time response of Fig. 5.10a: for low values of Γ_e the viscous strain appears very soon (even during the primary consolidation) and the slope of the secondary phase is small. An increase of Γ_e induces a delay in the development of viscous deformation (with an initial phase with a negligible creep strain) and a large final slope of the secondary compression. It is worth adding that for high values of Γ_e, the descending parts of the creep curves are not exactly linear and assume a slight downward concavity. Such concavity could be made vanishingly small by assuming that the viscosity function consists of a second order polynomial in the logarithmic of strain rate (as discussed in the Appendix). The different curves of Fig. 5.10a converge to the same point (where the viscous strain rate becomes null), since

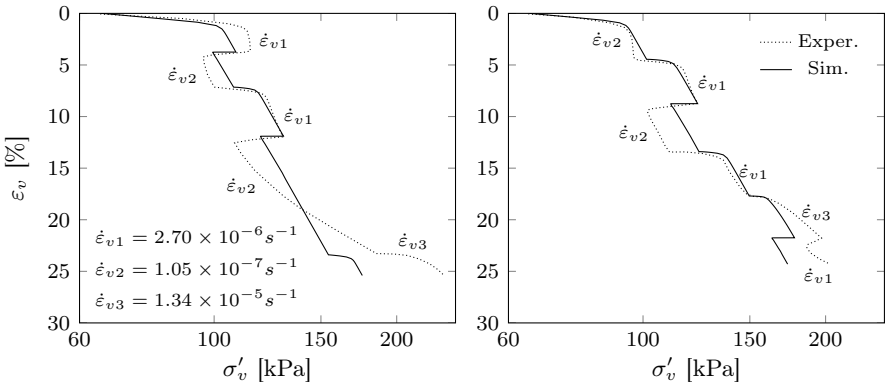

Figure 5.9: Simulation of CRS tests at variable strain rates, on Batiscan clay (Leroueil, Kabbaj, et al. 1985).

the same value of $\dot{\varepsilon}_{\min}$ has been assumed.

The effects induced by the parameter $\dot{\varepsilon}_{\min}$ are shown in Fig. 5.10b: $\dot{\varepsilon}_{\min}$ affects the time duration of the viscous creep, which is the largest, the smaller $\dot{\varepsilon}_{\min}$. As a result the final parts of all creep curves result to be horizontally translated, still remaining parallel to each other.

Figure 5.10c shows the effects induced by the parameter α_{e}, ruling the partition between instantaneous and viscous deformations. This means that, if we consider the entire deformation phenomenon (up to $\dot{\varepsilon} = 0$), α_{e} is the ratio between the instantaneous strain, and the total strain at the end of the deformation process. The effect induced by α_{e} on the global delayed response is similar to the effect of Γ_{e}.

Finally the parameter κ affects the total amount of the elastic strain at the end of the creep deformation process and has the same role it has in the classical Cam-Clay theory.

5.6 Hints for model calibration

Here follows some hints for the calibration of the 6 constitutive parameters of the model. The calibration should begin with the classic compressibility parameters κ and λ which can be easily obtained from the results of oedometer tests. In fact compression curves at different strain rates keep unchanged their slopes in

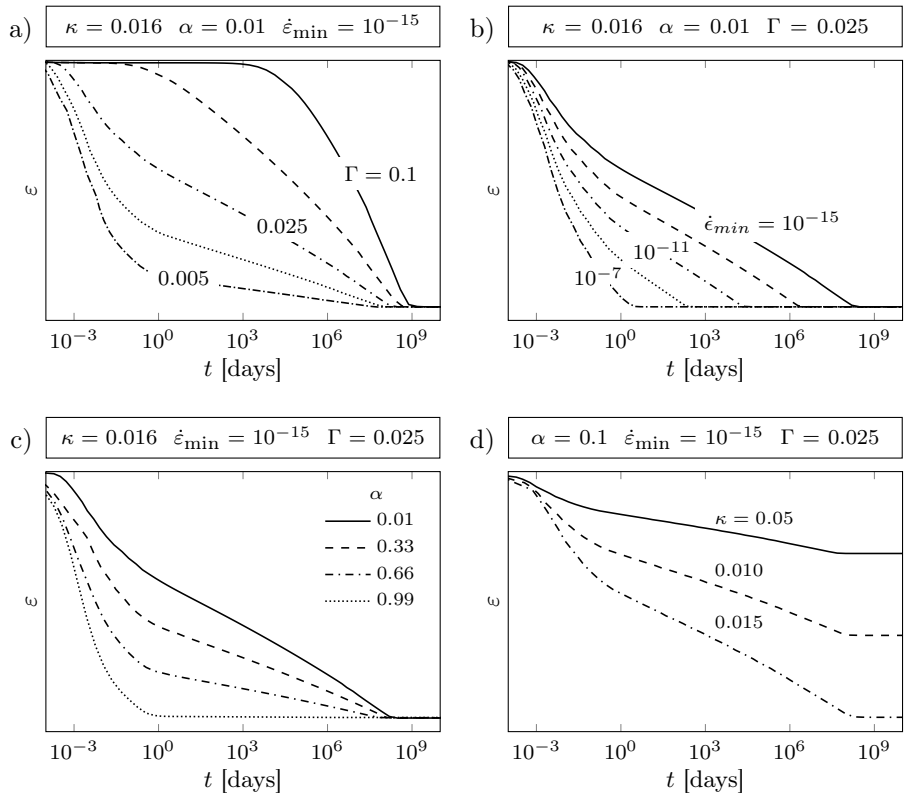

Figure 5.10: Parametric analyses of constitutive model:
a) effect of Γ; b) effect of $\dot{\varepsilon}_{\min}$; c) effect of α;
d) effect of κ (or λ).

a $\varepsilon - \log \sigma$ plot. Moreover a change of the viscous parameters (i.e. Γ_e, α_e, Γ_p, α_p and $\dot{\varepsilon}_{\min}$) doesn't affect the slope of the compression curve κ and λ (fig. 5.11). Thus κ and λ can be considered uncoupled from the other parameters.

The constitutive parameter $\dot{\varepsilon}_{\min}$ defines the minimum viscous strain rate of the model affecting the mechanical behaviour. When the strain rate, either in the elastic or in the elasto-plastic regime, becomes equal to $\dot{\varepsilon}_{\min}$ the value of the viscosity function becomes negligible (eq. (5.6)), thus the creep phenomenon comes to an end. In the range of values of interest, the effects of $\dot{\varepsilon}_{\min}$ on the

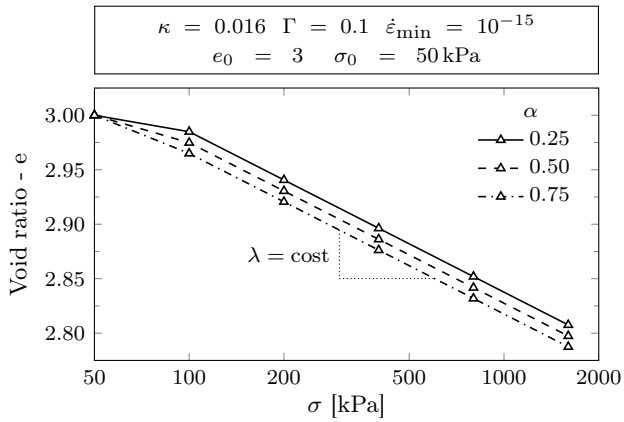

Figure 5.11: Parametric analyses of constitutive model: effect of α on the slope of oedometer compression line.

slope of creep deformations in a logarithmic of time plot (fig. 5.10b) are small. For typical fine grained soils, $\dot{\varepsilon}_{\min}$ can be chosen in the range $10^{-10} \div 10^{-15}$, implying a duration o the creep phenomenon ranging between 3 thousand and 1 million years (fig. 5.5). The possibility of modelling such a slow creep processes could be exploited in the analyses of viscous phenomena involving geological time scales.

The definition of the other parameters (α_e, α_p, Γ_e and Γ_p) which are particularly devoted to describe the viscous phenomena is more complex, because the effects induced by these parameters are coupled to each other, as can be grasped from Figs. 5.10a and 5.10c. Although the effects induced by the two coupled of parameters ($\alpha_e - \Gamma_e$ or $\alpha_p - \Gamma_p$) are similar (namely a change of slope of the creep response in the logarithmic of time plot), the physical mechanisms that are simulated are very different, as mentioned before.

The choice of α_e and α_p is conveniently performed from the results of conventional oedometer tests, by evaluating the ratio between the primary deformation and the total deformation in each load increment. To this aim, reference should be made to Fig. 5.1, where the intersection of the dotted line with the vertical axis permits to evaluate an indicative value of α_e and α_p.

Once the values of α_e and α_p have been calibrated, the values of Γ_e and Γ_p can be selected from the slopes of the creep curves in the logarithmic of time plots (namely the well-known coefficient of secondary consolidation $C_{\alpha\varepsilon}$). Since

the simulated slope $C_{\alpha\varepsilon}$ is the result of both α_e and Γ_e in the elastic regime (or α_p and Γ_p for the plastic regime), it is then possible to plot the contours of the simulated ratio C_α/C_c (defined according to Mesri and Godlewski (1977)) in a plot $\alpha_e \div \Gamma_e$ (or $\alpha_p \div \Gamma_p$ for the plastic regime), as shown in Fig. 5.12. These values were obtained numerically, from the simulation of four standard load increments in purely elastic (Fig. 5.12a) or elasto-plastic (Fig. 5.12b) regime, with null initial strain rate $\dot{\varepsilon}^v = 0$. The contour plots shown in Fig. 5.12 are then useful for a first, tentative evaluation of the constitutive parameters Γ_e and Γ_p.

For the sake of completeness, the values of the constitutive parameters that have been calibrated on 4 inorganic and organic clays having very different index properties (see Table 3.1 of Section 3.2) are shown in Fig. 5.12. If we consider that the simulated ratio C_α/C_c depends on the entire previous stress-strain history, it can be easily understood that the C_α/C_c values shown in Fig. 5.12 are only approximate and must be used as a first attempt. There is however a fairly good agreement between accurately calibrated C_α/C_c ratios and the approximated values expected from Fig. 5.12. The main exception concerns the elasto-plastic regime of the two tested peats for which C_α/C_c ratio is strongly affected by the initial preconsolidation pressure.

The observed typical range of variation of Γ is $0.001 \div 0.5$: the smallest values are for inorganic clays and elastic regime.

5.7 Hints for the selection of initial conditions

In the proposed viscous model, a very important role is played by the initial conditions, in particular by the initial value of the preconsolidation pressure of the viscoplastic mechanism (σ^v_{pc}). This initial state variable, through eqn. (5.5b), is related to the initial viscoplastic strain (ε^v_p) and coincides with the conventional preconsolidation pressure, if the soil element had the opportunity, during its geologic history, to complete the secondary compression process under the applied preconsolidation stress (thus the viscous plastic strain rate $\dot{\varepsilon}^p$ could become negligible, see 5.5). The same problem should be afforded also for the initial viscoelastic strain and its rate (ε^e and $\dot{\varepsilon}^e$).

We can generally assume that, for soils under field conditions that have been remained unchanged in the previous 5-10 thousands years, it can be reasonably assumed that viscoelastic and viscoplastic strain rates are negligible ($\dot{\varepsilon}^e = 0$ and $\dot{\varepsilon}^p = 0$), thus $\sigma_{pc,v} = \sigma_{pc,i}$. Otherwise such initial condition must be found in the previous geologic stress-strain history of the soil, and the most recent history

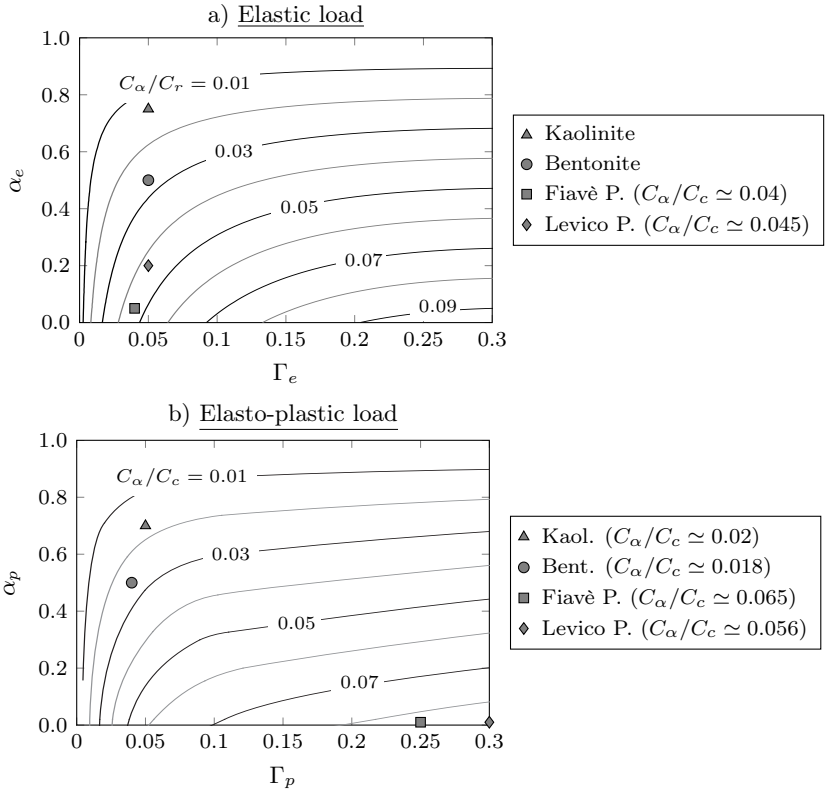

Figure 5.12: Calibration chart.

must therefore be simulated for defining the appropriate initial conditions for the problem under examination.

In contrast, for the short-term, instantaneous plastic response, there is no particular problem in the definition of the initial conditions, in fact the choice of the initial instantaneous preconsolidation pressure ($\sigma_{\mathrm{pc,i}}$) is performed with the same approach used in the classical Cam-Clay model.

5.8 Comparison between model simulations and experimental results

This model has been validated on several oedometer tests performed on three different peats (named Levico, Fiavè and Egna) with different amounts of organic content and index properties (see Section 3.2 for the complete description), and on two inorganic clays (industrial Kaolinite and Bentonite) with very different mechanical and hydraulic properties. The laboratory analyses involved several types of oedometer tests (Incremental Loading, Constant Rate of Strain, Constant Rate of Stress, Rowe Cell MSL) involving standard and non-standard stress increment, and loading histories, in order to highlight different aspects of soils' delayed response.

We are aware that a rigorous analysis of an oedometer test should be performed with a multiaxial constitutive model, capable of taking account of delayed response of vertical strains and horizontal stresses, however many practical problems do not require such a complex approach because the information provided by a simple 1D model are sufficient. Moreover, a simple 1D approach provides useful information for the formulation of a fully multiaxial constitutive framework, taking viscous deformation into account.

Param.	Peat (Fiavè)	Peat (Levico)	Kaolinite	Bentonite
κ	0.05	0.015	0.016	0.04
α_e	0.01	0.05	0.75	0.5
Γ_e	0.04	0.06	0.05	0.05
λ	0.28	0.10	0.065	0.133
α_p	0.01	0.01	0.75	0.5
Γ_p	0.45	0.40	0.05	0.05
$\dot{\varepsilon}_{min}$ [1/min]	10^{-10}	10^{-10}	10^{-10}	10^{-10}
$\sigma_{pc,1}$ [kPa]	3	6	2	5
$\sigma_{pc,2}$ [kPa]	3	2.5	2	5

Table 5.2: Calibrated constitutive parameters for the soils subjected to laboratory tests.

The calibration of the constitutive parameters have been obtained following the hints given in Section 5.6. Table 5.2 reports the calibrated values providing

the best fit for the four different soils taken into account.

It is worth observing that for peaty soils the behaviour is dominated by the viscous strain, as a result the partition coefficients α_e and α_p are very small with resepct to inorganic soils, whereas the viscous coefficient Γ_p is much larger than that one of inorganic soils.

5.8.1 Simulation of IL Oedometer Tests

The evolution of settlements measured in oedometer tests performed on inorganic clays, with the application of large load increments (i.e. *load increment ratio* $\Delta\sigma/\sigma$ equal to one), follows the classic 'S' shaped curve in a strain versus logarithmic of time plot. From such a plot the end of primary consolidation (EOP) can be easily estimated with Casagrande graphical method. In contrast the evolution of settlements of peaty soils is less curved and, since the 'S' shape is missing, it is generally difficult to evaluate the EOP.

Figure 5.13 shows the comparison between the simulations and the experimental results obtained in the two inorganic clays and in one of the peats. The left column shows the oedometer compression curves, whereas the other plots show three typical comparisons in a $\varepsilon - \log t$ plot.

It is worth emphasising that the calibration of the simulation have been conducted taking into account the full loading history, trying to obtain the best fit in all loading steps, thus certain compromises were required. However the agreement between the simulations and experimental measurements is excellent in terms of both compression curves time evolution of deformations.

It is well known (Mesri, D. Lo, et al. (1994) and Mesri, Stark, Ajlouni, et al. (1997)) that soils' delayed behaviour is deeply affected by the load increment ratio. In particular, the application of small load increments, typically induces negligible, initial primary and secondary settlements, subsequently the slope of the $\varepsilon - \log t$ curves in the secondary phase markedly increases (Section 3.4.2). The delayed response induced by small load increments is of interest in many engineering applications (e.g. re-levelling of a road embankments after settlement). This is why it is necessary to validate the reliability of the constitutive model under this kind of loading conditions.

To this aim it is convenient to introduce the effective surcharge ratio $R'_s = \sigma'_{vs}/\sigma'_{vf} - 1$ (Mesri and Feng 1991), where σ'_{vf} and σ'_{vi} represent the effective vertical pressure at the end and at the beginning of the loading increment.

Figure 5.14 shows the comparison between simulations and measurements obtained from small loading and unloading steps on Fiavè Peat (see Section 3.4.2 and 3.4.3). The results are plotted in a $\varepsilon - \log t$ plot. The constitutive model

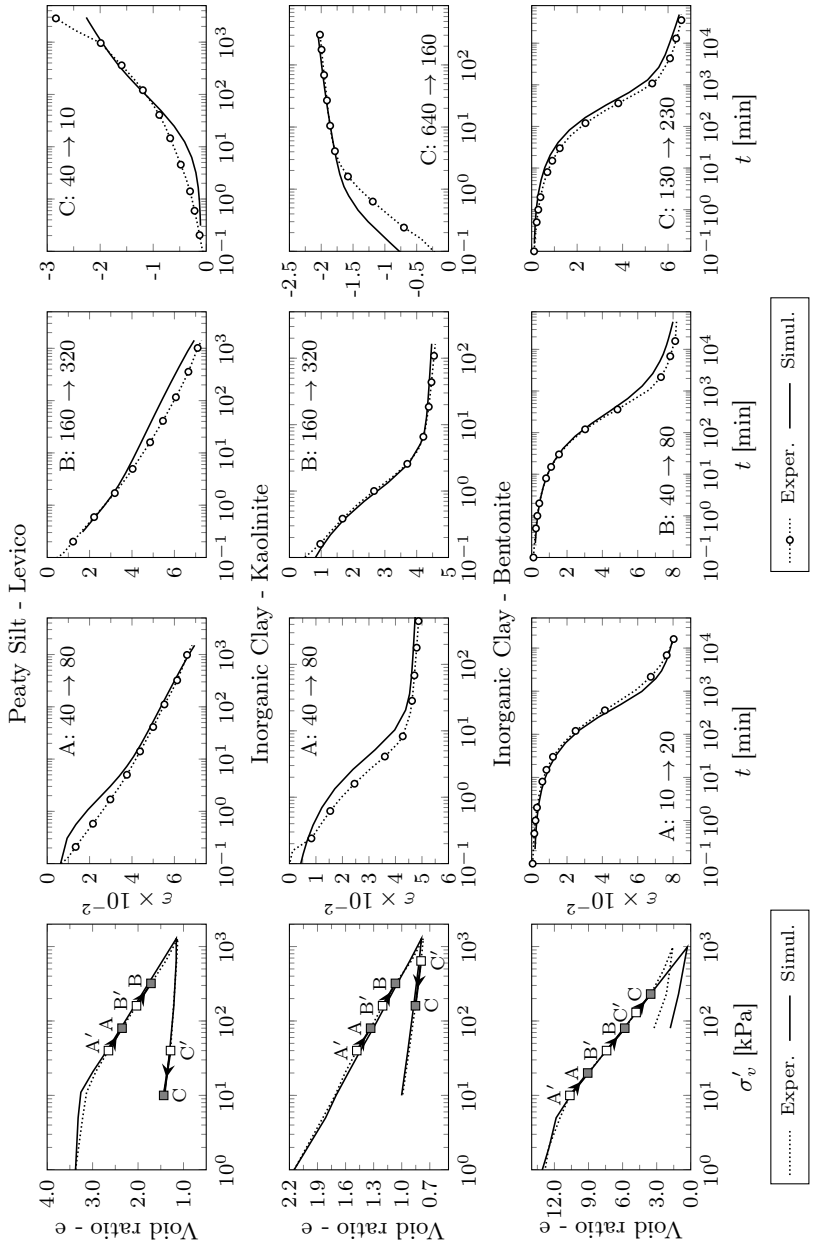

Figure 5.13: Simulation of peaty soils and inorganic clays behaviour.

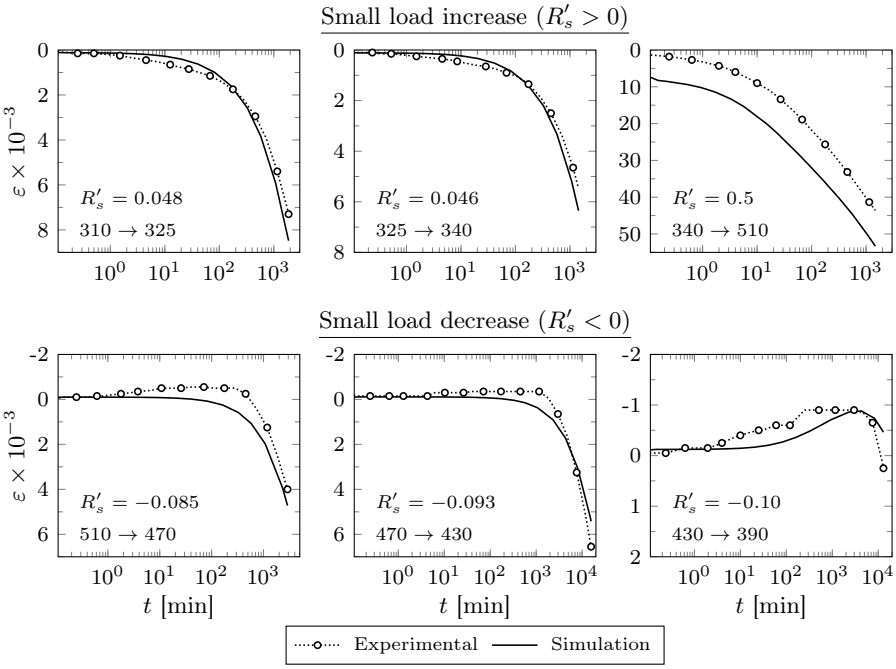

Figure 5.14: Small loading and unloading on Fiavè Peat (Section 3.4.2 and 3.4.3): experiment vs. simulation.

correctly simulates the creep curves induced by small load increments ($R'_s > 0$), involving the mentioned negligible primary compression and the continuously increase of the slope in the secondary compression.

The delayed response peaty upon a small unloading ($R'_s < 0$) is fairly unexpected although it was firstly highlighted by (Samson & La Rochelle, 1972). This kind of response is of interest for pre-loading embankments and is typical also of inorganic clays (Mesri and Feng (1991), Mesri and Ajlouni (2007)): after an initial phase of delayed swelling, a second phase of of delayed compression occurs. The excellent comparisons between simulations and measurements obtained on Fiavè Peat is shown in Fig. 5.14.

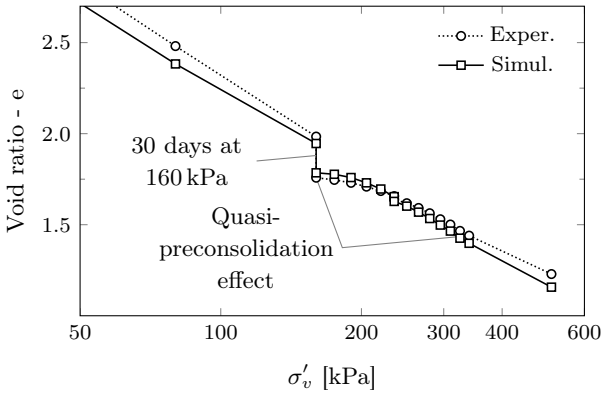

Figure 5.15: Simulation of quasi-preconsolidation effect for Fiavè peat (Specimen A).

5.8.2 Quasi preconsolidation effect

As mentioned in Section 5.4, the quasi-preconsolidation effect induced by ageing, is a well-known aspect of the rheological behaviour of fine-grained soils. This effect was firstly mentioned by Leonards and Ramiah (1960), subsequently explained by Bjerrum (1967), and later confirmed by many others (e.g. Mesri and Castro 1987).

In Section 3.4.1 has been analysed the quasi-preconsolidation induced by ageing on Fiavè peat by using IL oedometer tests. The sample was kept at the constant vertical stress of 160 kPa for 30 days, then the loading process was resumed, through the application of small load increments (about 10% of the applied load), each one lasting 24 hours. As shown in Fig. 5.15, the resulting quasi-preconsolidation pressure induced by 30 days aging was about 250 kPa. Model simulations are compared with experimental results in fig. 5.15: the agreement between the two is excellent.

5.8.3 Constant Rate of Strain (CRS) Oedometer Tests

CRS oedometer tests (Gorman et al. 1978, Leroueil, Kabbaj, et al. 1985) are sometimes used to evaluate the compression behaviour of soils with shorter experimental tests. The results of CRS tests performed at different strain rates, are parallel curves spaced in function of $\log \dot{\varepsilon}$. This kind of behaviour is consis-

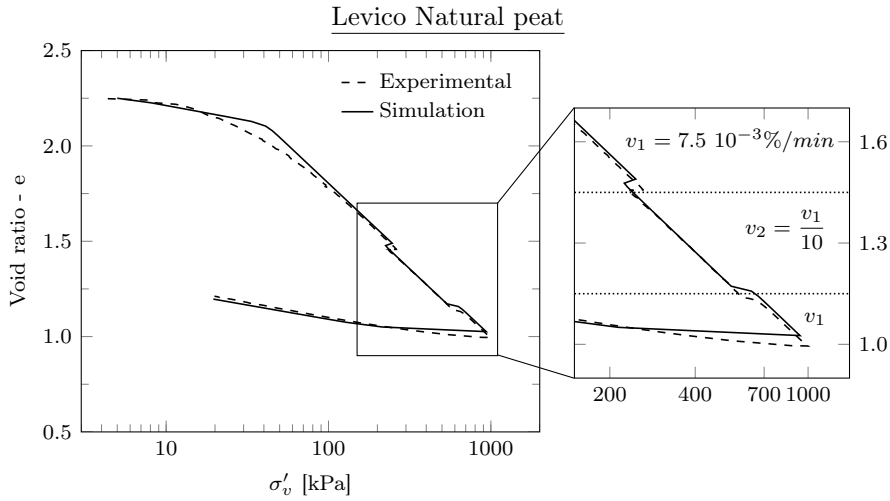

Figure 5.16: Simulation of Constant rate of strain test (CRS) on Levico natural peat.

tent with the isotach concepts that were proposed for the first time by Suklje (1957). The simulation of CRS test results is thus a precious means of validation of constitutive model reliability.

The CRS tests performed on Levico peat shown in Section 3.4.4 were simulated using the calibration obtained from the IL tests described in Subsection 5.8.1. The sample was initially loaded at the strain rate of 7.5×10^{-3} %/min; then, at a vertical effective stress of 260 kPa, the strain rate was reduced to 7.5×10^{-4} %/min and kept constant up to a vertical stress of 580 kPa. The initial strain rate of 7.5×10^{-3} %/min was subsequently resumed until the end of the test. Figure 5.16 shows the comparison between simulations and experimental results. The model correctly predicts the effects induced by the abrupt change of applied strain rate.

5.8.4 Constant Rate of Stress (CRSS) Oedometer Tests

As compared to CRS oedometer tests that are fairly widely used, Constant Rate of Stress oedometer Test (CRSS) are rarely used because they require a

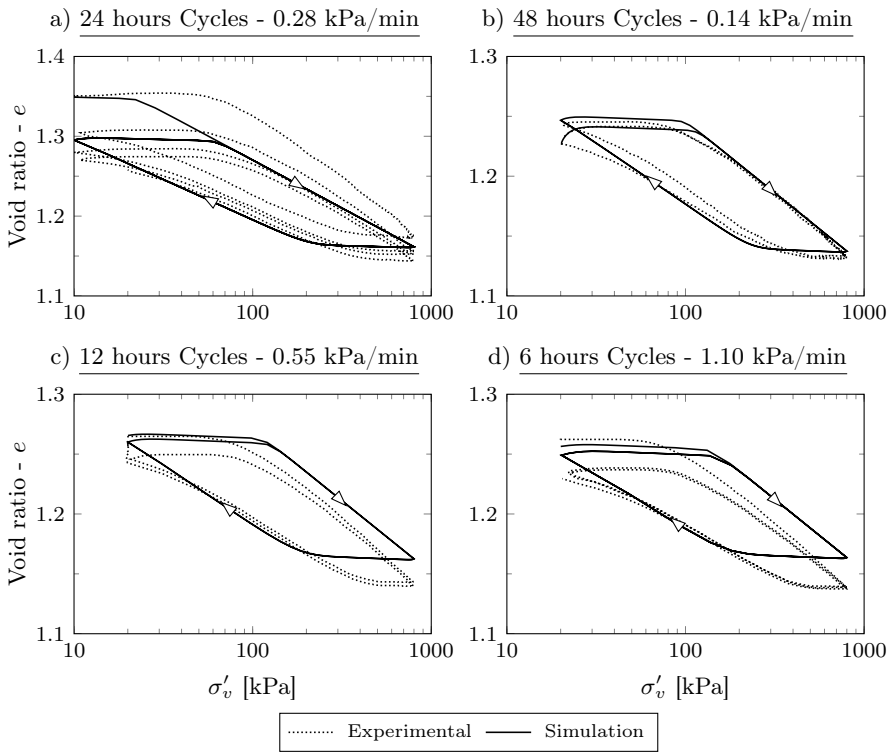

Figure 5.17: Simulation of CRSS Tests for Levico peat (Specimen A) (Section 3.4.5).

more complex experimental setup, necessarily involving a computer-controlled pneumatic piston. The advantage of this kind of tests however is that it permits to validate model response upon load reversals. In fact, the general soil response measured in CRSS tests is fairly similar to that one of CRS tests, except for the load reversals, as shown below.

It is worth adding that, despite its applicative importance in geotechnical engineering, soil delayed behaviour under unload-reload cycles has been rarely subjected to experimental investigations (Acosta-Martinez et al. 2005, Kawabe, Kongkitkul, et al. 2011, Kawabe and Tatsuoka 2013).

The unload-reload CRSS tests performed on Levico peat showed in Section

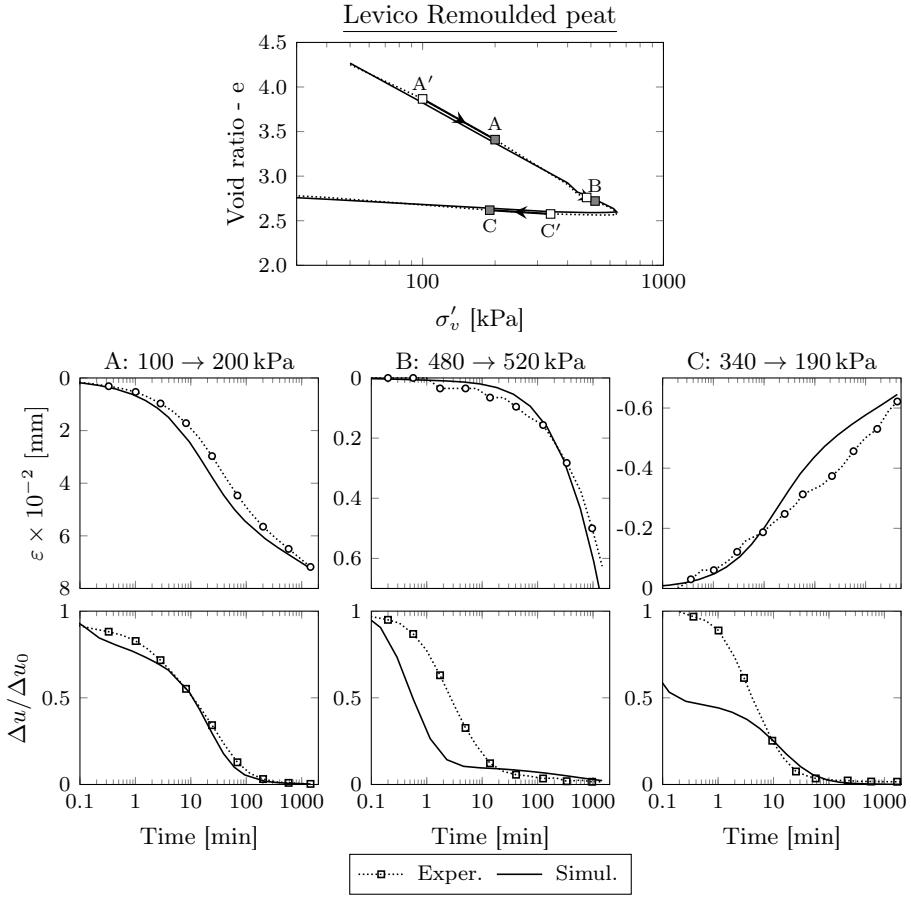

Figure 5.18: Simulation Rowe cell test on Levico remoulded peat (Section 3.4.6).

3.4.5 have been considered. A peat sample was first loaded and unloaded in a standard IL test, then it was subjected to several load-unload, CRSS cycles at different stress rates. The amplitude of load-unload cycles ranged between 10-20 kPa and 800 kPa. The applied constant stress rate ranged between 0.14 kPa/min (48-hour lasting, load cycle) and 1.10 kPa/min (6-hour lasting, load

cycle).

In figure 5.17, laboratory results are compared with model simulations. The agreement is very good, in terms of both amplitude of hysteresis loops and amount of deformation. Important to note is the excellent agreement between model simulations and measurements even in the first reloading phase (fig. 5.17a).

The measurements however have a slightly larger ratcheting response that is not accurately modelled by the proposed constitutive framework.

5.8.5 Rowe Cell Oedometer Tests

Finally, model simulations are compared with the pore pressure and vertical displacements measured on a small Rowe consolidation cell (Section 3.4.6). The experimental tests were performed on a remoulded specimen of Levico peat. The sample was first saturated by using an appropriate back pressure, then it was subjected to a conventional IL test, in which drainage was permitted only at the upper base of the specimen, whereas pore pressure was measured at the bottom base.

Figure 5.18 shows the evolution of the vertical strains and excess of pore pressures measured in three load increments. Model simulations are compared with the experimental measurements in Fig. (5.18). The calibrated values of the constitutive parameters are given in the Table 5.2 and obviously coincide with those used in the previous Subsections.

Model simulations are fairly consistent with the observed evolution of both vertical strain and pore pressure at bottom base, under both large and small load increments, under both an increase and a decrease of vertical load. The only exception is the pore pressure in the unloading step that, in the first phase, is rather different from the experimental measurements.

The hydro-mechanical coupled analyses were performed with the commercial FEM code ABAQUS (Hibbitt et al. 2009) on a 20 mm thick specimen, that was simulated with ten finite elements. The hydraulic conductivity was assumed variable according to Kozeny-Carman relationship, that was calibrated on the measurements showed in Chapter 3.

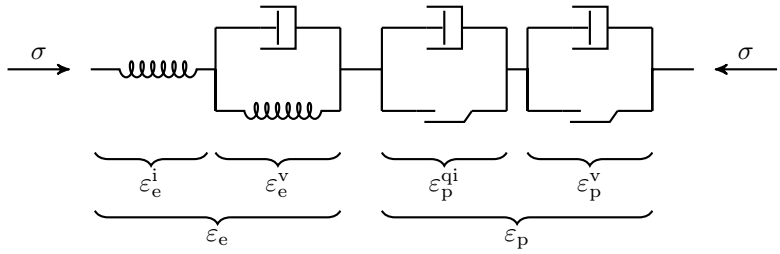

Figure 5.19: Modified rheological model.

5.9 Some considerations on the extension to multiaxial case

The extension of the model to multiaxial case implies the choice of a consistent viscoplastic framework for the simulation of the most important features of deviatoric viscous behaviour of clayey soils (Section 2.4). The next Chapter will present the basic constitutive assumptions needed for a general multiaxial formulation.

As discussed below, the decomposition of the plastic deformation into an instantaneous and a viscous mechanisms does not permit the simulation of typically observed viscous phenomena induced by the application of large deviatoric loads under undrained conditions. In fact, the existence of an (even small) instantaneous component of plastic deformation completely controls the global undrained soil response and the stress state reaches the critical state immediately, with negligible viscous effects. In contrast, under isotropic loading under drained conditions, this inconsistency does not reveal because the instantaneous component of plastic strain leads to an increment of plastic deformations without leading to failure, thus the instantaneous plastic strains are simply followed by the viscous plastic deformations.

As a result, in order to obtain a reliable multiaxial constitutive model, the plastic part of the proposed model must be modified by substituting the instantaneous mechanism with a viscous mechanism. In particular, the instantaneous plastic mechanism must be replaced by a quasi-instantaneous viscous mechanism (with the same mathematical structure and a different viscous coefficient). The resulting rheological model is shown in Figure 5.19, where ε_p^{qi} represents the quasi-instantaneous component of plastic strain. The governing relationships of

the modified model (obtained from eqs. 5.3 and 5.4) are given in eqns. 5.11.

$$\sigma_{\mathrm{e}}^{\mathrm{i}} = \sigma_0 \ \exp\left(\frac{\varepsilon_{\mathrm{e}}^{\mathrm{v}} - \varepsilon_0}{\alpha_{\mathrm{e}}\ \kappa}\right) \tag{5.11a}$$

$$\sigma_{\mathrm{e}}^{\mathrm{v}} = \sigma_0 \ \exp\left(\frac{\varepsilon_{\mathrm{e}}^{\mathrm{v}} - \varepsilon_0}{(1-\alpha_{\mathrm{e}})\ \kappa}\right)\left[1 + \psi_{\mathrm{e}}(\dot{\varepsilon}_{\mathrm{e}}^{\mathrm{v}})\right] \tag{5.11b}$$

$$\sigma_{\mathrm{p}}^{\mathrm{qi}} = \sigma_0 \ \exp\left(\frac{\varepsilon_{\mathrm{p}}^{\mathrm{v}} - \varepsilon_0}{\alpha_{\mathrm{p}}\ (\lambda-\kappa)}\right)\left[1 + \psi_{\mathrm{p}}^{\mathrm{qi}}(\dot{\varepsilon}_{\mathrm{p}}^{\mathrm{qi}})\right] \tag{5.11c}$$

$$\sigma_{\mathrm{p}}^{\mathrm{v}} = \sigma_0 \ \exp\left(\frac{\varepsilon_{\mathrm{p}}^{\mathrm{v}} - \varepsilon_0}{(1-\alpha_{\mathrm{p}})(\lambda-\kappa)}\right)\left[1 + \psi_{\mathrm{p}}^{\mathrm{v}}(\dot{\varepsilon}_{\mathrm{p}}^{\mathrm{v}})\right], \tag{5.11d}$$

where $\psi_{\mathrm{p}}^{\mathrm{qi}}(\dot{\varepsilon}_{\mathrm{p}}^{\mathrm{qi}})$ and $\psi_{\mathrm{p}}^{\mathrm{v}}(\dot{\varepsilon}_{\mathrm{p}}^{\mathrm{v}})$ are the viscosity function for the two plastic mechanisms defined as follows:

$$\psi_{\mathrm{p}}^{\mathrm{qi}}(\dot{\varepsilon}_{\mathrm{p}}^{\mathrm{qi}}) = \Gamma_{\mathrm{p}}^{\mathrm{qi}} \ln\left(\frac{\dot{\varepsilon}_{\mathrm{p}}^{\mathrm{qi}}}{\dot{\varepsilon}_{\min}} + 1\right) \tag{5.12a}$$

$$\psi_{\mathrm{p}}^{\mathrm{v}}(\dot{\varepsilon}_{\mathrm{p}}^{\mathrm{v}}) = \Gamma_{\mathrm{p}}^{\mathrm{v}} \ln\left(\frac{\dot{\varepsilon}_{\mathrm{p}}^{\mathrm{v}}}{\dot{\varepsilon}_{\min}} + 1\right), \tag{5.12b}$$

in which the two viscosity coefficients $\Gamma_{\mathrm{p}}^{\mathrm{qi}}$ and $\Gamma_{\mathrm{p}}^{\mathrm{v}}$ rule the development of the deformation of the quasi-instantaneous and viscous mechanisms, respectively.

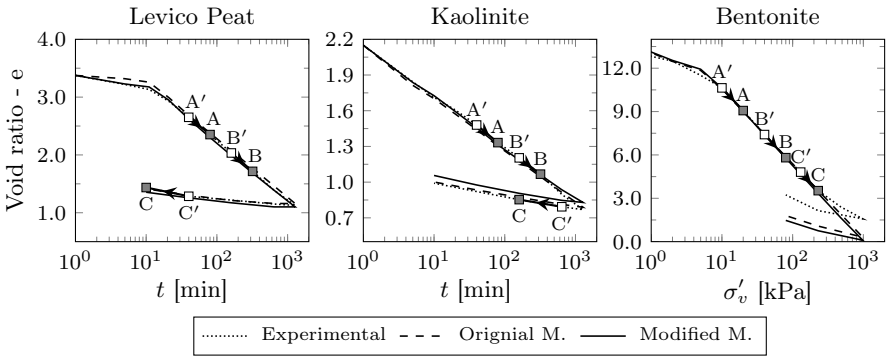

Figure 5.20: Comparison of the simulations of oedometer tests on different soils obtained with original and modified model: oedometer compression curves.

Parameter	Peat (Levico)		Kaolinite		Bentonite	
	Original	Modified	Original	Modified	Original	Modified
κ	0.015	0.015	0.016	0.02	0.04	0.04
α_e	0.05	0.04	0.75	0.75	0.5	0.5
Γ_e	0.06	0.048	0.05	0.05	0.05	0.05
λ	0.10	0.115	0.065	0.07	0.133	0.14
α_p	0.01	0.04	0.75	0.75	0.5	0.5
Γ_p^{qi}	-	0.03	-	0.005	-	0.005
Γ_p^{v}	0.40	0.30	0.05	0.05	0.05	0.05
$\dot{\varepsilon}_{min}$ [1/min]	10^{-10}	10^{-10}	10^{-10}	10^{-10}	10^{-10}	10^{-10}
$\sigma_{pc,1}$ [kPa]	4	3	5	5	5	5
$\sigma_{pc,2}$ [kPa]	4	3	5	5	5	5

Table 5.3: Comparison between the calibrated constitutive parameters of the original and modified models.

The effect of this constitutive assumption on the general response of the model will be analysed in Chapter 6. In this section the results of the modified model will be compared with the original instantaneous viscous model in order to highlight that the use of two viscous mechanisms (one quasi-instantaneous and one viscous) does not substantially affect the general 1D response and the simulation exposed in this Chapter.

Figure 5.20 shows the comparisons between the simulations of the oedometer compression curves obtained with the original instantaneous-viscous model and with the modified viscous-viscous model for Levico peat, Kaolinite and Bentonite. Table 5.3 shows the best calibrations for the two models. The use of a viscous-viscous model with very different viscous coefficients (adopting $\Gamma_p^{qi} \simeq 1/10\Gamma_p^{v}$) does not affect the global response of the model and the best calibration of constitutive parameters remains the same. The only parameter that must be modified in order to obtain a good simulations is λ that must be slightly increased with respect to the original value used in the instantaneous-viscous model.

The comparisons between the response in terms of time-strain curves for the test of Figure 5.20 are shown in Fig. 5.21, where it is possible to note that also the strain history behaviour is simulated with a good accuracy by the modified

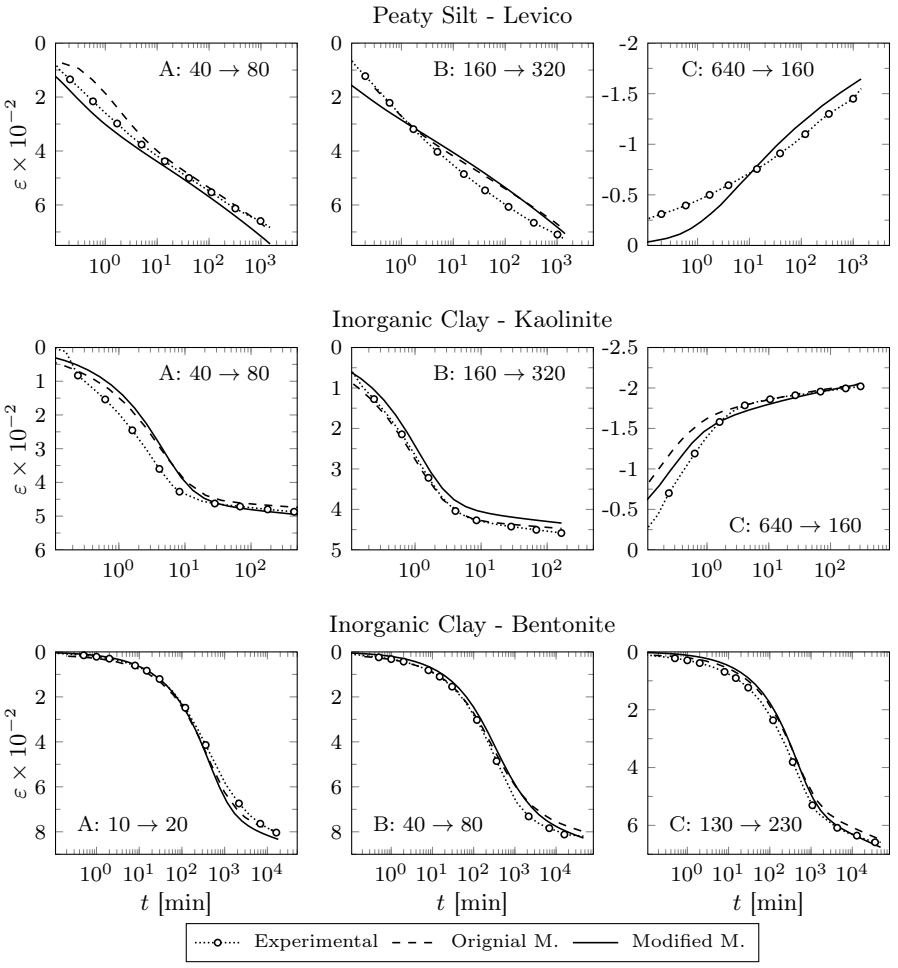

Figure 5.21: Comparison of the simulations of oedometer tests on different soils obtained with original and modified model: time-strain curves.

model.

Figures 5.22 shows the comparisons between the instantaneous-viscous and the quasi-instantaneous-viscous models in the simulated evolution of pore pres-

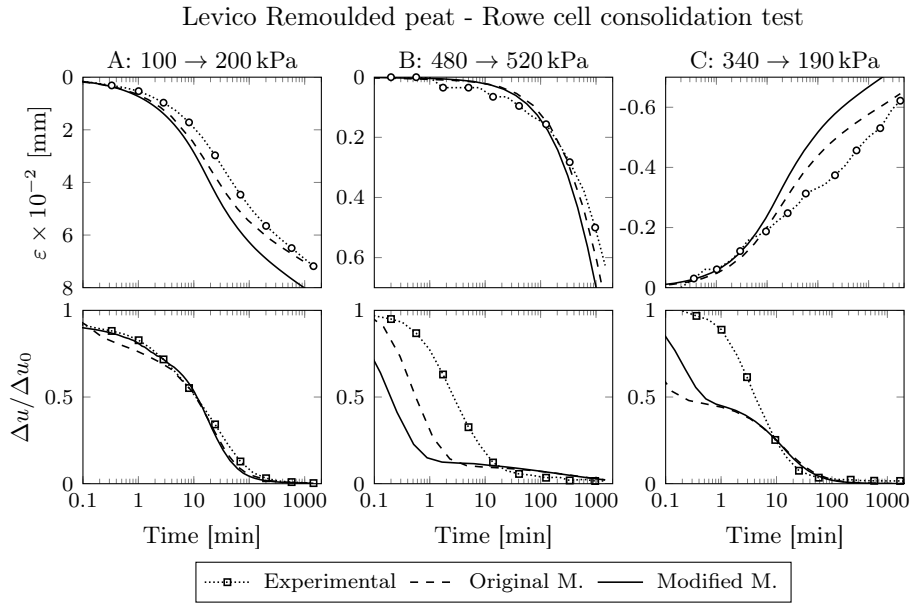

Figure 5.22: Comparison of the simulations of Rowe cell consolidation test obtained with original and modified model:

sures in the Rowe cell, It can be observed that even in this case, model simulations are scarcely affected by the quasi-instantaneous plastic mechanism.

The comparison can be extended also to the other experimental evidences of 1D solid response (see Section 5.8), thus demonstrating that the quasi-instantaneous plastic mechanism does not affect the good consistency of the original model (based on an instantaneous plastic mechanism in addition to the viscous mechanism), provided the values of $\Gamma_{\mathrm{p}}^{\mathrm{qi}}$ are kept sufficiently smaller with respect to $\Gamma_{\mathrm{p}}^{\mathrm{v}}$ (with a ratio of about 1:10).

5.10 Conclusions

The proposed model can be considered at first an in-depth and rigorous validation of the isotach concepts that were firstly proposed by Suklje 1957, and later

extended by Bjerrum 1967. The proposed model is not however a simple implementation of the isotach concepts, because it emphasises the need of considering two deformation mechanisms with two different velocities: the first is a short term mechanism (that was here approximated with an instantaneous mechanism for the sake of simplicity), the second is a long term, viscous mechanism. The two mechanisms contribute in different proportions to the final response of fine grained soils: in inorganic clays short- and long- term mechanisms have approximately the same amplitude, whereas in peats, the short-term mechanism is vanishingly small as compared to the long-term.

The proposed framework was shown to be capable of simulating the most important aspects of the delayed soils' response, under a variety of loading and unloading conditions.

The key ingredients of the model are the strain decomposition in four components (elastic and plastic, instantaneous and viscous, according to eq. (5.1)) and the logarithmic viscosity function (eq. (5.6)). These two ingredients permit to accurately simulate the major features of viscous response of a wide range of fine grained soils (ranging from inorganic to highly organic clays and peats) under a wide range of loading and unloading conditions.

In the final part of the Chapter the effects of a slight modification of the proposed framework have been analysed. In particular, the effects of using two viscous mechanisms (one quasi-instantaneous and one viscous) have been discussed. If the viscosity of the two viscous mechanisms are assumed to be fairly different with resepct to each other, then the simulations of the 1D model are practically unaffected by the new assumtion. The need for a double viscous plastic mechanism is related to the simulation of viscous effects on samples which are loaded to failure, under undrained conditions, as discussed in the next Chapter.

CHAPTER 6

The proposed multiaxial rate dependent, two yield surfaces constitutive model

The general multiaxial rate dependent constitutive model presented in this chapter is the extension of the one-dimensional approach proposed in Chapter 5. The model is based on the overstress approach and is characterized by two yield surfaces (to model the instantaneous and the viscous part of the plastic deformation). The viscous behaviour is governed by the definition of a proper logarithmic viscosity function. The model has been validated both in normally consolidated and in overconsolidated regimes.

6.1 Introduction

The constitutive model proposed in this Chapter, is the multi-axial extension of the viscoelastic-viscoplastic unidimensional constitutive model presented in Chapter 5.

From theoretical point of view, the natural extension of the mono-dimensional rheological model approach is represented by the overstress theory of Malvern (1951) and Perzyna (1963a) (Section 4.4.2). The concept of overstress in multi-axial stress space is the generalization of the stress sustained by the dashpot in a 1D Bingham model. For this reason the extension of uni-axial model has been performed using the overstress framework of viscoplasticity.

The fundamental assumptions of the 1D model are maintained. In particular, the strain decomposition in four components, the logarithmic viscosity functions, and the presence of viscous deformation both in elastic and plastic regime are the basic hypotheses of the multi-axial model. The only modification is the use of

two viscoplastic mechanisms (one quasi-instantaneous and one viscous) instead of a plastic part composed by an instantaneous and a viscous mechanisms. This modification permits a reliable simulation of viscous effects in undrained tests, without affecting the reliability of one-dimensional simulations (see Section 5.9).

In order to simulate the main features of triaxial stress-strain-time response of clays shown in Chapter 2 some further constitutive hypothesis have been proposed. One of the most interesting aspects of the multi-axial model is the applicability to both normally consolidated and highly overconsolidated clays with results consistent for the two soil conditions.

The proposed multi-axial model can simulate all the viscous effects shown in the presentation of 1D model and can also predict with good accuracy many peculiar aspects of triaxial time dependent behaviour. In particular, the following aspects can be reliably simulated: the strain rate effect both in normally consolidated (Tatsuoka et al. 1998) and highly overconsolidated regimes (Augustesen et al. 2004), the tertiary creep phenomenon in undrained triaxial tests, and the triaxial relaxation (and the related strain rate effects) (Lacerda and Houston 1973; Silvestri et al. 1988).

In the first part of the Chapter, the additional constitutive hypotheses for the extension to 3D case, and the numerical implementation in FE environment, are described. In the second part, the model is used for the simulation of a series of experiments on clay and peat.

6.2 Theoretical framework

The constitutive model is developed in general stress space in the small strain framework. In the following pages, the boldface characters denote second order tensor quantities, and the blackboard bold characters denote the fourth order tensor quantities. The symbol ':' indicates the double-index contraction of the tensor product; $\boldsymbol{\sigma}$ denotes the effective stress tensor, and the symbol $\boldsymbol{\varepsilon}$ indicates the strain tensor. $\boldsymbol{I}$ represents the identity tensor.

In the following, all the stress quantities are effective stresses and the usual prime has been omitted. The formulation of the model focuses on the mechanical response of the solid skeleton, while the coupling with the liquid phase has been treated separately with the classical consolidation theory.

The proposed viscoplastic approach can be applied as an extension starting from a selected rate-independent framework. For the sake of effectiveness, the viscoplastic formulation has been developed using the Modified Cam-Clay elastoplastic framework (Roscoe and Burland 1968). In this way it is possible to

highlight the major feature of the proposed viscous model in a relatively simple rate-independent framework.

6.2.1 Rate-independent elastoplasticity

First of all, let us briefly recall the basic concepts of Modified Cam-Clay rate-independent elastoplasticity. The strain is decomposed into elastic and plastic parts (eq. (6.1)). The elastic response is defined in eq. (6.2) depending on two material constants (the slope of swelling line, κ, in a volumetric strain - $\log p$ plane, where $p = I_1/3$ is the mean effective pressure, and the shear modulus G) and on two reference parameters (the reference pressure p_0 and the reference volumetric strain $\varepsilon_{\mathrm{v0}}$).

$$\boldsymbol{\varepsilon} = \boldsymbol{\varepsilon}_{\mathrm{e}} + \boldsymbol{\varepsilon}_{\mathrm{p}}, \tag{6.1}$$

$$\boldsymbol{\sigma} = 2G\,\boldsymbol{\epsilon}_{\mathrm{e}} + p_0 \exp\left[\frac{\varepsilon_{\mathrm{e,vol}} - \varepsilon_{\mathrm{v0}}}{\kappa}\right]\boldsymbol{I}. \tag{6.2}$$

In eq. (6.2) $\varepsilon_{\mathrm{e,vol}} = \operatorname{tr}\boldsymbol{\varepsilon}_{\mathrm{e}}$ is the volumetric strain (i.e. the first strain invariant) and $\boldsymbol{\epsilon}_{\mathrm{e}} = \boldsymbol{\varepsilon}_{\mathrm{e}} - 1/3\operatorname{tr}\boldsymbol{\varepsilon}_{\mathrm{e}}\,\boldsymbol{I}$ is the deviatoric elastic strain tensor.

The yield function (in the following named *static yield function*) is

$$f^{\mathrm{s}}(\boldsymbol{\sigma}, p_{\mathrm{c}}) = \frac{3\,J_2}{(M\,k_\theta)^2} + \left(\frac{I_1}{3}\right)^2 + \frac{I_1}{3}\,p_{\mathrm{c}} = 0, \tag{6.3}$$

in which $I_1 = \operatorname{tr}\boldsymbol{\sigma}$ is the first stress invariant; $J_2 = 1/2\ \boldsymbol{s} : \boldsymbol{s}$ is the second deviatoric stress invariant (where $\boldsymbol{s} = \boldsymbol{\sigma} - (\boldsymbol{\sigma} : \boldsymbol{I})\boldsymbol{I}/3$ is the deviatoric component of $\boldsymbol{\sigma}$); p_{c} is the scalar defining the size of the yield surface; M is the critical state stress ratio for axisymmetric compression; and k_θ is a dimensionless scaling function which affects the shape of the yield surface in the deviatoric section. Many formulation of k_θ are presented in the literature, among these, the Willam and Warnke (1975) formulation of eq. (6.4) has been chosen for its smoothness and flexibility.

$$k_\theta = \frac{2\,m}{(1+m) - (1-m)\,\sin(3\,\theta)}, \tag{6.4}$$

where m is the material parameter defined as the ratio between the radii of the section in the deviatoric plane through the surface for axisymmetric extension and compression (see Fig. 6.1). In order to ensure the yield surface convexity $0.778 \leq m \leq 1$. The parameter θ represents the Lode's angle defined as follows:

$$\frac{-\pi}{6} \leq \theta = \frac{1}{3}\sin^{-1}\left(\frac{-3\sqrt{3}\,J_3}{2\,J_2^{3/2}}\right) \leq \frac{\pi}{6}, \tag{6.5}$$

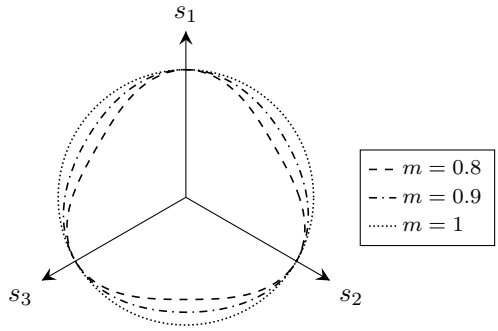

Figure 6.1: Deviatoric section of Modified Cam-Clay model

in which J_3 is the third deviatoric invariant defined as the determinant of $\boldsymbol{s}$.

The Cam-Clay model presents a volumetric hardening rule in which the hardening parameter p_c depends on plastic volumetric strain $\varepsilon_{\mathrm{p,vol}} = \operatorname{tr} \boldsymbol{\varepsilon}_\mathrm{p}$ as follows:

$$p_\mathrm{c} = p_0 \, \exp\left(\frac{\varepsilon_{\mathrm{p,vol}} - \varepsilon_{\mathrm{v0}}}{\lambda - \kappa}\right) \tag{6.6a}$$

$$\frac{\dot{p}_\mathrm{c}}{p_\mathrm{c}} = \frac{\dot{\varepsilon}_{\mathrm{p,vol}}}{\lambda - \kappa}, \tag{6.6b}$$

where κ and λ are the slopes of normal compression line in a volumetric strain - $\log(I_1/3)$ plane.

The flow rule is associated and the evolution of the plastic strain can be expressed as

$$\dot{\boldsymbol{\varepsilon}}_\mathrm{p} = \dot{\gamma} \, \frac{\partial f^\mathrm{s}}{\partial \boldsymbol{\sigma}}. \tag{6.7}$$

The plastic multiplier defined in eq. (6.7) $\dot{\gamma}$ and the yield surface must satisfy the Kuhn-Tucker conditions:

$$\dot{\gamma} \geq 0 \quad f^\mathrm{s} \leq 0 \quad \dot{\gamma} \, f^\mathrm{s} = 0. \tag{6.8}$$

6.2.2 Viscoplastic formulation

The definition of the viscoplastic behaviour was derived from the overstress theory (Malvern 1951, Perzyna 1966). In the overstress approach, the strain

rate is divided into an elastic, $\dot{\boldsymbol{\varepsilon}}_{\mathrm{e}}$, and a viscoplastic part, $\dot{\boldsymbol{\varepsilon}}_{\mathrm{p}}^{\mathrm{v}}$. The viscoplastic strain rate is defined in the following way:

$$\dot{\boldsymbol{\varepsilon}}_{\mathrm{p}}^{\mathrm{v}} = \gamma \left\langle \Phi(f^{\mathrm{s}}) \right\rangle \frac{\partial f^{\mathrm{s}}}{\partial \boldsymbol{\sigma}}, \tag{6.9}$$

where γ denotes the viscosity constant of the material, f is the yield function and the symbol $\langle \Phi(f^{\mathrm{s}}) \rangle$ is defined as follows:

$$\left\langle \Phi(f^{\mathrm{s}}) \right\rangle = \begin{cases} 0 & \text{for } f^{\mathrm{s}} \leq 0 \\ \Phi(f^{\mathrm{s}}) & \text{for } f^{\mathrm{s}} > 0 \end{cases}. \tag{6.10}$$

The function $\Phi(f^{\mathrm{s}})$ is an arbitrary positive function representing the viscosity properties of the materials and may be chosen on the basis of experimental evidence.

One of the outstanding features of the overstress theory is the fact that the current stress states can lie outside the yield surface and the yield surface has, in general, a value larger than zero. Therefore the consistency condition (eq. (6.8)) is not directly applicable to the formulation of Perzyna (1966). Nevertheless, starting from eq. (6.9) it is possible to define a new viscoplastic yield surface called *dynamic yield surface* depending on the viscoplastic strain rate (eq. (6.11)b) that satisfies the Kuhn-Tucker conditions (eq. (6.11)).

$$f^{\mathrm{s}}(\boldsymbol{\sigma}, p_{\mathrm{c}}) \neq 0 \tag{6.11a}$$

$$f^{\mathrm{d}}(\boldsymbol{\sigma}, p_{\mathrm{c}}, \dot{\boldsymbol{\varepsilon}}_{\mathrm{p}}^{\mathrm{v}}) = 0 \tag{6.11b}$$

$$\dot{\lambda} \geq 0 \quad f^{\mathrm{d}} \leq 0 \quad \dot{\lambda}\, f^{\mathrm{d}} = 0. \tag{6.11c}$$

The definition of the *dynamic yield surface* is useful for the numeric implementation and leads to a more efficient solution algorithm with respect to the classical Perzyna's approach. This approach is similar to the consistency model proposed by W. Wang et al. (1997).

The meaning of the *dynamic yield surface* is more clear as when applied to a practical case. The definition of the viscoplastic dynamic yield condition for a Modified Cam-Clay model is

$$f^{\mathrm{d}}(\boldsymbol{\sigma}, p_{\mathrm{c}}, \dot{\boldsymbol{\varepsilon}}_{\mathrm{p}}^{\mathrm{v}}) = \frac{3\, J_2}{(M\, k_\theta)^2} + \left(\frac{I_1}{3}\right)^2 + \frac{I_1}{3}\, p_{\mathrm{c}} \left[1 + \Phi^{-1}(\dot{\boldsymbol{\varepsilon}}_{\mathrm{p}}^{\mathrm{v}})\right] = 0, \tag{6.12}$$

where the viscosity function $\Phi^{-1}(\dot{\boldsymbol{\varepsilon}}_{\mathrm{p}}^{\mathrm{v}})$ is a positive scalar function of viscoplastic strain rate derived from eq. (6.9).

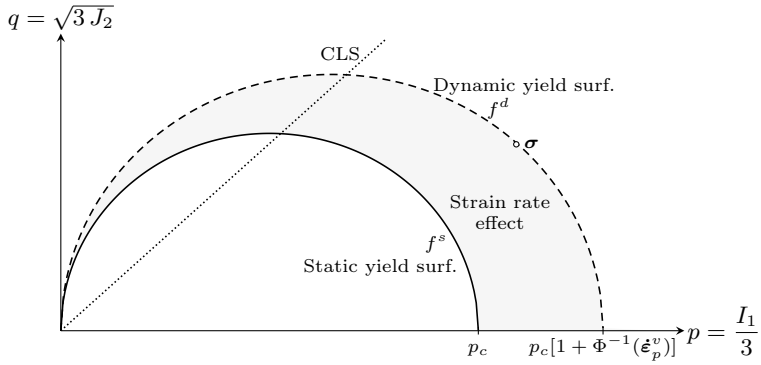

Figure 6.2: Sketch of static and dynamic Modified Cam-Clay yield surfaces in the p-q plane

Observing eq. (6.12) the role of the viscoplastic strain rate on the material behaviour can be clearly understood. In particular, the scalar function $\Phi^{-1}(\dot{\varepsilon}_{\mathrm{p}}^{\mathrm{v}})$ acts like a multiplicative scalar of the hardening parameter p_{c}. The resulting *dynamic yield surface* has the shape of a hardened *static yield surface* whose size is governed by $\dot{\varepsilon}_{\mathrm{p}}^{\mathrm{v}}$ (Fig. 6.2).

In the original overstress formulation the flow rule is associated and the viscous effect is related to the whole viscoplastic strain rate tensor (eq. (6.9)).

6.2.3 Modelling approach to delayed behaviour of clays and organic soils

In this section the general overstress model will be used for modelling viscous behaviour of clays and organic soils. In order to implement a reliable model, it is important to review some of the most significant experimental evidence, regarding the viscous behaviour of cohesive soils:

E1 in the soil strain process the existence of two deformation mechanisms is immediately recognizable: one instantaneous (or quasi-instantaneous) and one delayed. This kind of strain decomposition is valid both in the elastic and elastoplastic regime;

E2 the strain rate does not influence the critical state slope (Whitman and Richardson 1963);

E3 the isotache concept (Suklje 1957, Bjerrum 1967): the viscous deformations presents a linear behaviour with respect to the logarithm of time;

E4 soils exhibit tertiary creep under constant deviatoric stress both in undrained (Murayama and Shibata 1958, Campanella and Vaid 1972) and drained conditions (Tavenas et al. 1978);

E5 the peak strength obtained from highly overconsolidated clay depends on the strain rate (Augustesen et al. 2004);

E6 the viscoelastic response observed experimentally follows the same general rules of the viscoplastic one;

The proposed constitutive model was developed starting from the overstress viscoplastic theory and from these seven fundamental experimental observations. In this section the original overstress model was modified and adapted in order to reproduce the major features of soil viscous behaviour.

E1: Strain decomposition

The delayed behaviour of soils was investigated in detail by means of oedometer and triaxial laboratory tests. Focusing the attention on the most simple case of oedometric compression the deformation process is divided into primary consolidation (related to the volume change of the void ratio due to water expulsion and described by the consolidation theory of Terzaghi (1925)) and secondary compression (due to creep deformations of the solid skeleton).

Although in the elastic region the viscous deformations are often neglected this kind of behaviour can be found both in elastic and elastoplastic regime (see Section 3.4.3). From the modelling point of view this observation means that the deformation is decomposed into four parts: two elastic and two plastic.

Focusing on plastic regime this assumption implies the existence of two yield surfaces related to the two deformation phenomena. The direct extension of the uniaxial model presented in Section 5 implies the use of an instantaneous and a viscous yield surfaces. This assumption leads to the impossibility of simulating delayed phenomena under undrained loading. In fact, in these conditions, the application of a deviatoric stress leads to the immediate development of instantaneous plastic deformations and the soil instantaneously approaches the failure while the development of viscous deformation is still negligible.

In order to simulate viscous effects in general drained and undrained conditions, the instantaneous part of the plastic strain must be substituted by a

quasi-instantaneous deformation mechanism. From the modelling point of view this is achieved by using two viscous yield surfaces with very different viscous coefficients. The final result is that the deviatoric viscous phenomena under undrained conditions are mainly associated with the quasi-instantaneous yield surface.

The resulting strain decomposition is shown in eq. (6.13), that is a modified multiaxial version of eq. (5.1).

$$\dot{\boldsymbol{\varepsilon}} = \underbrace{\dot{\boldsymbol{\varepsilon}}_{\mathrm{e}}^{i} + \dot{\boldsymbol{\varepsilon}}_{\mathrm{e}}^{\mathrm{v}}}_{\dot{\boldsymbol{\varepsilon}}_{\mathrm{e}}} + \underbrace{\dot{\boldsymbol{\varepsilon}}_{\mathrm{p}}^{qi} + \dot{\boldsymbol{\varepsilon}}_{\mathrm{p}}^{v}}_{\dot{\boldsymbol{\varepsilon}}_{\mathrm{p}}} \tag{6.13}$$

where the strain increment tensor is decomposed in four components: instantaneous elastic ($\dot{\boldsymbol{\varepsilon}}_{\mathrm{e}}^{\mathrm{i}}$), viscoelastic ($\dot{\boldsymbol{\varepsilon}}_{\mathrm{e}}^{\mathrm{v}}$), quasi-instantaneous plastic ($\dot{\boldsymbol{\varepsilon}}_{\mathrm{p}}^{\mathrm{qi}}$) and viscoplastic ($\dot{\boldsymbol{\varepsilon}}_{\mathrm{p}}^{\mathrm{v}}$).

The presence of two viscous mechanisms with different characteristic time scales clearly highlights the existence of two micromechanical viscous mechanisms, that cause different deformations and rearrangements at grain-size level (for example: a compressive and a sliding rearrangements). A future development of this work will be the identification of the microscale mechanisms which are responsible for the two observed time scales. This goal can be achieved with further experimental evidences showing the viscous mechanism under isotropic compression and shear, and with microscopic investigations (e.g. SEM analyses).

The four-component strain decomposition implies the definition of two constitutive parameters, called *repartition coefficients* α_{e} and α_{p}. The coefficient α_{e} governs the split of the deformation between the quasi-instantaneous and the viscous components of elastic strains, whereas α_{p} governs the split between the instantaneous and the viscous components of plastic strains. The range of variation of the *repartition coefficients* is between 0 and 1. $\alpha_{\mathrm{e}} = 0$ means that all the elastic deformation is instantaneous, on the contrary if $\alpha_{\mathrm{e}} = 1$ the resulting elastic strain is purely viscous. The same effect is valid for the plastic repartition coefficient α_{p}: for $\alpha_{\mathrm{p}} = 0$ the entire plastic strain is governed by the quasi-instantaneous yield surface, while for $\alpha_{\mathrm{p}} = 1$ the plastic strain is entirely associated to the viscous yield surface.

The general relation eq. (6.13) allows the prediction of viscous behaviour of soil both in the elastic and elastoplastic regime.

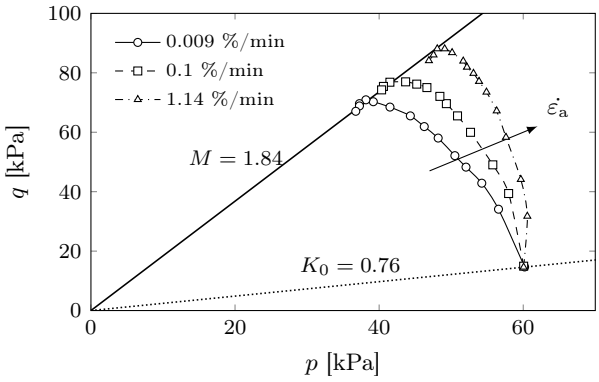

Figure 6.3: Stress paths of CAU triaxial tests performed at different strain rates on Sackville clay (Hinchberger and Rowe 2005).

E2: Critical State Behaviour

Observing the response of clayey and organic soil subjected to undrained triaxial tests with different axial strain rates (Whitman and Richardson 1963; Hinchberger and Rowe 2005), it is possible to observe that the strength of soil in terms of maximum deviatoric stress is affected by the loading strain rate but the results of different tests lead to the same critical state envelope (Fig. 6.3).

In terms of overstress theory the uniqueness of the Critical State Line (CSL) with respect to different strain rates in the $p-q$ space has the important consequence that the viscous response is related only to the volumetric component of the viscoplastic strain rate ($\dot{\varepsilon}^{\mathrm{v}}_{\mathrm{p,vol}} = \mathrm{tr}\,\dot{\boldsymbol{\varepsilon}}^{\mathrm{v}}_{\mathrm{p}}$). This assumption allows as to rewrite the equation eq. (6.11)b as follows:

$$f^{\mathrm{d}}(\boldsymbol{\sigma}, p_{\mathrm{c}}, \dot{\varepsilon}^{\mathrm{v}}_{\mathrm{p,vol}}) = 0. \tag{6.14}$$

This hypothesis is essential for the good prediction of the critical state response. When the stress state reaches the critical state the volumetric part of viscoplastic strain rate approaches zero and also the viscous effect vanishes ensuring the uniqueness of the CS loci.

E3: Viscosity function

The delayed response of the model was derived referring to the viscoplastic regime. The viscous law obtained for the plastic deformation was used, with

some adjustments, to the viscoelastic mechanism.

Analysing the mathematical structure of the viscoplastic overstress theory it is clear that the key factor affecting the model results is the choice of an appropriate viscosity function ($\Phi^{-1}(\dot{\boldsymbol{\varepsilon}}^{\mathrm{v}}_{\mathrm{p}})$ in eq. (6.12)).

In the case of soils the typical time-strain curve, obtained from a constant stress 1D oedometer test or from a triaxial creep test performed at constant deviatoric stress, is almost linear with respect to the logarithm of elapsed time after the end of the primary consolidation (Section 2.2.2). This evidence was first highlighted by Suklje (1957) who introduced the isotach concept, and then confirmed by many authors for a wide range of soils in different conditions (Murayama and Shibata 1958; Bjerrum 1967; Berre and Nersen 1972; Mesri 1973; Mesri and Godlewski 1977; Tavenas et al. 1978).

Starting from this experimental observation a logarithmic based viscosity function was chosen in the formulation of the viscoplastic model:

$$\Phi^{-1}(\dot{\varepsilon}_{\mathrm{p,vol}}) = \Gamma \ln\left(\frac{\dot{\varepsilon}_{\mathrm{p,vol}}}{\dot{\varepsilon}_{\mathrm{min}}} + 1\right). \tag{6.15}$$

This function is made of a logarithmic term, similar to the one introduced by Malvern (1951) and later proposed again by Perzyna (1963b). This formulation is the same as the unidimensional model presented in Section 5.2.1 and allows the modelling of the linear $\varepsilon - \log t$ behaviour.

Two material parameters are associated with the viscosity function: the principal viscosity coefficient Γ, that defines the global behaviour and the slope of the viscosity function; and the scaling factor $\dot{\varepsilon}_{\mathrm{min}}$ that influences the duration of the viscous phenomenon. Figure 6.4 briefly shows the effect of the two parameters on the shape of the viscosity function.

The multiaxial and the uniaxial models ware formulated with the same main hypothesis. The only difference between uniaxial and multiaxial model is that the instantaneous mechanism is repalced by a quasi-instantaneous mechanism. As a consequence, it is necessary to define two viscoplastic viscosity functions characterized by two different values of the viscous parameter Γ_{p}, namely $\Gamma^{\mathrm{qi}}_{\mathrm{p}}$ and $\Gamma^{\mathrm{v}}_{\mathrm{p}}$ (while the reference strain rate $\dot{\varepsilon}_{\mathrm{min}}$ can be assumed equal for the two mechanisms).

The calibration of the viscosity coefficients can be performed starting from the viscous mechanism with the procedure proposed in Section 5.6. The value of the quasi-instantaneous coefficient $\Gamma^{\mathrm{qi}}_{\mathrm{p}}$ can be reasonably assumed of about 1/10 of $\Gamma^{\mathrm{v}}_{\mathrm{p}}$. In fact this value ensures the reliability of 1D simulations (Section 5.9). Unfortunately, published experimental data do not permit to verify the

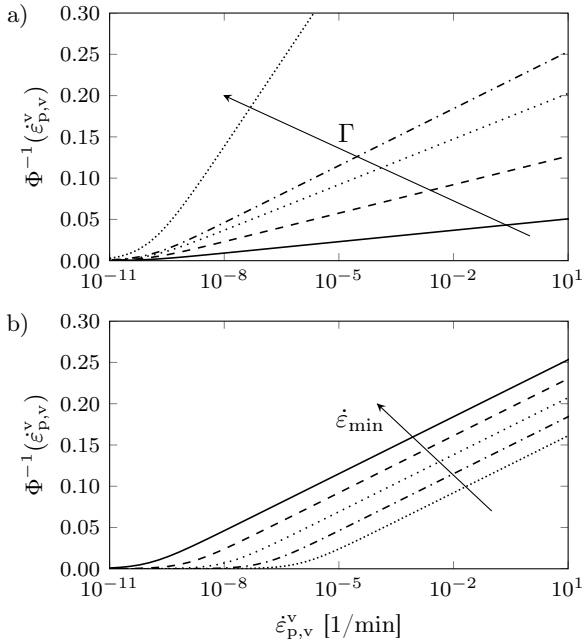

Figure 6.4: Parametric analysis the viscosity function:
a) influence of Γ b) influence of $\dot{\varepsilon}_{min}$.

consistency of the value of Γ_p^{qi} selected as described above (i.e. starting from the Γ_p^v calibrated in 1D conditions) for the modelling observed viscous effects under drained and undrained triaxial tests. This validation in fact requires further experimental tests and will be the subject of a future development of the work.

The following sections will focus on the definition of the deviatoric behaviour of the multiaxial model, while the global response of the model will be analysed in the discussion of the results.

E4: Flow rule

Another peculiar aspect of viscous behaviour of clayey soils is the phenomenon called tertiary creep observed in triaxial creep tests performed maintaining the stress constant and observing the development of the deformation. For low levels of deviatoric stress the strain rate decreases with time and the response is almost

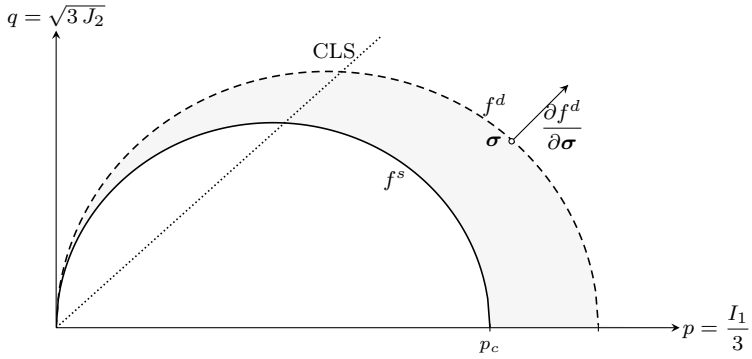

Figure 6.5: Sketch of associative flow rule for Modified Cam-Clay yield surface in the p-q plane

linear in a $\log \dot{\varepsilon}_\mathrm{a} - \log t$. Increasing the deviatoric stress level after a period of stationary decreasing the strain rate tends to increase and the specimen reaches failure.

The phenomenon of tertiary or acceleration creep is interesting from the modelling point of view and has been observed by many authors in undrained triaxial creep tests (Murayama and Shibata 1958, Campanella and Vaid 1972, Campanella and Vaid 1974, Vaid and Campanella 1977, Vaid, Robertson, et al. 1979). Tavenas et al. (1978) found tertiary creep also in drained conditions.

It is worth noting that the drained creep test is a true creep test unlike the undrained creep test. In the first case in fact the effective stress is indeed maintained constant during all the creep phase, whereas in the latter the mean effective stress decreases, when the pore pressure builds up, while the deviatoric stress remains constant. Therefore drained creep represents a pure creep process, whereas undrained creep does not (Augustesen et al. 2004).

As reported in the previous section, the classical overstress theory considers an associative flow rule. In the proposed formulation this hypothesis leads to the computation of the plastic flow direction on the dynamic yield surface, f^d (fig. 6.5).

The hypothesis of associative flow rule leads to the results of the undrained triaxial creep tests shown in Figure 6.6, in which the stress paths of two simulations of creep tests are reported. Considering an associate flow rule allows the simulation of tertiary creep in undrained triaxial test both in normally consoli-

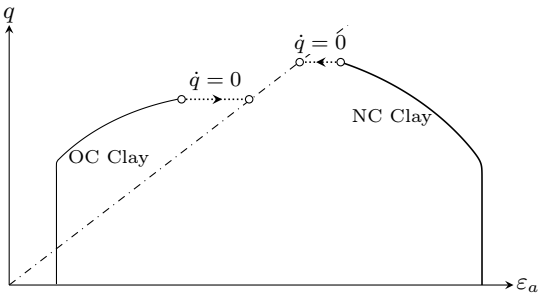

Figure 6.6: Summary of the stress paths of the simulation undrained tertiary creep in the normally consolidated, and overconsolidated states

dated and in highly overconsolidated regimes. From Figure 6.6 it is possible to observe the uniqueness of the failure envelope.

For example, referring to the case of normally consolidated clay, the decrease of isotropic effective stress, due to the development of creep deformations reaches the critical state line after a certain period of creep (Fig. 6.6). The hypothesis that the viscous phenomena depends only on the volumetric part of the plastic deformations leads to the unstable evolution of the axial strain rate that abruptly increases when the effective stress approaches the Critical State Line and the viscous effect vanishes.

On the other hand, the hypothesis of associated flow rule results in the inability of predicting tertiary creep in drained triaxial tests. If the deviatoric creep stress is below the CSL the simulation shows a undefined decrement of viscous strain rate, whereas if you try to apply a deviatoric load above the CSL the specimen immediately fails when flow vector becomes vertical (i. e. when the state of stress reaches the CSL).

To the best of the author's knowledge the only experimental evidence regarding the tertiary creep in drained creep tests is that by Tavenas et al. (1978). These tests were performed on an undisturbed soft sensitive clay (Saint Alban clay) that has an important quasi-preconsolidation due to the effect of ageing and possibly thixotropic hardening (Leroueil, Tavenas, et al. 1979). In this case the delayed deformation could be related to the viscous destructuration of the cementation bonds and might be consequently modelled with a different approach related to destructuration.

For this reason an associative flow rule was chosen. Section 6.2.4 will propose some further consideration about the modelling of drained tertiary creep.

E5: Highly Overconsolidated soils behaviour

Section 2.4.4 briefly summarized the experimental evidence of strain rate effect on highly overconsolidated clays (Vaid, Robertson, et al. 1979; Tavenas et al. 1978; Lefebvre and LeBoeuf 1986; Zhu et al. 1999). The main outcome of this experimental work is that the peak strength obtained from triaxial tests, performed on highly overconsolidated clays, is affected by the applied strain rate. In particular, the greater the axial strain rate, the greater the strength of the material. This observation points out that the overstress concept holds true also in the overconsolidated regime.

The proposed model is based on two yield surfaces; in the overconsolidated regime the strain softening of the viscous yield surface is delayed by the presence of the rate dependent overstress while the quasi-instantaneous surface rapidly softens as soon as the state of stress comes out from the static quasi-instantaneous yield surface. As a consequence, if the initial values of the two preconsolidation pressures are similar, under shearing the quasi-instantaneous surface may soon becomes smaller than the viscous one due to the softening. This effect is examined in Fig. 6.7a, where a strain controlled triaxial drained test is simulated. The evolution of the instantaneous yield surface for strain softening leads to the abrupt decreasing of p_c^{qi} whereas the viscous yield surface remains almost fix due to the viscous overstress effects (Fig. 6.7a). Observing the development of the preconsolidation pressures during the constant strain rate loading, is possible to notice that, after a certain strain level, the value of p_c^{qi} becomes lower than p_c^{v} (Fig. 6.7c), and also the state of stress returns inside the viscous static yield surface.

This peculiar condition is considered unacceptable in this work because, if the isotropic load were resumed, there would be an initial phase in which plastic strains would occur with negligible viscous effects (due to the quasi-instantaneous yield surface) and this phenomenon was never observed experimentally. In order to avoid the quasi-instantaneous yield surface to lay inside the viscous surface, it is necessary to modify the formulation for the strongly overconsoldated field.

Many different options were considered to solve this problem and the most reliable solution resulted in changing gradually from a two yield surfaces model to a single viscous yield surface model.

In order to maintain a consistent evolution of the material properties a modification in the viscous properties of quasi-instantaneous yield surface has been gradually inserted when the material is loaded in the overconsolidated regime. This modification consist in the definition of a transition viscous coefficient for

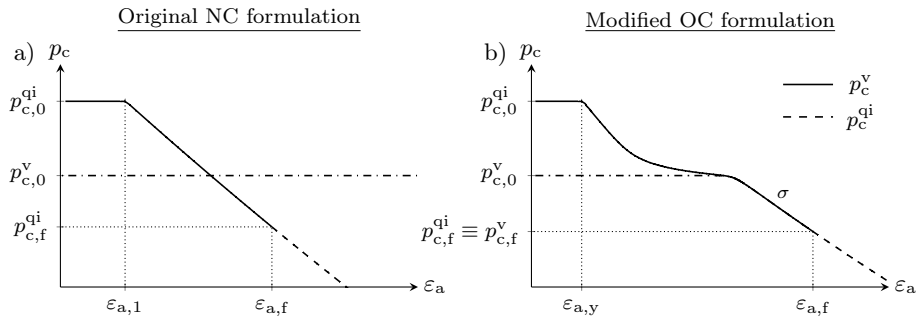

Figure 6.7: Viscous effect in OC regime: a) evolution of preconsolidation pressures for the original NC formulation; b) evolution of preconsolidation pressures for the modified OC formulation

the quasi-instantaneous yield surface as follows:

$$\Gamma_p^{qi} = \begin{cases} \Gamma_p^{qi} & \text{for } \dfrac{p_c^{qi}[1+\Phi^{-1}(\dot{\varepsilon}_{p,vol}^{qi})]}{2} - \dfrac{I_1}{3} \leq 0 \\ \Gamma_{p,OC}^{qi} & \text{for } \dfrac{p_c^{qi}[1+\Phi^{-1}(\dot{\varepsilon}_{p,vol}^{qi})]}{2} - \dfrac{I_1}{3} > 0 \end{cases}, \tag{6.16}$$

or equivalently:

$$\Gamma_p^{qi} = \begin{cases} \Gamma_p^{qi} & \text{for } \operatorname{tr}\dfrac{\partial f^{d,qi}}{\partial \boldsymbol{\sigma}} \geq 0 \\ \Gamma_{p,OC}^{qi} & \text{for } \operatorname{tr}\dfrac{\partial f^{d,qi}}{\partial \boldsymbol{\sigma}} < 0 \end{cases}. \tag{6.17}$$

The term $\operatorname{tr}(\partial f^{d,qi}/\partial \boldsymbol{\sigma})$ rules the transition between NC and OC regimes. In particular, if $\operatorname{tr}(\partial f^{d,qi}/\partial \boldsymbol{\sigma}) \geq 0$ the modified quasi-instantaneous yield surface coincides with the inviscid formulation, and if $\operatorname{tr}(\partial f^{d,qi}/\partial \boldsymbol{\sigma}) < 0$ the modified viscous coefficient is considered.

The modified quasi-instantaneous yield surface must satisfy the two limit conditions when the element is loaded in OC regime:

- $f^{d,qi}$ is the classical quasi-instantaneous surface when ($p_c^{qi} \gg p_c^v$). This behaviour corresponds to the use of the initial value of the viscous coefficient $\Gamma_{p,OC}^{qi} = \Gamma_p^{qi}$;
- f^i must evolve together with $f^{v,d}$ when the two preconsolidation pressures are coincident ($p_c^i \equiv p_c^v$).

The modified yield surface has been formulated in order to ensure a smooth transition from the quasi-instantaneous-viscous model to the purely viscous model through a proper definition of the viscous coefficient $\Gamma^{\mathrm{qi}}_{\mathrm{p,OC}}$. In particular, the softening reduction of the static yield surfaces and the viscous increase of the dynamic yield surfaces must be harmonized in order to obtain a smooth transition to a unique static yield surface. Following this hypothesis, when the two preconsolidation pressures become equals ($p^{\mathrm{qi}}_{\mathrm{c}} = p^{\mathrm{v}}_{\mathrm{c}}$) the two static surfaces evolve together, and the model holds consistent also for the successive different load conditions.

Taking into account the repartition coefficient α_{p}, the viscous coefficient of the modified quasi-instantaneous surface $\Gamma^{\mathrm{qi}}_{\mathrm{p,OC}}$ was defined in order to have two coincident yield surfaces when the difference $p^{\mathrm{qi}}_{\mathrm{c}} - p^{\mathrm{v}}_{\mathrm{c}}$ vanishes.

The use of an exponential relationship between the viscous coefficient for OC regime, $\Gamma^{\mathrm{qi}}_{\mathrm{p,OC}}$, and $p^{\mathrm{qi}}_{\mathrm{c}} - p^{\mathrm{v}}_{\mathrm{c}}$ (eq. (6.18)) leads to consistent results.

$$\Gamma^{\mathrm{qi}}_{\mathrm{p,OC}} = \Gamma^{\mathrm{qi}}_{\mathrm{p}} + (\tilde{\Gamma}^{\mathrm{qi}}_{\mathrm{p}} - \Gamma^{\mathrm{qi}}_{\mathrm{p}}) \exp\left[-\frac{p^{\mathrm{i}}_{\mathrm{c}} - p^{\mathrm{v}}_{\mathrm{c}}}{p_0}\right], \tag{6.18}$$

where the parameter $\tilde{\Gamma}^{\mathrm{qi}}_{\mathrm{p}}$ is the value of the viscous coefficient for $p^{\mathrm{qi}}_{\mathrm{c}} = p^{\mathrm{v}}_{\mathrm{c}}$, that can be calculated from eq. (6.19) obtained by imposing that $\dot{p}^{\mathrm{qi}}_{\mathrm{c}} = \dot{p}^{\mathrm{v}}_{\mathrm{c}}$, and $f^{\mathrm{d,i}} = f^{\mathrm{d,v}}$

$$\tilde{\Gamma}^{\mathrm{qi}}_{\mathrm{p}} = \frac{\Gamma^{\mathrm{v}}_{\mathrm{p}} \ln\left(\dfrac{\dot{\varepsilon}^{\mathrm{v}}_{\mathrm{p,vol}}}{\dot{\varepsilon}_{\mathrm{min}}}\right)}{\ln\left(\dfrac{\alpha_{\mathrm{p}}}{1-\alpha_{\mathrm{p}}}\right) + \ln\left(\dfrac{\dot{\varepsilon}^{\mathrm{v}}_{\mathrm{p,vol}}}{\dot{\varepsilon}_{\mathrm{min}}}\right)}. \tag{6.19}$$

The results of the modified viscous coefficient are shown in Figure 6.7b-d. Observing the evolution of the two preconsolidation pressures, it is possible to highlight the smooth transition from two yield surfaces to a unique yield surface.

It is worth noting that the transition between normally consolidated and highly overconsolidated behaviour is smooth due to the fact that the viscoplastic behaviour is related to volumetric part of the plastic deformation. At the critical state the two formulation are identical and the two surfaces behave as inviscid mechanisms for both NC and OC conditions.

E6: Viscoelastic formulation

Soils exhibit viscous behaviour both in elastic and elastoplastic regimes and the major features observed in the laboratory tests are valid also in the pure elastic

case. The extension to the viscoelastic-viscoplastic case was conducted adopting a viscoelastic viscosity function similar to that one proposed for the viscoplastic approach (eq. (6.15)).

The first part of the elastic strain (following the strain decomposition of eq. (6.13)) is assumed to be perfectly instantaneous and is governed by the elastic law of Modified Cam-Clay (eq. (6.2)) through the *repartition elastic coefficient*, α_{e}, in which the elastic deformation, $\boldsymbol{\varepsilon}_{\mathrm{e}}$, is substituted by the instantaneous part of the elastic strain, $\boldsymbol{\varepsilon}_{\mathrm{e}}^{i}$.

$$\boldsymbol{\sigma} = \boldsymbol{\sigma}_{\mathrm{e}}^{i} = \frac{2G}{\alpha_{\mathrm{e}}}\,\boldsymbol{\epsilon}_{\mathrm{e}}^{i} + p_0 \exp\left[\frac{\varepsilon_{\mathrm{e,vol}}^{i} - \varepsilon_{\mathrm{v0}}}{\alpha_{\mathrm{e}}\,\kappa}\right]\boldsymbol{I}. \tag{6.20}$$

The viscoelastic formulation was split in two parts separating the volumetric and the deviatoric parts

$$\begin{aligned}\boldsymbol{\sigma} = \boldsymbol{\sigma}_{\mathrm{e}}^{\mathrm{v}} = \frac{2G}{1-\alpha_{\mathrm{e}}}\,\boldsymbol{\epsilon}_{\mathrm{e}}^{\mathrm{v}}\left(1 + \Phi_{\mathrm{e,dev}}^{-1}(\dot{\boldsymbol{\epsilon}}_{\mathrm{e}}^{\mathrm{v}} : \dot{\boldsymbol{\epsilon}}_{\mathrm{e}}^{\mathrm{v}})\right) + \\ + p_0 \exp\left[\frac{\varepsilon_{\mathrm{e,vol}}^{i} - \varepsilon_{\mathrm{v0}}}{(1-\alpha_{\mathrm{e}})\,\kappa}\right]\left(1 + \Phi_{\mathrm{e,vol}}^{-1}(\dot{\varepsilon}_{\mathrm{e,vol}}^{\mathrm{v}})\right)\boldsymbol{I},\end{aligned} \tag{6.21}$$

where $\boldsymbol{\epsilon}_{\mathrm{e}}^{\mathrm{v}}$ is the deviatoric viscoelastic strain tensor, and $\dot{\varepsilon}_{\mathrm{e,vol}}^{\mathrm{v}} = \operatorname{tr}\dot{\boldsymbol{\varepsilon}}_{\mathrm{e}}^{\mathrm{v}}$ is the volumetric component of the viscoelastic strain.

Observing equations (6.20) and (6.21) the role of the *repartition coefficient* introduced in the previous section is more clearer.

The viscoelastic viscosity function slightly differs from the viscoplastic one in order to permit the simulation of both loading and unloading processes. The only differences are the introduction of the sign of the viscoelastic strain rate before the logarithm, and the use of the absolute value inside the logarithm. In eq. (6.22) the viscoelastic viscosity functions are shown.

$$\Phi_{\mathrm{e,vol}}^{-1}(\dot{\varepsilon}_{\mathrm{e}}^{\mathrm{v}}) = \Gamma_{\mathrm{e}}\,\frac{\dot{\varepsilon}_{\mathrm{e}}^{\mathrm{v}}}{|\dot{\varepsilon}_{\mathrm{e}}^{\mathrm{v}}|}\ln\left(\frac{|\dot{\varepsilon}_{\mathrm{e}}^{\mathrm{v}}|}{\dot{\varepsilon}_{\min}} + 1\right) \tag{6.22a}$$

$$\Phi_{\mathrm{e,dev}}^{-1}(\dot{\boldsymbol{\epsilon}}_{\mathrm{e}}^{\mathrm{v}} : \dot{\boldsymbol{\epsilon}}_{\mathrm{e}}^{\mathrm{v}}) = \Gamma_{\mathrm{e}}\,\frac{\dot{\boldsymbol{\epsilon}}_{\mathrm{e}}^{\mathrm{v}} : \dot{\boldsymbol{\epsilon}}_{\mathrm{e}}^{\mathrm{v}}}{|\dot{\boldsymbol{\epsilon}}_{\mathrm{e}}^{\mathrm{v}} : \dot{\boldsymbol{\epsilon}}_{\mathrm{e}}^{\mathrm{v}}|}\ln\left(\frac{|\dot{\boldsymbol{\epsilon}}_{\mathrm{e}}^{\mathrm{v}} : \dot{\boldsymbol{\epsilon}}_{\mathrm{e}}^{\mathrm{v}}|}{\dot{\varepsilon}_{\min}} + 1\right). \tag{6.22b}$$

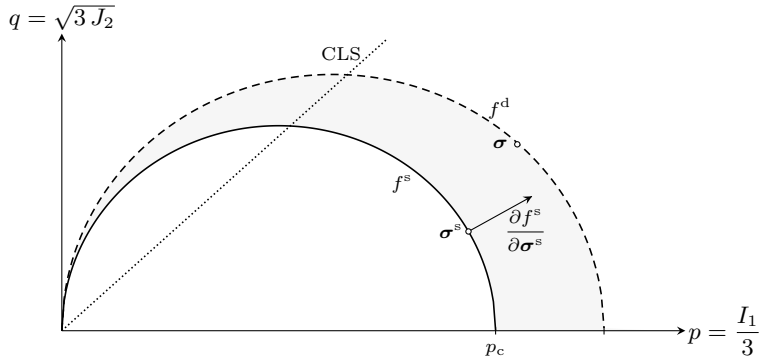

Figure 6.8: Sketch of associative flow rule for Modified Cam-Clay yield surface in the p-q plane

6.2.4 Some consideration on simulation of tertiary creep in triaxial drained creep tests

The proposed model, based on the assumption of associative flow rule, is unable to predict the tertiary creep phenomenon in triaxial drained conditions.

In order to simulate this peculiar behaviour observed experimentally by Tavenas et al. (1978) the possibility of a different formulation based on a non associative flow rule as proposed by Namikawa (2001) was explored.

The adoption of a non-associative flow rule implies the introduction of a new stress, called *static stress*, lying on the static yield surface, that allows the definition of the flow rule on the *static yield surface*. This hypothesis allows the prediction of tertiary creep in the normally consolidated range but has the drawback to be not applicable to the overconsolidated field and to overestimate, in an unacceptable manner, the volumetric strain during the test (and, as a consequence, the shear induced pore pressure when simulating the undrained creep tests). In addition, the original model should be modified from an instantaneous-viscous model to a viscous-viscous model with two different viscous properties. With an instantaneous yield surface it is impossible to simulate drained tertiary creep because the soil immediately fails when the state of stress is above the critical state line.

The measurements of the shear induced pore pressure during the undrained creep phase performed by Campanella and Vaid (1974) demonstrated that the failure envelope of creep tests is coincident with that obtained from conventional

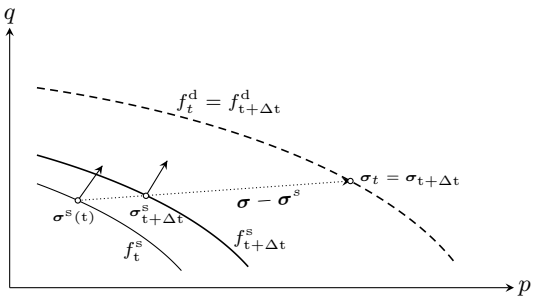

Figure 6.9: Example of the determination of the *static stress*, $\boldsymbol{\sigma}^{\mathrm{s}}$, for a drained triaxial creep test ($\boldsymbol{\sigma} = \mathrm{const}$)

constant strain rate tests. This observation is in agreement with the hypothesis of the associative flow rule and allows the accurate simulation of much experimental evidence concerning undrained tertiary creep. For this reason the model was formulated adopting an associative flow rule. As a result, the proposed model could simulate only undrained tertiary creep.

For the sake of completeness, the alternative approach of non-associative flow rule will be described. The *static stress* approach will be treated with a single viscous yield surface.

The principle of non associative flow rule is based on the definition of a *static stress* ($\boldsymbol{\sigma}^{\mathrm{s}}$) lying on the static yield surface that evolves toward the effective stress during the creep process. This concept was realized by Namikawa (2001) who, however, proposed a very complicate way to determine the *static stress*.

The modified flow rule is exposed in eq. (6.23) and sketched in Figure 6.8.

$$\dot{\boldsymbol{\varepsilon}}_{\mathrm{p}}^{\mathrm{v}} = \dot{\gamma}\,\frac{\partial f^{\mathrm{s}}}{\partial \boldsymbol{\sigma}^{\mathrm{s}}}. \tag{6.23}$$

The definition of the *static stress*, $\boldsymbol{\sigma}^{\mathrm{s}}$, is crucial in defining the model response. It was developed avoiding the introduction of new parameters or laws, using the evolution of the static yield surface as governing rule. In particular, the static stress was defined through an additional consistency condition by imposing that $\boldsymbol{\sigma}^{\mathrm{s}}$ lies on the static yield surface and that the stress rate, $\dot{\boldsymbol{\sigma}}^{\mathrm{s}}$, has the direction of $\boldsymbol{\sigma} - \boldsymbol{\sigma}^{\mathrm{s}}$.

The concept for the determination of the static stress has been summarized

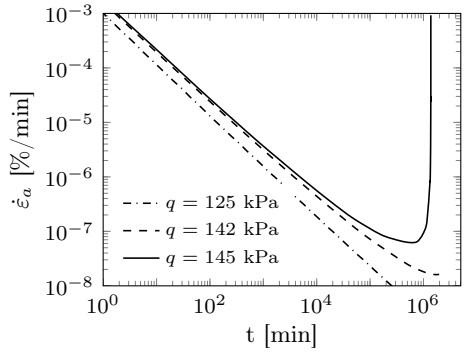

Figure 6.10: a) Simulation of tertiary creep in drained triaxial tests with the *static stress* approach ($\sigma_c = 100$ kPa, $M = 0.85$)

in the following system of equation:

$$\begin{cases} f^{\mathrm{s}}(\boldsymbol{\sigma}^{\mathrm{s}}, p_{\mathrm{c}}) = 0 \\ \dot{\boldsymbol{\sigma}}^{\mathrm{s}} = \dot{\alpha}\,(\boldsymbol{\sigma} - \boldsymbol{\sigma}^{\mathrm{s}}) \end{cases}, \tag{6.24}$$

where $0 < \dot{\alpha} \leq 1$ is a scalar multiplier. Although the *static stress* loses its meaning in the elastic range, it is useful, from a computational point of view, to assume that $\boldsymbol{\sigma} = \boldsymbol{\sigma}^{\mathrm{s}}$ when the stress state lies inside the yield surface. In this way the evolution law of eq. (6.24) directly supplies the right *static stress* as soon as the stress state enters in the viscoelastic regime.

The results of the *static stress* approach are shown in Figure 6.10. It is possible to highlight the capability of the model to reproduce tertiary creep when the creep stress level lies above the critical state line.

Figure 6.9 shows a sketch of the determination of the *static stress* for a general drained triaxial creep test. In this case the stress $\boldsymbol{\sigma}$ and the dynamic yield surface are constant with time while the static yield surface evolves as a result of strain hardening. The *static stress* moves towards $\boldsymbol{\sigma}$ and the two are coincident when the static and the dynamic yield surface coincide (i.e. when the viscoplastic volumetric strain rate vanishes). This kind of formulation also holds true for a generic stress history.

The evolution law of $\boldsymbol{\sigma}^{\mathrm{s}}$ together with the hypothesis of viscous behaviour depending from volumetric viscoplastic strain allow the simulations of the tertiary creep also in drained condition. The results for undrained creep tests

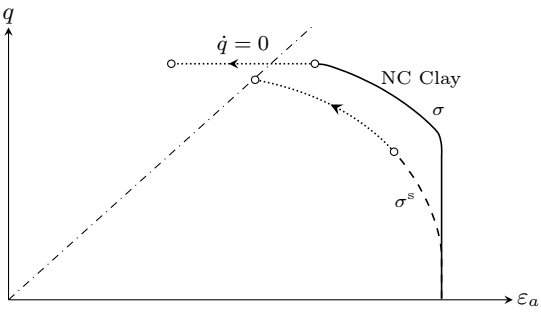

Figure 6.11: Summary of the stress paths of the simulation undrained tertiary creep for NC clay with the hypothesis of non associative flow rule

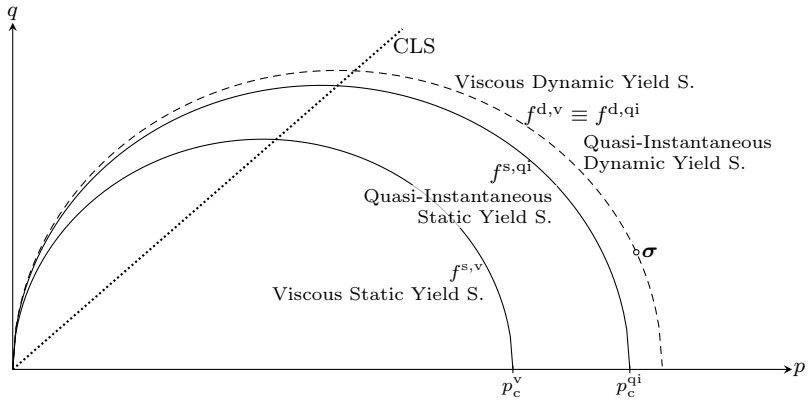

Figure 6.12: Summary of the two yield surface viscoplastic model

show a strong overestimation of the pore pressure during the creep phase that does not find confirmation in the experimental evidence. Figure 6.11 shows an example of stress path (including the evolution of the *static stress*) during a undrained creep test. The unrealistic value of pore pressure when the specimen undergoes to creep rupture can be easily appreciated.

6.3 Numerical integration of the model

From the constitutive hypotheses exposed in the previous sections, it is possible to define the main features of the proposed general stress-strain-time constitutive model.

Starting from the constitutive laws for the elastic instantaneous (eq. (6.20)) and viscoelastic (eq. (6.21)) parts it is possible to write the general system of equation for the resolution of the viscoelastic-viscoplastic mechanisms. In eq. (6.25) the system of four equations made of the viscoelastic residual (divided into volumetric and deviatoric parts), and of the two dynamic yield surfaces is reported. Eq. (6.26) shows the hardening rules for the static yield surfaces.

$$\begin{cases} r^{\mathrm{vol}}(\varepsilon^{i}_{\mathrm{e,vol}}, \varepsilon^{\mathrm{v}}_{\mathrm{e,vol}}, \dot{\varepsilon}^{\mathrm{v}}_{\mathrm{e,vol}}) = p_0 \exp\left[\dfrac{\varepsilon^{i}_{\mathrm{e,vol}} - \varepsilon_{\mathrm{v0}}}{\alpha_{\mathrm{e}}\,\kappa}\right] + \\ \qquad\qquad -p_0 \exp\left[\dfrac{\varepsilon^{i}_{\mathrm{e,vol}} - \varepsilon_{\mathrm{v0}}}{(1-\alpha_{\mathrm{e}})\,\kappa}\right]\left(1 + \Phi^{-1}_{\mathrm{e,vol}}(\dot{\varepsilon}^{\mathrm{v}}_{\mathrm{e,vol}})\right) = 0 \\ \boldsymbol{r}^{\mathrm{dev}}(\boldsymbol{\epsilon}^{i}_{\mathrm{e}}, \boldsymbol{\epsilon}^{\mathrm{v}}_{\mathrm{e}}, \dot{\boldsymbol{\epsilon}}^{\mathrm{v}}_{\mathrm{e}}) = \dfrac{2G}{\alpha_{\mathrm{e}}}\,\boldsymbol{\epsilon}^{i}_{\mathrm{e}} - \dfrac{2G}{1-\alpha_{\mathrm{e}}}\,\boldsymbol{\epsilon}^{\mathrm{v}}_{\mathrm{e}}\left(1 + \Phi^{-1}_{\mathrm{e,dev}}(\dot{\boldsymbol{\epsilon}}^{\mathrm{v}}_{\mathrm{e}} : \dot{\boldsymbol{\epsilon}}^{\mathrm{v}}_{\mathrm{e}})\right) = \mathbf{0} \\ f^{\mathrm{d,qi}}(\boldsymbol{\sigma}, p^{\mathrm{qi}}_{\mathrm{c}}, \dot{\varepsilon}^{\mathrm{qi}}_{\mathrm{p,vol}}) = \dfrac{3\,J_2}{(M\,k_\theta)^2} + \left(\dfrac{I_1}{3}\right)^2 + \dfrac{I_1}{3}\,p^{\mathrm{qi}}_{\mathrm{c}}\,\left[1 + \Phi^{-1}(\dot{\varepsilon}^{\mathrm{qi}}_{\mathrm{p,vol}})\right] = 0 \\ f^{\mathrm{d,v}}(\boldsymbol{\sigma}, p^{\mathrm{v}}_{\mathrm{c}}, \dot{\varepsilon}^{\mathrm{v}}_{\mathrm{p,vol}}) = \dfrac{3\,J_2}{(M\,k_\theta)^2} + \left(\dfrac{I_1}{3}\right)^2 + \dfrac{I_1}{3}\,p^{\mathrm{v}}_{\mathrm{c}}\,\left[1 + \Phi^{-1}(\dot{\varepsilon}^{\mathrm{v}}_{\mathrm{p,vol}})\right] = 0\,, \end{cases} \tag{6.25}$$

$$p^{\mathrm{qi}}_{\mathrm{c}} = p_0\,\exp\left(\frac{\varepsilon^{\mathrm{qi}}_{\mathrm{p,vol}} - \varepsilon_{\mathrm{v0}}}{\alpha_{\mathrm{p}}\,(\lambda - \kappa)}\right) \tag{6.26a}$$

$$p^{\mathrm{v}}_{\mathrm{c}} = p_0\,\exp\left(\frac{\varepsilon^{\mathrm{v}}_{\mathrm{p,vol}} - \varepsilon_{\mathrm{v0}}}{(1-\alpha_{\mathrm{p}})\,(\lambda - \kappa)}\right) \tag{6.26b}$$

Fig. 6.12 shows a sketch of the yield surfaces in a generic instant of viscoplastic loading. The generic stress state satisfies the two sets of Kuhn-Tucker conditions of the quasi-instantaneous (eq. (6.8)) and the viscous surfaces (eq. (6.11)).

The numerical implementation has been performed through a fully implicit back-Euler algorithm. Thus, once a strain increment $\Delta\boldsymbol{\varepsilon}$ is assigned (from the

FEM code) in a given time step increment Δt, the strain increment is initially assumed instantaneous elastic. As a result a non linear system of equations must be initially solved to evaluate the two elastic increments $\Delta\boldsymbol{\varepsilon}^{\mathrm{i}}_{\mathrm{e}}$ and $\Delta\boldsymbol{\varepsilon}^{\mathrm{v}}_{\mathrm{e}}$, namely from eqns. (6.20) and (6.21). The trial values of the viscoelastic problem are defined as follows:

$$\boldsymbol{\varepsilon}^{\mathrm{i,trial}}_{\mathrm{e,n+1}} = \boldsymbol{\varepsilon}^{\mathrm{i}}_{\mathrm{e,n}} + \Delta\boldsymbol{\varepsilon}, \quad \boldsymbol{\varepsilon}^{\mathrm{v,trial}}_{\mathrm{e,n+1}} = \boldsymbol{\varepsilon}^{\mathrm{v}}_{\mathrm{e,n}}, \tag{6.27}$$

where $\boldsymbol{\varepsilon}^{\mathrm{i}}_{\mathrm{e,n}}$ and $\boldsymbol{\varepsilon}^{\mathrm{v}}_{\mathrm{e,n}}$ are the instantaneous elastic and viscoelastic strains evaluated at the previous time step.

Since the viscoelastic formulation splits the volumetric and the deviatoric components the system for the determination of the viscoelastic state becomes

$$\begin{cases} r^{\mathrm{vol}}((\varepsilon^{\mathrm{i}}_{\mathrm{e,vol}})^{\mathrm{trial}}_{\mathrm{n+1}}, (\varepsilon^{\mathrm{v}}_{\mathrm{e,vol}})^{\mathrm{trial}}_{\mathrm{n+1}}, (\dot{\varepsilon}^{\mathrm{v}}_{\mathrm{e,vol}})^{\mathrm{trial}}_{\mathrm{n+1}}) = p_0 \exp\left[\dfrac{(\varepsilon^{\mathrm{i}}_{\mathrm{e,vol}})^{\mathrm{trial}}_{\mathrm{n+1}} - \varepsilon_{\mathrm{v0}}}{\alpha_{\mathrm{e}}\,\kappa}\right] \\ \qquad\qquad -p_0 \exp\left[\dfrac{(\varepsilon^{\mathrm{i}}_{\mathrm{e,vol}}))^{\mathrm{trial}}_{\mathrm{n+1}} - \varepsilon_{\mathrm{v0}}}{(1-\alpha_{\mathrm{e}})\,\kappa}\right]\left(1 + \Phi^{-1}_{\mathrm{e,vol}}((\dot{\varepsilon}^{\mathrm{v}}_{\mathrm{e,vol}}))^{\mathrm{trial}}_{\mathrm{n+1}})\right) = 0 \\ \boldsymbol{r}^{\mathrm{dev}}(\boldsymbol{\epsilon}^{\mathrm{i,trial}}_{\mathrm{e,n+1}}, \boldsymbol{\epsilon}^{\mathrm{v,trial}}_{\mathrm{e,n+1}}, \dot{\boldsymbol{\epsilon}}^{\mathrm{v,trial}}_{\mathrm{e,n+1}}) = \dfrac{2G}{\alpha_{\mathrm{e}}}\,\boldsymbol{\epsilon}^{\mathrm{i,trial}}_{\mathrm{e,n+1}} \\ \qquad\qquad -\dfrac{2G}{1-\alpha_{\mathrm{e}}}\,\boldsymbol{\epsilon}^{\mathrm{v,trial}}_{\mathrm{e,n+1}}\left(1 + \Phi^{-1}_{\mathrm{e,dev}}(\dot{\boldsymbol{\epsilon}}^{\mathrm{v,trial}}_{\mathrm{e,n+1}} : \dot{\boldsymbol{\epsilon}}^{\mathrm{v,trial}}_{\mathrm{e,n+1}})\right) = \mathbf{0} \end{cases} \tag{6.28}$$

The non-linear problem was solved with a conventional Newton-Rapson scheme. The *elastic* stress that is computed using eqn. (6.20), constitutes the so-called *elastic predictor*. If both yield conditions are not violated, then the computed *elastic* stress and the viscoelastic strains are valid, and the next time step is considered.

$$\begin{gathered} f^{\mathrm{s,qi}}(\boldsymbol{\sigma}^{\mathrm{trial}}_{\mathrm{n+1}}, p^{\mathrm{qi}}_{\mathrm{c,n}}) \le 0 \qquad f^{\mathrm{s,v}}(\boldsymbol{\sigma}^{\mathrm{trial}}_{\mathrm{n+1}}, p^{\mathrm{v}}_{\mathrm{c,n}}) \le 0, \\ \boldsymbol{\varepsilon}^{\mathrm{i}}_{\mathrm{e,n+1}} = \boldsymbol{\varepsilon}^{\mathrm{i,trial}}_{\mathrm{e,n+1}}, \quad \boldsymbol{\varepsilon}^{\mathrm{v}}_{\mathrm{e,n+1}} = \boldsymbol{\varepsilon}^{\mathrm{v,trial}}_{\mathrm{e,n+1}}, \quad \boldsymbol{\sigma}_{\mathrm{n+1}} = \boldsymbol{\sigma}^{\mathrm{trial}}_{\mathrm{n+1}}. \end{gathered} \tag{6.29}$$

Alternatively, the *elastic* stress may violate one or both the yield stress conditions. In the former case we must solve a non-linear system that includes eqns. (6.28), plus the consistency equation for the dynamic viscous yield surface, and the strain decomposition rule (eq. (6.30)). The trial initial value of the viscoplastic strain is assumed equal to the viscoplastic strain evaluated at the

previous time step $\boldsymbol{\varepsilon}^{\mathrm{v}}_{\mathrm{p,n+1}} = \boldsymbol{\varepsilon}^{\mathrm{v}}_{\mathrm{p,n}}$.

$$f^{\mathrm{d,v}}(\boldsymbol{\sigma}_{\mathrm{n+1}}, p^{\mathrm{v}}_{\mathrm{c,n+1}}, (\dot{\varepsilon}^{\mathrm{v}}_{\mathrm{p,vol}})_{\mathrm{n+1}}) = \frac{3\,J_2}{(M\,k_\theta)^2} + \left(\frac{I_1}{3}\right)^2 + \frac{I_1}{3}\,p^{\mathrm{v}}_{\mathrm{c,n+1}}\,\left[1 + \Phi^{-1}((\dot{\varepsilon}^{\mathrm{v}}_{\mathrm{p,vol}})_{\mathrm{n+1}})\right] = 0, \tag{6.30}$$

$$\Delta\boldsymbol{\varepsilon}_{\mathrm{n+1}} = \Delta\boldsymbol{\varepsilon}^{\mathrm{i}}_{\mathrm{e,n+1}} + \Delta\boldsymbol{\varepsilon}^{\mathrm{v}}_{\mathrm{e,n+1}} + \Delta\boldsymbol{\varepsilon}^{\mathrm{v}}_{\mathrm{p,n+1}},$$

where three unknowns are involved, namely $\Delta\varepsilon^{\mathrm{i}}_{\mathrm{e}}$, $\Delta\varepsilon^{\mathrm{v}}_{\mathrm{e}}$ and $\Delta\varepsilon^{\mathrm{v}}_{\mathrm{p}}$.

In contrast, if both yield conditions are violated, we must solve a non-linear system with a further equation, namely eqns. (6.28 and 6.30a) plus the following two equation (deduced from the consistency of the dynamic quasi-instantaneous surface (**??**), and from the strain decomposition)

$$f^{\mathrm{d,qi}}(\boldsymbol{\sigma}_{\mathrm{n+1}}, p^{\mathrm{qi}}_{\mathrm{c,n+1}}, (\dot{\varepsilon}^{\mathrm{qi}}_{\mathrm{p,vol}})_{\mathrm{n+1}}) = \frac{3\,J_2}{(M\,k_\theta)^2} + \left(\frac{I_1}{3}\right)^2 + \frac{I_1}{3}\,p^{\mathrm{qi}}_{\mathrm{c,n+1}}\,\left[1 + \Phi^{-1}((\dot{\varepsilon}^{\mathrm{qi}}_{\mathrm{p,vol}})_{\mathrm{n+1}})\right] = 0, \tag{6.31}$$

$$\Delta\boldsymbol{\varepsilon}_{\mathrm{n+1}} = \Delta\boldsymbol{\varepsilon}^{\mathrm{i}}_{\mathrm{e,n+1}} + \Delta\boldsymbol{\varepsilon}^{\mathrm{v}}_{\mathrm{e,n+1}} + \Delta\boldsymbol{\varepsilon}^{\mathrm{qi}}_{\mathrm{p,n+1}} + \Delta\boldsymbol{\varepsilon}^{\mathrm{v}}_{\mathrm{p,n+1}},$$

where four unknowns are involved, namely $\Delta\varepsilon^{\mathrm{i}}_{\mathrm{e}}$, $\Delta\varepsilon^{\mathrm{v}}_{\mathrm{e}}$, $\Delta\varepsilon^{\mathrm{qi}}_{\mathrm{p}}$ and $\Delta\varepsilon^{\mathrm{v}}_{\mathrm{p}}$. The trial initial value of the quasi-instantaneous plastic strain is assumed equal to the quasi-instantaneous plastic strain evaluated at the previous time step $\boldsymbol{\varepsilon}^{\mathrm{qi}}_{\mathrm{p,n+1}} = \boldsymbol{\varepsilon}^{\mathrm{qi}}_{\mathrm{p,n}}$.

In all cases the non-linear problems were solved with a conventional Newton-Rapson scheme.

The integration algorithm is summarized in Box 2, in which is possible to recognize the elastic predictor (step 1) and the three cases of: viscoelastic increment (step 3.i), plastic increment that violates only the viscous yield condition (step 3.ii), and plastic increment that violates both the yield conditions (step 3.iii).

The strain decomposition and the definition of the discretized strain rate (point 0 in Box 2) hold valid for all the subsequent steps. In order to evaluate the initial state through the classical elastic predictor procedure, it is necessary to define the *trial viscoelastic state* by solving the viscoelastic problem (eq. (Box 2.1)). Once the prescribed $\Delta\boldsymbol{\varepsilon}$ has been divided between the instantaneous and viscous elastic mechanisms, it is possible to check the plastic admissibility (point 3). Since two yield surfaces have been defined, we have three possible cases:

Box 2: Fully implicit algorithm for numerical integration of the multiaxial model

0. Strain decomposition of the discretized problem:

$$\boldsymbol{\varepsilon}^{\mathrm{i}}_{\mathrm{e,n+1}} + \boldsymbol{\varepsilon}^{\mathrm{v}}_{\mathrm{e,n+1}} + \boldsymbol{\varepsilon}^{\mathrm{qi}}_{\mathrm{p,n+1}} + \boldsymbol{\varepsilon}^{\mathrm{v}}_{\mathrm{p,n+1}} = \boldsymbol{\varepsilon}_n + \Delta\boldsymbol{\varepsilon}_{\mathrm{n+1}}$$

$$\dot{\boldsymbol{\varepsilon}}^{\mathrm{v}}_{\mathrm{e,n+1}} = \frac{\boldsymbol{\varepsilon}^{\mathrm{v}}_{\mathrm{e,n+1}} - \boldsymbol{\varepsilon}^{\mathrm{v}}_{\mathrm{e,n}}}{\Delta t_{\mathrm{n+1}}},\ \dot{\boldsymbol{\varepsilon}}^{\mathrm{v}}_{\mathrm{p,n+1}} = \frac{\boldsymbol{\varepsilon}^{\mathrm{v}}_{\mathrm{p,n+1}} - \boldsymbol{\varepsilon}^{\mathrm{v}}_{\mathrm{p,n}}}{\Delta t_{\mathrm{n+1}}},\ \dot{\boldsymbol{\varepsilon}}^{\mathrm{qi}}_{\mathrm{p,n+1}} = \frac{\boldsymbol{\varepsilon}^{\mathrm{qi}}_{\mathrm{p,n+1}} - \boldsymbol{\varepsilon}^{\mathrm{qi}}_{\mathrm{p,n}}}{\Delta t_{\mathrm{n+1}}}$$

1. Initialize:

$$\boldsymbol{\varepsilon}^{\mathrm{i,trial}}_{\mathrm{e,n+1}} = \boldsymbol{\varepsilon}^{\mathrm{i}}_{\mathrm{e,n}} + \Delta\boldsymbol{\varepsilon},\ \boldsymbol{\varepsilon}^{\mathrm{v,trial}}_{\mathrm{e,n+1}} = \boldsymbol{\varepsilon}^{\mathrm{v}}_{\mathrm{e,n}},\ \boldsymbol{\varepsilon}^{\mathrm{qi}}_{\mathrm{p,n+1}} = \boldsymbol{\varepsilon}^{\mathrm{qi}}_{\mathrm{p,n}},\ \boldsymbol{\varepsilon}^{\mathrm{v}}_{\mathrm{p,n+1}} = \boldsymbol{\varepsilon}^{\mathrm{v}}_{\mathrm{p,n}}$$

2. Elastic predictor: solve the viscoelastic problem and evaluate the *trial viscoelastic state*

from $\left\{\boldsymbol{\sigma}^{\mathrm{i}}_{e}(\boldsymbol{\varepsilon}^{\mathrm{i,trial}}_{\mathrm{e,n+1}}) - \boldsymbol{\sigma}^{\mathrm{v}}_{e}(\boldsymbol{\varepsilon}^{\mathrm{v,trial}}_{\mathrm{e,n+1}}, \dot{\boldsymbol{\varepsilon}}^{\mathrm{v,trial}}_{\mathrm{e,n+1}})\right\} = \{\mathbf{0}\}$ (Box 2.1)

obtain $\boldsymbol{\varepsilon}^{\mathrm{i,trial}}_{\mathrm{e,n+1}}\ ,\ \boldsymbol{\varepsilon}^{\mathrm{v,trial}}_{\mathrm{e,n+1}}$

3. Check the plastic admissibility (with $\boldsymbol{\sigma}^{\mathrm{trial}}_{\mathrm{n+1}} = \boldsymbol{\sigma}^{\mathrm{i}}_{e}(\boldsymbol{\varepsilon}^{\mathrm{i,trial}}_{\mathrm{e,n+1}})$)

i IF $f^{\mathrm{s,qi}}(\boldsymbol{\sigma}^{\mathrm{trial}}_{\mathrm{n+1}}, p^{\mathrm{qi}}_{\mathrm{c,n}}) \le 0$ AND $f^{\mathrm{s,v}}(\boldsymbol{\sigma}^{\mathrm{trial}}_{\mathrm{n+1}}, p^{\mathrm{v}}_{\mathrm{c,n}}) \le 0$

THEN $\boldsymbol{\varepsilon}^{\mathrm{i}}_{\mathrm{e,n+1}} = \boldsymbol{\varepsilon}^{\mathrm{i,trial}}_{\mathrm{e,n+1}}\ ,\quad \boldsymbol{\varepsilon}^{\mathrm{v}}_{\mathrm{e,n+1}} = \boldsymbol{\varepsilon}^{\mathrm{v,trial}}_{\mathrm{e,n+1}}\ ,\quad \boldsymbol{\sigma}_{\mathrm{n+1}} = \boldsymbol{\sigma}^{\mathrm{trial}}_{\mathrm{n+1}}$

ii IF $f^{\mathrm{s,qi}}(\boldsymbol{\sigma}^{\mathrm{trial}}_{\mathrm{n+1}}, p^{\mathrm{qi}}_{\mathrm{c,n}}) \le 0$ AND $f^{\mathrm{s,v}}(\boldsymbol{\sigma}^{\mathrm{trial}}_{\mathrm{n+1}}, p^{\mathrm{v}}_{\mathrm{c,n}}) > 0$

THEN Return mapping:

from $\begin{Bmatrix} \boldsymbol{\sigma}^{\mathrm{i}}_{e}(\boldsymbol{\varepsilon}^{\mathrm{i}}_{\mathrm{e,n+1}}) - \boldsymbol{\sigma}^{\mathrm{v}}_{e}(\boldsymbol{\varepsilon}^{\mathrm{v}}_{\mathrm{e,n+1}}, \dot{\boldsymbol{\varepsilon}}^{\mathrm{v}}_{\mathrm{e,n+1}}) \\ f^{\mathrm{d,v}}(\boldsymbol{\sigma}^{\mathrm{i}}_{\mathrm{e,n+1}}, p^{\mathrm{v}}_{c,n+1}, \dot{\boldsymbol{\varepsilon}}^{\mathrm{v}}_{\mathrm{p,n+1}}) \end{Bmatrix} = \begin{Bmatrix} \mathbf{0} \\ 0 \end{Bmatrix}$ (Box 2.2)

obtain $\boldsymbol{\varepsilon}^{\mathrm{i}}_{\mathrm{e,n+1}}\ ,\ \boldsymbol{\varepsilon}^{\mathrm{v}}_{\mathrm{e,n+1}}\ ,\ \boldsymbol{\varepsilon}^{\mathrm{v}}_{\mathrm{p,n+1}}\ ,\ \boldsymbol{\sigma}_{\mathrm{n+1}}$

iii IF $f^{\mathrm{s,qi}}(\boldsymbol{\sigma}^{\mathrm{trial}}_{\mathrm{n+1}}, p^{\mathrm{qi}}_{\mathrm{c,n}}) > 0$ AND $f^{\mathrm{s,v}}(\boldsymbol{\sigma}^{\mathrm{trial}}_{\mathrm{n+1}}, p^{\mathrm{v}}_{\mathrm{c,n}}) > 0$

THEN Return mapping:

from $\begin{Bmatrix} \boldsymbol{\sigma}^{\mathrm{i}}_{e}(\boldsymbol{\varepsilon}^{\mathrm{i}}_{\mathrm{e,n+1}}) - \boldsymbol{\sigma}^{\mathrm{v}}_{e}(\boldsymbol{\varepsilon}^{\mathrm{v}}_{\mathrm{e,n+1}}, , \dot{\boldsymbol{\varepsilon}}^{\mathrm{v}}_{\mathrm{e,n+1}}) \\ f^{\mathrm{d,qi}}(\boldsymbol{\sigma}^{\mathrm{i}}_{\mathrm{e,n+1}}, p^{\mathrm{qi}}_{c,n+1}, \dot{\boldsymbol{\varepsilon}}^{\mathrm{qi}}_{\mathrm{p,n+1}}) \\ f^{\mathrm{d,v}}(\boldsymbol{\sigma}^{\mathrm{i}}_{\mathrm{e,n+1}}, p^{\mathrm{v}}_{c,n+1}, \dot{\boldsymbol{\varepsilon}}^{\mathrm{v}}_{\mathrm{p,n+1}}) \end{Bmatrix} = \begin{Bmatrix} \mathbf{0} \\ 0 \\ 0 \end{Bmatrix}$ (Box 2.3)

obtain $\boldsymbol{\varepsilon}^{\mathrm{i}}_{\mathrm{e,n+1}}\ ,\ \boldsymbol{\varepsilon}^{\mathrm{v}}_{\mathrm{e,n+1}}\ ,\ \boldsymbol{\varepsilon}^{\mathrm{qi}}_{\mathrm{p,n+1}}\ ,\ \boldsymbol{\varepsilon}^{\mathrm{v}}_{\mathrm{p,n+1}}\ ,\ \boldsymbol{\sigma}_{\mathrm{n+1}}$

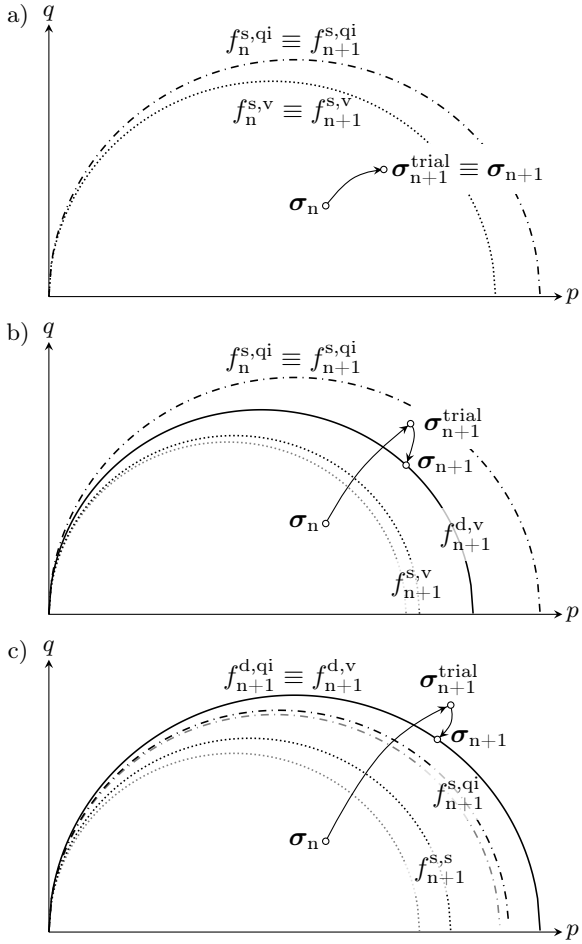

Figure 6.13: Sketch of the possible *trial viscoelastic state* for the discretized problem: a) viscoelastic load; b) state of stress between the two yield surfaces; c) state of stress outside the two yield surfaces.

i the state of stress lies inside the two static yield surfaces: the problem is purely viscoelastic and the trial elastic strains coincide with the final values (Fig. 6.13a);

ii the state of stress lies between the static viscous and the quasi-instantaneous yield surfaces: the problem is viscoplastic, but only the viscous yield surface is active (Fig. 6.13b). In the solving system the only consistency condition to ensure is that of the viscous dynamic yield surface (eq. (Box 2.2));

iii the state of stress lies outside the two static yield surfaces: the problem is viscoplastic, and the two yield surfaces (quasi-instantaneous and viscous) are active (Fig. 6.13c). The solving system must satisfy the equilibrium of the viscoelastic state and the consistency of the dynamic viscous yield surface and of the dynamic quasi-instantaneous yield surface (eq. (Box 2.3));

Figure 6.13 shows the three possible *trial viscoelastic states*, and the corresponding final consistent state.

In order to apply the model to a general boundary value problem taking into account the hydro-mechanical two phase coupled phenomena, the proposed model has been numerically implemented in the commercial finite element code ABAQUS Standard (Hibbitt et al. 2009) through the Fortran User Subroutine UMAT. Up to now only an axisymmetric version of the model has been implemented whereas the multiaxial version is in finalization.

6.3.1 Tangent operator

The implementation of the model within an implicit finite element environment needs the definition of the tangent modulus (de Souza Neto et al. 2008). Given all the variables at t_n, and the prescribed increments of time Δt, and strain $\Delta\boldsymbol{\varepsilon}$, the task is to define the exact tangent operator

$$\boldsymbol{D} \equiv \frac{\delta\boldsymbol{\sigma}_{\mathrm{n+1}}}{\delta\boldsymbol{\varepsilon}_{\mathrm{n+1}}} = \frac{\delta\boldsymbol{\sigma}_{\mathrm{n+1}}}{\delta(\Delta\boldsymbol{\varepsilon})}. \tag{6.32}$$

The definition of $\boldsymbol{D}$ can be done by linearising the system of time-discrete equation of Box 2. In this section, the derivation of the tangent operator will be briefly exposed. In order to avoid the redundancy of the formulation the notation has been contracted by introducing some further scalar quantities.

The elastic law for the general multiaxial viscoelastic-viscoplastic problem of equation (6.20) can be rewritten in the following incremental form:

$$\delta\boldsymbol{\sigma} = \mathbb{E}^{\mathrm{i}} : \delta\boldsymbol{\varepsilon}_{\mathrm{e}}^{\mathrm{i}} = \mathbb{E}^{\mathrm{i}} : [\delta\boldsymbol{\varepsilon} - \delta\boldsymbol{\varepsilon}_{\mathrm{e}}^{\mathrm{v}} - (\delta\lambda^{\mathrm{qi}} + \delta\lambda^{\mathrm{v}})\,\boldsymbol{Q}], \tag{6.33}$$

where $\delta\boldsymbol{\varepsilon}_e^i$ is the instantaneous elastic part of the strain increment, $\delta\boldsymbol{\varepsilon}_e^v$ is the instantaneous elastic part of $\delta\boldsymbol{\varepsilon}$, $\delta\lambda^{\mathrm{qi}}$ is the plastic multiplier of the quasi-instantaneous plastic mechanism, and $\delta\lambda^{\mathrm{v}}$ is the plastic multiplier of the viscoplastic mechanism. The fourth-order tensor $\mathbb{E}^{\mathrm{i}}$ is the elastic stiffness tensor associated to the instantaneous mechanism, and the second order tensor $\boldsymbol{Q}$ represents, with the hypothesis of associated flow rule, the direction of the plastic flow

$$\boldsymbol{Q} = \frac{\partial f^{\mathrm{d,qi}}}{\partial \boldsymbol{\sigma}} = \frac{\partial f^{\mathrm{d,v}}}{\partial \boldsymbol{\sigma}}. \tag{6.34}$$

The stress increment, expressed in terms of the viscoelastic mechanism, is

$$\delta\boldsymbol{\sigma} = \mathbb{E}^{\mathrm{v}} : \delta\boldsymbol{\varepsilon}_{\mathrm{e}}^{\mathrm{v}} \tag{6.35}$$

in which the fourth-order tensor $\mathbb{E}^{\mathrm{v}}$ is the elastic stiffness tensor associated to the viscous mechanism.

The two elastic stiffness tensors are defined starting from the material parameters κ, G, and of the repartition coefficient α_e, that governs the split of the deformability between the instantaneous and the viscous components of elastic strain.

The system of equations governing the behaviour of the model has been exposed in eq. (6.25), and can be written in the contracted form by condensing the first two sets of equations (deviatoric and volumetric viscoelastic residuals) in one unique total residual

$$\begin{cases} \boldsymbol{r}(\boldsymbol{\varepsilon}_{\mathrm{e}}^{\mathrm{i}}, \boldsymbol{\varepsilon}_{\mathrm{e}}^{\mathrm{v}}, \dot{\boldsymbol{\varepsilon}}_{\mathrm{e}}^{\mathrm{v}}) = \boldsymbol{\sigma}_{\mathrm{e}}^{\mathrm{i}}(\boldsymbol{\varepsilon}_{\mathrm{e}}^{\mathrm{i}}) - \boldsymbol{\sigma}_{\mathrm{e}}^{\mathrm{v}}(\boldsymbol{\varepsilon}_{\mathrm{e}}^{\mathrm{v}}, \dot{\boldsymbol{\varepsilon}}_{\mathrm{e}}^{\mathrm{v}}) = \mathbf{0} \\ f^{\mathrm{d,qi}}(\boldsymbol{\sigma}, p_{\mathrm{c}}^{\mathrm{qi}}, \dot{\varepsilon}_{\mathrm{p,vol}}^{\mathrm{qi}}) = \dfrac{3\,J_2}{(M\,k_\theta)^2} + \left(\dfrac{I_1}{3}\right)^2 + \dfrac{I_1}{3}\,p_{\mathrm{c}}^{\mathrm{qi}}\,\left[1 + \Phi^{-1}(\dot{\varepsilon}_{\mathrm{p,vol}}^{\mathrm{qi}})\right] = 0 \\ f^{\mathrm{d,v}}(\boldsymbol{\sigma}, p_{\mathrm{c}}^{\mathrm{v}}, \dot{\varepsilon}_{\mathrm{p,vol}}^{\mathrm{v}}) = \dfrac{3\,J_2}{(M\,k_\theta)^2} + \left(\dfrac{I_1}{3}\right)^2 + \dfrac{I_1}{3}\,p_{\mathrm{c}}^{\mathrm{v}}\,\left[1 + \Phi^{-1}(\dot{\varepsilon}_{\mathrm{p,vol}}^{\mathrm{v}})\right] = 0\,. \end{cases} \tag{6.36}$$

The increment of the residuals of the discretized problem results in

$$\delta r(\boldsymbol{\varepsilon}_{\mathrm{e}}^{\mathrm{i}}, \boldsymbol{\varepsilon}_{\mathrm{e}}^{\mathrm{v}}, \dot{\boldsymbol{\varepsilon}}_{\mathrm{e}}^{\mathrm{v}}) = \mathbb{E}^{\mathrm{i}} : \delta\boldsymbol{\varepsilon}_{\mathrm{e}}^{\mathrm{i}} + \mathbb{E}^{\mathrm{v}} : \delta\boldsymbol{\varepsilon}_{\mathrm{e}}^{\mathrm{v}} + \frac{\partial r}{\partial \dot{\boldsymbol{\varepsilon}}_{\mathrm{e}}^{\mathrm{v}}} \frac{1}{\delta t} : \delta\boldsymbol{\varepsilon}_{\mathrm{e}}^{\mathrm{v}} = 0 \tag{6.37}$$

$$\delta f^{\mathrm{d,qi}}(\boldsymbol{\sigma}, p_{\mathrm{c}}^{\mathrm{qi}}, \dot{\varepsilon}_{\mathrm{p,vol}}^{\mathrm{qi}}) = \frac{\partial f^{\mathrm{d,qi}}}{\partial \boldsymbol{\sigma}} : \delta\boldsymbol{\sigma} + \frac{\partial f^{\mathrm{d,qi}}}{\partial p_{\mathrm{c}}^{\mathrm{qi}}} \frac{\partial p_{\mathrm{c}}^{\mathrm{qi}}}{\partial \varepsilon_{\mathrm{p,vol}}^{\mathrm{qi}}} \operatorname{tr}\boldsymbol{Q}\, \delta\lambda^{\mathrm{qi}} + \frac{\partial f^{\mathrm{d,qi}}}{\partial \dot{\varepsilon}_{\mathrm{p,vol}}^{\mathrm{qi}}} \frac{1}{\delta t} \operatorname{tr}\boldsymbol{Q}\, \delta\lambda^{\mathrm{qi}} = 0 \tag{6.38a}$$

$$\delta f^{\mathrm{d,v}}(\boldsymbol{\sigma}, p_{\mathrm{c}}^{\mathrm{v}}, \dot{\varepsilon}_{\mathrm{p,vol}}^{\mathrm{v}}) = \frac{\partial f^{\mathrm{d,v}}}{\partial \boldsymbol{\sigma}} : \delta\boldsymbol{\sigma} + \frac{\partial f^{\mathrm{d}}}{\partial p_{\mathrm{c}}^{\mathrm{v}}} \frac{\partial p_{\mathrm{c}}^{\mathrm{v}}}{\partial \varepsilon_{\mathrm{p,vol}}^{\mathrm{v}}} \operatorname{tr}\boldsymbol{Q}\, \delta\lambda^{\mathrm{v}} + \frac{\partial f^{\mathrm{d,v}}}{\partial \dot{\varepsilon}_{\mathrm{p,vol}}^{\mathrm{v}}} \frac{1}{\delta t} \operatorname{tr}\boldsymbol{Q}\, \delta\lambda^{\mathrm{v}} = 0 \tag{6.38b}$$

Starting from equations (6.37) and (6.33) it is possible to obtain $\delta\boldsymbol{\varepsilon}_{\mathrm{e}}^{\mathrm{v}}$:

$$\delta\boldsymbol{\varepsilon}_{\mathrm{e}}^{\mathrm{v}} = \left(\mathbb{E}^{\mathrm{i}} - \mathbb{E}^{\mathrm{v}} - \frac{\partial r}{\partial \dot{\boldsymbol{\varepsilon}}_{\mathrm{e}}^{\mathrm{v}}} \frac{1}{\delta t}\right)^{-1} \mathbb{E}^{\mathrm{i}} : (\delta\boldsymbol{\varepsilon} - (\delta\lambda^{\mathrm{qi}} + \delta\lambda^{\mathrm{v}})\, \boldsymbol{Q}) \tag{6.39}$$

$$\begin{aligned}
\delta\boldsymbol{\sigma} &= \mathbb{E}^{\mathrm{i}} : (\delta\boldsymbol{\varepsilon} - (\delta\lambda^{\mathrm{i}} + \delta\lambda^{\mathrm{v}})\, \boldsymbol{Q}) \\
&\quad - \mathbb{E}^{\mathrm{i}} : \left[\left(\mathbb{E}^{\mathrm{i}} - \mathbb{E}^{\mathrm{v}} - \frac{\partial r}{\partial \dot{\boldsymbol{\varepsilon}}_{\mathrm{e}}^{\mathrm{v}}} \frac{1}{\delta t}\right)^{-1} \mathbb{E}^{\mathrm{i}}\right] : (\delta\boldsymbol{\varepsilon} - (\delta\lambda^{\mathrm{qi}} + \delta\lambda^{\mathrm{v}})\, \boldsymbol{Q}) \\
&= \mathbb{E}^{\mathrm{i}} \left[\mathbb{I} - \mathbb{I} : \left(\mathbb{E}^{\mathrm{i}} - \mathbb{E}^{\mathrm{v}} - \frac{\partial r}{\partial \dot{\boldsymbol{\varepsilon}}_{\mathrm{e}}^{\mathrm{v}}} \frac{1}{\delta t}\right)^{-1} \mathbb{E}^{\mathrm{i}}\right] : (\delta\boldsymbol{\varepsilon} - (\delta\lambda^{\mathrm{i}} + \delta\lambda^{\mathrm{v}})\, \boldsymbol{Q}) \\
&= \mathbb{E}^{\mathrm{ve}} : (\delta\boldsymbol{\varepsilon} - (\delta\lambda^{\mathrm{qi}} + \delta\lambda^{\mathrm{v}})\, \boldsymbol{Q}),
\end{aligned} \tag{6.40}$$

where $\mathbb{E}^{\mathrm{ve}}$ is the viscoelastic matrix defined as follows

$$\mathbb{E}^{\mathrm{ve}} = \mathbb{E}^{\mathrm{i}} \left[\mathbb{I} - \mathbb{I} : \left(\mathbb{E}^{\mathrm{i}} - \mathbb{E}^{\mathrm{v}} - \frac{\partial r}{\partial \dot{\boldsymbol{\varepsilon}}_{\mathrm{e}}^{\mathrm{v}}} \frac{1}{\delta t}\right)^{-1} \mathbb{E}^{\mathrm{i}}\right]. \tag{6.41}$$

In order to contract the notation it is possible to introduce the two scalar quantities

$$h^{\mathrm{qi}} = -\frac{\partial f^{\mathrm{d,qi}}}{\partial p_{\mathrm{c}}^{\mathrm{qi}}} \frac{\partial p_{\mathrm{c}}^{\mathrm{qi}}}{\partial \varepsilon_{\mathrm{p,vol}}^{\mathrm{qi}}} \operatorname{tr}\boldsymbol{Q} \qquad h^{\mathrm{v}} = -\frac{\partial f^{\mathrm{d,v}}}{\partial p_{\mathrm{c}}^{\mathrm{v}}} \frac{\partial p_{\mathrm{c}}^{\mathrm{v}}}{\partial \varepsilon_{\mathrm{p,vol}}^{\mathrm{v}}} \operatorname{tr}\boldsymbol{Q}. \tag{6.42a}$$

$$g^{\mathrm{qi}} = -\frac{\partial f^{\mathrm{d,qi}}}{\partial \dot{\varepsilon}_{\mathrm{p,vol}}^{\mathrm{qi}}} \frac{1}{\delta t} \operatorname{tr}\boldsymbol{Q} \qquad g^{\mathrm{v}} = -\frac{\partial f^{\mathrm{d,v}}}{\partial \dot{\varepsilon}_{\mathrm{p,vol}}^{\mathrm{v}}} \frac{1}{\delta t} \operatorname{tr}\boldsymbol{Q}. \tag{6.42b}$$

From equations (6.38a) and (6.40)

$$\boldsymbol{Q} : \mathbb{E}^{\mathrm{ve}} : (\delta\boldsymbol{\varepsilon} - (\delta\lambda^{\mathrm{qi}} + \delta\lambda^{\mathrm{v}})\,\boldsymbol{Q}) - h^{\mathrm{qi}}\,\delta\lambda^{\mathrm{qi}} - g^{\mathrm{qi}}\,\delta\lambda^{\mathrm{qi}} = 0 \tag{6.43}$$

$$\delta\lambda^{\mathrm{qi}} = \frac{\boldsymbol{Q} : \mathbb{E}^{\mathrm{ve}} : (\delta\boldsymbol{\varepsilon} - \delta\lambda^{\mathrm{v}}\,\boldsymbol{Q})}{\boldsymbol{Q} : \mathbb{E}^{\mathrm{ve}} : \boldsymbol{Q} + h^{\mathrm{qi}} + g^{\mathrm{qi}}} \tag{6.44}$$

For the sake of effectiveness, a new scalar quantity has been introduced

$$s^{\mathrm{qi}} = \boldsymbol{Q} : \mathbb{E}^{\mathrm{ve}} : \boldsymbol{Q} + h^{\mathrm{qi}} + g^{\mathrm{qi}} \tag{6.45}$$

$$\delta\boldsymbol{\sigma} = \mathbb{E}^{\mathrm{ve}} : (\delta\boldsymbol{\varepsilon} - (\delta\lambda^{\mathrm{i}} + \delta\lambda^{\mathrm{v}})\,\boldsymbol{Q}) \tag{6.46}$$

$$= \mathbb{E}^{\mathrm{ve}} : (\delta\boldsymbol{\varepsilon} - \delta\lambda^{\mathrm{v}}\,\boldsymbol{Q}) - \frac{\boldsymbol{Q} : \mathbb{E}^{\mathrm{ve}} : (\delta\boldsymbol{\varepsilon} - \delta\lambda^{\mathrm{v}}\,\boldsymbol{Q})}{s^{\mathrm{qi}}}\,\mathbb{E}^{\mathrm{ve}} : \boldsymbol{Q}. \tag{6.47}$$

From equations (6.38b) and (6.46)

$$\boldsymbol{Q} : \left(\mathbb{E}^{\mathrm{ve}} : (\delta\boldsymbol{\varepsilon} - \delta\lambda^{\mathrm{v}}\,\boldsymbol{Q}) - \frac{\boldsymbol{Q} : \mathbb{E}^{\mathrm{ve}} : (\delta\boldsymbol{\varepsilon} - \delta\lambda^{\mathrm{v}}\,\boldsymbol{Q})}{s^{\mathrm{qi}}}\,\mathbb{E}^{\mathrm{ve}} : \boldsymbol{Q}\right) - h^{\mathrm{v}}\,\delta\lambda^{\mathrm{v}} + g^{\mathrm{v}}\delta\lambda^{\mathrm{v}} = 0 \tag{6.48}$$

$$\delta\lambda^{\mathrm{v}} = \frac{\boldsymbol{Q} : \mathbb{E}^{\mathrm{ve}} : \left(\delta\boldsymbol{\varepsilon} - \dfrac{\boldsymbol{Q} : \mathbb{E}^{\mathrm{ve}} : \delta\boldsymbol{\varepsilon}}{s^{\mathrm{qi}}}\,\boldsymbol{Q}\right)}{\left(1 + \dfrac{\boldsymbol{Q} : \mathbb{E}^{\mathrm{ve}} : \boldsymbol{Q}}{s^{\mathrm{qi}}}\right)\boldsymbol{Q} : \mathbb{E}^{\mathrm{ve}} : \boldsymbol{Q} + h^{\mathrm{v}} + g^{\mathrm{v}}} \tag{6.49}$$

where the denominator will be denoted with

$$s^{\mathrm{v}} = \left(1 + \frac{\boldsymbol{Q} : \mathbb{E}^{\mathrm{ve}} : \boldsymbol{Q}}{s^{\mathrm{qi}}}\right)\boldsymbol{Q} : \mathbb{E}^{\mathrm{ve}} : \boldsymbol{Q} + h^{\mathrm{v}} + g^{\mathrm{v}} \tag{6.50}$$

In order to obtain a direct relationship between $\delta\sigma$ and $\delta\varepsilon$, $\delta\lambda^{\mathrm{qi}}$ has been calculated from eq. (6.49) and eq. (6.44)

$$\delta\lambda^{\mathrm{qi}} = \frac{1}{s^{\mathrm{qi}}}\left[\boldsymbol{Q} : \mathbb{E}^{\mathrm{ve}} : \delta\boldsymbol{\varepsilon} - \frac{1}{s^{\mathrm{v}}}\left(\boldsymbol{Q} : \mathbb{E}^{\mathrm{ve}} : \left(\delta\boldsymbol{\varepsilon} - \frac{\boldsymbol{Q} : \mathbb{E}^{\mathrm{ve}} : \delta\boldsymbol{\varepsilon}}{s^{\mathrm{qi}}}\,\boldsymbol{Q}\right)\right)\boldsymbol{Q} : \mathbb{E}^{\mathrm{ve}} : \boldsymbol{Q}\right]. \tag{6.51}$$

The substitution of the equations (6.49) and (6.51) in eq. (6.40) allow the determination of the stress increment starting from strain and time increments

$$\begin{aligned}\delta\boldsymbol{\sigma} = \mathbb{E}^{\mathrm{ve}} : \Bigg\{ \delta\boldsymbol{\varepsilon} - \frac{1}{s^{\mathrm{qi}}} \Bigg[\boldsymbol{Q} : \mathbb{E}^{\mathrm{ve}} : \delta\boldsymbol{\varepsilon} \\ - \frac{1}{s^{\mathrm{v}}} \left(\boldsymbol{Q} : \mathbb{E}^{\mathrm{ve}} : \left(\delta\boldsymbol{\varepsilon} - \frac{\boldsymbol{Q} : \mathbb{E}^{\mathrm{ve}} : \delta\boldsymbol{\varepsilon}}{s^{\mathrm{qi}}} \boldsymbol{Q} \right) \right) \boldsymbol{Q} : \mathbb{E}^{\mathrm{ve}} : \boldsymbol{Q} \Bigg] \boldsymbol{Q} \\ - \frac{1}{s^{\mathrm{v}}} \left[\boldsymbol{Q} : \mathbb{E}^{\mathrm{ve}} : \left(\delta\boldsymbol{\varepsilon} - \frac{\boldsymbol{Q} : \mathbb{E}^{\mathrm{ve}} : \delta\boldsymbol{\varepsilon}}{s^{\mathrm{qi}}} \boldsymbol{Q} \right) \right] \boldsymbol{Q} \Bigg\} \end{aligned} \tag{6.52}$$

$$\begin{aligned}\delta\boldsymbol{\sigma} = \mathbb{E}^{\mathrm{ve}} : \delta\boldsymbol{\varepsilon} - \frac{1}{s^{\mathrm{qi}}} \Big[(\mathbb{E}^{\mathrm{ve}} : \boldsymbol{Q}) \otimes (\mathbb{E}^{\mathrm{ve}} : \boldsymbol{Q}) \Big] : \delta\boldsymbol{\varepsilon} \\ + \frac{\boldsymbol{Q} : \mathbb{E}^{\mathrm{ve}} : \boldsymbol{Q}}{s^{\mathrm{qi}}\, s^{\mathrm{v}}} \Big\{ \Big[(\mathbb{E}^{\mathrm{ve}} : \boldsymbol{Q}) \otimes (\mathbb{E}^{\mathrm{ve}} : \boldsymbol{Q}) \Big] : \delta\boldsymbol{\varepsilon} \\ - \frac{\boldsymbol{Q} : \mathbb{E}^{\mathrm{ve}} : \boldsymbol{Q}}{s^{\mathrm{qi}}} \Big[(\mathbb{E}^{\mathrm{ve}} : \boldsymbol{Q}) \otimes (\mathbb{E}^{\mathrm{ve}} : \boldsymbol{Q}) \Big] : \delta\boldsymbol{\varepsilon} \Big\} \\ - \frac{1}{s^{\mathrm{v}}} \Big\{ \Big[(\mathbb{E}^{\mathrm{ve}} : \boldsymbol{Q}) \otimes (\mathbb{E}^{\mathrm{ve}} : \boldsymbol{Q}) \Big] : \delta\boldsymbol{\varepsilon} \\ - \frac{\boldsymbol{Q} : \mathbb{E}^{\mathrm{ve}} : \boldsymbol{Q}}{s^{\mathrm{qi}}} \Big[(\mathbb{E}^{\mathrm{ve}} : \boldsymbol{Q}) \otimes (\mathbb{E}^{\mathrm{ve}} : \boldsymbol{Q}) \Big] : \delta\boldsymbol{\varepsilon} \Big\} \end{aligned} \tag{6.53}$$

$$\begin{aligned}\delta\boldsymbol{\sigma} = \mathbb{E}^{\mathrm{ve}} : \delta\boldsymbol{\varepsilon} - \left[\frac{1}{s^{\mathrm{qi}}} - \frac{\boldsymbol{Q} : \mathbb{E}^{\mathrm{ve}} : \boldsymbol{Q}}{s^{\mathrm{qi}}\, s^{\mathrm{v}}} \left(1 - \frac{\boldsymbol{Q} : \mathbb{E}^{\mathrm{ve}} : \boldsymbol{Q}}{s^{\mathrm{qi}}} \right) \right. \\ \left. + \frac{1}{s^{\mathrm{v}}} \left(1 - \frac{\boldsymbol{Q} : \mathbb{E}^{\mathrm{ve}} : \boldsymbol{Q}}{s^{\mathrm{qi}}} \right) \right] \Big[(\mathbb{E}^{\mathrm{ve}} : \boldsymbol{Q}) \otimes (\mathbb{E}^{\mathrm{ve}} : \boldsymbol{Q}) \Big] : \delta\boldsymbol{\varepsilon} \end{aligned} \tag{6.54}$$

The tangent operator results

$$\frac{\delta\boldsymbol{\sigma}}{\delta\boldsymbol{\varepsilon}} = \mathbb{E}^{\mathrm{ve}} - \left[\frac{1}{s^{\mathrm{qi}}} + \frac{1}{s^{\mathrm{v}}} \left(1 - \frac{\boldsymbol{Q} : \mathbb{E}^{\mathrm{ve}} : \boldsymbol{Q}}{s^{\mathrm{qi}}} \right)^2 \right] \Big[(\mathbb{E}^{\mathrm{ve}} : \boldsymbol{Q}) \otimes (\mathbb{E}^{\mathrm{ve}} : \boldsymbol{Q}) \Big] \tag{6.55}$$

6.4 Analysis of the model response

This section will analyse the general response of the model that will be compared comparison with the major features of the delayed behaviour of soil. The multi-axial constitutive approach presented in this paper represents the extension of the uni-axial model presented in Chapter 5 and maintains most of the principal constitutive hypotheses. In Chapter 5 the simulations of a wide range of oedometer tests and an extensive exposition of the calibration method have been presented. The results exposed for the uni-axial formulation hold their general effectiveness and the calibrations of the viscous parameters can be transposed to the multi-axial model with slight adjustments related to the introduction of a quasi-instantaneous mechanism instead of a purely instantaneous one.

6.4.1 Outline of the calibration of the model

Starting from the exposition of the theoretical constitutive hypotheses the model parameters can be divided in two groups:

1. the parameters describing the selected rate-independent elastoplastic framework: in the case of Modified Cam-Clay model there are five material constants (κ, λ, G, M, and m, defined in Section 6.2.1) that allow the definition of both the elastic and elastoplastic behaviour;

2. the viscous parameters that define the delayed behaviour. For the proposed model were defined six viscous parameters (Γ_{e}, α_{e}, $\Gamma_{\mathrm{p}}^{\mathrm{qi}}$, $\Gamma_{\mathrm{p}}^{\mathrm{v}}$, α_{p}, and $\dot{\varepsilon}_{\mathrm{min}}$ defined in Section 6.2.3).

The overall eleven parameters can be determined from triaxial and oedometer tests. The calibration of the elastoplastic material constants can be done following the classical rate-independent approach; in particular, it is important to highlight that the deformability (κ, and λ) and critical state parameters (M, and m) do not depend on the strain rate and can be determined with the classical testing procedures.

The viscous parameters can be efficiently evaluated from oedometer tests that allow the definition of both the viscoplastic and the viscoelastic behaviour. In particular, the repartition coefficients (α_{e} and α_{p}) and the viscous parameters (Γ_{e}, $\Gamma_{\mathrm{p}}^{\mathrm{v}}$) are related to each others (as demonstrated in Section 5.6) and can be approximately estimated starting from the ratio C_α/C_{c}. The reference strain rate $\dot{\varepsilon}_{\mathrm{min}}$ for the classical engineering application can be assumed as a constant (a suggestive value could be $\dot{\varepsilon}_{\mathrm{min}} = 10^{-15}$). The viscous coefficient of the

quasi-instantaneous yield surface can be assumed, as a first attempt, equal to $1/10\,\Gamma_{\mathrm{p}}^{\mathrm{v}}$ and subsequently it can be adjusted with a trial-and error procedure, for obtaining the best fitting with the experimental results.

The extensive experimental analysis performed on peats and inorganic clays in oedometric conditions reported in Chapters 2 and 5 allowed the calibration of the uni-axial model. On the same materials we conducted some triaxial tests with different strain rates and with stepwise variation of the strain rate. The simulation of this tests demonstrates that the calibrations of the viscous parameters obtained from oedometer tests hold true in the axisymmetric case without modifications.

6.4.2 Example of typical model response

The proposed model was developed starting from a series of experimental evidences. The delayed behaviour of soil can be explored by means of different laboratory tests (e.i creep, stress relaxation, constant rate of strain). A reliable constitutive model must be able to predict, in the same framework and with the same set of parameters, all the features arising from the different experimental approaches.

In the following the simulation of a series of triaxial tests with different characteristics will be proposed, for a detailed discussion of model response under oedometric conditions see Chapter 5.

Tertiary creep

One of the most peculiar aspects of the delayed behaviour of soils, is the mentioned phenomenon of tertiary creep. As stated in the presentation of the constitutive hypothesis, the model is able to simulate the creep behaviour in undrained conditions. Figure 6.15 compares the model results obtained simulating the experimental evidences of Vaid and Campanella (1977) and Vaid, Robertson, et al. (1979). Due to convergence problems (implying the need of implementing a line search algorithm), the simulations were temporary obtained with a single viscous yield surface, with constitutive parameters ($\Gamma_{\mathrm{p}}^{\mathrm{v}} = 0.006$).

The work by Vaid and Campanella (1977) (and the companion earlier paper by Campanella and Vaid (1974)) shows the tertiary creep on a normally consolidated clay subjected to an undrained compression. Figure 6.14, shows the comparison between experimental results and simulation of a series of creep tests. Observing the results of the simulation it is possible to highlight the capabilities of the model to simulate the creep rupture. The time of failure is

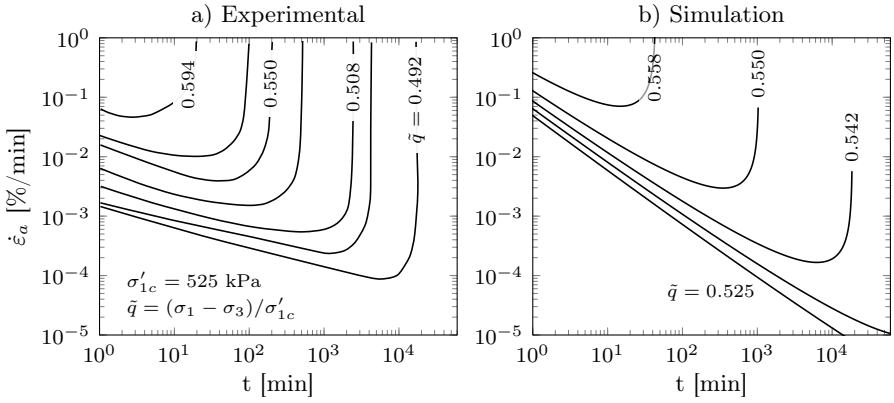

Figure 6.14: Simulation of undrained triaxial creep tests on normally consolidated clay (Vaid and Campanella 1977): a) experimental results; b) numerical simulations

approximatively caught by the model, but the range of deviatoric stress range interested by the tertiary creep is narrower than the measured one. Also the slopes of the numerical $\log \dot{\varepsilon}_a - \log t$ curves are slightly different from the experimental results. This differences could be related to material anisotropy that influences the orientation of the yield surface.

Figure 6.15, shows the comparison between experimental results and simulation of the creep tests on a highly overconsolidated clay performed by Vaid, Robertson, et al. (1979). The OCR at the beginning isotropic consolidation phase was about 22. The results were obtained assuming that the quasi-instantaneous and the viscous yield surfaces initially coincide with each other, thus soil response turns out to be equal to the response that would be obtained with a single viscous yield surface. Model simulations have the same behaviour of the normally consolidated clay, and are consistent with the experimental observations. Vaid, Robertson, et al. (1979) reported also the measurements of the pore pressure during the creep phase. Comparing the experimental pore pressure development with one predicted by the model, it is possible to highlight the good capability of the model to simulate the instability of the pore pressure related to the approach to the creep rupture. The main difference concerns to the pore pressure at the beginning of the creep phase that is related to the excess of pore pressure developed during the loading phase (and are deeply affected by a pos-

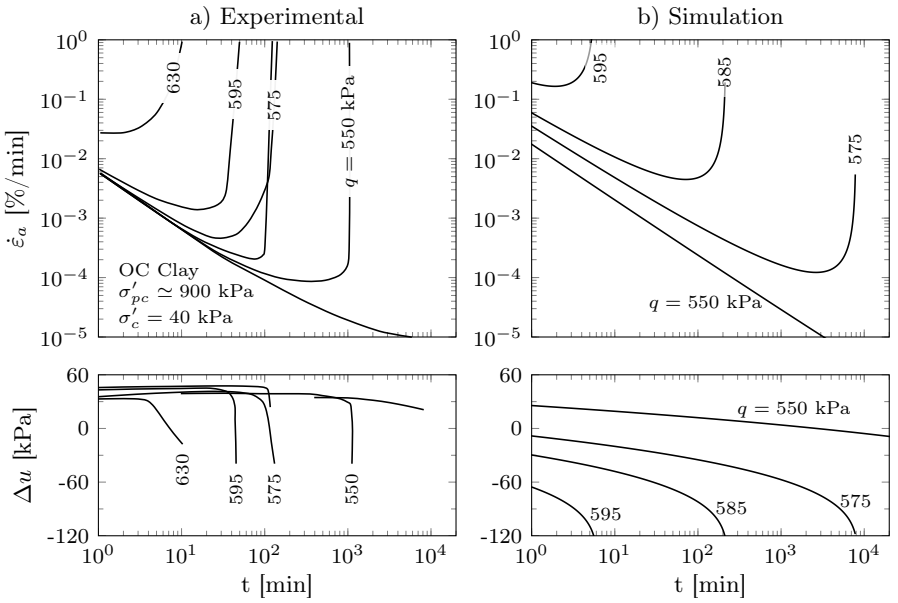

Figure 6.15: Simulation of undrained triaxial creep tests on highly overconsolidated clay (Vaid, Robertson, et al. 1979): a) experimental results; b) numerical simulations

sible elastic and plastic anisotropy). In this case, the slope of the $\log \dot{\varepsilon}_a - \log t$ curves is simulated with excellent accuracy by the model.

Strain rate effect in Normally Consolidated field

The stress-strain response in the normally consolidated regime follows the isotach behaviour. The analysis of the deviatoric stress-axial strain curve for a classical triaxial test performed at different strain rates shows that the increment in the loading rate causes an increment in the deviatoric stress. This effect is evident performing a triaxial test with stepwise variation of the strain rate. In this case the stress-strain curve jumps between the curves obtained at different undrained triaxial tests with constant strain rate (Tatsuoka et al. 1998).

Figure 6.16 shows the comparison between the undrained triaxial tests performed on Fujinomori clay by Tatsuoka et al. (1998) and the numerical simula-

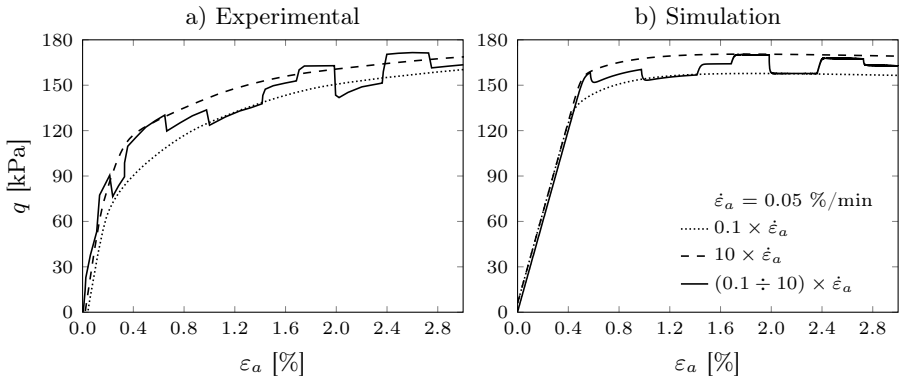

Figure 6.16: Simulation of TxCU tests with stepwise constant strain rate on Fujinomori clay (Tatsuoka et al. 1998): a) experimental results; b) numerical simulations

tion obtained with a typical calibration for inorganic clay. It can be observed that the model is able to catch the isotach behaviour and the size of the steps in the stress-strain curve can be simulated.

Relaxation response of Normally Consolidated clays

Another important aspect of the delayed response of soils is the stress relaxation behaviour. The typical relaxation test consists in loading the specimen until the relaxation strain is reached and then the strain is maintained constant for the relaxation period. The load can be possibly recovered and the relaxation procedure repeated at another strain level. Although the creep tests or the classical triaxial tests have been more extensively used for the study of time effects, the relaxation tests provide a better insight into the shear strength mobilization in clay (Silvestri et al. 1988).

The first exhaustive work on stress relaxation of clays was presented by Lacerda and Houston (1973) that performed several tests on different soils. One of the most interesting outcomes by Lacerda and Houston (1973) is the observation that the ratio between the relaxed deviatoric stress and the deviatoric stress at the beginning of relaxation phase is linear with logarithm of time after an initial latent time. In addition, the latent time is influenced by the strain rate of load before the beginning of relaxation.

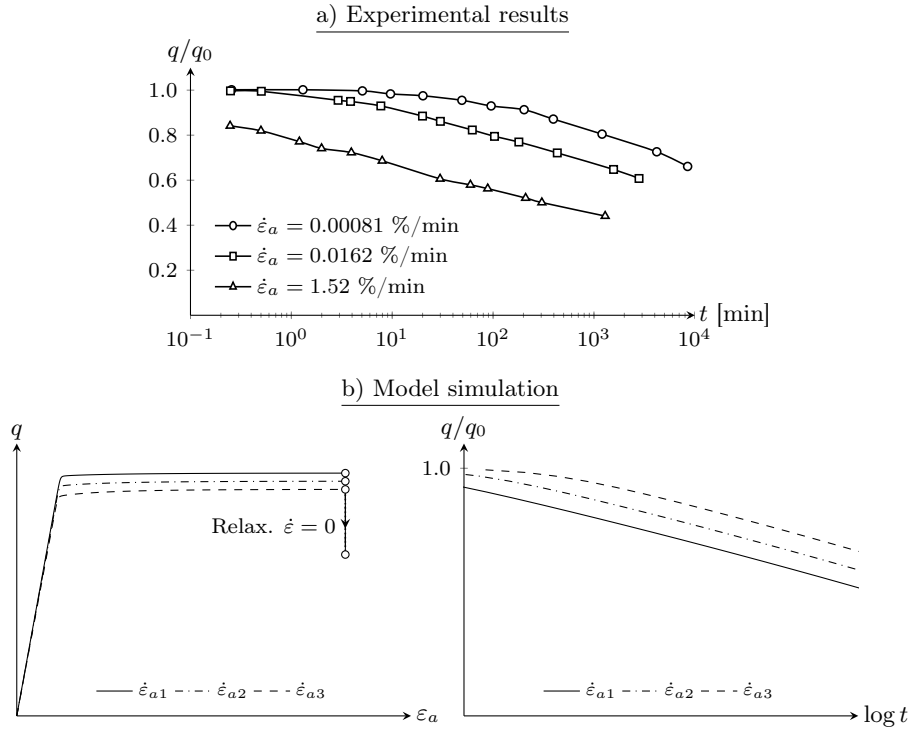

Figure 6.17: Simulation of strain rate effects in undrained triaxial relaxation test: a) experimental results (Lacerda and Houston 1973); b) model simulations

Figure 6.17 reports the model simulation of a series of relaxation tests performed after a shear phase conducted at different strain rates (with $\dot{\varepsilon}_1 > \dot{\varepsilon}_2 > \dot{\varepsilon}_3$). The curves before the relaxation phase are, as expected, influenced by the strain rate and the relaxation deviatoric stress ratio follows exactly the rules determined experimentally by Lacerda and Houston (1973).

Another interesting work on triaxial relaxation tests on clay is that one by Silvestri et al. (1988). These Authors conduced a series of undrained triaxial relaxation tests on a soft sensitive clay consolidated in both isotropic and anisotropic stress conditions. The main outcome of the work is the accurate measurements of the pore pressure during the relaxation tests (with

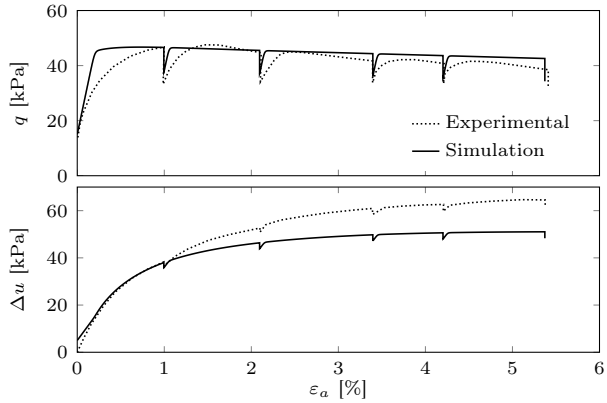

Figure 6.18: Simulation of undrained triaxial relaxation test on a soft sensitive clay. Isotropic Consolidated specimen, $\sigma'_c = 58kPa$ (Silvestri et al. 1988)

$\Delta u_{relax} \simeq 5 \div 10\%\, q$).

Figure 6.18 shows the results of one of the Silvestri et al. (1988) tests as compared with model simulations. The considered specimen was isotropically consolidated at the effective pressure of 58 kPa, loaded with the strain rate of 0.33%/h and submitted to various relaxation phases of 24 hours. It is worth noting the excellent agreement between the simulation and the experimental curves. In particular the deviatoric stress and the excess of pore pressure drops during the relaxation phase are modelled with very good accuracy. The difference in the final pore pressure is mainly related to the anisotropy of the experimental specimen (that implies a rotation in the orientation of the yield surface) with respect to the isotropy of our model.

Highly Overconsolidated clay behaviour

The time dependent behaviour of highly overconsolidated clays has been less investigated with respect to the normally consolidated ones. One of the most relevant experimental observation of strain rate effect on overconsolidated clays is the dependence of the peak strength on the rate of loading (Vaid, Robertson, et al. 1979; Lefebvre and LeBoeuf 1986; Zhu et al. 1999). An interpretation of this aspects has been outlined by Tavenas et al. (1978), and summarized

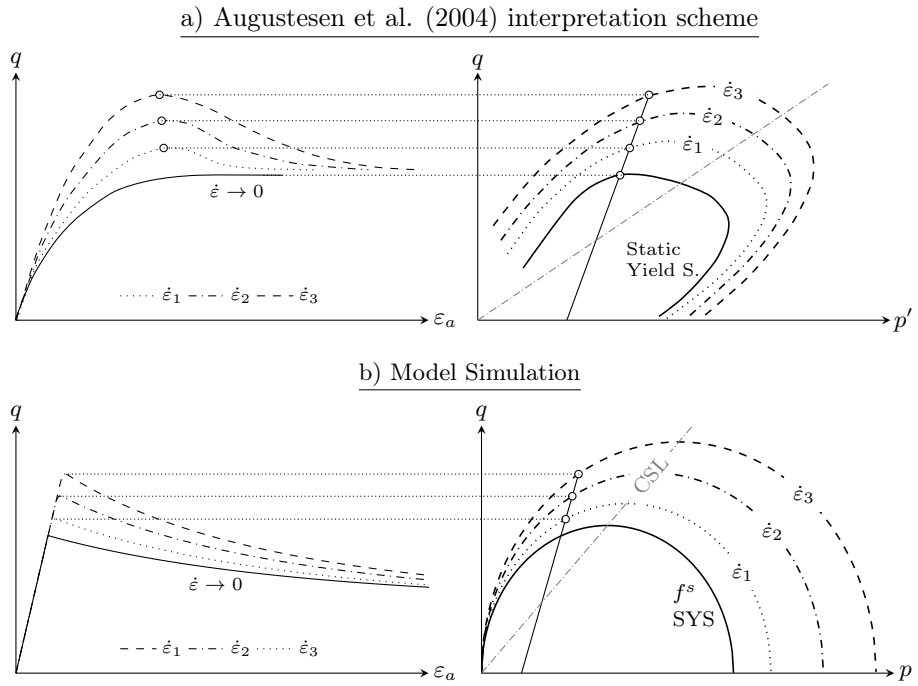

Figure 6.19: Strain rate effect on highly OC clay: a) interpretation scheme by Augustesen et al. (2004); b) model simulation.

by Augustesen et al. (2004) that reports an interesting sketch comparing the stress-strain curves to the *limit state surfaces* depending on the strain rates.

The simulation of triaxial drained tests with different strain rates on highly overconsolidated clay is reported in figure 6.19. The results were obtained assuming that the quasi-instantaneous and the viscous yield surfaces initially coincide with each other (thus soil response turns out to be equal to the response that would be obtained with a single viscous yield surface). The stress-strain curves are related to the relative *limit state surfaces* (that corresponds to the *dynamic yield surface* in correspondence of the peak strength). The simulated behaviour is consistent with the experimental results by the cited authors. The peak strength is affected by the strain rate while the stress at the critical state converged to the same final value for the specimens loaded with extremely low

strain rate.

A further interesting aspect related to the variation of the peak strength is the response to stepwise variation in the strain rate.

6.5 Comparison between model simulations and experimental results

A triaxial consolidated drained test was performed by the author on a peat remoulded sample of Levico peat. The soil properties of Levico peat have been shown in Section 3.2. The remoulded sample was obtained by adding distilled water up to a water content approximately $1.5 \times w_L$, by pouring the liquid soil into a consolidation cell and by consolidating at the vertical stress of 30 kPa in order to leave a sufficient consistency to enable the preparation of the triaxial specimen. When mounted in a Bishop-Wesley triaxial apparatus (Bishop and Wesley 1975) with side drains the specimen was subjected to saturation and isotropic consolidation up to 700 kPa and then unloaded up to 70 kPa resulting in an over-consolidation ratio of 10. The loading-unloading process lasted for about one month. After the consolidation phase the sample was sheared with stepwise strain rate with three different strain rates ($v_1 = 4.2 \times 10^{-3}$ %/min, $v_2 \simeq 5.1 \times 10^{-4}$ %/min and $v_3 \simeq 2.0 \times 10^{-4}$ %/min). The greater strain rate was selected in order to maintain the shearing phase drained (Head and Epps 2014).

Figure 6.20 shows the results of the drained triaxial test performed on Levico Peat. The stepwise variation of the strain rate has been highlighted. The change in the loading rate has a great influence on the stress-strain response, as observed in the normally consolidated regime, while has negligible influence on the volumetric strain.

Figure 6.20 shows also model simulations. The peak in the first stage markedly overestimated the real behaviour. This effect is related to the shape of the Modified Cam-Clay yield surface which does not match very well the real soil yield surface in the overconsolidated regime. The latter in fact is better represented by the Hvorslev surface. The overestimation of the elastic field leads to the excessively large peak in the stress-strain curve and could be better simulate adopting a more realistic yield surface. Despite the erroneous simulation of the first phase the subsequent part of the curve is well simulated. In particular, the stepwise variation in the deviatoric stress, due to the change in the strain rate, is predict with good accuracy as well as the volumetric strain behaviour.

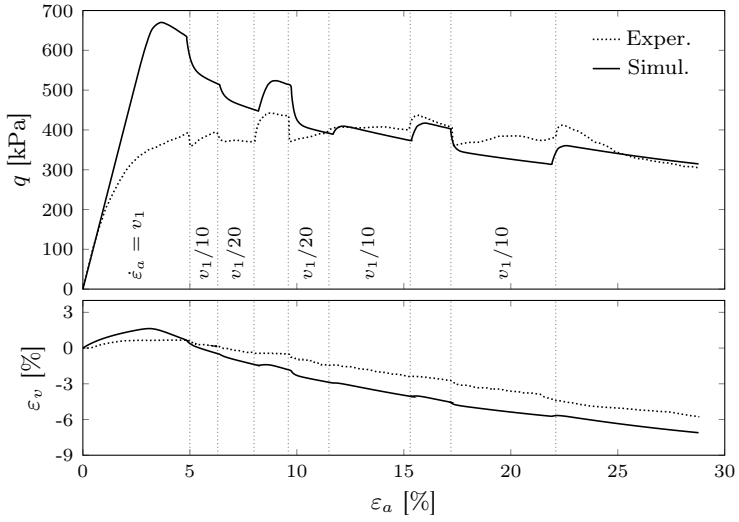

Figure 6.20: Simulation of drained triaxial test on overconsolidated remoulded Levico peat

6.6 Conclusions

The proposed multi-axial formulation is the extension of the uni-axial described in Chapter 5 by using the framework of viscoplastic overstress theory.

The key ingredients of the model are the strain decomposition in four components (elastic and plastic, quasi-instantaneous and viscous), the logarithmic viscosity function, and the unitary framework to modelling the response of NC and OC clays. These three ingredients permit to accurately simulate the major features of viscous response in a wide range of conditions. In particular, the tertiary creep phenomenon in undrained conditions, the strain rate effect in NC and OC regimes and the stress relaxation can be efficaciously simulated with the proposed approach.

CHAPTER 7

Simulation of the settlements evolution of an embankment built on organic clay

This chapter describes the simulation of the settlement of an embankment founded on a thick layer of organic clay by using the proposed constitutive approach. The case of study is the Torchio embankment (Province of Trento, Italy) that settles of about 1 m during the first year from the beginning of the construction. The simulation has been conducted through a simplified approach by using the 1D proposed model, and the results are in excellent agreement with field measurements.

7.1 Introduction

The aim of a constitutive model in the field of civil engineering is to describe the material behaviour in order to predict the response of real structures and to supply reliable tools for the optimal design of structural and infrastructural systems. In geotechnical engineering the problem of modelling is even more complex due to the uncertainty in the definition of soil mechanical properties and of their spatial distribution.

The validation of the constitutive model conducted on the base of laboratory tests is extremely useful to test the capabilities of the framework to catch different aspects of soil behaviour. Nevertheless, the application to real problems is much more complex due to errors in determining the real soil parameters

Figure 7.1: Aerial picture of the Torchio roundabout, embankment, and bridge abutment (http://www.provincia.tn.it/).

and the effective boundary conditions. This Chapter is describes the application of the uni-dimensional model to the simulation of the settlements of a road embankment founded on a thick layer of organic clay.

7.2 Description of the site and geotechnical investigations

The real case examined is the embankment located in Torchio, in the district of Pergine Valsugana (Trentino, northern Italy). The infrastructure was built in 2009 and consists of two parts: a trapezoidal embankment that connects a road bridge to the crossing, and the circular embankment of the roundabout (Figure 7.1).

The thickness of the embankment is of about 8 m at the roundabout and 10.5 m at the bridge abutment, and its side slope is of about 60° with an intermediate berm. The specific weight of the embankment is of $19\,\mathrm{kN/m^3}$. The sides were reinforced through geotexiles, and the embankment foundation in proximity of the bridge has been reinforced with a large number of piles to reduce the settlements of the road near the bridge abutment.

The subsoil in the area of Torchio embankment has been investigated through a series of geotechnical boring. The resulting stratigraphy consists of a thick layer of silty sand that lies on a thick layer of organic silty clay. In many areas

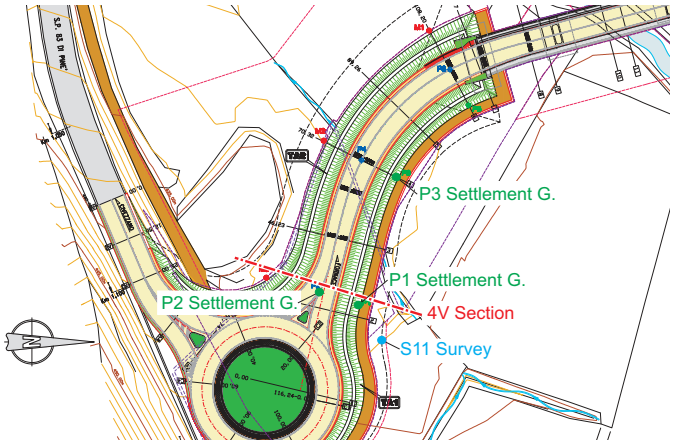

Figure 7.2: Plane view of the road crossing with the position of the settlement gauge P2, of the geotechnical boring S11, and of the examined section S4.

narrow layers of peat have also been founded. The bedrock depth is variable and grows with the distance from the roundabout.

The model simulation here shown has been conducted referring to the section 4V (Fig. 7.1), situated in proximity of the roundabout to avoid the perturbation effects of the piles installed near the bridge abutment.

Among the geotechnical investigations available for the site of Torchio, the most interesting for our simulations is boring S11, that was performed nearby the roundabout (Fig. 7.1). The stratigraphy deduced from boring S11 is shown in Figure 7.3 and consists of a layer of organic silt 1.0 m thick, under which there are a layer of silty sand 8.3 m thick, a layer of peat 1.10 m thick, a layer of organic silty clay 7.3 m thick, a thin gravel layer, and the bedrock at depths in excess of 19.70 m. The ground water table is 1.0 m deep.

From boring S11 an undisturbed sample with a Shelby sampler was obtained, with a diameter of 101.6 mm 12.35 m depth (SH1). The index properties of the soil obtained through laboratory characterization are shown in Table 7.4. The soil can be classified as organic silty clay of medium plasticity. The oedometric compression curve of the test performed on undisturbed sample SH1 is shown in Figure 7.4, and the related compression and swelling indexes are of 0.499 and 0.147 respectively. The preconsolidation pressure evaluated with Casagrande's

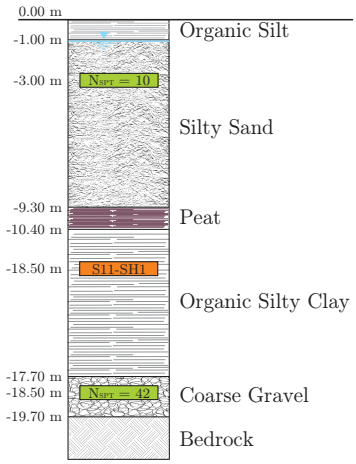

Figure 7.3: Stratigraphy of Torchio embankment soil obtained from S11 boring.

well-known graphical method is about 90 kPa.

The mechanical properties of sand and gravel layers can be deducted from the standard penetration tests performed at 3.0 and 18.0 m depth. In particular, the values of N_{SPT} were 10 for the silty sand layer at 3.0 m depth, and 42 for the gravel layer at 18.0 m depth.

The peat layer has not been subjected to any kind of mechanical investigation. In the following the properties of this thin layer will be assumed like those of a typical Trentino peat (see Chapter 3).

Starting from field and laboratory investigation performed in the design phase, the engineers evaluated the risk of great settlements of the embankment and prescribed the realization of a high number of piles in proximity of the bridge abutment to avoid excessive settlement of the bridge. In addition, a series of fixed extensometers was installed from the beginning of the construction to monitor the evolution of vertical deformation of the embankment.

7.3 Measurements of embankment settlements

In order to evaluate the settlements of the embankment due to the construction a series of fixed extensometers has been installed in different points of the

Specimen	SH1
Mean Specific Gravity G_s	2.07
Natural water content w (%)	68.2
Liquid limit w_L (%)	59.1
Plastic limit w_p (%)	44.3
Plastic index I_p (%)	14.8
Compression index C_c	0.499
Swelling index C_s	0.147

Table 7.1: Index properties from boring S11, specimen SH1 (18.5 m deep).

embankment. Figure 7.1 shows the positions of the three settlement gauges: P1 and P2 have been placed near the roundabout insertion (at Section 4V) in the centre of the embankment and at the toe, respectively, and P3 has been collocated at the toe of the embankment next to the piles improved foundation of the embankment.

The installation of the settlement gauges dates back to the beginning of June 2009 and the construction began at the beginning of August. The construction of the embankment can be sketched in two phases: the first phase involved the construction of the embankment up to the intermediate berm and took about 30 days, from August to September 2009; the second phase involved the upper layer of the embankment from the berm to the road level and was conducted in 15 days starting from the beginning of April 2010. The construction stage versus time has been reported in Figure 7.5a, in which $q_a/q_{a,max}$ represents the normalized load of the embankment with reference to the final load per unit of area.

Figure 7.5 shows the measured settlements of the three extensometers gauges SG 1-SG 2-SG 3. It is possible to highlight that near the roundabout (where the embankment is founded on the natural soil) the settlement is of about 1.00 m in the centre (SG2), and about 0.80 m at the toe of embankment (SG1). The settlement measured by the extensometers located in the zone affected by the presence of the foundation piles amounted to about 0.20 m. From an engineering point of view it is worth noting that the installation of the piles for the reduction of the settlements in proximity of the bridge abutment effectively reached their scope. On the other hand, the differential settlement between point P1 and P3

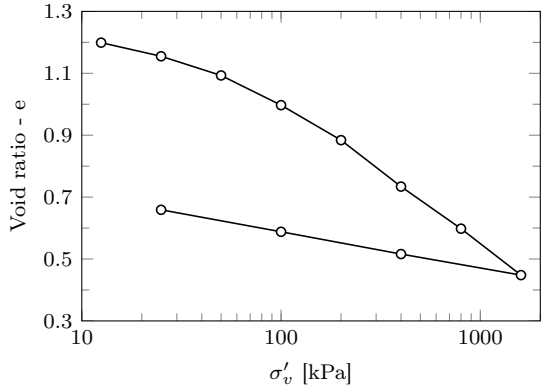

Figure 7.4: Oedometric Compression Curve for boring sample SH1 - S11.

(that are distant about 40 m) is more than 0.6 m after one year. This value is incompatible with the serviceability of the road and needs a series of expensive maintenance operations.

Another interesting observation that can be obtained from the settlement gauges measurements is the huge secondary deformation of the soil. Starting from the oedometric test results, it is possible to estimate the coefficient of consolidation and to evaluate when the primary consolidation (EOP) ended by means of the consolidation theory (Terzaghi 1925). c_v for the thick clay layer is about $5.6 \times 10^{-2}\,\mathrm{cm}^2/\mathrm{s}$, and the length of drainage path is of 4.15 m; the resulting EOP is of about 40 days. The settlement between the EOP and the beginning of the second construction phase measured by SG 2 is of about 0.20 m; the secondary settlement accumulated in a few months is about $25 \div 30$ % of the primary one.

7.4 Finite element simulation

The problem of the embankment of Torchio involves a multiaxial state of stress and should be considered with a three-dimensional approach. In this phase a preliminary mono-dimensional analysis has been performed in order to evaluate the capability of the constitutive relationship to simulate the most important features of the structure response. A global three-dimensional analysis will be presented in a future work. Despite the huge simplification introduced by the

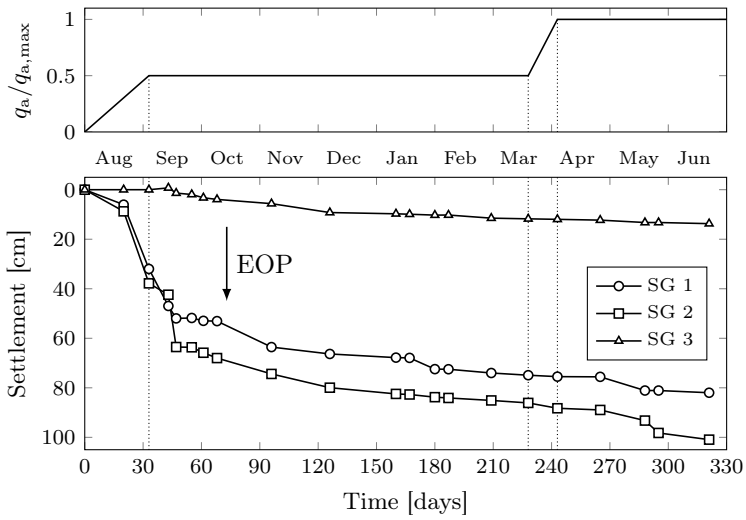

Figure 7.5: Settlements measured after the embankment construction.

mono-dimensional assumption, the results obtained with the simple 1D model provide useful information about the efficacy of the proposed constitutive approach.

The reduction of the 3D problem to uni-dimensional case has been performed by estimating the increments of total vertical stress induced by the embankment construction in the different layers. This estimation was based on the elasticity theory of semi-infinite half space by taking into account the presence of the embankment and of the roundabout.

The hydro-mechanical coupled analyses were performed with the commercial FEM code ABAQUS (Hibbitt et al. 2009), by using axial symmetric elements having linear pore pressure (4 nodes) and quadratic solid displacements (8 nodes). The element size in vertical direction (Y) is 0.1 m, and null horizontal displacements were imposed at all nodes. The resulting mesh consists of 195 elements, involving about 2380 degrees of freedom. Figure 7.6 shows the finite element mesh with the applied boundary conditions and the adopted stratigraphy.

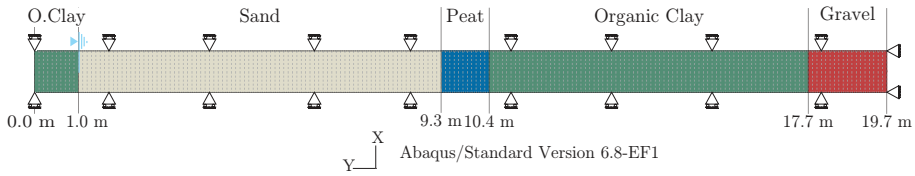

Figure 7.6: Finite element mesh used for 1D analysis of Torchio embankment.

7.4.1 Calibration of the constitutive parameters

The calibration of the constitutive parameters has been performed from the available laboratory and field investigations. In particular, the oedometer test of sample S11-SH1 and the Standard Penetration Tests performed during boring S11 has been used.

The oedometer test performed on the undisturbed specimen SH1 of organic clay (Fig. 7.4) was simulated with the 1D model following the calibration procedure described in Sections 5.6 and 5.7. The best calibration values are sum-

Param.	Torchio Org. Clay$^{(1)}$	Torchio Peat$^{(2)}$
κ	0.03	0.09
α_e	0.1	0.05
Γ_e	0.02	0.1
λ	0.1	0.4
α_p	0.1	0.05
Γ_p	0.05	0.1
$\dot{\varepsilon}_{min}$ [1/min]	10^{-10}	10^{-10}
σ^i_{pc} [kPa]	90	70
σ^v_{pc} [kPa]	50	70
K [m/s]	1.67×10^{-8}	1.67×10^{-8}

$^{(1)}$: calibrated on S11-SH1 oedometer test
$^{(2)}$: assumed from typical peat values (Chapter 3)

Table 7.2: Calibrated constitutive parameters for Torchio organic clay and peat.

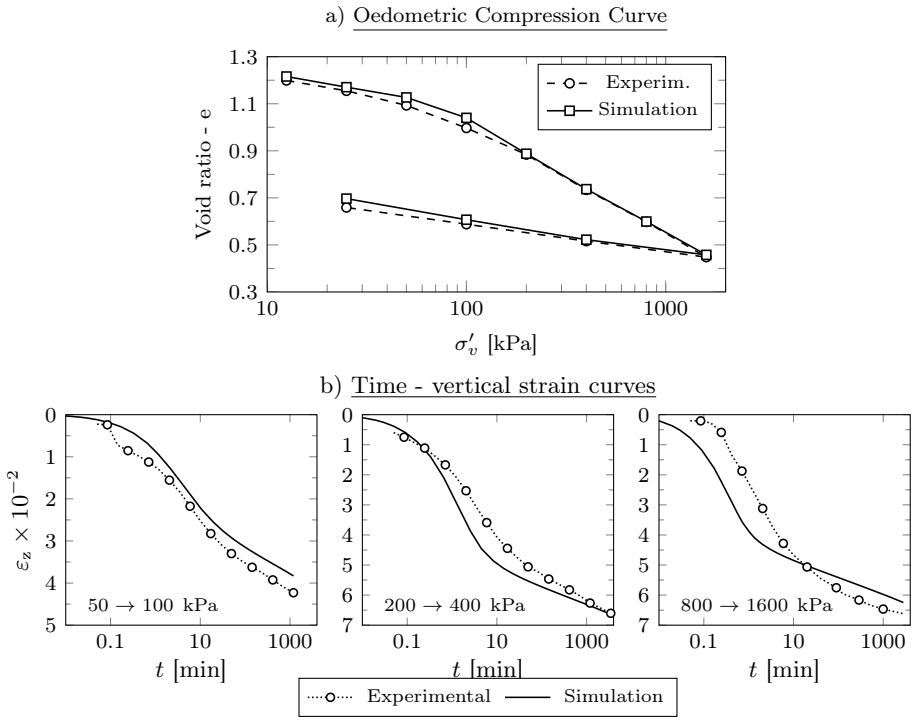

Figure 7.7: Simulation of oedometer test S11-SH1:
a) oedometer compression curve;
b) examples of time-vertical strain curves.

marized in Table 7.2.

The results in terms of oedometer compression curve are shown in Figure 7.7a. The agreement between the experimental and the simulated curve is excellent.

Another fundamental aspect of the calibration procedure is the comparison between the laboratory and simulated time-vertical strain curves during the oedometric steps. This comparison allows a direct evaluation of the coefficient of secondary consolidation, and the precision of the calibration with respect to the secondary effects can be easily deduced. Figure 7.7b shows the evolution of

deformation of three oedometric steps. It is worth noting the agreement between experimental and simulated curves especially in terms of slope of secondary consolidation. The permeability of the organic clay layer was estimated from the oedometer test and results 1.67×10^{-8} m/s.

The final settlements of the embankment are mainly affected by the layer of organic clay (situated at 10.4-17.7 m depth) due to its high thickness and deformability. An accurate description of the organic clay behaviour leads to the good simulation of the overall response. For this reason, the mechanical properties of the other layers can be deduced from empirical correlations without distorting the simulation results.

In particular, the same calibration obtained for the thick organic clay layer was used also for the superficial layer of organic clay, and the peat layer was assumed similar to that of other peats (Section 5.8.1).

The incoherent layers of sand and gravel were assumed linear elastic, and their elastic coefficients were estimated starting from the standard penetration test performed during boring S11. Many studies suggested an empirical correlation between N_{SPT} and Young modulus for sand and gravel. In this application the following correlation was used (Bowles 1988):

$$E = \begin{cases} 600\,(N_{\mathrm{SPT}} + 6) & \text{for } N_{\mathrm{SPT}} \leq 15 \\ 600\,(N_{\mathrm{SPT}} + 6) + 2000 & \text{for } N_{\mathrm{SPT}} > 15 \end{cases}, \tag{7.1}$$

where the Young modulus E is expressed in KPa. The estimated young modulus were 12600 kPa for the sand layer (assuming $N_{\mathrm{SPT}} = 15$, slightly higher than the measured value at 3 m to account the depth effect), and 30800 kPa for the gravel layer. The Poisson's ratio and the permeability was assumed 0.35 and 1.67×10^{-4} m/s for both the incoherent soils (Bowles 1988).

7.4.2 Evaluation of stress increment induced by embankment construction

The increment of stress field induced by the embankment construction was estimated with the classical elastic solution for semi-infinite half space. The reference point considered in the simulation corresponds to the settlement gauge P2 of Figure 7.2. The geometry of the problem is sketched in Figure 7.8, and consists of a truncated cone that represents the roundabout, and a trapezoidal prism that represents the embankment. The estimation of the stress increment field has been performed by calculating the increments induced at each soil layer by the two equivalent uniform loads corresponding to the embankment (a

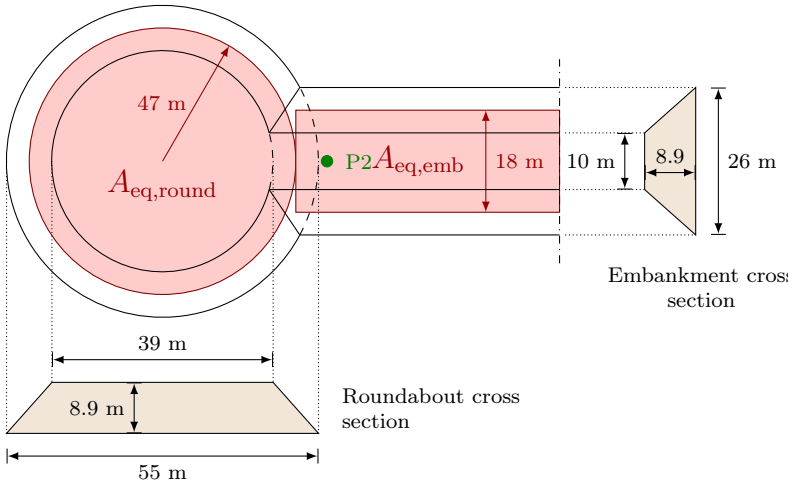

Figure 7.8: Sketch of the geometry for the determination of increment of stress field; $A_{\text{eq,emb}}$ and $A_{\text{eq,round}}$ are the equivalent areas for the estimation on stress increment

rectangular equivalent area) and the roundabout (a circular equivalent area). The dimensions of the equivalent areas and their position with respect to the reference point P2 are sketched in Figure 7.8. The superimposition of the two effects allows the estimation of the stress increment at each layer.

The load applied at the end of the construction on the equivalent areas was calculated from the specific weight of the embankment and results $q_{\text{a,max}} = 19\,\text{kN/m}^3 \times 8.9\,\text{m} = 169.1\,\text{kPa}$.

Starting from the geometrical characteristics of the problem it is possible to determine the stress increment field. From Boussinesq theory the stress increment at depth z induced by the rectangular loading area of embankment is:

$$\Delta\sigma_{\text{emb}} = \frac{q_{\text{a}}}{\pi}\left[\arctan\left(\frac{L\,B}{c\,z}\right) + \frac{L\,B\,z}{c}\left(\frac{1}{m^2} + \frac{1}{n^2}\right)\right], \tag{7.2}$$

where L is the major side of the loading area (100 m in the considered case), B is the minor semi-side of the loading area (9 m in the considered case); the

Layer	z [m]	Δz [m]	$\bar{z}$ [m]	$\Delta\sigma_{\text{emb}}$ [kPa]	$\Delta\sigma_{\text{round}}$ [kPa]	$\Delta\sigma_{\text{tot}}$ [kPa]
Org. Clay	0-1	1	0.5	84.86	75.77	160.62
Sand	1-2	1	1.5	84.70	74.54	159.25
	2-3	1	2.5	84.16	73.32	157.48
	3-4	1	3.5	83.08	71.95	155.02
	4-5	1	4.5	81.42	71.03	152.46
	5-6	1	5.5	79.27	70.01	149.28
	6-7	1	6.5	76.71	69.08	145.79
	7-8	1	7.5	73.90	67.81	141.70
	8-9.3	1.3	8.65	70.49	66.53	137.03
Peat	9,3-10,4	1.1	9.85	66.90	65.38	132.28
Org. Clay	10.4-11.4	1	10.9	63.81	63.85	127.66
	11.4-12.4	1	11.9	60.97	62.78	123.75
	12.4-13.4	1	12.9	58.26	61.71	119.97
	13.4-14.4	1	13.9	55.68	60.64	116.33
	14.4-15.4	1	14.9	53.25	59.57	112.83
	15.4-16.4	1	15.9	50.97	58.50	109.48
	16.4-17.7	1.3	17.05	48.53	57.13	105.66
Gravel	17.7-19.5	1.8	18.6	45.51	55.60	101.11

Table 7.3: Stress increment field induced by embankment and roundabout construction below point P2.

coefficients c, m, and n are geometric quantities defined as follows

$$c = \sqrt{L^2 + B^2 + z^2} \tag{7.3a}$$

$$m^2 = L^2 + z^2 \tag{7.3b}$$

$$n^2 = B^2 + z^2. \tag{7.3c}$$

The stress increment induced by the circular equivalent area was estimated starting from literature tables of $\Delta\sigma/q_{\text{app}}$ in function of z/R, where R is the radius of the loading area (Viggiani 1999).

The calculated stress field at the end of the construction is shown in Table 7.3, and was applied to the finite element mesh as equivalent body forces

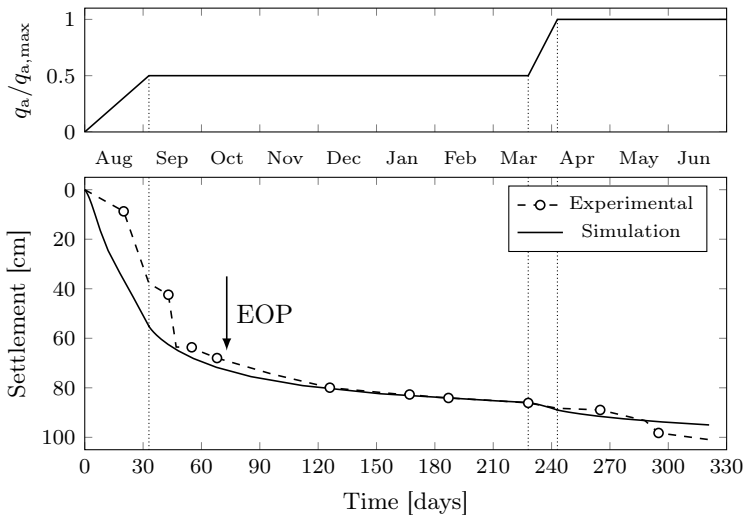

Figure 7.9: Simulation of Torchio embankment settlement ($q_{a,max} = 19\ kN/m^3\ \times 8.9\,m = 169.1\,kPa$).

following the loading history shown in Figure 7.5.

7.4.3 Results of finite element simulation

The finite element mesh shown in Figure 7.6 was used to simulate the settlements of point P2 (Fig. 7.2) in proximity of the roundabout insertion.

The mechanical parameters of the soil layers were calibrated or estimated starting from laboratory and field investigation obtained from boring S11 performed near the reference section 4V. The load history is reported in Figure 7.5 and is composed by two construction phases with an interruption of 6 months.

The results obtained from the simulation are shown in Figure 7.9. The match between the simulations and field measurements is excellent for both the primary and the secondary phase.

It is worth noting that the delayed effects on the real embankment are mainly related to the response of the thick layer of organic clay. The accurate calibration of the organic clay layer performed using an oedometer laboratory test allows the estimation of secondary behaviour of the entire model with very good accuracy.

7.5 Conclusions

This Chapter presents an application of the proposed constitutive approach to the simulation of the settlements of an embankment built on organic clay.

The presented elaboration is based on a simplified mono-dimensional problem by considering a column of soil below the measure point subjected to uniaxial strain conditions. The stress increment field has been estimated from elasticity theory and the mechanical properties of the layers have been calibrated starting from laboratory and field geotechnical borings conducted in proximity of the reference point. In particular, the viscous properties of organic clay layer have been calibrated by fitting the oedometric compression curve and the $t - \varepsilon_z$ curves with the simulation results.

Despite the simplification introduced adopting a mono-dimensional model, the resulted settlement are in excellent agreement with the measured values. This confirms the validation of the model obtained on laboratory tests.

A future interesting application is the simulation of the entire problem with the proposed multi-axial model taking into account the complex geometry of the real case.

CHAPTER 8

Conclusions

The extensive use of FEM for the design of civil structures requires increasing attention to the definition of models that provide a reliable response. In the field of geotechnical engineering this task is usually more difficult compared to structural analysis, due to the uncertainty in the definition of material properties and of their spatial distribution.

The response of real structures founded on clayey soils is deeply affected by time-dependent phenomena, and to obtain realistic simulations of real soil behaviour the use of a constitutive framework that accounts for time dependency in the formulation of the stress-strain law is essential.

In this work, a new modelling approach of the stress-strain-time behaviour of clayey soils is proposed. The model is formulated in the framework of overstress theory, by assuming the isotach concept as a viscous rule for soil's solid skeleton. In order to obtain the isotach response a logarithmic viscosity function is used.

The main innovative aspects of the proposed constitutive approach are:

- the definition of two deformation mechanisms for the instantaneous and the viscous parts of the deformation. This hypothesis allows the simulation of a wide range of soils with very different viscous behaviours. From the modelling point of view, splitting the plastic deformation into two mechanisms implies the definition of two yield surfaces: a quasi-instantaneous surface and a viscous surface that both follow the overstress viscoplastic theory;

- the presence of viscous deformations also in the elastic regime. The viscoelastic behaviour has been rarely accounted for in soil modelling, although is essential for the simulation of unloading and reloading phases;

- the multiaxial approach is general and can be applied to both normally consolidated and highly overconsolidated clays.

The presence of two viscous mechanisms with different characteristic time scales clearly highlights the existence of two micromechanical viscous mechanisms, that cause different deformations and rearrangements at grain-size level (for example: a compressive and a sliding rearrangements). A future development of this work will be the identification of the microscale mechanisms which are responsible for the two observed time scales. This goal can be achieved with further experimental evidences showing the viscous mechanism under isotropic compression and shear, and with microscopic investigations (e.g. SEM analyses).

The model has been implemented in the finite element code Abaqus in order to solve the hydro-mechanical coupled problem. A challenging aspect of the numerical implementation is the solution of the highly non-linear problem with an increased number of unknowns related to the four components of the total deformation, resulting from the introduction of two different elastic and plastic deformation mechanisms.

In order to validate the constitutive approach, several established literature experimental datasets have been simulated both in oedometric conditions (to validate the isotach concept; the concept of preconsolidation induced by ageing at constant stress; the effects of strain rate on the preconsolidation pressure; the concept of constant C_α/C_c ratio; and the secondary deformations induced by a small stress increment ratio), and triaxial conditions (to validate the strain rate effect both in normally consolidated and strongly overconsolidated regimes; the tertiary creep phenomenon in undrained triaxial tests; and the triaxial relaxation).

In addition, an extensive experimental program has been carried out on three different peats with very different organic contents. An extensive set of oedometer tests with various loading conditions and a number of triaxial tests have been carried out. The simulation of these experiments corroborates the capabilities of the model to predict the delayed behaviour of peat, also for very complicate boundary conditions.

This work is concluded with the simulation of the settlements of a real embankment founded on organic clay. Despite the introduced simplifying hypotheses, the simulation results are in excellent agreement with the field measurements of settlements.

Bibliography

Acosta-Martinez, H., F. Tatsuoka, and J.Z. Li (2005). "Viscous property of clay in 1-D compression: evaluation and modelling". In: *Proc. 16th ICSMGE, Osaka*, pp. 779–783.

Adachi, T. and F. Oka (1982). "Constitutive equations for normally consolidate clay based on elasto-viscoplasticity". In: *Soils and Foundations* 22.4, pp. 57–70.

Adachi, T. and M. Okano (1974). "A constitutive equation for normally consolidated clay". In: *Soils and Foundations* 14.4, pp. 55–73.

ASTM-D2435-11 (2011). *Standard Test Methods for One-Dimensional Consolidation Properties of Soils Using Incremental Loading*. West Consho-hock-en, PA. URL: `www.astm.org`.

ASTM-D2974-14 (2014). *Standard Test Methods for Moisture, Ash, and Organic Matter of Peat and Other Organic Soils*. West Conshohocken, PA. URL: `www.astm.org`.

ASTM-D422-63 (2007). *Standard Test Method for Particle-Size Analysis of Soils*. West Conshohocken, PA. URL: `www.astm.org`.

ASTM-D4318-10 (2010). *Standard Test Methods for Liquid Limit, Plastic Limit, and Plasticity Index of Soils*. West Conshohocken, PA. URL: `www.astm.org`.

ASTM-D6913-04 (2009). *Standard Test Methods for Particle-Size Distribution (Gradation) of Soils Using Sieve Analysis*. West Conshohocken, PA. URL: `www.astm.org`.

ASTM-D7015-13 (2013). *Standard Practices for Obtaining Intact Block (Cubical and Cylindrical) Samples of Soils*. West Conshohocken, PA. URL: `www.astm.org`.

ASTM-D854-14 (2014). *Standard Test Methods for Specific Gravity of Soil Solids by Water Pycnometer*. West Conshohocken, PA. URL: `www.astm.org`.

Augustesen, A., M. Liingaard, and P.V. Lade (2004). "Evaluation of time-dependent behavior of soils". In: *International Journal of Geomechanics* 4, pp. 137–156.

Barden, L. (1965). "Consolidation of Clay with Non-linear Viscosity". In: *Géotechnique* 15.4, pp. 345–362.

Berre, T. and K. Nersen (1972). "Oedometer tests with different specimen heights on a clay exhibiting large secondary compression". In: *Géotechnique* 22.1, pp. 53–70.

Berry, P.L. and B. Vickers (1975). "Consolidation of Fibrous Peat". In: *Journal of Geotechnical Engineering Division* 101.8, pp. 741–753.

Bishop, A.W. and H.T. Lovenbury (1969). "Creep characteristics of two undisturbed clays". In: *Proc. 7th ICSMFE*. Mexico, pp. 29–37.

Bishop, A.W. and L.D. Wesley (1975). "A hydraulic triaxial apparatus for controlled stress path testing". In: *Géotechnique* 25.4, pp. 657–670.

Bjerrum, L. (1967). "Engineering Geology of Norwegian Normally - Consolidated Marine Clays as Related to Settlements of Buildings". In: *Géotechnique* 17.2, pp. 83–118.

Bowles, J.E. (1988). *Foundation Analysis and Design*. Kentucky: MacGraw-Hill, p. 1125.

Campanella, R.G. and Y.P. Vaid (1972). "Creep rupture of a saturated natural clay". In: *6th International Congress on Rheology*, p. 18.

— (1974). "Triaxial and plane strain creep rupture of an undisturbed clay". In: *Canadian Geotechnical Journal* 11.1.

Casagrande, A. (1948). *Classification and identification of soils*. Soil mechanics series, no. 29; Publications from the Graduate School of Engineering, no. 432.

Christensen, R.W. and T.H. Wu (1964). "Analysis of Clay Deformation as a Rate Process". In: *Journal of the Soil Mechanics and Foundation Division, ASCE* 90.6, pp. 125–160.

Crawford, C.B. (1965). "The resistance of soil structure to consolidation". In: *Canadian Geotechnical Journal* 2.2, pp. 90–97.

Crawford, C.B. and K.I. Morrison (1996). "Case histories illustrate the importance of secondary-type consolidation settlements in the Fraser River delta". In: *Canadian Geotechnical Journal* 33.6, pp. 866–878.

de Souza Neto, E.A., D. Peric, and D.R.J. Owen (2008). *Computational Methods for Plasticity: Theory and Applications*. John Wiley, p. 791.

Den Haan, E.J. (1994). "Summary of session 1: One-dimensional behaviour". In: *Proc. Int. Workshop on Advances in Understanding and Modelling the Mechanical Behaviour of Peat*. Ed. by E. J. Den Haan, R. Termaat, and T. B. Edil. Rotterdam: Balkema, pp. 131–140.

Dhowian, A.W. and T.B. Edil (1980). "Consolidation Behavior of Peats". In: *Geotechnical Testing Journal* 3.3, pp. 105–114.

Di Prisco, C. and S. Imposimato (1996). "Time dependent mechanical behaviour of loose sands". In: *Mechanics of Cohesive-Frictional Materials* 1.September 1995, pp. 45–73.

Feda, J. (1992). *Creep of Soils, and related phenomena*. Elsevier S, p. 422.

Feng, T.W. (2000). "Fall-cone penetration and water content relationship of clays". In: *Géotechnique* 50.2, pp. 181–187.

Fox, P.J. and T.B. Edil (1996). "Effects of stress and temperature on secondary compression of peat". In: *Canadian Geotechnical Journal* 33.3, pp. 405–415.

Fox, P.J., T.B. Edil, and L.T. Lan (1992). "C_α/C_c concept applied to compression of peat". In: *Journal of Geotechnical Engineering* 118.8, pp. 1256–1263.

Gorman, C.T. (1981). *Strain-Rate Selection in the Constant-Rate-of-Strain Consolidation Test*. Tech. rep. Kentucky Transportation Research Program, p. 15.

Gorman, C.T. et al. (1978). "Constant-Rate-of-Strain and Controlled Gradient Consolidation Testing". In: *Geotechnical Testing Journal* 1.1, pp. 3–15.

Graham, J., J.H. Crooks, and A.L. Bell (1983). "Time effects on the stress-strain behaviour of natural soft clays". In: *Géotechnique* 33.3, pp. 327–340.

Gunaratne, M., P. Stinnette, and A.G. Mullins (1998). "Compressibility relations for peat and organic soil". In: *Journal of Testing and Evaluation* 26.1, pp. 1–9.

Hamilton, J.J. and C.B. Crawford (1959). "Improved determination of preconsolidation pressure of a sensitive clay". In: *Papers on soils, ASTM STP 254*. Philadelphia, pp. 254–271.

Hartlén, J. and W. Wolski (1996). *Embankments on Organic Soils*. Elsevier, p. 425.

Haupt, P. (2002). *Continuum Mechanics and Theory of Materials*. Springer Berlin Heidelberg, p. 643.

Head, K.H. (2014). *Manual of Soil Laboratory Testing - Vol I: Soil Classification and Compaction Tests*. III editio. Whitteles Publishing, p. 416.

Head, K.H. and R.J. Epps (2014). *Manual of Soil Laboratory Testing - Vol III: Effective Stress Tests*. 3 edition. Whitteles Publishing, p. 448.

Hibbitt, D., B. Karlsson, and P. Sorensen (2009). *ABAQUS Standard user's manual, Version 6.9-EF*. Hibbitt, K. Pawtucket, RI, USA.

Hinchberger, S.D. and G. Qu (2009). "Viscoplastic constitutive approach for rate-sensitive structured clays". In: *Canadian Geotechnical Journal* 46.6, pp. 609–626.

Hinchberger, S.D. and R.K. Rowe (2005). "Evaluation of the predictive ability of two elastic-viscoplastic constitutive models". In: *Canadian Geotechnical Journal* 42.6, pp. 1675–1694.

Hohenemser, K. and W. Prager (1932). "Uber die gesetze der mechanik isotroper kontinua". In: *ZAMM* 12, pp. 216–226.

Hu, L.B. and T. Hueckel (2007). "Creep of saturated materials as a chemically enhanced rate-dependent damage process". In: *International Journal for Numerical and Analytical Methods in Geomechanics* 31, pp. 1537–1565. DOI: 10.1002/nag.

Huat, B.B.K., A. Asadi, and S. Kazemian (2009). "Experimental Investigation on Geomechanical Properties of Tropical Organic Soils and Peat Department of Civil Engineering". In: *American Journal of Engineering and Applied Sciences* 2.1, pp. 184–188.

Kavazanjian, E. and J.K. Mitchell (1977). "A general stress-strain-time formulation for soils". In: *Proc. 9th International Conference on Soil Mechanics and Foundation Engineering*, pp. 113–120.

Kawabe, S., W. Kongkitkul, and F. Tatsuoka (2011). "1D Compression with Unload/Reload Cycles on Soft Clay and its Simulation". In: *Proc. 14th Asian Regional Conference on SMGE, Hong-Kong*.

Kawabe, S. and F. Tatsuoka (2013). "Creep characteristics of clay in one - dimensional compression with unloading / reloading cycles". In: *18th International Conference on Soil Mechanics and Geotechnical Engineering*. Leroueil, pp. 235–238.

Kazemian, S. et al. (2011). "A state of art review of peat : Geotechnical engineering perspective". In: *International Journal of the Physical Schiences* 6.8, pp. 1974–1981. DOI: 10.5897/IJPS11.396.

Kutter, B.L. and N. Sathialingam (1992). "Ealstic viscoplastic modeling of the rate-dependent behavior of clays". In: *Géotechnique* 42.3, pp. 427–441.

Lacerda, W.A. and W.N. Houston (1973). "Stress relaxation in soils". In: *Proceedings of the 8th International Conference on Soil Mechanics and Foundation Engineering*, pp. 221–227.

Ladd, C.C. et al. (1977). "Stress-deformation and strenght characteristics". In: *Proc. 9th International Conference on Soil Mechanics and Foundation Engineering*. Japan, pp. 421–494.

Lancellotta, R. (2008). *Geotechnical Engineering*. Ed. by Taylor & Francis, p. 520.

Landva, A. O. and P. La Rochelle (1983). *Compressibility and shear characteristics of Radforth peats*. West Conshohocken, PA.

Lansivaara, T. and S. Nordal (2000). "Strain rate approach to creep evaluation". In: *13th Nordic Geotechnical Conference NGM-2000*, pp. 25–32.

Lefebvre, G. and D. LeBoeuf (1986). "Rate Effects and Cyclic Loading of Sensitive Clays". In: *Journal of Geotechnical Engineering* 113.5, pp. 476–489.

Leonards, G.A. and P. Girault (1961). "A study of the one-dimensional consolidation test". In: *5th International Conference on Soil Mechanics and Foundation Engineering*, pp. 213–218.

Leonards, G.A. and B.K. Ramiah (1960). "Time effects in the consolidation of clays". In: *ASTM STP 254*. Philadelphia: ASTM, pp. 116–130.

Leroueil, S., M. Kabbaj, et al. (1985). "Stress–strain–strain rate relation for the compressibility of sensitive natural clays". In: *Géotechnique* 35.2, pp. 159–180. ISSN: 0016-8505. DOI: 10.1680/geot.1985.35.2.159.

Leroueil, S., F. Tavenas, et al. (1979). "Behavior of destructured natural clays". In: *Journal of Geotechnical Engineering Division* 105.GT6, pp. 759–778.

Liingaard, M., A. Augustesen, and P.V. Lade (2004). "Characterization of models for time-dependent behavior of soils". In: *International Journal of Geomechanics* 4, pp. 157–177.

Lo, K.Y. (1961). "Secondary compression of calys". In: *Journal of the Soil Mechanics and Foundation Division, ASCE* 87.SM4, pp. 61–87.

Lowe, J., E. Jonas, and V. Obrician (1969). "Controlled gradient consolidation test". In: *Journal of Soil Mechanics and Foundation Division* 95.SM1, pp. 77–97.

Malvern, L.E. (1951). "The propagation of longitudinal waves of plastic deformation in a bar of material exhibiting a strain-rate effect". In: *Journal of Applied Mechanics* 118, pp. 203–208.

Matsui, T. and N Abe (1985). "Elasto/viscoplastic constitutive equation of normally consolidated clays based on flow surface theory". In: *Int. Conf. on Numerical Methods in Geomechanics*, pp. 407–413.

Mesri, G. (1973). "Coefficient of secondary compression". In: *Journal of the Soil Mechanics and Foundation Division, ASCE* 99.SM1, pp. 123–137.

Mesri, G. and M. Ajlouni (2007). "Engineering Properties of Fibrous Peats". In: *J. of Geotechnical and Geoenvironmental Engineering* 133, pp. 850–866.

Mesri, G. and A. Castro (1987). "C_α/C_c concept and K_0 during secondary compression". In: *Journal of Geotechnical Engineering* 113.3, pp. 230–247.

Mesri, G. and Y.K. Choi (1985). "Settlement Analysis of Embankments on Soft Clays". In: *Journal of Geotechnical Engineering* 111.4, pp. 441–464. ISSN: 0733-9410.

Mesri, G. and T.W. Feng (1991). "Surcharging to Reduce Secondary Settlements". In: *Proceedings, International Conference on Geotechnical Engineering for Coastal Development. Theory to Practice, Yokohama, Japan*, pp. 359–364.

Mesri, G. and P.M. Godlewski (1977). "Time and Stress-Compressibility Interrelationship". In: *Journal of the Geotechnical Engineering Division* 103.5, pp. 417–430.

Mesri, G., D.O.K. Lo, and T.W. Feng (1994). "Settlement of Embankments on Soft Clays". In: *ASCE Specialty Conference - Geotechnical Special Publication 40, 1*, pp. 8–56.

Mesri, G., T.D. Stark, M. Ajlouni, et al. (1997). "Secondary compression of peat with or without surcharging". In: *Journal of Geotechnical and Geoenvironmental Engineering* 123.5, pp. 411–421.

Mesri, G., T.D. Stark, and C.S. Chen (1994). "C_α/C_c Concept Applied to Compression of Peat - Discussion". In: *Journal of Geotechnical Engineering* 120.4, pp. 764–767.

Murayama, S. (1983). "Formulation of stress-strain-time behavior of soils under deviatoric stress condition". In: *Soils and Foundations* 23.2, pp. 43–57.

Murayama, S. and T. Shibata (1958). "On the rheological characters of clay, Part 1". In: *Disaster Prevention Research Institute Kyoto University Bulletin* 26, pp. 1–43.

— (1961). "Rheological properties of clays". In: *Proc. 5th ICOSOMEF*. Paris, pp. 269–274.

Naghdi, P.M. and S.A. Murch (1963). "On the mechanical behaviour of viscoelastic/plastic solids". In: *Journal of Applied Mechanics* 30.3, pp. 321–328.

Namikawa, T. (2001). "Delayed plastic model for time-dependent behaviour of materials". In: *International Journal for Numerical and Analytical Methods in Geomechanics* 25.6, pp. 605–627.

Navarro, V. and E.E. Alonso (2001). "Secondary compression of clays as a local dehydration process". In: *Géotechnique* 51.10, pp. 859–869.

Nova, R. (1982). "A viscoplastic constitutive model for normally consolidated clay". In: *IUTAM Conference on Deformation and Failure of Granular Materials*. Delft, pp. 5–29.

Oka, F., T. Adachi, and Y. Okano (1986). "Two-dimensional consolidation analysis using an elasto-viscoplastic constitutive equation". In: *International Journal for Numerical and Analytical Methods in Geomechanics* 10.1, pp. 1–16.

Olszak, W. and P. Perzyna (1966). "The constitutive equations of the flow theory for a non-stationary yield condition". In: *Applied Mechanics 1966*, pp. 545–553.

Perzyna, P. (1963a). "The constitutive equations for rate sensitive plastic materials". In: *Quarterly of Applied Mathematics* 20.4, pp. 321–332.

— (1963b). “The constitutive equations for work-hardening and rate sensitive plastic materials”. In: *Proceedings of Vibration Problems*, pp. 281–290.
— (1966). “Fundamental problems in Viscoplasticity”. In: *ADVANCES IN APPLIED MECHANICS* 9, pp. 244–368.
— (1974). “Physical theory of viscoplasticity for small deformations”. In: *Mechanics Research Communications* 1, pp. 187–190.
Prager, W. (1937). “Mecanique des solides isotropes au delà du domaine elastique”. In: *Memorial Sci. Math.* 87.
Prevost, J.H. (1976). “Undrained Stress-Strain-Time Behavior of Clays”. In: *Journal of Geotechnical Engineering Division* 102.12, pp. 1245–1259.
Roscoe, K.H. and J.B. Burland (1968). “On the generalised stress-strain behaviour of wet clay”. In: *Engineering Plasticity*. Ed. by J. Heyman and F. A. Leckie. Cambridge. Cambridge, pp. 535–609.
Rowe, R.K., M.D. MacLean, and K.L. Soderman (1984). “Analysis of a geotextile-reinforced embankment constructed on peat”. In: *Canadian Geotechnical Journal* 21, pp. 563–576.
Santagata, M., A. Bobet, and C.T. Johnston (2008). “One-dimensional compression behavior of a soil with high organic matter content”. In: *Journal of Geotechnical and Geoenvironmental Engineering* 134.1, pp. 1–13.
Schmertmann, J.H. (1983). “Time effects on the stress-strain behaviour of natural soft clays - Discussion”. In: *Géotechnique* 33.3, pp. 433–444.
Sekiguchi, H. (1977). “Rheological characteristics of clays”. In: *Proc. 9th International Conference on Soil Mechanics and Foundation Engineering*, pp. 289–292.
Sheahan, T.C., C.C. Ladd, and J.T. Germaine (1994). “Time-Dependent Triaxial Relaxation Behavior of a Resedimented Clay”. In: *Geotechnical Testing Journal* 17.4, pp. 444–452.
Silvestri, V. et al. (1988). “Triaxial relaxation tests on a soft clay”. In: *Advanced Triaxial Testing of Soil and Rock, ASTM STP 977*, pp. 321–337.
Singh, A. and J.K. Mitchell (1968). “General Stress-Strain-Time Function for Soils”. In: *Journal of the Soil Mechanics and Foundations Division* 94.1, pp. 21–46.
Skrzypek, J.J. (1993). *Plasticity and creep*. Ed. by R. B. Hetnarski. CRC Press, p. 542.
Smith, R.E. and H.E. Wahls (1969). “Consolidation under constant rates of strain”. In: *Journal of Soil Mechanics and Foundation Division* 95.SM2, pp. 519–539.

Suklje, L. (1957). "The Analysis of the Consolidation Process by the Isotaches Method". In: *Proceedings of the Fourth International Conference on Soil Mechanics and Foundation Engineering*, pp. 200–206.

Tanabashi, Y. et al. (1988). "Case studies on long-term settlement of soft clay ground". In: *Proceedings: Second International Conference on Case Histories in Geotechnical Engineering, St. Louis*. 3, pp. 1655–1662.

Tatsuoka, F. et al. (1998). "Some new aspects of time effects on the stress-strain behaviour of stiff geomaterials". In: *Proc. of the 2nd Inter. Conf. on Hard Soils-Soft Rocks Napoli*.

Tavenas, F. et al. (1978). "Creep behavior of an undisturbed lightly overconsolidated clay". In: *Canadian Geotechnical Journal* 15.3, pp. 402–423.

Terzaghi, K. (1925). *Erdbaumechanik auf bodenphysikalischer grundlage*. F. Deutick. Leipzig u. Wien, p. 399.

Terzaghi, K., R.B. Peck, and G. Mesri (1996). *Soil Mechanics in Engineering Practice*. Ed. by John Wiley & Sons. Third. New York, p. 549.

Tian, W.M. et al. (1994). "Drained creep of undisturbed cohesive marine sediments". In: *Canadian Geotechnical Journal* 31.6, pp. 841–855.

Vaid, Y.P. and R.G. Campanella (1977). "Time-dependent behavior of undisturbed clay". In: *Journal of the Geotechnical Engineering Division* 103.7, pp. 693–709.

Vaid, Y.P., P.K. Robertson, and R.G. Campanella (1979). "Strain rate behaviour of Saint-Jean-Vianney clay". In: *Canadian Geotechnical Journal* 16, pp. 34–42.

Viggiani, C. (1999). *Fondazioni*. Napoli: Hevelius, p. 565.

Walker, L.K. and G.P. Raymond (1968). "The Prediction of Consolidation Rates in a Cemented Clay". In: *Canadian Geotechnical J.* 5.4, pp. 192–216.

Wang, W.M., L.J. Sluys, and R. De Borst (1997). "Viscoplasticity for instabilities due to strain softening and strain-rate softening". In: *International Journal for Numerical Methods in Engineering* 40, pp. 3839–3864.

Wang, Y.H. and D. Xu (2007). "Dual Porosity and Secondary Consolidation". In: *Journal of Geotechnical and Geoenvironmental Engineering* 133.7, pp. 793–801.

Whitman, R.V. and A.M. Richardson (1963). "Effect of Strain-Rate Upon Undrained Shear Resistance of a Saturated Remoulded Fat Clay". In: *Géotechnique* 13.4, pp. 310–324.

Willam, K.J. and E.P. Warnke (1975). "Constitutive models for the triaxial behavior of concrete". In: *Proceedings of the International Assoc. for Bridge and Structural Engineering*, pp. 19, 1–30.

Wood, D. Muir (1991). *Soil Behaviour and Critical State Soil Mechanics*. Cambridge, p. 462.

Yang, J. and A.P. Dykes (2006). "The liquid limit of peat and its application to the understanding of Irish blanket bog failures". In: *Landslides* 3, pp. 205–216.

Yin, J.H. (1999). "Non-linear creep of soils in oedometer tests". In: *Géotechnique* 49.5, pp. 699–707.

Yin, J.H. and J. Graham (1989). "Viscous elastic plastic modeling of one-dimensional time-dependent behavior of clays". In: *Canadian Geotechnical Journal* 26.2, pp. 199–209.

— (1994). "Equivalent times and one-dimensional elastic viscoplastic modeling of time-dependent stress-strain behavior of clays". In: *Canadian Geotechnical Journal* 31.1, pp. 42–52.

Yin, J.H., J.G. Zhu, and J. Graham (2002). "A new elastic viscoplastic model for time-dependent behaviour of normally and overconsolidated clays: theory and verification". In: *Canadian Geotechnical Journal* 39.1, pp. 157–173.

Zhu, J.G., J.H. Yin, and S.T. Luk (1999). "Time-Dependent Stress-Strain Behavior of Soft Hong Kong Marine Deposits". In: *Geotechnical Testing Journal* 22.2, pp. 118–126.